

© 2011 by Andrew Allen Mills. All rights reserved.

DESIGN, CONSTRUCTION, AND CHARACTERIZATION OF AN
ULTRA-SENSITIVE, HIGH-PRECISION FAST ION-BEAM SPECTROMETER FOR
THE STUDY OF MOLECULAR IONS

BY

ANDREW ALLEN MILLS

DISSERTATION

Submitted in partial fulfillment of the requirements
for the degree of Doctor of Philosophy in Chemistry
in the Graduate College of the
University of Illinois at Urbana-Champaign, 2011

Urbana, Illinois

Doctoral Committee:

Associate Professor Benjamin J. McCall, Chair
Professor Alexander Scheeline
Professor Martin Gruebele
Professor Gary Eden

Abstract

This dissertation details the design, construction and characterization of a sensitive, fast ion beam spectrometer to record the absorption spectra of molecular ions. It is the first work to use the noise immune cavity-enhanced optical heterodyne molecular spectroscopy (NICE-OHMS) technique in conjunction with a fast ion beam. Additionally, it is the first work outlining direct electronic spectroscopy in an ion beam. Direct spectroscopy of a fast molecular ion beam offers many advantages over competing techniques, including the generality of the approach to any molecular ion, the complete elimination of spectral confusion due to neutral molecules, and the mass-identification of individual spectral lines. Fast ion beam spectroscopy allows for sub-Doppler absorption spectra to be recorded. While some techniques, such as velocity modulation spectroscopy, provide semi-rigorous ion/neutral discrimination, the spectrometer employed in this dissertation provides a rigorous, spatial discrimination against background neutrals. The major challenge is the intrinsic weakness of absorption and dispersion signals resulting from the relatively low ion density in the beam.

The primary goal of designing this instrument is to enable acquisition of cold, rotationally-resolved, gas-phase spectra of molecular ions in the 2 - 5 μm region. For this dissertation in particular, the goal was to build an instrument able to acquire the uncooled, rotationally-resolved, gas-phase spectrum of N_2^+ in the near IR at 920 nm, using an ion beam. By characterizing this instrument in terms of linewidth and sensitivity, we are confident that we can move on to the next steps, of building a difference frequency generation laser, performing mid-IR spectroscopy, and implementing supersonic cooling. The spectra obtained in the mid-IR will be valuable for applied astronomical and fundamental spectroscopic research.

Direct infrared spectroscopy of an ion beam was pioneered by the Saykally group in 1989-1990, but has not been attempted since that time. Our ion beam instrument uses a Ti:Sapphire laser to produce near-IR (NIR) radiation at 920 nm. NICE-OHMS is set up using two electrooptic modulators and a medium finesse cavity ($F=450$) with a free spectral range of 113 MHz. The optical cavity increases the path length of absorption, and the heterodyne spectroscopy reduces the noise to near the shot noise limit. The laser is calibrated to sub-MHz accuracy using an optical frequency comb. A fast ion beam instrument was constructed, using the

most recent advances in ion beam technology, including cylindrical benders and a beam-modulated time-of-flight mass spectrometer. The cylindrical benders help to maximize the ion density in the interaction region, and the mass spectrometer offers improved resolution and online mass analysis. The ion beam is made collinear with the laser beam inside of the NICE-OHMS cavity. The NIR NICE-OHMS setup has a noise equivalent absorption of $2 \times 10^{-11} \text{ cm}^{-1} \text{ Hz}^{-1/2}$, which is 50 times more sensitive than the previous instrument. Several transitions of the $1-0$ band of the $A^2\Pi_u - X^2\Sigma_g^+$ Meinel system of N_2^+ with line widths of ~ 120 MHz have been measured. An optical frequency comb is used to calibrate the absolute value of the transition frequencies to within 8 MHz of the values obtained for a sub-Doppler calibrated positive column discharge. The rotational temperature of the ions in the plasma was measured to be ~ 750 K.

To my beloved wife, Elizabeth, who has brought eternal love and and happiness into my life.

Acknowledgments

I would like to gratefully acknowledge my advisor, Ben McCall, for the ideas and scientific guidance he gave me as I was building this instrument. I am also grateful to Professors Alexander Scheeline, Gary Eden, and Martin Gruebele for their time, thoughtful review, input, and guidance. I am indebted to the talented machinists at the School of Chemical Sciences machine shop: Bill Knight, Mike Harland, Tom Wilson, Roger Smith, Dave Hire, and Rob Brown, for their skill, patience and friendship. I will miss the Analytical and Physical Chemistry department secretaries, Julie Sides, Beth Myler, Connie Knight, and Theresa Struss, and thank them for their help along the way. I am grateful for Jim Wentz and his work helping me build, design, and troubleshoot electrical circuits, as well as designing and building many circuits. I am grateful to all the University of Illinois, School of Chemical of Sciences support staff and faculty who have in some way helped me in my education. I'm grateful to my undergraduate research advisor, Paul Farnsworth at BYU who began to teach me how to be a scientist, as well as my high school chemistry teacher Gary Kuykendal, who first interested me in chemistry.

I am grateful to many of my co-workers for their help and cooperation. I'd like to thank my former roommate and labmate, Brian Brumfield for being a good friend, teacher, and example of scientific thinking. I am indebted to Brian Siller's expertise in computer programming, and am grateful for the tutoring he gave me on C, Igor, LabWindows, LabVIEW and Python programming. Brian's scientific help was instrumental as he developed the laser locking system, and NICE-OHMS spectroscopy that eventually allowed us to record an ion beam signal. I am also grateful for the experience Holger Kreckel and Manori Perera brought to building up the final version of the ion beam instrument. It has been a pleasure to work with Mr. Michael Porambo as he has started to take over the work with the ion beam instrument. I'm grateful for Brian Tom, and the example he gave to the group by being the first to graduate, and teaching me a lot about leadership.

I'd like to thank Susanna Widicus Weaver for her help in getting started in lab, teaching me cavity alignment, and starting the development of the ion beam spectrometer. I'd like to thank Jeffrey Carter, who began work on the cold cathode ion source and provided friendship through the years, as well as Kyle Ford who also worked on the ion beam project. Kyle Crabtree and I enjoyed building the difference frequency

generation laser together, and we both learned a lot through that process. I enjoyed conversing with other members of the McCall group and thank them for the time and support they gave.

I would like to thank my family and close personal friends for their support throughout my doctoral program. I would not be at this point in my life if it weren't for my parents who always encouraged me to learn. I am grateful for my amazing wife, Elizabeth, whose love, patience, confidence, and care have been the mainstay of my happiness since we met.

Table of Contents

List of Tables	x
List of Figures	xi
Chapter 1 Introduction	1
1.1 Molecular Ions	1
1.2 Beginnings of Ion Spectroscopy	1
1.3 Velocity Modulation Spectroscopy	2
1.4 Fast Ion Beams	5
1.5 Indirect Ion Beam Methods	6
1.6 Non-Classical Molecular Ions	8
Chapter 2 Laser Systems	13
2.1 Titanium Sapphire Laser System	13
2.2 YAG Laser System	16
2.3 Difference Frequency Generation Laser System	20
2.3.1 Difference Frequency Generation Layout	21
2.3.2 Difference Frequency Generation Sellmeier Curves	25
Chapter 3 Optical Frequency Comb	30
3.1 Principles of Operation	31
3.1.1 Repetition Frequency Lock	34
3.1.2 Offset Frequency Lock	34
3.2 System Startup	37
3.2.1 DDS & Temperature Controller	37
3.2.2 Software & Modelocking	38
3.2.3 Obtaining Carrier Envelope Offset Beat	40
3.2.4 Carrier Envelope Offset and Repetition Frequency Locking	40
3.2.5 Frequency Doubled Comb Radiation	44
3.2.6 Collinearity of Comb and CW Radiation	44
3.2.7 Comb Radiation at the Correct Wavelength	45
3.2.8 Obtaining CW Beat Note	45
3.2.9 Optimizing CW Beat Note	46
3.3 Measurement of Ti:Sapphire laser	47
3.3.1 CW Beat Note Sign Determination	47
3.3.2 Carrier Envelope Offset Beat Note Sign Determination	49
3.3.3 Comb Mode Number Determination	51
3.3.4 Measurement of Laser Frequency	52
3.3.5 Recording Frequency Comb Data	53
3.4 Scanning Comb	54

Chapter 4 Spectroscopic Method	56
4.1 Noise Immune Cavity Enhanced Optical Heterodyne Molecular Spectroscopy	56
4.2 Optical Setup	57
4.3 Modifications to Laser Table	61
4.4 Cavity Setup	62
4.5 Cavity Mounts	62
4.6 Line shape and Sensitivity Equations	63
4.7 Detector	66
4.8 Expected Line Shape	68
4.9 Saturation Effects	70
Chapter 5 Fast Ion Beam System	78
5.1 Overall Design Approach	78
5.1.1 Previous Direct Absorption Measurements of Ion Beams	78
5.1.2 Overview of New Ion Beam Instrument	80
5.2 Vacuum Considerations	82
5.3 Instrument Base	86
5.3.1 Steel Pipe Holders	88
5.4 Cold Cathode Source	89
5.4.1 Source Construction and Operation	89
5.4.2 Source Power Supplies	92
5.5 Ion Optical System	93
5.5.1 Ion Optics Power Supplies	95
5.5.2 Extraction and First Einzel Lens	97
5.5.3 X-Y Steerers	97
5.5.4 Cylindrical Deflectors	97
5.6 First Faraday Cup	98
5.7 Achieving Ion Beam and Laser Beam Overlap	99
5.8 Second Cylindrical Deflector	100
5.9 Mass Spectrometer	101
5.10 Beam Profile Monitors	108
5.11 Brewster Windows	108
5.12 Spectroscopic Applications	109
Chapter 6 N_2^+ in the Ion Beam	112
6.1 Daily Experimental Procedure	113
6.2 Data Analysis	116
6.3 Doppler Split Examples	120
6.4 Comb Calibrated Spectra	124
6.5 Boltzmann Analysis	125
6.6 Sensitivity	126
6.7 Noise	129
Chapter 7 Future Work and Conclusions	131
7.1 Mid-IR NICE-OHMS DFG Laser	131
7.2 Indirect Terahertz Spectroscopy of HN_2^+	132
7.3 Indirect Terahertz Spectroscopy of Molecular Ions	137
7.3.1 Indirect Terahertz Spectroscopy of CH^+	137
7.3.2 Indirect Terahertz Spectroscopy of CO^+	141
7.3.3 Indirect Terahertz Spectroscopy of HCO^+	148
7.3.4 Indirect Terahertz Spectroscopy of HCNH^+ and HCS^+	151
7.4 Infrared Spectrum of C_3H_3^+	152

Appendix A	Appendix for Laser Drawings	155
A.1	Neutral Density Filter Wheels	155
A.2	SHG Oven Mount	155
A.3	Frequency Tripler	156
A.4	Peltier Cooling	157
A.5	LabWindows Temperature Controller Program	159
A.6	Sellmeier Curve Solving Program	180
A.7	Sellmeier DFG Temperature Lookup Table	181
A.8	NICE-OHMS Optics Mounts	187
Appendix B	Appendix for Optical Frequency Comb	188
B.1	Resetting Mode Lock	188
B.2	Photonic Crystal Fiber XYZ Stage Alignment	189
B.3	Enabling XML-RPC Server	190
B.4	Reading Comb Values from XML server	192
B.5	List of Python Commands	192
Appendix C	Appendix for Spectroscopic Methods	195
C.1	Phase Shifter Calibration	195
C.2	Laser Table Modifications	196
C.3	Brass Cavity Mounts I	197
C.4	Brass Cavity Mounts II	200
C.5	LabVIEW Data File Output	202
C.6	Lookup Table of Bessel Functions	204
C.7	Saturation Modeling Program	206
C.7.1	Experimental NIR Saturation	206
C.7.2	Theoretical MIR Saturation	208
Appendix D	Appendix for Ion Beam System	210
D.1	Welch Pump Exhaust Adapter	210
D.2	Varian Turbo Pump Water Cooling Adapters	210
D.3	80-20 Building Materials	211
D.4	Steel Pipe Holders	212
D.5	Source	214
D.6	Einzel Lens 1	216
D.7	Steerers	219
D.8	Cylindrical Deflectors	219
D.9	Faraday Cup 1	222
D.10	Drift Region	224
D.11	Einzel Lens 2	224
D.12	Faraday Cup 2	225
D.13	Beam Modulated Time of Flight Pulser Plates	227
D.14	MS Iris	229
D.15	Electron Multiplier Mount	229
D.16	Brewster Windows	231
Appendix E	Appendix for N_2^+ in Ion Beam	232
E.1	Igor Data File Reader	232
Abbreviations		263
References		265

List of Tables

2.1	Idler and pump wavelengths for DFG	23
2.2	The focusing parameter can be numerically integrated	27
2.3	DFG power parameters	28
2.4	Accuracy of temperature tuning curves.	28
4.1	Cavity parameters for the DLASFIB and SCRIBES instruments	61
4.2	Heterodyne detector calibration data.	68
5.1	Percentage species within N_2^+ ion beam.	106
5.2	Resolving power of TOF-MS and a Wien filter	107
6.1	Line fit data for determining if the signal is dispersion or absorption.	122
6.2	Data for calculating the rotational temperature of N_2^+ in the ion beam.	125
6.3	Expected and observed signal strengths for several representative scans of the ion beam.	128
7.1	Line list of HN_2^+	135
7.2	Reconstruction of rotational spectrum of HN_2^+	136
7.3	Rovibrational spectrum of CH^+ calculated with PGopher.	139
7.4	Rovibrational spectrum of CO^+ calculated with PGopher.	142
7.5	Rovibrational spectrum of HCO^+ calculated with PGopher.	149
A.1	PPLN Temperature for DFG quasi phase matching per poling channel.	181
B.1	Important command set for XML-RPC in Fiber Comb Control v0.4.25.	193
B.2	Remaining command set for XML-RPC in Fiber Comb Control v0.4.25.	193
C.1	Phase shifter calibration data with the phase shift (ϕ) as a function of voltage.	195
C.2	Phase shifter lookup table.	196
C.3	Column names and description.	203
C.4	Example of data file.	204
C.5	Values of Bessel functions.	204
D.1	80-20 parts purchased for construction of instrument base.	212

List of Figures

1.1	Illustration of lock-in demodulation and velocity modulation	4
1.2	Simulation of $C_3H_3^+$ at 25 K (red) and 1000 K (blue).	5
1.3	Mass of ions observed with velocity modulation spectroscopy	5
1.4	Illustration of ground penetration into ion source.	6
1.5	CH_5^+ spectrum with interfering CH_4 lines.	9
1.6	First attempt of ion beam instrument constructed at the University of Illinois.	10
2.1	Optical layout of Ti:Sapphire ring laser	14
2.2	Ti:Sapphire thick etalon transmission and dither lock.	15
2.3	Optical layout for YAG doubling PPLN and sub-Doppler iodine lock.	18
2.4	Doppler broadened YAG scan over an iodine line	19
2.5	Mechanical overview of Peltier cooling of iodine cell.	19
2.6	Base mount for the YAG.	20
2.7	Explanation of coherence length and QPM in a PPLN.	22
2.8	Optical overview of first DFG setup.	24
2.9	LabWindows program interface for controlling the PPLN crystal temperature.	25
2.10	Temperature curves for the DFG.	26
2.11	Numerical integrations of focusing parameter.	28
2.12	Examples of temperature transfer function of IR generation.	29
3.1	An octave spanning frequency comb can precisely measure its own offset frequency.	32
3.2	Pictures of optical frequency comb optical layout.	33
3.3	Optical layout of FC1500 frequency comb.	34
3.4	Electrical layout of the repetition frequency lock.	34
3.5	Electrical layout of the offset frequency lock.	35
3.6	Optical layout for making cw laser collinear to comb	36
3.7	Electrical signal path of unknown beat signal, starting from the avalanche photodiode	36
3.8	Location of electronics, fiberlaser, and amplifier switches for system startup.	37
3.9	Direct digital synthesizer and temperature controller	38
3.10	Comb software screen shot	38
3.11	Two spectrum analyzers and oscilloscope.	39
3.12	Software controls for the carrier envelope offset and repetition frequency lockboxes	41
3.13	Picture of the lockboxes used for locking the carrier envelope offset and repetition frequency	42
3.14	Oscilloscope trace of of the error signals generated by the locking electronics	42
3.15	A screenshot of the “Counters View” box of the Fiber-comb software.	43
3.16	A picture of the DDS screen	43
3.17	Dialogue for controlling the frequency doubled comb	43
3.18	Signal BNC connections for frequency comb	46
3.19	CW beat sign determination	48
3.20	Chart for determining sign of CW and CEO frequency	49
3.21	Explanation of how to determine the sign of the cw and CEO beat frequency	50

3.22	How to input sign value into LabView collection program	51
3.23	Unambiguous comb mode determination	52
3.24	Evaluation of unambiguous comb mode determination	53
3.25	How to determine which direction to scan the repetition frequency of the comb	55
4.1	Optical and detection layout for NICE-OHMS.	57
4.2	Relative phase shift of 150 MHz phase shifter with respect to input voltage.	59
4.3	How to determine the sign of the Doppler shift of the AOM	60
4.4	Cavity linewidth for a finesse of 450 with 113 MHz FSR and sideband spacing.	61
4.5	Designs for modifications to ion beam laser table.	62
4.6	Overview of stable cavity mounts made of brass.	63
4.7	Graphs indicating detector calibration	67
4.8	Doppler splitting due to the fast ion beam (a) and velocity modulation (b).	69
4.9	Effect of heterodyne on the absorption and dispersion signals	69
4.10	Velocity modulated heterodyne NICE-OHMS line shape for absorption and dispersion	70
4.11	Spectrum analyzer trace of the frequency modulated Ti:Sapphire laser	70
4.12	Bessel functions of the zeroth and first kind for modulation index between zero and two. . . .	71
4.13	Graphs of Bessel function values as a function modulation depth (β)	71
4.14	Transit time for a molecule passing a laser beam.	73
4.15	Spectral intensity profile for an ion passing collinearly through a laser beam.	73
4.16	Lineshape simulations as a function of saturation parameter	76
4.17	Simulation of lineshapes for absorption and dispersion with experimental saturation parameters	77
4.18	Simulations of absorption and dispersion for expected mid-IR power	77
5.1	DLASFIB instrumental layout	79
5.2	Schematic of SCRIBES instrument	81
5.3	High vacuum pumps on SCRIBES instrument	84
5.4	Pressure measurement on SCRIBES instrument	84
5.5	Electrical feedthroughs for SCRIBES instrument	85
5.6	Supersonic pumping vacuum scheme	85
5.7	Ion beam system base	87
5.8	Steel pipe holds support SCRIBES instrument	89
5.9	Modifications for cold cathode source	90
5.10	Schematic of cold cathode source.	91
5.11	Source (discharge and floating) power supplies	93
5.12	SimION simulations of ion trajectories	94
5.13	SimION simulations of potential energy surface	94
5.14	Screen shot of LabVIEW program ion optics control	96
5.15	Schematic drawing of drift tube with overlap irises and linear motion manipulators.	99
5.16	Schematic drawing of drift tube.	99
5.17	Schematic drawing of assembled pneumatic retractable Faraday cup.	101
5.18	Example Wien filter mass spectrum from the DLASFIB instrument. [12]	102
5.19	Pulsing plates used to modulate continuous ion beam into pulsing	103
5.20	Schematic drawing of pulse trains.	103
5.21	Photo of electron multiplier detector	104
5.22	Example mass spectrum of a cathodic extraction of N_2^+ at 6 kV.	105
5.23	Example mass spectrum of a cathodic extraction of N_2^+ at 4 kV.	105
5.24	Beam energy spread measurements of mass spectrometer	106
5.25	Hydrogen plasma reveals different source behavior for anodic and cathodic extraction.	107
5.26	Beam profile monitor traces for N_2^+ ion beam	108
5.27	Vertical offset induced by Brewster windows	109
5.28	Fast ion beam linewidth reduction	110
6.1	Example cavity enhanced velocity modulation spectroscopic signal	113

6.2	Example spectroscopic signal of N_2^+ with 2 kV beam voltage.	116
6.3	Example spectroscopic signal detector DC baseline and corresponding AC signal.	117
6.4	Example spectroscopic fractional signal of N_2^+ with 2 kV beam voltage.	117
6.5	Example picoammeter readings N_2^+ at 2 kV.	118
6.6	Example ion current and ion density of N_2^+ as a function of beam voltage.	119
6.7	Linewidth and ΔV as a function of float voltage.	120
6.8	Beam voltage monitor read by Keithley source meter.	120
6.9	Dispersion and absent absorption features of N_2^+	121
6.10	Fractional data while changing θ_{fm}	122
6.11	Doppler split components and fits at 2 and 6 kV	122
6.12	Comparison of N_2^+ in a positive column and ion beam	123
6.13	Red and blue split components of the $Q_{22}(14,5)$ line of N_2^+ calibrated with the frequency comb.	124
6.14	Boltzmann plot for temperature analysis.	126
6.15	Testing amplifier saturation by adding RF attenuation.	128
7.1	Optical layout for NICE-OHMS compatible DFG layout.	132
7.2	Spectra of HN_2^+	133
7.3	Fraction of band for HN_2^+ as a function of rotational temperature.	133
7.4	HN_2^+ energy level diagram for the lower and upper vibrational states	137
7.5	Spectra of CH^+	138
7.6	Fraction of band for CH^+ as a function of rotational temperature.	138
7.7	Spectra of CO^+	142
7.8	Fraction of band for CO^+ as a function of rotational temperature.	142
7.9	Spectra of HCO^+	149
7.10	Fraction of band for HCO^+ as a function of rotational temperature.	149
7.11	The simulated rovibrational spectra of $c\text{-}C_3H_3^+$ at 25 K.	153
7.12	Spectra at 25 and 1000 K illustrate the need for thermal relaxation to enable spectroscopy.	153
7.13	Zoom in of band origin for $C_3H_3^+$	154
A.1	Neutral density filter wheel assembly.	155
A.2	Mounts for SHG oven interface.	156
A.3	Electrical schematic for circuit provide a frequency tripler at 10 kHz.	157
A.4	Brass water-cooled Peltier cooler cold finger.	158
A.5	Adapter plates for mounting the 1st and 2nd EOM's to rotation stages.	187
B.1	Mode-lock indicator and "PControl Laser" sliders.	188
B.2	Fiber-laser "Scramble Dialogue"	189
B.3	Python script used to extract frequency comb values from XML server.	192
C.1	Designs for modifications to ion beam laser table.	197
C.2	Schematics for non-vacuum compatible brass cavity mount designs.	199
C.3	Schematics for cavity alignment tools.	199
C.4	Schematics for vacuum compatible brass cavity mount	201
D.1	Schematic of adapter for welch pump exhaust.	210
D.2	Schematics for water cooling adapters for Varian turbo pumps	211
D.3	Schematics for construction of steel pipe holders.	213
D.4	Engineering schematic of the front ferrule, machined from stainless steel.	214
D.5	Schematic for PEEK and aluminum back electrode adapters and holders.	215
D.6	Homemade PEEK adapter screw used for connecting discharge voltage to back electrode.	215
D.7	Schematics for water cooling setup necessary for anodic extraction.	215
D.8	Schematics for the first Einzel lens, machined out of stainless steel.	217
D.9	Photo of assembled Einzel lens.	218
D.10	Schematics for electrostatic benders, machined from stainless steel.	220

D.11 Photo of assembled cylindrical bender.	221
D.12 Schematics for the first Faraday cup.	223
D.13 Schematics for irises for achieving laser beam / ion beam overlap.	224
D.14 Schematic drawing for modifications of Einzel lens 1	225
D.15 Schematic drawings for Faraday cup 2.	226
D.16 Schematic drawings for MS ion optics pulser.	228
D.17 Schematic drawing of end iris.	229
D.18 Schematic drawings for electron multiplier mount	230
D.19 Schematic drawing of Brewster window holders.	231

Chapter 1

Introduction

1.1 Molecular Ions

A fundamental understanding of ion chemistry has broad impact on flame chemistry [14] (including soot nucleation [15]), plasma etching processes [16], atmospheric sciences, [17] and the interstellar medium. [18,19] This is because the ions' charge makes them highly reactive, and ion chemistry dominates systems even in low relative abundances. The same reactivity that makes them interesting also makes them difficult to produce and study in large quantities, as they must be continuously created (in a gas discharge) or created and isolated (in an ion trap or beam). [6] Ions normally constitute only a few parts per million of the total gas density of a discharge. [20] Some of the methods used to study ions spectroscopically include direct spectroscopy on a DC discharge source, velocity modulation on an AC discharge source, [20] photoelectron spectroscopy, ion trap measurements, and ion beam measurements. [6]

1.2 Beginnings of Ion Spectroscopy

Initial spectroscopic measurements of ions were made with indirect methods, as discussed in Section 1.4. Initial optical emission and absorption studies relied on electrical discharges, which were typically spectrally congested and performed with low resolution (3 GHz). [21] Dixon and Woods demonstrated the ability of DC discharges to produce ions in densities high enough to allow for direct absorption experiments in the microwave. [3,20,22,23] Eventually tunable IR absorption work was performed in glow discharges and hollow cathode lamps. The first mid-infrared spectroscopy of a glow discharge occurred in 1980 when Oka recorded the spectrum of the ν_2 band of H_3^+ in a DC discharge with a difference frequency generation (DFG) laser in a multi-pass configuration. [24] Other molecular ions like HeH^+ and NeH^+ soon followed. [25–27] These early spectroscopic studies on DC glow discharges and hollow cathodes were often hampered by interfering signals from neutral absorbers, which are several orders of magnitude more abundant. [28]

1.3 Velocity Modulation Spectroscopy

The invention of velocity modulation spectroscopy (VMS) by Rich Saykally’s group [20] in 1983 allowed for the absorption signal from ions to be recorded while the absorption signal from neutral molecules was avoided. At the time, several ion beam studies had been published that yielded the absorption spectrum of HeH^+ [29], D_3^+ [30], and HD^+ , [31] by monitoring changes in the charge-transfer cross sections of these molecules. The velocity shift introduced by the fast ion beam allowed the ionic absorption to be shifted into resonance with a fixed frequency laser. Saykally postulated that the electric field shift of an AC voltage discharge plasma would modulate the ions by the same order of magnitude as the Doppler linewidth, and could then be used to distinguish between species modulated by electric fields (such as ions) and those that are not. VMS works by using a high voltage AC discharge (near 20 kHz) [28] to create and modulate the velocity of ions in a positive column. The signal can then be demodulated using a lock-in amplifier to extract the ionic absorption signals and discriminate against the unmodulated neutral signals. This discrimination only occurs when the lock-in is demodulated at the first harmonic of the plasma modulation (1f). VMS was first used to record the ν_1 band of HCO^+ . [20] Other cations like HN_2^+ , H_3O^+ and NH_4^+ , [32] and anions, OH^- [33], N_3^- , NCO^- , NCS^- , NH_2^- , FHF^- [34] soon followed. The VMS line shapes have been described by Farley. [35]

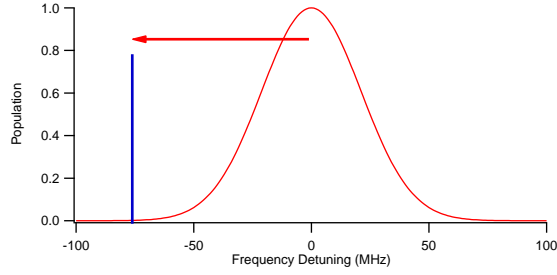
VMS has been the mainstay of molecular ion spectroscopy, and in the last 28 years, approximately fifty molecular ions have been studied, as reviewed in [28]. VMS has been used at wavelengths ranging from the UV to the millimeter-wave [36,37]. While no major technological advances had been made in VMS between 2004 and 2010, several additional molecules have been studied, including FeCO^+ [38] and FeO^+ [39] in the millimeter/submillimeter range, D_2O^+ [40], SO^+ [41], and H_3O^+ [42] in the mid-infrared.

While the ion/neutral discrimination of VMS has been very useful, it is not a rigorous discrimination of ions from the neutrals. Slight asymmetries between the positive and negative half cycles lead to concentration modulation of short lived neutral species, with a lifetime, τ , less than the inverse of the modulation frequency, f_{mod}). [20,28] Additionally, neutrals that undergo charge exchange can be observed using velocity modulation at the modulation frequency, [28] especially metastable helium atoms. [43] Further, demodulating the signal at twice the plasma modulation frequency (2f) results in a five-fold enhancement in the strength of the neutral signal, and almost completely overpowers the ion signal. [20] This occurs because the neutral formation follows essentially the absolute value of the electric field. Because the plasma is shut off twice during each cycle, the absorption of neutral molecules are concentration modulated at 2f yielding absorption sensitivity comparable to velocity modulation. [28] Therefore, any technique which demodulates at 2f will lose the ion/neutral discrimination.

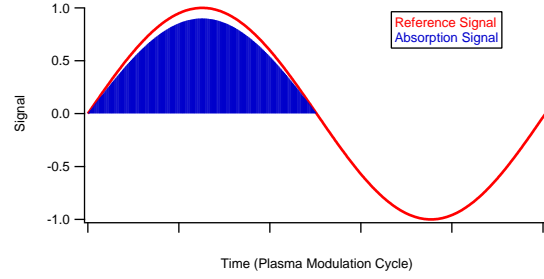
Most improvements to VMS before 2010 focused on improving the signal-to-noise ratio (S/N) to allow for the study of weak transitions or trace ions. The addition of optically heterodyned frequency modulation to VMS reduced the noise levels to close to the shot noise limit. [44, 45] Further increases in the S/N must come through the signal by increasing the path-length. The longest path lengths for VMS were traditionally modified White cells [44, 45] which had an effective path length of around 8 m. The S/N ratio of such experiments could be further improved by extending the optical path length using an external cavity. As traditional (1f demodulation) VMS relies on the difference in the ion drift velocity between the two half-cycles of an AC discharge, the 1f signal vanishes in any bidirectional multi-pass cell, including a cavity. The reason that the 1f signal vanishes with counter-propagating laser beams is explained in Figure 1.1. When the laser is located on the red side of the transition, over the course of a modulation cycle the center position of the ion population is shifted into the laser frequency and absorbs laser light. That absorption will occur in phase with the reference signal as shown in Figure 1.1(b). The lock-in amplifier multiplies the signal by the reference signal (giving a positive signal) and averages over the entire cycle, yielding a net positive signal. When multi-pass laser light passes through Figure 1.1(c), the light is absorbed when the ions are modulated in either direction. The lock-in multiplies the absorption by both the positive and negative values of the reference signal, yielding a value that is equal in magnitude and opposite in sign. When the lock-in amplifier averages over the cycle, a net value of zero is recorded Figure 1.1(d). However, if the lock-in amplifier is demodulated at twice the reference frequency, and the phase is adjusted, a net positive signal can be observed Figure 1.1(e). However, as stated above, 2f demodulation is sensitive to the neutral absorption signals, as well.

In addition to the non-rigorous spectroscopic ion/neutral discrimination, the harsh plasma conditions of plasma discharge experiments also increase the rotational and vibrational temperatures, typically to several hundred Kelvin. For example, CH_3^+ has been studied by the Oka group in a liquid-nitrogen cooled discharge cell, where the rotational, vibrational, and translational temperatures were reported as 371, 700, and 830 K, respectively, [20] indicating that the translational and rotational temperatures are not completely equilibrated. [28] Furthermore, until recently, [13] all VMS experiments produced Doppler-limited line widths (~ 1 GHz at optical wavelengths) (300 MHz at mid-IR wavelengths). [28] For small diatomic molecules, the spectra remain relatively simple to assign and line intensities are fairly strong, but larger (e.g., C_3H_3^+) or highly fluxional (e.g., CH_5^+) molecular ions are more challenging targets, as each individual transition is weaker due to quantum dilution.

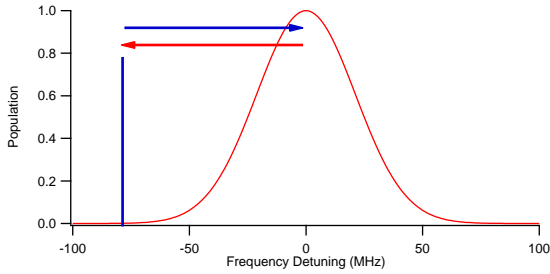
One measure of how dilute a spectrum will be is to calculate the “fraction of band” (FOB). The FOB is the ratio of the intensity of strongest line to the total integrated intensity of the entire band. It can be



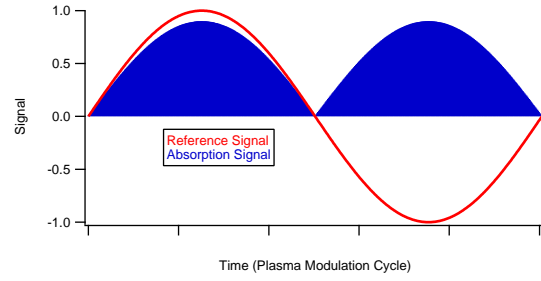
(a) Doppler profile of a population of ions centered at a line center (red) with the laser position indicated (blue) with single pass laser radiation. During a modulation cycle, the absorption will be in phase with the positive value of the modulation voltage. The arrow indicates the direction of the velocity modulation with respect to the frequency axis.



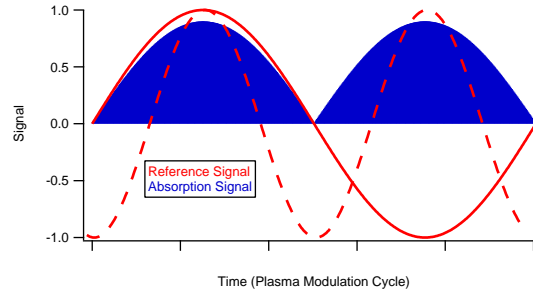
(b) Time domain view of signal and reference signal for 1f detection with single pass laser radiation.



(c) Doppler profile of a population of ions centered at a line center (red) with the laser position indicated (blue) for multi pass laser radiation. The arrows indicate the direction of the velocity modulation with respect to the frequency axis for two directions of laser light. Because the laser light is traveling both directions during each modulation half-cycle, an absorption signal will be observed during both half-cycles.



(d) Time domain view of signal and reference signal for 1f detection for multi pass laser radiation.



(e) Time domain view of signal and reference signal for 2f detection for multi pass laser radiation.

Figure 1.1: Illustration of lock-in operation for single pass (a,b), and multi-pass (c,d); with 1f demodulation (b,d) and 2f demodulation (e) (1f (solid red) and 2f demodulation (dotted red)).

estimated with calculations of the rotational constants, Hönl-London factors, and the temperature. The FOB decreases with increasing temperature and the weight of the molecule (the FOB increases with increasing value of the rotational constants). For instance, a simulation of the $C_3H_3^+$ spectrum is shown in Figure 1.2, indicating the quantum dilution at two different rotational temperatures. The fraction of band decreases

from 3.8% at 25 K to 0.2% at 1000 K.

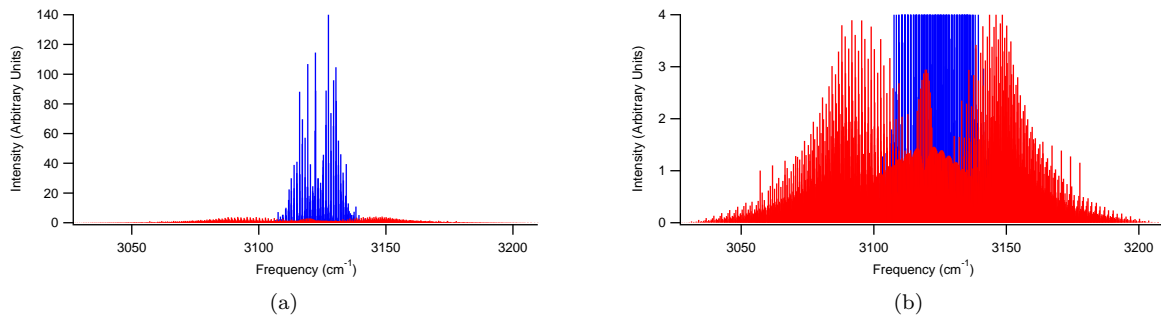


Figure 1.2: Simulation of $C_3H_3^+$ at 25 K (red) and 1000 K (blue).

Figure 1.3 shows a plot of ions observed using velocity modulation spectroscopy, [28, 46] where the number of atoms in the molecule is plotted as a function of its molecular mass. 52% of the ions contain only two atoms, 30% have three atoms, 12% have four atoms, 5% have five atoms, and only 1.5% have six atoms. Only one six-atom ion has been observed (CH_5^+).

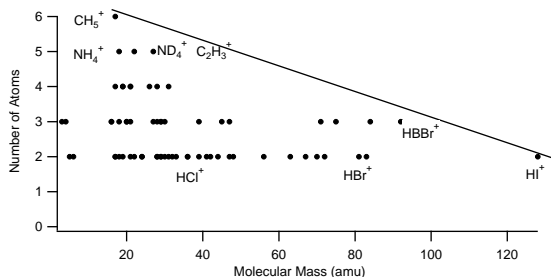


Figure 1.3: Ions observed with velocity modulation spectroscopy illustrate the extremes of either a light central atom with several lighter atoms surrounding it, or a single large mass atom with a single low mass atom attached.

1.4 Fast Ion Beams

Before glow discharge plasmas and direct absorption VMS were used to study molecular ions, indirect ion beam methods were used to measure ionic absorption spectra. Ion beams allow for mass selection with magnetic or electrostatic separation using Wien velocity filters or quadrupoles, respectively. [6] However, this advantage came with the drawback of reduced ion density, on the order of $10^4 - 10^7 \text{ cm}^{-3}$ compared to the 10^{10} cm^{-3} for positive columns. Both number densities are quite low compared to the spectroscopy of neutral molecules often taken at atmospheric pressures (10^{19} cm^{-3}). [6] The ion density in a beam is limited to 10^7 cm^{-3} because at higher densities the beam expands due to the space charge interaction. [47]

The first ion beam/laser beam interactions were studied by Hall and coworkers at JILA who measured the electron photodetachment of negative atomic ions in a photoelectron spectrometer with a pulsed (fixed-frequency) ruby laser. [48] Later, tunable dye lasers were used to photodetach S^- and measure the fine-structure splitting of an electronic state. [49] In 1966, Trujillo pointed out that fast ion beams reduce the relative beam energy spread compared to the average velocity. This enabled the study of collision cross sections of Ar with two collinear molecular ion beams. [50] Kaufman then suggested, in 1976, that the collinear laser beam/ion beam geometry could be used to reduce the Doppler linewidth of absorption features. [51] In theory, the linewidth would continue to decrease with increasing beam voltage. In practice however, kilovolt power supplies are more stable than megavolt sources. [6] Usually, the kinematic linewidth is not the limiting linewidth. Rather the main cause of Doppler width in ion beams are instabilities in accelerating potentials and the extraction of ions from different potentials within the ion source, [6] as illustrated in Figure 1.4.

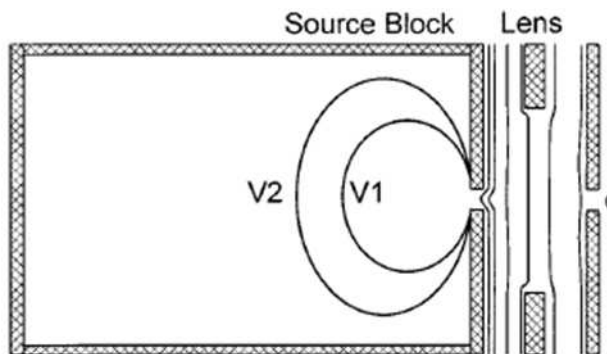


Figure 1.4: Illustration of ground penetration into ion source. A simple aperture in the source plate allows a variable voltage gradient. $V_1=99.97\%$ of V_{Beam} and $V_2=99.98\%$ of V_{Beam} , [6] leading to extraction from different potentials.

Many groups routinely used direct current quadrupole benders to change the orientation of the ion beam. [52] By manipulating the position of the ions, the ions can be spatially separated from background neutrals, leading to a rigorous ion/neutral discrimination. Additionally, the mass selection allows one to unambiguously assign the absorption to specific species. This mass selection can dramatically simplify the process compared to indirect photoelectron spectroscopy, [6] and compared to the “ion soup” of VMS.

1.5 Indirect Ion Beam Methods

It is commonly thought that the small concentration with which ions can be created means that direct absorption spectroscopy is usually impractical. [6] Therefore indirect means of spectroscopic measurement, such

as charge exchange, fluorescence, photoelectron production, predissociation and electron photo-detachment processes are used. Some indirect methods involve inefficient processes like charge exchange [53] and fluorescence, [54] and some other indirect measurements are more sensitive, being based on charged particle measurements. The problem with these indirect processes is that not all molecules will undergo the processes that produce them, and so they are not general techniques.

The first indirect, infrared absorption spectrum of a molecular ion with fast ion beam occurred by measuring the charge exchange of molecular ions through a gas target (H_2). An ion beam is produced and Doppler shifted into resonance with a high power laser beam. At resonance, the laser transfers population between different ro-vibrational states. The cross sections for charge exchange for different vibrational levels differ by several percent, and therefore the amount of ion beam passing through the gas target changed. This detection mechanism is very general if there is no excited state population loss mechanism (like fluorescence). [53] Using this method, the Wing group measured a spectrum of HeH^+ [29], D_3^+ , [30] and H_2D^+ [31]. A mid-IR, multi-line CO laser was used to pump the molecular transitions, and the ion beam was Doppler-tuned into resonance by changing the beam voltage (and velocity) of the ion beam. Five transitions were measured and showed a discrepancy of 8 GHz between the calculated values and the experimental values for the frequencies of the transitions. Later in 1982, Bernath, Wong, and Amano used a tuneable DFG laser in DC discharges of He and Ne to report the observation of HeH^+ , $^{20}\text{NeH}^+$ and $^{22}\text{NeH}^+$, [25] measuring 11 transitions of $^{20}\text{NeH}^+$ and 8 of $^{22}\text{NeH}^+$. [26]

Although inefficient, fluorescence measurements of ion beams can be used to measure optical spectra of ions. Rosner demonstrated this in 1978 by measuring the hyperfine structure of Xe^+ using fluorescence measurements of an ion beam of xenon. [55] Later, fluorescence spectroscopy was used to measure the spin-rotation and magnetic hyperfine constants of the X and B states of N_2^+ . [56,57]

Photoelectron spectroscopy is an indirect absorption technique which takes advantage of the photoelectric effect, that an atom (or molecule) can be ionized with sufficient photon energy, and the emitted photoelectron has a characteristic energy dependent on the original electronic, vibrational, and rotation state of the precursor molecule. Photoelectron spectra can be very complicated, and cannot be used to measure the spectroscopy of ions that do not have a stable precursor (even when the ion is easily formed in a discharge source). [6] Therefore, photoelectron spectroscopy cannot measure H_3^+ , C_3H_3^+ or CH_5^+ . Additionally, photoelectron spectroscopy can only measure positive ions. [6]

The final three indirect ion beam absorption methods, pre-dissociation, photo-fragment and electron-detachment spectroscopy produce low resolution spectra, unsuitable for rotationally resolved work. Pre-dissociation is an indirect absorption method which can be particularly sensitive due to the high gain of

charged particle detectors. However, it is limited to use with molecules with excited states with a high propensity for dissociation. Predissociation occurs when a bond breaks after a photon of energy greater than the dissociation energy of the excited state is absorbed. Predissociation is more likely in molecules that absorb wavelengths shorter than 200 nm. [58] The O_2^+ molecule is often studied in crossed ion beam predissociation studies. [59–61]

Similarly, photo-fragmentation spectroscopy (*i.e.*, a laser induced dissociation) is used when the excited electronic state of a molecule is not bound, and the daughter ions of fragmentation can be measured with mass spectrometry. An N_2^+ ion beam was studied with photo-fragmentation spectroscopy but was limited to 30 GHz resolution. [62,63] Like predissociation, photo-fragmentation spectroscopy can be quite sensitive, but is limited to molecular systems where the spectroscopic excited state is unbound, like N_2^+ (cited earlier) and Cs_2^+ . [64]

Finally electron-detachment spectroscopy can also be a fairly sensitive technique. However molecular anions are difficult to produce, as most negative ions do not have bound electronic states. [65,66] However, the absorption spectrum of C_2^- , [67] OH^- , [68] and NH^- [65,69,70] have been measured.

1.6 Non-Classical Molecular Ions¹

The limitations of the spectroscopic techniques discussed above are highlighted by the case of CH_5^+ . This molecular ion is particularly interesting because it lacks a classical structure [72] and acts as the prototypical non-classical carbocation. [73] The only published high-resolution spectrum of CH_5^+ was recorded by the Oka group [7] in a liquid nitrogen-cooled discharge of H_2 and CH_4 , and was identified by a process of elimination, by removing the known spectral lines of H_3^+ , CH_3^+ , C_2H_3^+ , HCO^+ , HCNH^+ , the Rydberg spectrum of H_2 , and strong lines of CH_4 that remained due to a slight asymmetry in the AC plasma. This rich spectrum (~ 900 lines, due to the fairly high rotational temperature) may still contain some transitions of other ions, and certainly is missing some CH_5^+ transitions due to overlap with CH_4 lines. As a result of the complexity of the spectrum, it remains completely unassigned more than a decade since its publication. Figure 1.5 illustrates the complexity of acquiring lines for this molecular ion. The entire reported spectrum is shown in Figure 1.5(a) with four interfering lines shown in blue. A zoom of this frequency range (Figure 1.5b) shows, that these much stronger interfering neutral lines probably overlap the ion signal (as the weaker ionic signal would be over-powered by the neutrals).

Supersonic discharge expansions have been used to produce rotationally cold molecular ions, but the reduced rotational temperature comes with the price of lost ion/neutral discrimination. Although con-

¹Much of this section is adapted from Mills et al. 2011. [71]

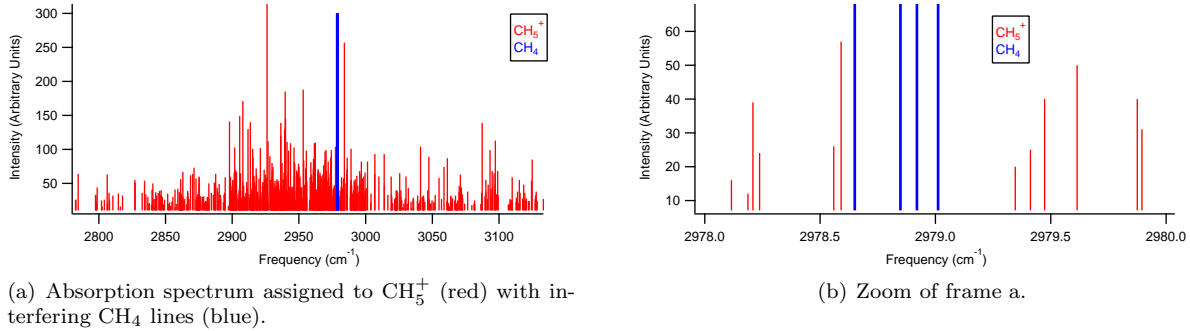


Figure 1.5: CH_5^+ spectrum with interfering CH_4 lines. [7]

centration modulation can provide some discrimination from background precursors, [74] radicals [75] and excited states of stable neutrals still congest and complicate the recorded spectrum. In particular, the Nesbitt group recorded a spectrum of a supersonically expanding $\text{H}_2:\text{CH}_4$ plasma, the broad outline of which has been published. [76] Their spectrum contains many transitions that coincide with Oka's, but also many transitions that do not. Because of the lack of ion/neutral discrimination, it is possible that some of these transitions may be due to excited CH_4 . They have proposed [77] the use of four-line combination differences to help assign the spectrum, but this effort requires higher precision in the determination of line centers. The ideal experiment for studying the spectra of complex ions such as CH_5^+ may be a combination of a supersonic expansion ion source with fast ion beam spectroscopy.

Fast ion beam spectroscopy offers rigorous ion/neutral discrimination (by physically separating ions from neutrals), reduced Doppler line widths (from the kinematic compression), and also allows mass identification of each spectral line (from Doppler splittings). The only direct absorption ion beam spectrometer (prior to the present work) was developed in the late 1980s by the Saykally group at Berkeley. [12] This instrument was successfully used to measure the mid-IR absorption spectra of HF^+ , [12] HN_2^+ , HCO^+ , [78] H_3O^+ and NH_4^+ , [79] but was abandoned after a few years, as it did not have sufficient sensitivity to pursue the spectra of larger or fluxional ions at the rotational temperature of uncooled ion sources.

With an eye to applications such as CH_5^+ , a second-generation direct ion beam spectrometer has been designed and constructed for the near-IR, which incorporates a number of technological advances from the past two decades and is also designed to eventually be supplied ions with a continuous supersonic expansion discharge source. [80] This approach combines ultra-sensitive spectroscopy (discussed in Chapter 4), rotational cooling, and very high precision line center determination (discussed in Chapter 3); we refer to it as Sensitive, Cooled, Resolved Ion BEam Spectroscopy (SCRIBES).

This dissertation describes an important step toward SCRIBES, in the form of a new ion beam instrument

that uses a Ti:Sapphire laser (the future pump laser for a mid-IR difference frequency laser) in concert with noise immune cavity-enhanced optical heterodyne molecular spectroscopy (NICE-OHMS) [81] as a sensitive direct spectroscopic probe of the ion beam. This instrument uses a time-of-flight mass spectrometer (TOF-MS) to provide mass analysis of constituents of the ion beam at spectroscopically relevant beam energies. An optical frequency comb is used to accurately and precisely measure the frequencies of the observed transitions. The initial proof of concept system studied in this work is the $1 - 0$ band of the $A^2\Pi_u - X^2\Sigma_g^+$ Meinel system of N_2^+ , which is an important species in atmospheric aurorae and electrical discharges. Because the line centers of many transitions in this band have already been measured at Doppler-limited resolution, [82] N_2^+ serves as a useful benchmark of the capabilities of our fast ion beam spectrometer.

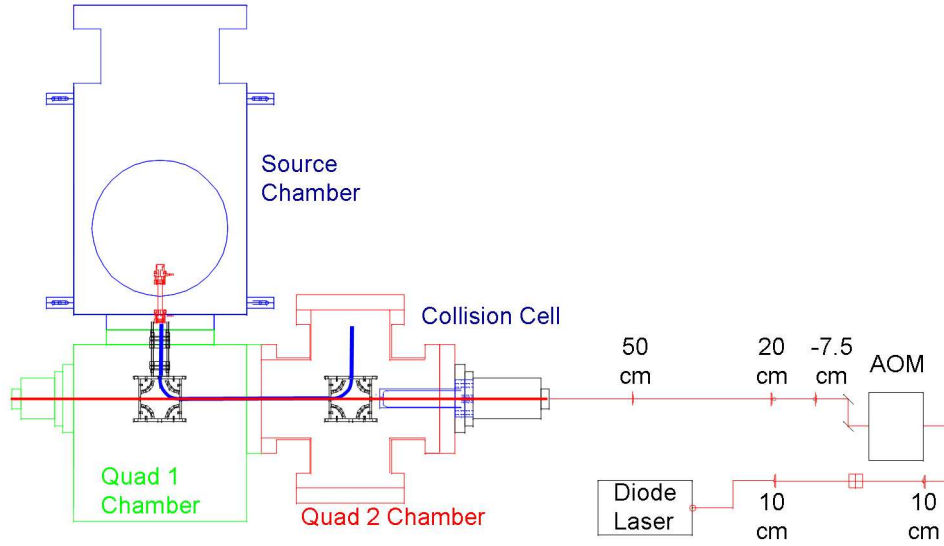


Figure 1.6: Initial ion beam instrument constructed at the University of Illinois. The source chamber is outlined in blue, the first DC quadrupole chamber is outlined in green, the second quadrupole chamber is outlined in red. The cold cathode source is shown inside the source chamber (red), and produces an ion beam (blue). The ion beam is extracted with plate lenses and passes into the DC quadrupole. The ions fly through a drift region and are turned by a second DC quadrupole. A high pressure CO_2 collision cell is used to neutralize fast neutrals (blue). A diode laser produces radiation at 950 nm. Two lenses are used to pass the laser beam through an optical isolator, two 10 cm lenses, and through an acousto-optic modulator (AOM). Three mode-matching lenses are used to match the first order beam of the AOM to the ring-down cavity. Two 99.98% 1 meter radius of curvature mirrors are used to form a ring-down cavity.

Several iterations of the SCRIBES instrument were tried before a successful system was developed. The penultimate implementation will be described briefly (see Figure 1.6), as background for changes implemented to the design described in this dissertation. Initially, two DC electrostatic quadrupole benders were used to turn the ion beam into and out of the drift region, and only one 2000-L/s turbo-molecular pump was used to provide vacuum on the entire system. Cavity ring-down spectroscopy (CRDS) [83] was set up, and

attempted numerous times, but no absorption signal was observed. One large limitation with using CRDS with N_2^+ in an ion beam is the relatively large charge exchange cross section between N_2^+ and molecular N_2 . [84] The charge transfer was apparent because the ring-down time was adversely affected when ions were flying through the drift region, even though the ions were deflected 90° away from the ring-down mirrors. Later it was found that $\sim 0.5 \mu\text{A}$ of current was created on a Faraday cup, indicating that fast neutrals were hitting the collector of the Faraday cup. Therefore, it was ascertained that the fast ion beam of N_2^+ was interacting with the background molecules of nitrogen and a charge transfer reaction was occurring. [84]



This reaction has a cross section of 30 \AA^2 at 4 kV. [84] At 2×10^{-5} Torr, the flight distance would be 6.9 m before 99% of ions would exchange their charge. Because the ions traveled 0.43 meters, approximately 6% of the beam was charge exchanged into fast neutrals which would not be affected by the quadrupole, would hit the ring-down mirrors and damage them. A high pressure collision cell (~ 100 mTorr CO_2) was introduced to decelerate the fast neutrals. Once the CRDS mirrors were no longer damaged by the residual fast neutral beam, CRDS was attempted again. However, today we believe that too much laser power was used. We estimate that the saturation parameter was ~ 900 , which would reduce the observed absorption by a factor of 30. During this time, we also noticed that the turbo-molecular pumps induced vibrations to the laser table. While the effect on cavity ring-down time was minimal, it precluded using higher stability cavities which require less vibration. When no signal absorption was obtained with CRDS, a more sensitive spectroscopic technique was decided upon and it was also decided that the ion beam instrument should be removed from the laser table. Cavity enhanced absorption spectroscopy, utilizing a Pound-Drever-Hall (PDH) locking technique [85] was implemented on a positive column discharge cell, and the new technique of cavity enhanced velocity modulation spectroscopy (CEVMS) was invented, and characterized. [13, 46] All of the PDH implementation will be described in the dissertation of Mr. Brian Siller. CEVMS was attempted on the fast ion beam, however the absorption was still photo-bleached, and unobserved. The NICE-OHMS technique was then implemented and characterized on a positive column. [86] The implementation of NICE-OHMS spectroscopy allowed for both a dispersion and absorption signal to be recorded. As discussed in Chapter 4, the absorption signal is still expected to be unobservable, but the dispersion signal is able to be recorded.

This dissertation describes the laser system in Chapter 2, including the information relevant for the DFG construction. Chapter 3 describes the optical frequency comb, and describes the theory, daily operation,

care, interfacing, and how the data is transferred to the LabVIEW data collection computer. Chapter 4 describes the noise immune cavity enhanced optical heterodyne molecular spectroscopy (NICE-OHMS) used to collect dispersion spectra of the ion beam. Chapter 5 describes the construction of the fast ion beam instrument during the present iteration of construction. Chapter 6 describes the spectroscopy as obtained from the fast ion beam spectrometer with the molecular ion, N_2^+ . This work, [71] describes the first direct dispersion spectroscopic measurement of an electronic transition of a molecular ion in an ion beam. The technique is fully general to any molecule which can be produced in a discharge (or supersonic discharge) plasma. Currently, McCall group members are converting the system to the mid-infrared.

Chapter 2

Laser Systems

A cw-Titanium Sapphire (Ti:Sapphire) ring laser was used to probe $1 - 0$ band of the $A^2\Pi_u - X^2\Sigma_g^+$ Meinel system of N_2^+ . As described in the introduction, the NICE-OHMS spectroscopy was developed and benchmarked on a high ion-density positive column. [86] Once the spectroscopy was understood, it was integrated with the ion beam. After the ion beam spectroscopy was bench-marked with the Ti:Sapphire laser, the optics for the Ti:Sapphire NICE-OHMS spectroscopy setup were removed and NICE-OHMS difference frequency generation (DFG) setup construction began. This chapter will focus on the Ti:Sapphire ring laser, and the cw-neodymium doped-yttrium:aluminum:garnet (YAG) laser used as pump lasers for the DFG. This chapter will describe the setup for locking of the cw-YAG laser to an iodine line, but details of the implementation of the NICE-OHMS DFG, as well as the iodine lockbox will be described in future dissertations from the McCall group.

2.1 Titanium Sapphire Laser System

The Ti:Sapphire is a complex laser used to generate coherent radiation between 690 and 1020 nm. The laser consists of 5 parts: pump lasers to pump the lasing medium, the Ti:Sapphire lasing medium, a cavity to produce narrow longitudinal modes, frequency selective elements to generate a single frequency, and a reference cell to stabilize the laser to a single frequency.

The Ti:Sapphire laser consists of three lasers: a diode laser that is used to pump a neodymium-doped yttrium orthovanadate ($Nd:YVO_4$) laser, which in turn pumps the Ti:Sapphire. The diode laser is a gallium aluminum arsenide semiconductor ($GaAlAs$) p/n junction. When forward biased, the recombination of electrons and holes produces photons. Continuous current produces a population inversion, and a laser can be formed by proper cavity geometry. This laser emits light at 809 nm. [87]

The diode laser optically pumps the $Nd:YVO_4$ laser (Spectra Physics Millennia). YVO_4 lases when Nd^{3+} ions are pumped from their ground state to an excited band and non-radiatively relax to the $^4F_{3/2}$ electronic state. Fluorescence to the $^4I_{11/2}$ state emits radiation at 1064 nm. [88, 89] The output of the

Nd:YVO₄ is frequency doubled by a second harmonic generating (SHG) lithium triborate LiB₃O₅ (LBO) crystal, producing 532 nm radiation. The SHG output pumps the Ti:Sapphire laser (Sirah Matisse TS). A Ti:Sapphire laser involves a four-level solid state laser system tunable between 690-1020 nm. The lasing medium of a Ti:Sapphire is a 0.1% Ti₂O₃ doping of Ti³⁺ in a medium of sapphire (Al₂O₃).

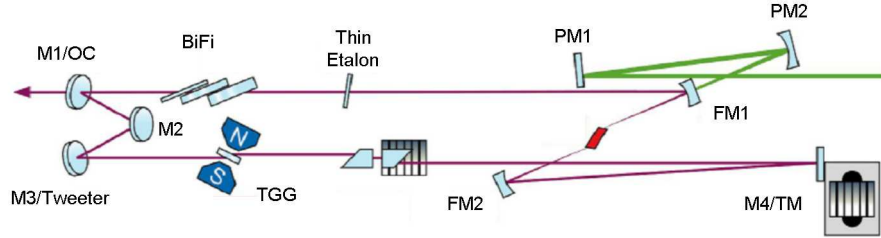
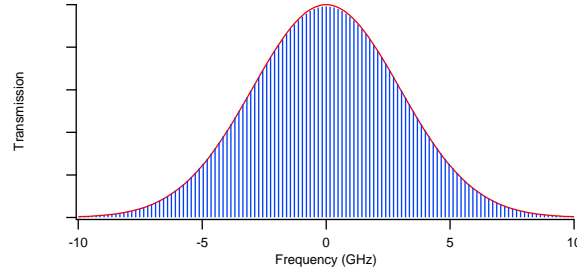


Figure 2.1: Optical layout of Ti:Sapphire ring laser, adapted from Matisse manual. [8] Abbreviations defined in text.

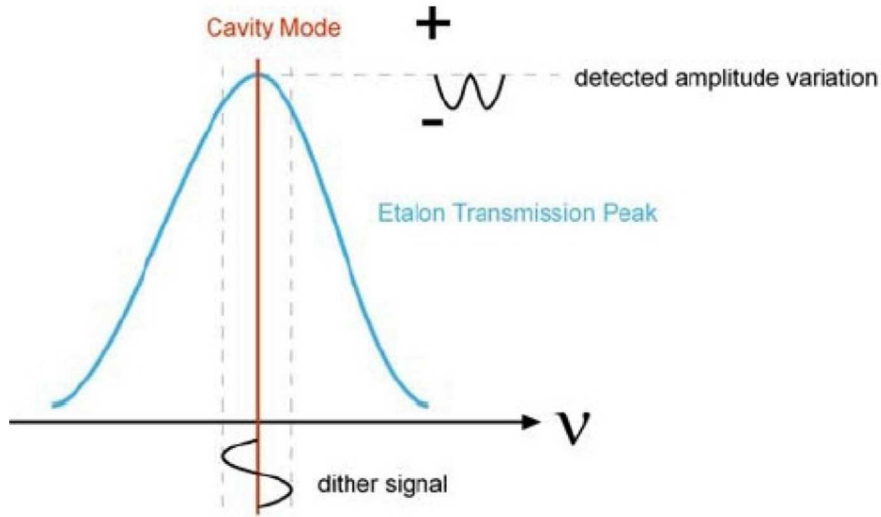
Figure 2.1 is a diagram of the Matisse Ti:Sapphire TS laser interior optical components which form the ring cavity and frequency selective portions of the laser. The 532 nm pump beam enters from the right, and is directed with the pump mirrors (PM1 and PM2) through the two focusing/folding mirrors (FM1 and FM2) and the Ti:Sapphire crystal. The ring cavity is formed when the fluorescence from the Ti:Sapphire crystal is reflected off of FM1, Mirror 1 (M1), Mirror 2 (M2), Mirror 3 (M3), Mirror 4 (M4) and FM2. M3 is a small mirror mounted on a fast piezoelectric transducer to change the laser frequency by changing the cavity length and handles the fast corrections to the etalon lock. M4 is a large mirror mounted on a slow piezoelectric transducer, and is used to handle the slow corrections to the laser frequency. The ring cavity can lase in both directions, clockwise and counterclockwise. Complicated intensity dynamics occur when both directions are present. [90–92] M2 is mounted out of plane and induces a small change to the polarization of light to both directions. A window of terbium-gallium-garnet (TGG) corrects the polarization of only the counterclockwise beam.

The Ti:Sapphire crystal emits radiation from 650-1050 nm. The ring-resonator cavity has a free spectral range (FSR) of 160 MHz. Therefore, frequency selective components are needed to select a single frequency of laser radiation. The first frequency-selective components are the Matisse optical sets (MOS), MOS1, MOS2 and MOS3. MOS1 are the shortwave optics (690-780 nm), MOS2 are the midwave optics (750-880 nm) and MOS3 are the longwave optics MOS3 (850-1020 nm). The birefringent filter (BiFi) consists of three plates with different thicknesses. The BiFi reduces the lasing range to several hundred GHz. The frequency which is chosen depends on the tilt of the plates and is changed with a stepper motor controlled

by the laser's digital signal processor (DSP). The thin etalon is a thin window with a FSR of 250 GHz which reduces the frequency span of longitudinal modes within the BiFi mode down to 250 GHz. The thin etalon tilt is controlled by a motor controlled mount. The Matisse commander program monitors the ratio of the output of the photodiode to the total laser power to keep the amount of power in a single mode constant and near minimum (thus suppressing other frequencies outside of the thin etalon FSR). The final frequency selective optic is a thick etalon with a 20 GHz free spectral range and a Finesse of about 3. Because $\text{Finesse} = \text{FSR} / \text{linewidth}$, the thick etalon linewidth is about 7 GHz. While 7 GHz is much higher than the longitudinal mode spacing of 160 MHz (see Figure 2.2a), the thick etalon is actively locked to the top of the etalon transmission (see Figure 2.2b). While the intensity difference between the maximum mode and the adjacent mode is only 1%, that is enough to ensure that only one mode lases.



(a) Thick etalon transmission width (7 GHz FWHM) and free spectral range (2 GHz) superimposed with 160 MHz longitudinal mode spacing.



(b) Piezo etalon (thick etalon) dither lock. [8]

Figure 2.2: Ti:Sapphire thick etalon transmission and dither lock.

The thick etalon is formed by two prisms with parallel base sides. One prism is adjusted by kinematic

mounts, and the separation between the prisms is controlled by a piezoelectric actuator. The thick etalon selects a single longitudinal cavity mode. In order to keep the thick etalon centered on the maximum of a cavity mode, a small dither is applied to the piezoelectric actuator and a top of fringe algorithm is used by the DSP.

After the frequency selective components have been properly implemented, depending on the frequency and mirror set, between 1-2 Watts exit the output coupler (M1). Typical powers of 1 W are achieved with MOS3 at 920 nm, and 2 W are achieved with MOS2 at 870 nm. Frequency stabilization occurs by locking the laser to an external, temperature-stabilized Fabry-Perot (FP) cavity. Frequency stabilization between 300 and 500 kHz is achieved by sending error signals from the FP cavity to the electronics that control the slow (M4) and fast (M3) piezo-actuated mirrors through the DSP.

Three photodiodes provide feedback and are necessary for the Matisse Commander software to lock and scan the Ti:Sapphire. One measures a fraction of the total power which leaks through M2. One measures the back-reflection off of the thin etalon, and one measures the Fabry-Perot cavity transmission in the reference cell. The system arrived with assemblies which hold square neutral density filters to make sure the proper light level arrives on the detectors. Sirah, through Newport, will sell a variable neutral density filter wheel assembly, but it is quite expensive. Instead, neutral density filter wheel assemblies were designed and installed. Designs for the ND filter wheels are shown in Section A.1. Continuously variable (0-4 OD) ND filter wheels (Thorlabs NDC-25C-4) are used to change the level of laser power reaching the various photodiodes.

2.2 YAG Laser System

The DFG laser is pumped by the cw-Ti:Sapphire laser and a cw-YAG laser. The lower frequency component of the DFG pump comes from an Innolight Mephisto 1000NE Nd:YAG. A Nd:YAG laser is a crystal of $\text{Y}_3\text{Al}_5\text{O}_{12}$ where 1% of the Y^{+} are replaced with Nd^{3+} ions. The crystal is pumped with 810 nm light from an internal diode laser. The laser can output up to 1 W with a 1 kHz linewidth (per 100 ms) at 1064 nm. While the optical frequency comb described in Chapter 3 has two combs that can measure the frequency of the Ti:Sapphire or the YAG, practical considerations with scanning the laser demand that only one laser be measured by the frequency comb at a time. While the YAG has an instantaneous narrow linewidth, there is some frequency drift that should be stabilized. A third-harmonic sub-Doppler dither lock to an iodine cell is used to stabilize the frequency of the YAG. [93] Because the YAG only produces the fundamental, an external periodically poled lithium niobate (PPLN) crystal is used to double the frequency of the fundamental, and

the doubled light is locked to an iodine line.

An optical layout of the frequency doubling setup is shown in Figure 2.3. The output of the YAG is elliptically polarized, so a quarter wave plate ($\lambda/4$ or QWP - Thorlabs WPQ05M-1064) is used to rotate the polarization into linear polarization, and a half wave plate ($\lambda/2$ or HWP - Thorlabs WPH05M-1064) is used to rotate the linear polarization into the vertical, as required by the SHG process. Wave plates rely on the birefringence (Δn) of an optical material to introduce a phase shift in the light. A half wave plate will induce a $\lambda/2$ phase rotation, and a quarter wave plate will induce a $\lambda/4$ rotation if a birefringent material has the correct length (L) (see Equations 2.1 and 2.2).

$$\frac{\lambda}{4} = 2\pi\Delta nL_1 \quad (2.1)$$

$$\frac{\lambda}{2} = 2\pi\Delta nL_2 \quad (2.2)$$

A 35 mm lens focuses the light into the PPLN crystal. The 1 cm PPLN crystal (Thorlabs SHG3-10) was held in an oven (Thorlabs PV10), which was controlled by a temperature controller (Thorlabs TC200). Schematics for the details of the SHG oven mounting system are given in Section A.2. The temperature of the PPLN crystal was set to 185° C. The output of the PPLN crystal was collimated by a 175 mm lens, and the 532 light was separated from the 1064 fundamental with a dichroic beam splinter (CVI Melles-Griot LWP-45-Rs-532-Ts-1064-PW-1025-UV). The 532 nm light was rotated into the horizontal by a HWP (Thorlabs WPH05M-532), and then passed through a polarizing beam splitter (PBS) (CVI Melles-Griot PBS-532-050), iris, and QWP (Thorlabs WPQ05M-532). The green light is then focused by a 250 mm lens and a mirror is placed at the focal plane of the lens as measured by a beam profiler. A 10 cm iodine cell (Thorlabs CQ19100-I) is placed between the lens and the mirror, and a ND filter wheel (0-2 OD Thorlabs NDC-50C-2) is placed between the cell and the mirror. The incident beam is steered back through the iris to make the pump and probe beams collinear. When the horizontally polarized light passes through the QWP, the light is converted to circularly polarized light. The reflection off of the mirror causes the a 180° rotation in the handedness of the circularly polarized light. When the back-reflection passes through the QWP the second time, the light is converted to vertically polarized light. The PBS then reflects the vertically polarized light through a 100 mm lens onto a silicon photodiode (Thorlabs DET 110).

The frequency of the YAG can be controlled by changing both the temperature of the crystal as well as the piezo voltage controlling the position of a mirror inside the laser cavity. The temperature of the YAG crystal is adjusted until the frequency of the SHG light is resonant with an iodine transition, and fluorescence is seen in the iodine cell. A small modulation voltage at 10 kHz is applied to the piezo transducer. The

reference signal is frequency tripled using a circuit designed and built by the SCS Electrical shop. Schematics for the tripler are provided in Section A.3. The tripler works by converting a sine wave to a square wave and filtering out everything but the third harmonic. The input sine wave is converted to a square wave using a comparator circuit. Because the fourier-transform of a square wave is essentially all harmonics, the fundamental, second, and third harmonics are also present. A narrow bandpass filter is built around the third harmonic, and the output is a sine wave at 30 kHz. Example spectra obtained by roughly scanning the temperature (and frequency) over an iodine line are shown in Figure 2.4. Figure 2.4(a) shows the unmodulated DC signal of the rovibronic line R(56) $v''=0 \rightarrow v'=32$. Figure 2.4(b) shows the 3f-demodulated lock-in output in red, and with vertical lines indicating the frequency of the iodine hyperfine components divided by two, shown in blue. The 3f-demodulated signal yields a third derivative line shape with a flat baseline. Having a flat baseline aids with the eventual locking of the YAG to the iodine line. 2.4(c) illustrates the large, sharp zero crossing near the center of the sub-Doppler feature which enables a tight lock to the iodine line. Instead of recording the output of the lock-in, the output can be used as an error signal input to lock to an iodine line. The details of the construction, and implementation of the lockbox will be described in the dissertation of Brian Siller.

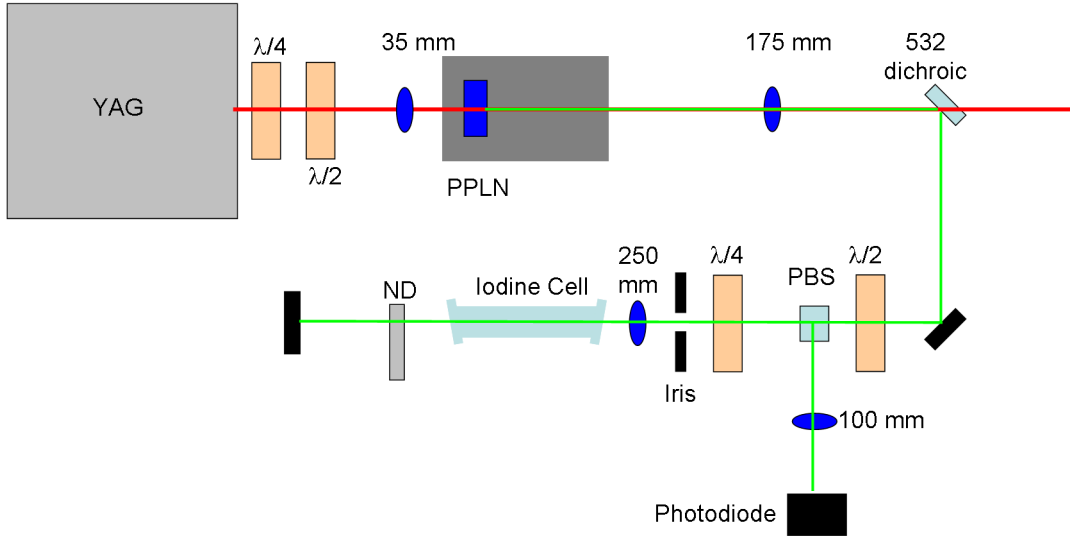


Figure 2.3: Optical layout for YAG doubling PPLN and sub-Doppler iodine lock. The YAG radiation is focused into the PPLN crystal. The PPLN crystal is held in an oven.

In order to reduce the vapor pressure of the iodine cell, a Peltier cooler was used. A Peltier cooler uses the Peltier effect to create a heat flux between the junction of two types of materials. It is able to transfer heat from one side of the device to the other by consuming electrical energy. When the device is used to cool, the opposite side will become warm. Something must remove the heat from the sink produced by the Peltier

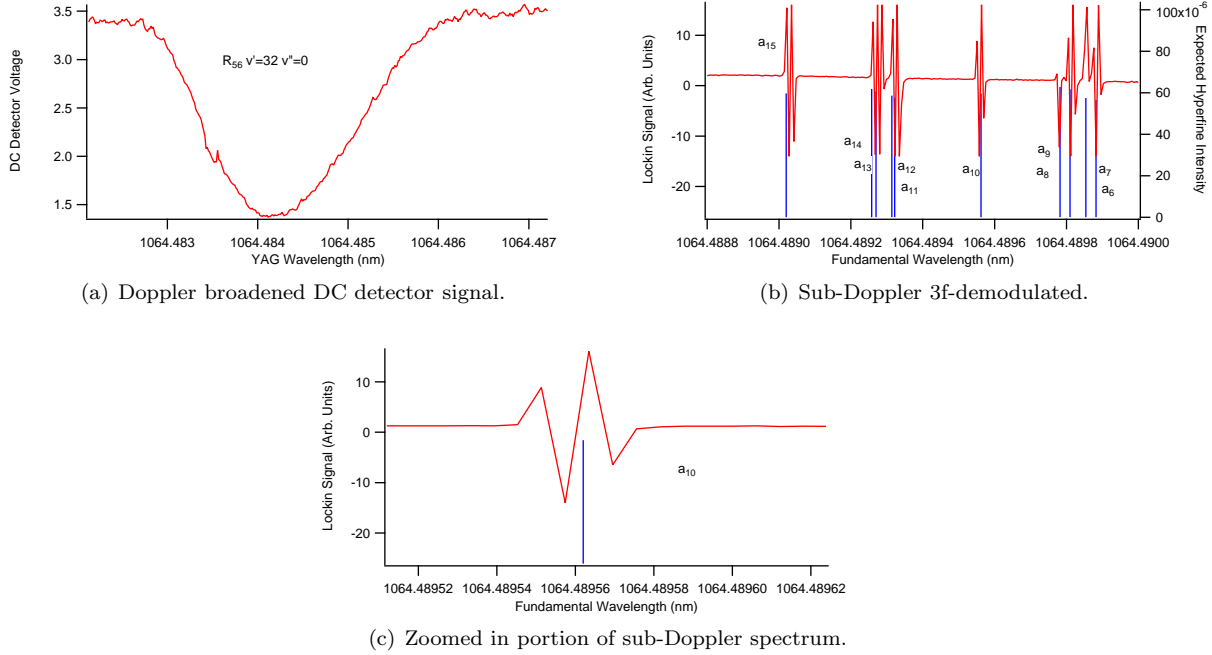


Figure 2.4: Doppler broadened (a) and sub-Doppler (b) spectra of iodine with (c) zoomed in at the a_{10} hyperfine component.

device if the source is to be kept cool. Therefore, a water cooling system was designed. An overview of the idea is shown schematically in Figure 2.5. The brass piece contains a reservoir into which the cold finger of the iodine cell can sit. When a quantity of thermal grease (Wakefield Solutions 120-2; newark.com 00Z1245) was placed inside the reservoir, the heat from the cell was transferred to the cold brass piece. Instructions and schematics for the construction of the Peltier cooler are given in Section A.4.

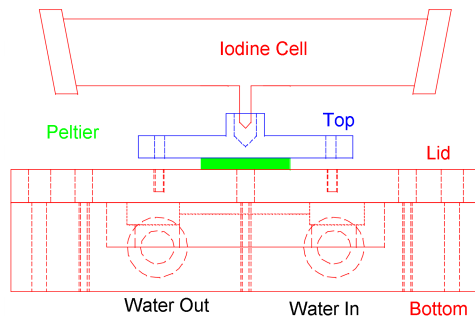


Figure 2.5: Mechanical overview of Peltier cooling of iodine cell.

The mounts required for the SHG and DFG ovens have a minimum beam height. The YAG laser needed a mount that was 2.5" above the height of the laser table. Therefore a mount was constructed to go under the YAG. Designs for the mounts are shown in Figure 2.6. The piece was constructed out of two, solid-aluminum plates and were connected together. The YAG rested on top of the mount. Because a solid piece

of aluminum would cost quite a bit more, two aluminum pieces were used and screwed together tightly. A block of aluminum was chosen in order to minimize vibrations that would be present if the laser were mounted on posts.

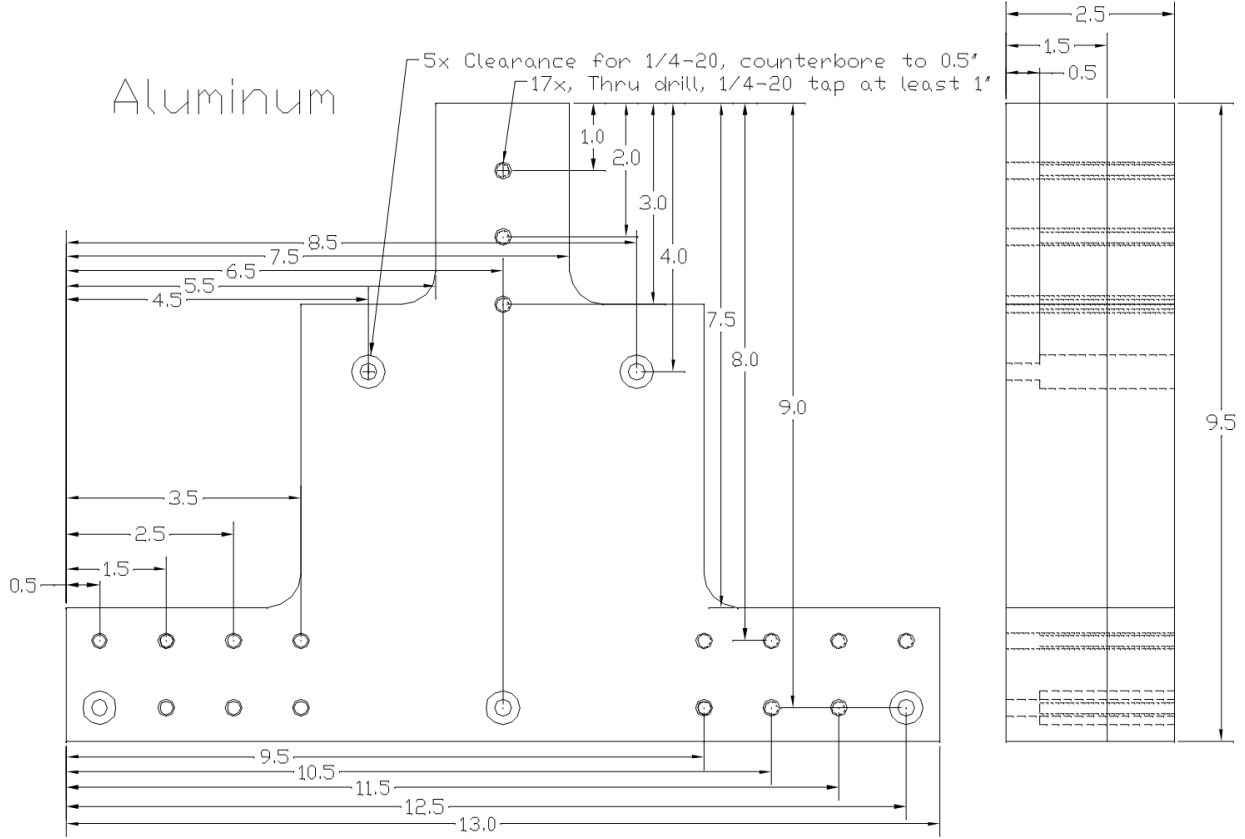


Figure 2.6: Base mount for the YAG.

2.3 Difference Frequency Generation Laser System

Earlier, for the spectroscopic work described by Brian Tom, [94, 95] a DFG laser was constructed. This system was used to characterize an ion source used in dissociative recombination experiments and reaction dynamics of hydrogenic plasmas in a hollow cathode cell. These results have been previously described, [96] therefore, only information relating to the construction of the DFG will be presented. The DFG laser was eventually disassembled when it was determined that the N_2^+ near-IR spectroscopy would require the Ti:Sapphire laser. Once the near-IR spectroscopy was completed, the NIR components were removed and a second DFG was constructed. The second DFG will be described in future McCall group dissertations.

Difference frequency generation is a parametric process between three photons of frequency ω_{pump} ,

ω_{signal} , ω_{idler} , where $\omega_{pump} - \omega_{signal} = \omega_{idler}$ and $\omega_{pump} > \omega_{signal} > \omega_{idler}$. Conservation of energy demands that $\omega_{pump} - \omega_{signal} = \omega_{idler}$. In this system, the cw ring Ti:Sapphire described above served as the pump laser and the Nd:YAG served as the signal laser. Conservation of momentum demands that the wave-vectors are also correctly phase matched. In a parametric process like DFG, however, the dispersion of the nonlinear material causes a periodic phase mismatch. The first DFG was built by Pine, and produced only ~ 500 nW [97] because of the destructive interference due to the phase mismatch. A phase mismatch occurs because the index of refraction of the non-linear material is dependent on the wavelength of light and the temperature of the material ($n(\lambda, T)$). For a three photon parametric process, $n_{pump} > n_{signal} > n_{idler}$ and $\lambda_{pump} < \lambda_{signal} < \lambda_{idler}$. Therefore, the wave vector, $\mathbf{k} = 2\pi n\hat{\mathbf{k}}/\lambda$, of each photon is not the same. Conservation of momentum requires that the phase mismatch ($\Delta\mathbf{k}$) is equal to zero, [98, 99] otherwise destructive interference of the DFG process reduces the amount of idler light created. [97] The phase mismatch for a DFG process is described by ($\Delta\mathbf{k} = \mathbf{k}_{Pump} - \mathbf{k}_{Signal} - \mathbf{k}_{idler}$) and for given wavelengths of λ_{pump} , λ_{signal} and λ_{idler} , will be equal to a coherence length Λ . The problem of the coherence length is shown in Figure 2.7(a). After the coherence length of the interaction, the DFG process begins to destructively interfere with itself, eventually going all the way to zero. If the polarization axis of the crystal could be inverted after the coherence length, the DFG process could continue increasing. This process is illustrated in Figure 2.7(b), and is called quasi-phase matching (QPM). It was first proposed in 1962 [100] as a way to overcome the problems associated with the phase mismatch and has been widely used in DFG applications. While QPM is not nearly as efficient as perfectly phase matched processes, it is still much better than no phase matching. The polarization axis can be inverted by periodically poling the non-linear crystal. When the crystal is grown, a high voltage electrode is applied to the crystal, and inverts that polarity every coherence length. [101] As the polarization changes with respect to the normal of the top and bottom surfaces of the DFG crystal, the input light is required to have vertically polarized input polarization, an effect accomplished with the half-wave plates and polarizing prisms. For a DFG built with a tunable Ti:Sapphire laser, a YAG laser, and a PPLN crystal with grating periods between 20 and 23 μm , the wavelengths of IR radiation and Ti:Sapphire radiation are given in Table 2.1.

2.3.1 Difference Frequency Generation Layout

The general setup for a DFG laser involves matching the spatial modes of the pump and signal lasers to the same size and position, as well as the polarization. For the Ti:Sapphire, the output was very collimated and no focusing optics were applied to it before it was made collinear to the YAG. The output of the horizontally

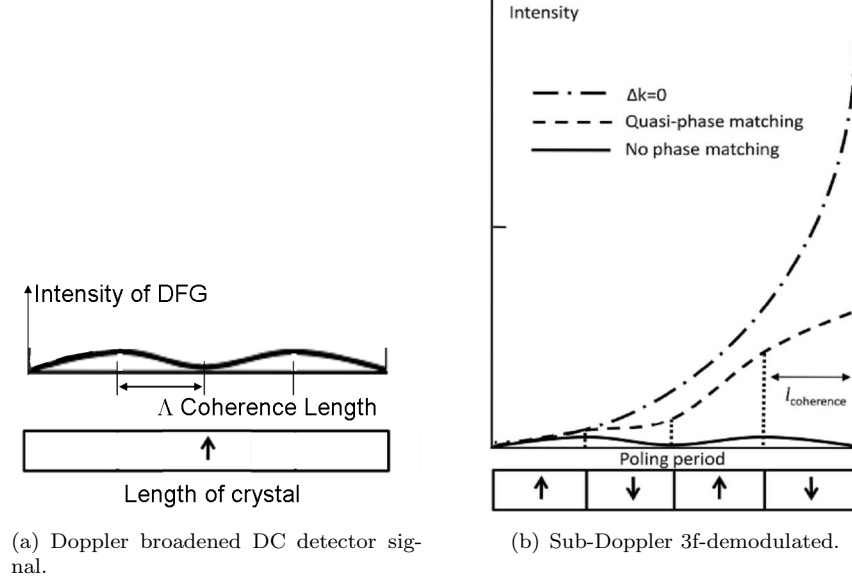


Figure 2.7: Explanation of coherence length and quasi phase matching in a periodically poled lithium niobate crystal. Adapted from [9]

polarized Ti:Sapphire was passed through an optical isolator (Optics For Research, IO-5-NIR-LP) to ensure that no back-reflections entered into the lasing or reference cell cavity. Because the optical isolator causes a 45° rotation of the light passing through, a half wave plate (Thorlabs AHWP05M-950) was necessary to bring the plane of polarization to the vertical. The output of the YAG is elliptically polarized with a 1:5 ratio. A quarter wave plate (Thorlabs WPQ05M-1064) is used to rotate the polarization into a linear polarized state. A half wave plate (Thorlabs WPH05M-1064) is then used to rotate the polarization into the vertically polarized state required by the AOM and the PPLN crystal. The YAG was then modulated by an acoustooptic modulator (Brimrose TEM-85-2-1064 (AOM); FFA-85-B2-F2.25-X (Driver); 50-55 dB extinction ratio (Option)), which spatially and temporally modulated the light intensity and imparted a frequency shift as well. The DFG was aligned to the first order light, and the 0 order light was picked off with a D shaped mirror (Thorlabs PFD10-03-P01 (Mirror); DMM1 (Mount)) and sent to a beam dump. All QWP and HWP were mounted in precision rotation mounts (Thorlabs PRM1).

The YAG was mode matched to have approximately the same spatial mode (beam size) as the Ti:Sapphire, with 25 cm and 20 cm focal length biconvex lenses (Thorlabs LB-1056-C & LB-1945-C, respectively). There was approximately 24.5" between the laser and the 25 cm lens, 23" before the 20 cm lens, and 30" before the achromatic lens. Biconvex lenses were chosen because they are ideal for use when the object and the image are on opposite sides of the lens and the image/object ratio is between 0.2 and 5. A custom coated dichroic mirror was purchased (CVI Melles-Griot SWP-45-Rs-1064-Ts-750-PW-1025-UV 1064/Ti:Sapphire)

Period	Idler Wavelength μm		Idler Frequency cm^{-1}		Pump Wavelength nm	
	min	max	min	max	min	max
20.00	2.802	2.863	3568.9	3492.8	771.166	775.715
20.25	2.864	2.929	3491.6	3414.1	775.788	780.480
20.50	2.93	2.996	3413.0	3337.8	780.551	785.159
20.75	2.997	3.07	3336.7	3257.3	785.227	790.150
21.00	3.071	3.152	3256.3	3172.6	790.216	795.476
21.25	3.153	3.242	3171.6	3084.5	795.540	801.089
21.50	3.243	3.344	3083.6	2990.4	801.150	807.172
21.75	3.345	3.463	2989.5	2887.7	807.231	813.924
22.00	3.464	3.613	2886.8	2767.8	813.979	821.944
22.25	3.614	3.825	2767.0	2614.4	821.996	832.440
22.50	3.826	4.72	2613.7	2118.6	832.488	868.271
22.25	4.721	4.936	2118.2	2025.9	868.305	875.317
22.00	4.937	4.982	2025.5	2007.2	875.349	876.753

Table 2.1: Idler wavelength determines pump wavelength and poling period needed for DFG process.

which transmits the Ti:Sapphire and reflects the YAG when the element is placed at 45° . A Glan laser polarizer (Newport 10GL08AR.16 calcite, coated 650-1000 nm) was used to ensure that only vertically polarized radiation was applied to the PPLN crystal. After the beams were combined, a flipper mirror was inserted to make sure that the beams were collinear over a long distance. The beams were passed through a 20 cm achromatic lens (Thorlabs AC254-200-B) before entering the PPLN crystal. Achromatic doublet lenses contain two lenses, with the first compensating for the chromatic aberrations of the second such that two wavelengths will focus to the same distance after passing through the lens pair. The 20 cm achromat focused the YAG and the Ti:Sapphire down to 82 and 69 μm beam waists approximately 190 mm away from the lens. These beam waists correspond to approximately 17 and 19 mm Rayleigh ranges. The crystal was placed with the entrance of the crystal near the beam waist.

After being focused by the achromatic doublet, the pump and signal lasers entered the PPLN crystal. The PPLN crystal was originally purchased from Thorlabs, as supplied by Stratopphase (DFG2-40). However, those parts are now obsolete and are serviced through Covesion. The PPLN crystal was housed in an oven (PV40) controlled by a temperature controller (Thorlabs TC200). Because the temperature of the PPLN crystal is supposed to change by no more than $10^\circ \text{ min}^{-1}$, and the program provided by Thorlabs did not have all of the functionality that we desired, a CVI/Labwindows program was written to control the temperature of the oven. The graphical user interface for this program is shown in Figure 2.9 and the code for the program is found in Appendix A.

The program can work in two modes: cycle or normal. Cycle mode is chosen whenever the user wants to change the temperature of the crystal. The mode is chosen by pressing the “Cycle” button, and entering in the desired set temperature. The user also selects a fast ($10^\circ \text{ min}^{-1}$) or slow (1° min^{-1}) speed, and a direction

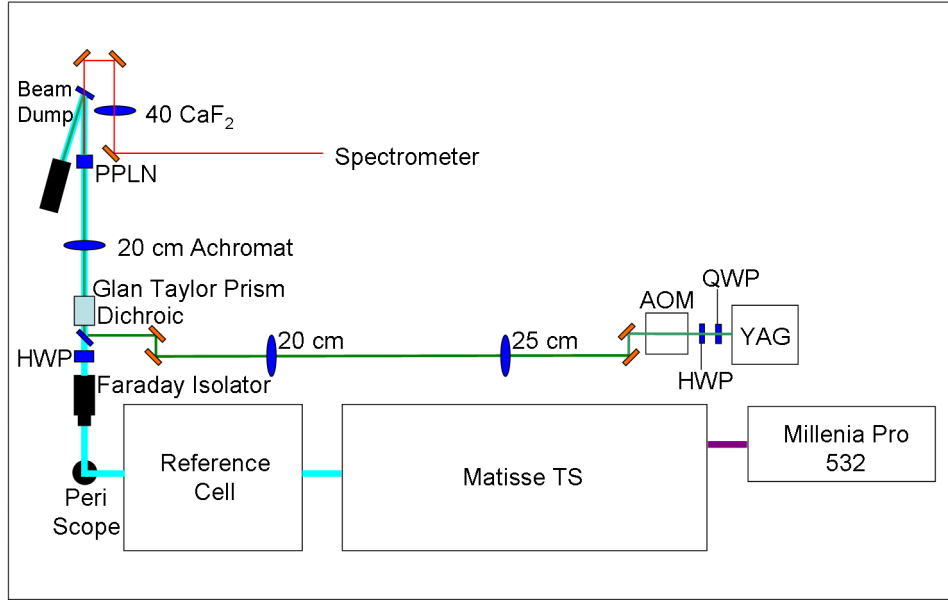


Figure 2.8: Optical overview of first DFG setup.

(up or down). The user then presses “Start” and the program will automatically change the temperature according to the rate indicated. The temperature scale bar indicates the temperature reading from the oven. Once the time ramp is completed, the program will automatically switch over to the “Normal” cycle, and stay at that temperature indefinitely. Small changes in temperature can be made under the “Normal” setting by changing the set temperature. The oven can be turned off by pressing disable (which shouldn’t happen unless the crystal is at or near room temperature). The temperature controller can have different control loop parameters (PID values) which can be changed by the user. Under the normal mode, the offset of the controller can be changed by pressing the De-Tune/Tune button. When the temperature is stable, the controller notes the difference between the actual temperature and the set temperature, and applies an offset to minimize the difference. With the correct optical layout, and the two lasers spatially mode matched, and focused down into the PPLN crystal, only the temperature of the crystal must be correctly set.

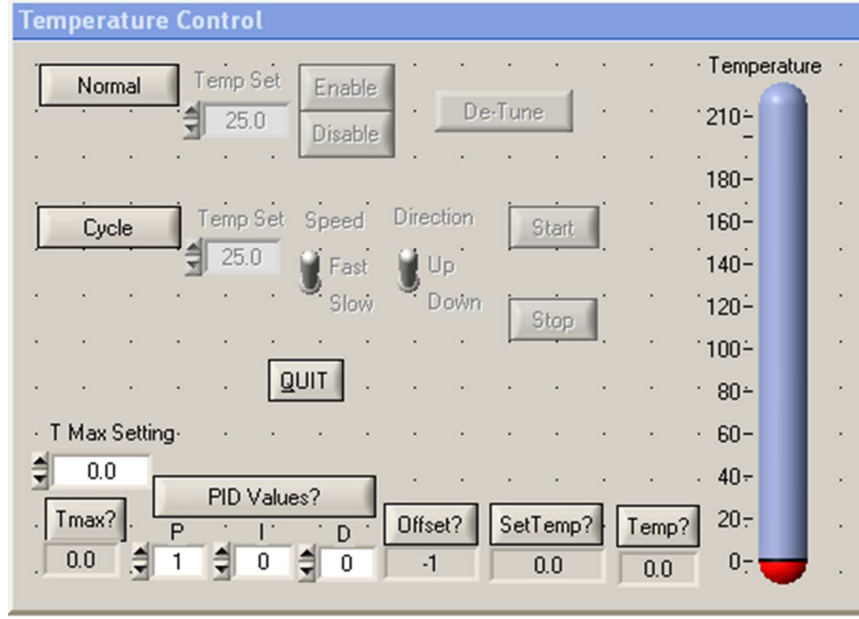


Figure 2.9: LabWindows program interface for controlling the PPLN crystal temperature.

2.3.2 Difference Frequency Generation Sellmeier Curves

The phase matching conditions are calculated by using the temperature and wavelength dependent dispersion equation, known as the Sellmeier equation. Initial coefficients for the Sellmeier equation for lithium niobate were given initially by Jundt [102] and more accurately by Deng. [103] The modified Sellmeier equation for the extraordinary index of refraction (n_e) is given by [103]

$$n_e^2 = a_1 + b_1 f + \frac{a_2 + b_2 f}{\lambda^2 - (a_3 + b_3 f)^2} + \frac{a_4 + b_4 f}{\lambda^2 - a_5^2} - (a_6 + b_5 f) \lambda^2 \quad (2.3)$$

where $a_1, a_2, a_3, a_4, a_5, a_6, b_1, b_2, b_3, b_4, b_5$ are the Sellmeier equation coefficients, and the f is a reduced temperature parameter given by

$$f = (t - 24.5)(t + 370.82) \quad (2.4)$$

where t is the temperature in °C.

Section A.6 contains the code for an Igor procedure file which determines the index of refraction for a given wavelength and temperature, solves the temperature to allow for optimal quasi-phase matching, and performs this for all channels of the PPLN crystal. The results of the solver function are shown in Figure 2.10. In addition to the chart shown in Figure 2.10, Table A.1 has a temperature look-up table for the quasi-phase matching conditions calculated for every 10 nm between 2.8 and 4.8 μm .

Once the pump and signal lasers were collinear and the beam waist was determined, the DFG crystal

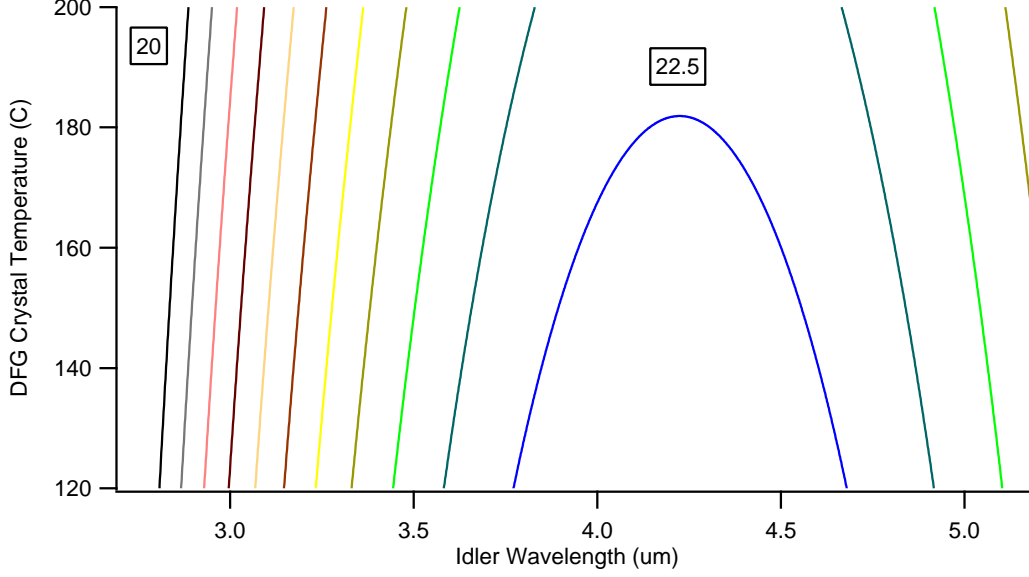


Figure 2.10: Temperature curves for the DFG. The poling period ranges from 20 μm to 22.5 μm .

temperature was increased to the values calculated using the Sellmeier equation, and mid-IR light was produced.

The expected power (mW) can be estimated (as informed by the engineers at Stratophase) to be

$$P_{Expected} = 0.3 \frac{\text{mW}}{\text{W}^2 \text{cm}} P(\text{W}^2) L(\text{cm}) \quad (2.5)$$

where P is the product of the pump and signal lasers and L is the length of the crystal. Initially, for an input power of 1.35 W from the Ti:Sapphire and 0.55 W from the YAG, with a 4 cm long crystal, we expected a 890 μW power level and observed 750 μW , or around 84% of the expected power. While this was enough power to perform cavity ringdown spectroscopy, one can verify that the DFG conversion was performing correctly by actually using the parameters of our DFG and comparing that to the expected theoretical values.

The theoretical conversion efficiency for DFG process is given by [104, 105]

$$P_i = \frac{4\omega_i^2 d_Q^2 L P_p P_s T h(\mu, \xi)}{\epsilon_0 \pi c^3 n_p n_s n_i} \frac{1}{k_s^{-1} + k_p^{-1}} \quad (2.6)$$

where ω_i is the frequency of the idler, L is the crystal length, P is the pump power for the pump and signal, T is the transmission through the crystal, ϵ_0 is the permittivity of free space, c is the speed of light, n is the index of refraction for the pump signal and idler, k_s and k_p are the wave vector magnitudes for the signal and the pump. d_Q is calculated from the nonlinear coefficient of a PPLN crystal (d_{33}) as $2 d_{33}/\pi$. As d_{33} of

PPLN is 24 pm/V; d_Q is 15.3 pm/V. (Note that [104] omits the transmission factor (T) and [105] is missing ω_i^2 and c^3 .) The focusing parameter, h , is given by [105]

$$h(\mu, \xi) = \frac{1}{2\xi} \int_{-\xi}^{\xi} d\tau \int_0^{\xi} \times \frac{1 + \tau\tau'}{(1 + \tau\tau')^2 + (\frac{1+\mu^2}{1-\mu^2})^2(\tau - \tau')^2} d\tau' \quad (2.7)$$

where $\mu = k_s/k_p$, and $\xi = L/b$, where b is the confocal parameter ($b = 2 \times Z_R$) for the focused light, and where Z_R is the Rayleigh range. Equation 2.7 can be numerically integrated; the values for the integration are found in Table 2.2, and a plot of the values is shown in Figure 2.11.

μ L/b	$h(\mu, \xi)$	$dh/d\mu$
0.1	0.091	0.62
0.2	0.153	0.39
0.3	0.192	0.25
0.4	0.217	0.17
0.5	0.234	0.12
0.6	0.246	0.08
0.7	0.254	0.06
0.8	0.26	0.04
0.9	0.264	0.02
1	0.266	0.02
1.1	0.268	0.01
1.2	0.269	0
1.3	0.269	0
1.4	0.269	0
1.5	0.269	-0.01
1.6	0.268	-0.013
2	0.263	-0.018
2.8	0.249	-0.017
3.5	0.237	-0.018
4	0.228	-0.018
4.5	0.219	-0.014
5	0.212	-0.016
5.5	0.204	-0.014
6	0.197	

Table 2.2: The focusing parameter was numerically integrated as a function of the confocal parameter (μ) and differentiated to determine the maximum value.

From the plot of the focusing parameter it is apparent that it reaches a maximum value between $\mu=1$ and 1.5. From Table 2.2, the derivative of h is found, and the maximum focusing parameter will occur when the $\mu=1.3$. In our case, $\mu=1$, and the value of h is 99% of the maximum at this value.

Table 2.3 includes the values used in Equation 2.6, and shows the expected power for the focusing parameters actually used. When compared to the actual expected values we see approximately 97% of the

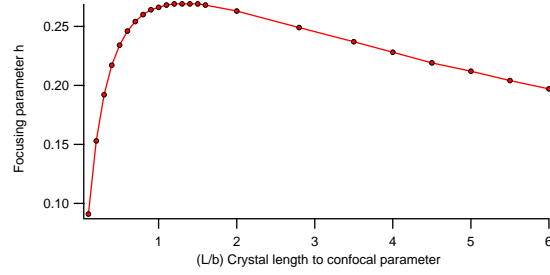


Figure 2.11: Numerical integrations of focusing parameter.

Description	Symbol	Value	Units
Idler angular frequency	ω_i	5.14E+14	s ⁻¹
Non-linear QPM	D_Q	1.53E-11	m/V
Crystal length	L	0.04	m
Power pump	P_p	1.35	W
Power signal	P_s	0.55	W
Crystal transmission	T	0.86	
focusing parameter	$h(\mu, \xi)$	0.267	
Pump n	n_p	2.151	
Signal n	n_s	2.149	
Idler n	n_i	2.083	
pump k	k_p	7618690	m ⁻¹
signal k	k_s	5905249	m ⁻¹
Confocal parameter	b	3.77	cm
Momentum s/p	μ	0.775	
	ξ (L/b)	1.06	
Calc'd power	P_i	776	μ W
Measured Power	P_i	750	μ W
	Ratio	0.97	

Table 2.3: Parameters used for calculating the expected power value.

expected mid-IR radiation, and therefore know that the system is very well aligned. However, the overall power efficiency ($P_{Out}/(P_1 \times P_2)$) is much lower ($\sim 0.1\%$).

Once the mid-IR light was produced, the accuracy of the phase matching curves could be tested. Results from the experimental and calculated temperatures are given in Table 2.4. For two frequencies in the same channel, the experimental maximum temperature was within 2° of the calculated value.

λ μm	T_{Exp} $^{\circ}\text{C}$	T_{Calc} $^{\circ}\text{C}$	Difference $^{\circ}\text{C}$	rel err %
3.668	155.7	153.6	1.7	1
3.621	139.4	135.7	1.3	1

Table 2.4: Accuracy of temperature tuning curves.

In order to know how far one should scan to determine the maximum temperature, two scans over the

crystal temperature were taken. The results are shown in Figure 2.12, and show that the FWHM of the temperature tuning range is $\sim 2.7^\circ$.

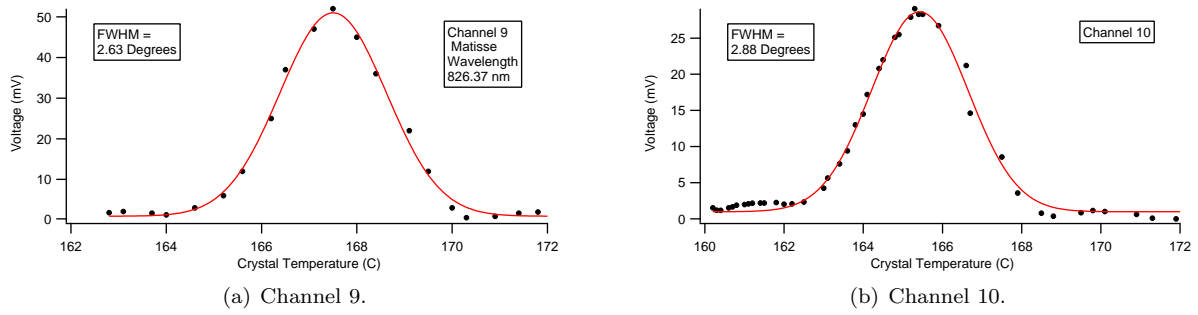


Figure 2.12: Examples of temperature transfer function of IR generation.

Chapter 3

Optical Frequency Comb

Until the year 2005, most wavelength measurements in the near and mid-IR were performed using a wavemeter with some 60 MHz accuracy, or calibration to a reference gas, whose absorption spectrum has previously been measured. In 2005, Roy Glauber, John Hall and Theodor Hänsch were awarded the Nobel prize in Physics. Glauber's contribution was for explaining the quantum theory of optical coherence. Hall and Hänsch were awarded for the contributions to the development of laser-based precision spectroscopy including the optical frequency comb. [106] Since that time, several papers have described the use of optical frequency combs to revolutionize spectroscopy. For instance, the accuracy of the frequency measurements have improved to 1 part in 10^{14} .

Using a frequency comb as a frequency reference, the absolute frequencies of certain spectroscopic lines have been measured to very high accuracy. For instance, the cesium D1 line at 894.6 nm and the hydrogen 1S-2S transition at 121 nm have been calibrated to a frequency comb with a pulse repetition rate measured to with 6 parts in 10^{16} . [107] Other experiments measure the transition frequency of laser cooled, trapped In^+ , which had a 43 Hz line width, giving the fractional uncertainty of the line center determination to 1.4×10^{-14} . [108] Fiber based frequency combs have repetition rates of between 100 and 250 MHz, but Ti:Sapphire based combs can have 1 GHz [109] and 10 GHz [110, 111] which forms the upper limit for femtosecond (fs) comb generation. The broadband nature of frequency combs has been utilized in single pass measurements to study the absorption of many transitions simultaneously for techniques such as breath analysis. [112] In other cases, portions of the comb are coupled to enhancement cavities to produce high accuracy (1×10^{-15}) and sensitive ($1 \times 10^{-6} \text{ cm}^{-1} \text{ Hz}^{-1/2}$) absorption signals over 4 THz. [113] Other techniques take advantage of the broadband nature of frequency combs by coupling them to astronomical spectrographs for precision radial velocity measurements to detect earth-like exoplanets. [114, 115] Current state-of-the-art astronomical spectrographs are limited to 60 cm/s velocity resolution by the thorium argon calibration. [116] Based on the fact that an increasing number of wavelength calibration points decreases the frequency uncertainty, [117] using more calibration lines from a frequency comb whose value is known more precisely will increase the accuracy of the spectrographs down to the 10 cm/s level.

Still other techniques have begun employing heterodyne techniques to utilize the broadband nature of the frequency comb. For instance, coupling a cw-laser and heterodyning it against the comb modes provides 1 MHz resolution heterodyne signals over a wide frequency range. [118] Single combs have been used with a mechanical interferometer forming an FT-IR spectrometer with comb radiation as the source, [119] while even more sophisticated techniques employ two coherent frequency combs to enable motionless Fourier transform spectroscopy to simultaneously measure 9 THz with 220 MHz resolution. [120, 121]. While the relative brightness of each comb mode is lower than a conventional cw laser, it is much higher than traditional FT-IR sources. By having many spectral elements, and small acquisition time, the detection efficiency is increased. [121]

Future spectroscopic work with frequency combs will mostly focus on terahertz (THz) generation using frequency combs with non-linear processes in GaAs crystals, [122] and comb generation from whispering gallery mode cavities employing spontaneous four-wave mixing in microring resonators allowing comb generation to a chosen free-spectral range and wavelength range. [123, 124]

This chapter will focus on the implementation of a turn-key MenloSystems, erbium doped fiber based frequency comb, purchased in 2008, and used for several publications [46, 71, 86]. As this is the first dissertation describing the use of the comb, some principles of operation, operating instructions, as well as interfacing documentation will be given. While numerous groups have utilized a frequency comb to obtain the absolute transition frequencies of molecular neutrals, in many cases combining them with sub-Doppler techniques to achieve a precision as good as 10 kHz, [125–130] the work described in this dissertation [71] (and earlier work published [46, 86] and not described in this dissertation) represent the first application of a frequency comb to determination of sub-Doppler line-centers of molecular ions.

3.1 Principles of Operation

The development of the frequency comb was a major achievement because frequencies can be measured much more accurately than any other physical quantity. [131]. A frequency comb utilizes the fact that mode-locked femtosecond lasers produce a fixed frequency spacing between all longitudinal modes in the laser. Due to the dispersion of the cavity, the group and phase velocities are not the same, producing a phase shift between the carrier wave and the peak envelope for each round trip. While this dispersion cannot be removed, it can be controlled and stabilized. A Fourier analysis of the frequencies found in the modelocked, phase-stabilized ultrafast laser shows that there are discrete laser modes which are separated by the repetition rate of the laser. The frequency of the n^{th} comb mode is $f_n = nf_{REP} + f_{CEO}$ where f_{REP} is the repetition rate, and

f_{CEO} is the offset. [132]. This equation shows how the very large optical frequency, f_n , can be described by two radio frequencies. While it is impossible to directly measure optical frequencies using a counter, it is relatively simple to measure the radiofrequency components, if they are stable. The repetition rate is readily measured using a photodiode, but the determination of the offset frequency can only occur if the frequency comb spans more than an optical octave. With the discovery of self-phase modulation of the gain medium, optical octave spanning frequency combs have been produced as described in references [133] and [134] and enable a self-reference of the carrier envelope offset [135].

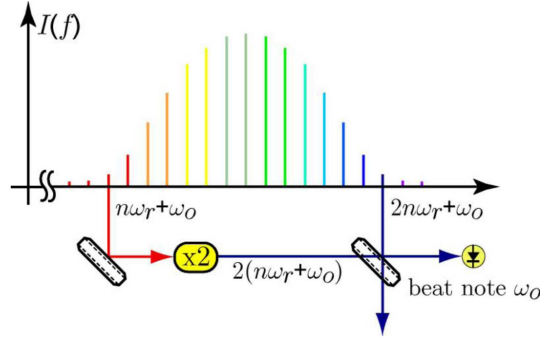


Figure 3.1: An octave spanning frequency comb can precisely measure its own offset frequency. Adapted from [10].

Comb self-referencing is accomplished when a comb mode from the red side of the frequency comb (with frequency $=nf_{REP} + f_{CEO}$) is frequency doubled using a periodically poled lithium niobate (PPLN) crystal, and the resultant frequency doubled comb mode ($2(nf_{REP} + f_{CEO})$) is heterodyned with a non-frequency doubled comb mode at the blue side of the original comb ($((2n)f_{REP} + f_{CEO})$), as illustrated in Figure 3.1. Heterodyne techniques have been used in radio engineering since 1920 where a strong reference local oscillator (LO) is mixed with a weak incoming signal. When two laser beams are superimposed on a detector, the intensity follows Equation 3.1 [136]. From Equation 3.1 it is apparent that a signal appears at the difference frequency between ω_{LO} and ω_s . This difference frequency can then be used to offset lock the carrier envelope offset of the pump laser.

$$I_R = I_s + I_{LO} + 2\sqrt{I_s I_{LO}} \cos[(\omega_{LO} - \omega_s)t + \phi] \quad (3.1)$$

An optical frequency comb (MenloSystems, FC1500) with a repetition rate of about 100 MHz was used to determine the frequency of the spectroscopic laser to sub-MHz accuracy. A photo of the frequency comb is shown in Figure 3.2, and a schematic of the optical layout is shown in Figure 3.3. A 200 MHz InGaAs-PIN photodiode is used to measure the carrier envelope offset frequency (f_{CEO}), and a 10-1000 MHz InGaAs-PIN

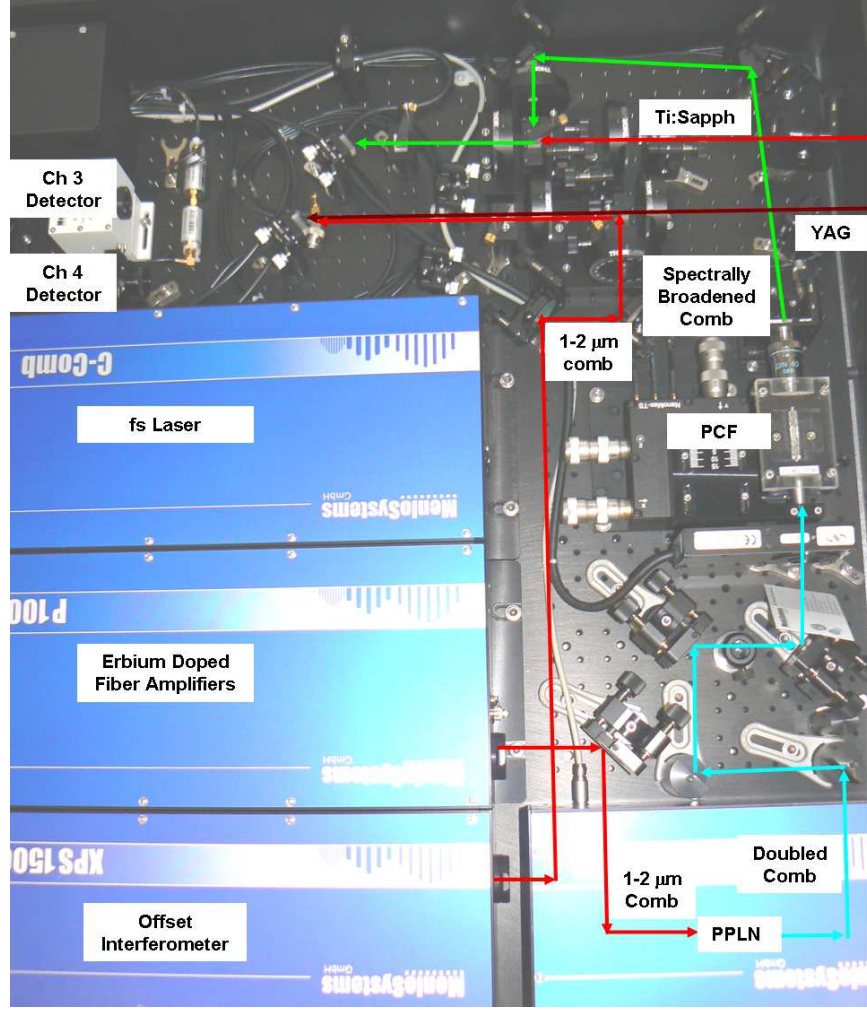


Figure 3.2: Pictures of optical frequency comb optical layout.

photodiode internal to the laser head measures the repetition frequency (f_{REP}). Using high-pass filters, the 10^{th} harmonic of the repetition frequency is measured in order to increase the phase sensitivity and frequency accuracy.

The frequency comb requires a 10 MHz reference. A global positioning system (GPS) disciplined high-stability oven-controlled crystal oscillator (Endrun technologies, Tycho-Meridian) provides a 10 MHz reference signal, with a quoted Allan variance in 1 s of 1×10^{-12} . The GPS antenna was installed on the roof of Roger Adams Laboratory, and a 100 foot cable was used to bring the GPS signal into the lab, and was connected to the Tycho oscillator. The oscillator uses the GPS signal to correct the time kept by the crystal. By averaging the corrections needed to keep the crystal synchronized with the GPS over a large time, a highly stable 10 MHz reference is produced. This 10 MHz signal then references the frequency comb, and heterodyne RF generator.

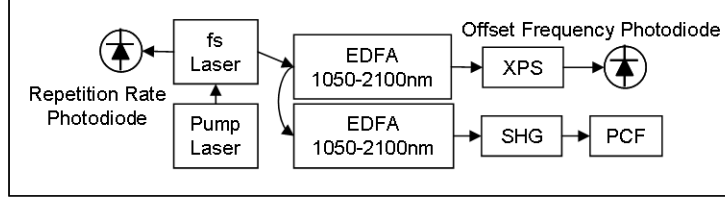


Figure 3.3: Optical layout of FC1500 frequency comb. fs=femtosecond laser, EDFA=erbium doped fiber amplifier, SHG=sum harmonic generation crystal, PCF=photonic crystal fiber, XPS=offset interferometer. Adapted from [10].

3.1.1 Repetition Frequency Lock

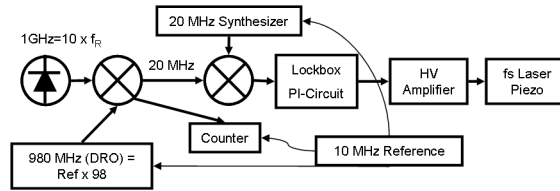


Figure 3.4: Electrical layout of the repetition frequency lock. Adapted from [10].

The electrical layout for the repetition frequency (f_{REP}) lock is shown in Figure 3.4. The tenth harmonic of the repetition rate is filtered from the fundamental (and other harmonics) impinging on the photodiode. That 1000 MHz signal is mixed with a reference signal from a dielectric resonant oscillator (DRO) at 980 MHz which is in turn referenced to the 10 MHz reference. The output of the first mixer, called the downmixed repetition rate (DMRR) is near 20 MHz. That 20 MHz signal is then mixed with a variable frequency at 20 MHz using a direct digital synthesizer (DDS). The output of the second mixer is fed into locking electronics as an error signal. The electronics process the signal, and feed the signal to a high voltage amplifier, which adjusts the piezoelectric transducer on the fs laser. The piezoelectric transducer adjusts the length of the cavity and changes the repetition rate. In this way the repetition frequency of the laser is locked with an Allan variance of 0.001 Hz. The DMRR can be converted to the repetition rate (f_{REP}) using Equation 3.2.

$$f_{REP} = \frac{DMRR + 980}{10} \quad (3.2)$$

3.1.2 Offset Frequency Lock

The electrical layout for the carrier envelope offset frequency (f_{CEO}) lock is shown in Figure 3.5. The output of the photodiode shown in Figure 3.1 is fed through RF filters and a phase detector. The reference signal is multiplied from 10 MHz to 20 MHz for the phase detector. The phase detector produces an error signal

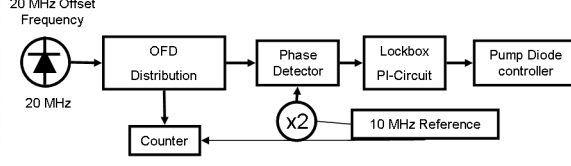


Figure 3.5: Electrical layout of the offset frequency lock. Adapted from [10].

which the lockbox uses to produce a process signal to control the power of the diodes used to pump the fs laser. The power changes the intensity-dependent index of refraction (n_2) through the Kerr effect. By changing the power in the laser, the offset can be locked to near 20 MHz. A portion of the comb radiation is sent to a photodiode, so that the absolute value of the beat frequency can be counted and recorded. Once f_{REP} and f_{CEO} are locked, these frequencies are referenced to GPS atomic clocks, and the comb can be used to precisely and accurately determine the frequency of laser radiation to the uncertainty of the reference (1×10^{-12}).

Because the comb spans an octave between 1.05 and 2.1 μm , and the Ti:Sapphire produces light between 0.7 and 0.950 μm , the comb light must be frequency doubled and spectrally broadened as shown in Figure 3.3. While the periodically-poled lithium niobate (LiNbO₃ or PPLN) crystal located in the XPS unit (see Figure 3.3) is not heated, more light is sent through the second PPLN crystal before going through the photonic crystal fiber (PCF), so this PPLN is heated to 185° C. The temperature controller inside the frequency comb rack must indicate that the PPLN crystal temperature is at this value before comb radiation is placed on the crystal. After the PPLN SHG stage, the comb radiation is centered at 785 nm and spans between 760 and 825 nm. In order for the full Ti:Sapphire wavelength range to be covered, the frequency doubled comb must be broadened with a nonlinear fiber. A photonic crystal fiber (PCF) spectrally broadens the doubled light. The fiber has a 2 μm core surrounded with air holes, which change the index of refraction and cause spectral broadening. After the PCF, the comb radiation can span between 450 and 950 nm, spanning the entire Ti:Sapphire wavelength range. The spectrally broadened comb light is then overlapped with the unknown near-IR laser whose frequency is to be determined.

The frequency of the CW laser is determined by measuring the beat note between the unknown laser and the comb. The beat note is measured by heterodyning the two lasers on a detector. In order to heterodyne the two lasers, they must be made collinear, have the same spatial mode (size), and polarization. Collinearity is accomplished as shown in Figure 3.6. Two polarizing beam splitters are used to enable collinearity and ensure that the light is in the same polarization. Two half wave-plates ($\frac{\lambda}{2}$) are used to rotate the comb radiation and the Ti:Sapphire radiation into vertically and horizontally linearly polarized

radiation, respectively. The vertically polarized comb light is reflected by the first polarizing beam splitter (PBS), and the horizontally polarized Ti:Sapphire radiation is transmitted. A third half wave-plate rotates both lasers to approximately 45° from the horizontal, and a second PBS selects out only the horizontally polarized radiation of both components. Beam collinearity is adjusted by steering mirrors of the Ti:Sapphire and the comb before the first PBS. After the beams are collinear, they are dispersed by a grating, and reflected onto an avalanche photodiode. The heterodyne beat signal then follows the electrical path outlined in Figure 3.7, passing through RF filters. (All cases use a 50 MHz low-pass (LP) filter, and in some cases a 20 MHz band-pass filter). That beat note is then fed to the counter which determines the frequency of the beat note (f_{Beat}).

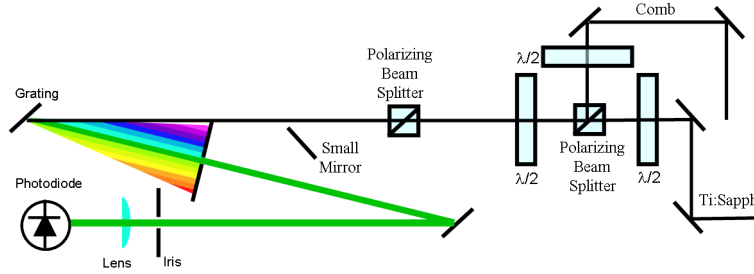


Figure 3.6: Optical layout for making cw laser collinear to comb. $\frac{\lambda}{2}$ - half wave plates. Adapted from [10].



Figure 3.7: Electrical signal path of unknown beat signal, starting from the avalanche photodiode. Adapted from [10].

Once f_{REP} , $|f_{CEO}|$ and $|f_{Beat}|$ have been determined, one must then determine the signs of $|f_{CEO}|$ and $|f_{Beat}|$. Instructions for the determination of the sign will be given in Section 3.3. If the wavelength of the unknown laser has been determined to within 50 MHz ($\frac{1}{2}$ of f_{REP}), and the signs of the beat-notes have been determined, Equation 3.3 can be used to determine the frequency of the laser to sub-MHz precision and accuracy.

$$f_{cw} = n f_{REP} \pm f_{CEO} \pm f_{Beat} \quad (3.3)$$

3.2 System Startup

Begin by ensuring that the frequency comb computer is on. Then turn on the power supplies for the control electronics by turning the keys illustrated in Figure 3.8 90° clock-wise. Begin with the overall electronics first, then the fiber-laser electronics, then the amplifier electronics. It may take several minutes for the mode-locked LED on the fiber-laser to stop blinking and be solidly illuminated, indicating mode lock.

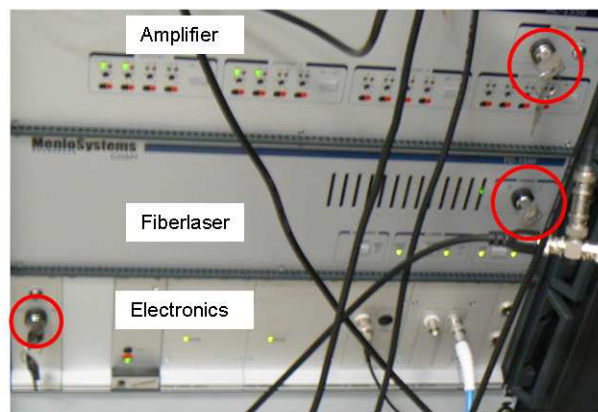


Figure 3.8: Location of electronics, fiberlaser, and amplifier switches for system startup.

3.2.1 DDS & Temperature Controller

The direct digital synthesizer (DDS) and Thorlabs temperature controller are shown in Figure 3.9. Turn on the DDS by flipping the switch located at the upper right-hand corner of the DDS. Gain local control of the DDS by pushing the knob in. Press the soft-key on the screen of the DDS located in the upper right-hand corner to toggle the RF output on and off. Begin with the RF output on. Ensure that the temperature controller is on, enabled, and set to 185°C. The set temperature of the crystal should never be changed by more than 10° per minute. For other questions dealing with the temperature controller, please refer to the TC200 Manual.



Figure 3.9: Direct digital synthesizer (DDS) on the left and the Thorlabs TC200 which controls the temperature of the periodically poled lithium niobate crystal for doubling the comb radiation.

3.2.2 Software & Modelocking

Launch the frequency comb software (Fiber Comb Control V.0.24). Upon start-up, there may be a non-fatal error if the DDS is not connected to the frequency comb computer. This is fine, hit OK. The comb software should look something like Figure 3.10. The green boolean indicators indicate that a control is activated. If a feature is inactive it will be red. First ensure that the laser is “on” by clicking the button located to the right of the green indicator and label for “Laser”. If mode lock is near, the “Laser Modelocked” indicator should turn green quite quickly and the laser will beep three times. If mode-lock is not obtained upon startup, first write down the four values of the “PControl Laser” sliders, and slowly move the sliders up and down by 10 single clicks on the arrows. If a mode locked state is not obtained, refer to Appendix B. Once mode-lock is obtained, the XPS amplifier can be turned on by clicking on the button marked “Amplifier XPS”. The mode-lock state should not be adjusted or lost when either amplifier is on, as they can be damaged should mode-lock be lost.

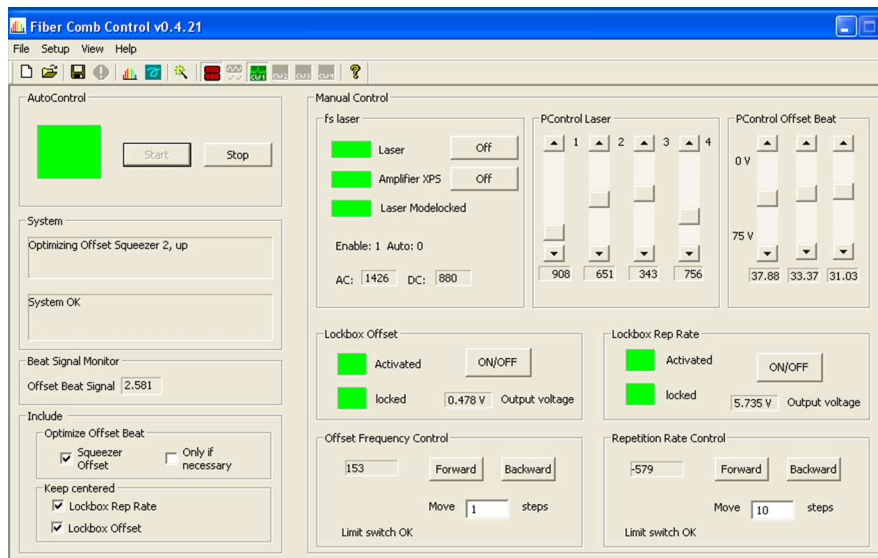


Figure 3.10: Comb software screen shot. “PControl Offset Beat” sliders are used to adjust the offset beat.

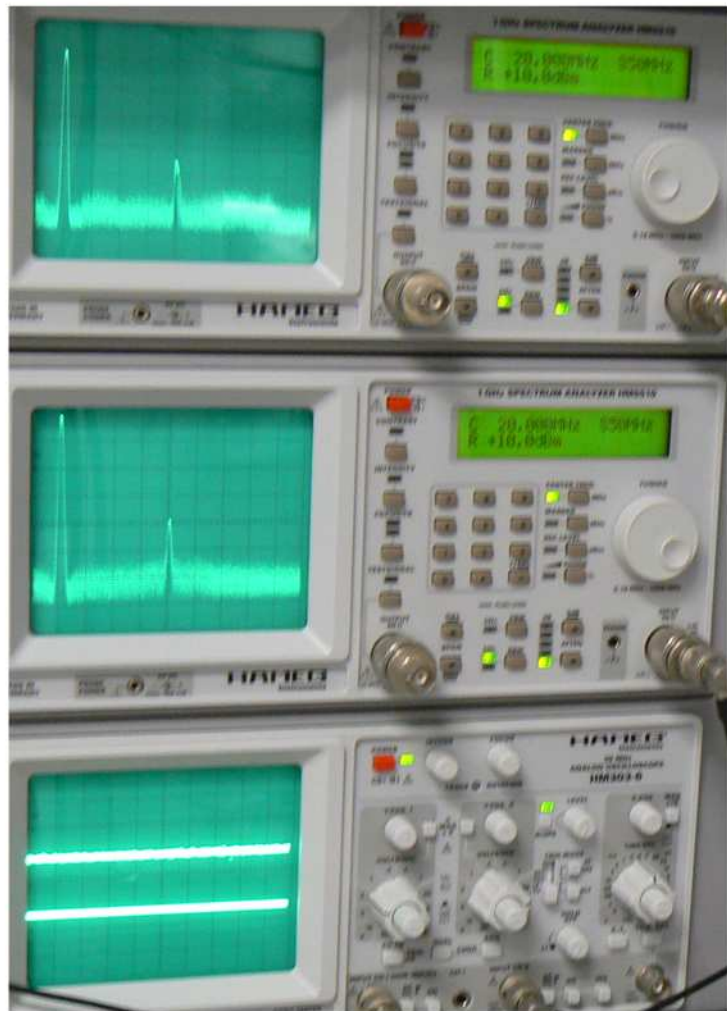


Figure 3.11: Two spectrum analyzers and oscilloscope.

3.2.3 Obtaining Carrier Envelope Offset Beat

The two spectrum analyzers and oscilloscope can then be turned on. A picture of those instruments is shown in Figure 3.11. Usually the top box (the upper spectrum analyzer) is used to monitor the carrier envelope offset beat (f_{CEO}). The lower spectrum analyzer monitors the unknown laser beat (f_{cw}), and the lowest box is an oscilloscope for monitoring the error signals of the f_{REP} and f_{CEO} lock. The upper spectrum analyzer's input should come from the monitor port of OFD100. After a spectrum analyzer is turned on, and before the signal is applied, the attenuation should be set to the highest level (40 dB) to ensure no damage occurs to the instrument. If no offset beat is observed after the amplifier is turned on, the attenuation should be reduced, up to a value of 10 dB of attenuation. If a signal is still not observed, one should return the attenuation to the highest level and observe the signal directly coming from the photodiode (the input to the OFD). After zooming out to at least 100 MHz from the zero frequency (by increasing the span of the sweep), the repetition beat note should be observed. If it is not observed, then the XPS light is not hitting the photodiode. If the repetition beat note is observed, it can be peaked up using the mirror before the photodiode inside of the XPS. Adjustment of this mirror should rarely occur. After the assurance of light hitting the detector has been obtained, one can then adjust the three “Squeezer” adjustments of the amplifier named “PControl Offset Beat” shown in the upper right-hand corner of Figure 3.10. These sliders can be moved much more vigorously than the “PControl Laser” sliders, and have little hysteresis. Observe the spectrum analyzer with low attenuation in the 0-50 MHz region while adjusting the sliders until a signal is obtained. Then optimize the signal while gradually increasing the attenuation until 20 dB of signal-to-noise (S/N) is obtained at 30 dB of attenuation.

3.2.4 Carrier Envelope Offset and Repetition Frequency Locking

Once the offset beat has 20 dB of S/N, one can then adjust f_{REP} and f_{CEO} . Before either lockbox is activated, one must first ensure that both lockboxes are centered within their capture range. This can be determined by observing the digital readout shown in the software lockbox controls, shown in Figure 3.12. If either lockbox is not centered, the value can be changed by turning the knob illustrated in Figure 3.13 while monitoring the digital readout until the numbers are near 0.5 and 5 V respectively. Once the lockbox offsets are centered, the carrier envelope offset (CEO) should be set to near 20 MHz. Press the “Center Frequency Button” on the spectrum analyzer coming from the carrier envelope offset OFD. Type in “20.” and then press “Center Frequency” again, and the spectrum analyzer will now show the middle vertical line as 20 MHz. If the offset beat is not at 20 MHz, move the CEO by pressing the “Forward” and “Backward” buttons shown in Figure 3.12 in steps of size between 1 and 10. As the CEO begins to approach the correct

value, the absolute value of the slope of the error signal, shown in the top trace of Figure 3.14, decreases. Once the absolute value of the slope of the error signal shows little decrease when a step of 1 is made, the CEO is in the correct place.

If the DDS were connected to the frequency comb computer, a similar procedure could be followed for the repetition frequency. However, as the DDS is scanned by the spectroscopy LabVIEW program and computer, the DDS must be manually reset. This is done by observing the “Downmixed Repetition Rate” (DMRR) shown in Figure 3.15, and manually changing the DDS to match this value. This is accomplished by pressing the knob of the DDS in (to gain local control of the device), and using the left and right arrows to move the indicating vertical arrow to the correct position and turning the knob to the correct value to match the DMRR. As the DDS was constructed in Germany, the European convention of using a comma as the decimal point, and periods to denote three digits is used. An example of the DDS screen is shown in Figure 3.16. As the frequency of the DDS is adjusted to the near the correct value, the error signal of f_{REP} , shown in lower trace in Figure 3.14, will begin to oscillate less often. Usually when the value is within 10 Hz, it is possible to lock f_{REP} . The lock is engaged either by pressing the “ON/OFF” software button shown in Figure 3.12 or by pressing the physical button on the lockbox shown in Figure 3.13.

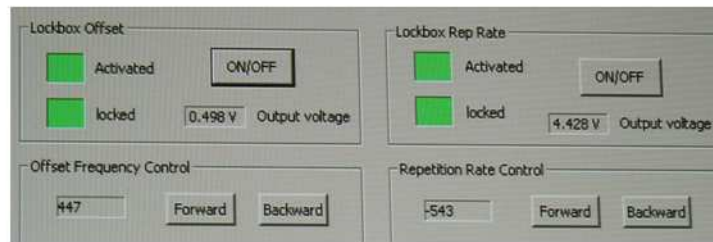


Figure 3.12: The software controls for the offset (left) and frequency (right) lockboxes indicate when the lock is activated, locked, and what the offset of the capture range is. Both lockboxes should be set to near the center of the travel. For the “Offset Lockbox” this should be 0.5V. For the “Rep Rate Lockbox” this should be 5V.



Figure 3.13: A picture of the lockboxes used for locking the carrier envelope offset (left) and frequency (right) of the fs-comb laser. The knob for adjusting the offset is circled in red. The button for turning the lock on and off glows green when engaged. The red LED to the right of the green switch is illuminated when the locking mechanism is engaged but not locked.

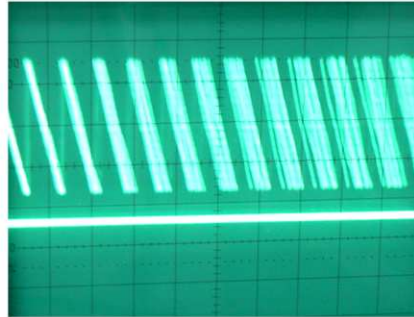


Figure 3.14: Oscilloscope trace of the error signals generated by the locking electronics when f_{CEO} is not locked (top), but f_{REP} is (bottom). When f_{REP} is unlocked, a sine wave is apparent in the bottom trace.



Figure 3.15: A screenshot of the “Counters View” box of the Fiber-comb software. The top value is the “Downmixed Repetition Rate” used to determine the repetition frequency of the fiber-laser as described by Equation 3.6 in Section 3.3 and as used to adjust the fiber-laser’s repetition frequency lock. The second value is the absolute value of “Offset Beat”, used as part of Equation 3.4 to determine the unknown cw laser’s frequency. “Channel #3” is the counter reading from the visible channel which is used to measure the absolute value of the beat frequency of the Ti:Sapphire laser. “CW Beat 2: 1064 nm” is the counter reading from the IR channel which is used to measure the absolute value of the beat frequency of the YAG laser. The reported Allan variances (Hz) are for the last 100-1000 data points taken and are only useful if the laser is actively stabilized to something (f_{REP} and f_{CEO} are actively stabilized, and their variance therefore has meaning).

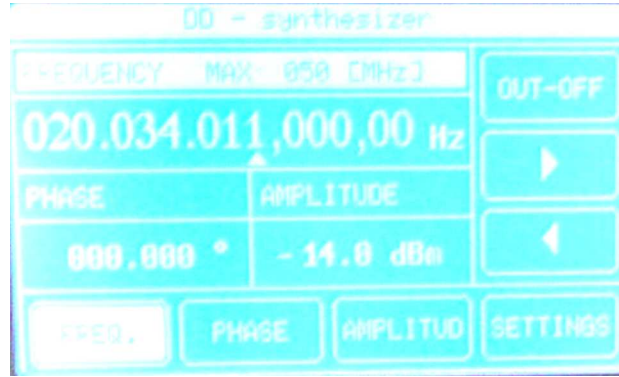


Figure 3.16: A picture of the DDS screen where the left and right arrows are apparent, as well as the display indicating 20, 034, 011.000 00 Hz. The indicating arrow is at the 1 Hz position

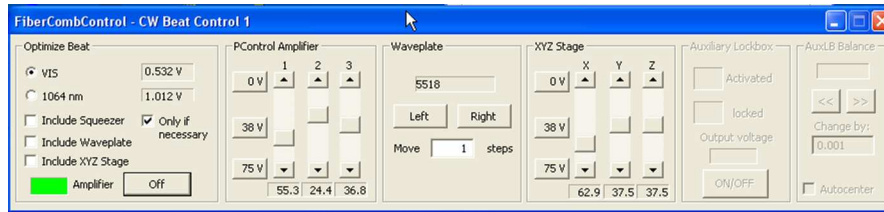


Figure 3.17: Dialogue for controlling the amplifier, waveplate, and piezo stage for the doubled comb radiation and photonic crystal fiber.

3.2.5 Frequency Doubled Comb Radiation

Once f_{REP} and f_{CEO} are locked, one can then turn the frequency doubled comb radiation on. This is accomplished by clicking the “ON/OFF” switch located in the bottom left corner of the “CW Beat Control” dialogue shown in Figure 3.17. Once the amplifier is on, the power output from the SHG stage should be measured using the Coherent power meter outside of the comb box. Approximately 80 mW of doubled comb radiation can be obtained when the “PControl Amplifier” sliders are adjusted. Once 70 - 80 mW is achieved, the light can enter the photonic crystal fiber (PCF). By placing a business card (or other TiO_2 laced surface) after the translation stage with the PCF, one can monitor the coupling by viewing the business card with an IR viewer. The XYZ stage controls shown in Figure 3.17 should be set to the middle setting by clicking on “38 V”. Then the XYZ micrometers should be manually adjusted to maximize the light passing through the fiber. If no light is seen, please refer to Appendix B. Once the light is visible without an IR viewer, optimization should continue until the brightest, whitest light comes out of the fiber (it will still be teal/green- but the whiter the color the better the broadening). A red glass filter reflects most of the visible comb radiation and only the NIR components pass through.

3.2.6 Collinearity of Comb and CW Radiation

The comb radiation bounces off of two mirrors and then is made collinear with the incoming Ti:Sapphire radiation on a polarizing beam splitter (PBS) as indicated in Figure 3.6. In order to increase the collinearity path length, a small mirror is inserted after the 2nd PBS and before the grating to reflect both lasers outside of the frequency comb box. The collinearity is adjusted with two mirrors before the half wave plates for the Ti:Sapphire or the comb radiation. Once suitable collinearity is achieved, the small mirror is removed and both lasers reflect off of the grating. Depending on the wavelength of the Ti:Sapphire, the Ti:Sapphire radiation may not reach the next mirror. The top screw of the grating adjusts the horizontal pointing of the grating by small amounts. The horizontal pointing of the grating should be adjusted such that the Ti:Sapphire spot appears near the center of the next steering mirror. If a large wavelength change was made (for instance, when the Ti:Sapphire Matisse Optical Sets are changed from MOS3 to MOS2), rotation of the entire grating mount will be necessary. The Ti:Sapphire beam spot should hit the iris in front of the detector. The next steering mirror can also be horizontally adjusted. The vertical pointing should seldom need adjusting.

3.2.7 Comb Radiation at the Correct Wavelength

Once the lasers are collinear and aligned to the detector, one must ensure that the light broadened by the PCF (described in Section 3.2.5) is at the correct wavelength. This is accomplished by placing a white piece of cardboard before the iris in front of the detector, and using a NIR viewer to look at the horizontally dispersed radiation of the comb light and compare the spatial distribution of comb light with that of the Ti:Sapphire. If there are “dark spots” in the dispersed comb where the Ti:Sapphire radiation is, the comb wavelength is not correct and no beat note can be observed. Adjust the “PControl Amplifier” sliders shown in Figure 3.17 until no dark spots are visible where the Ti:Sapphire radiation occurs.

3.2.8 Obtaining CW Beat Note

Once the cw laser and comb are collinear, spatially mode matched, of the same polarization, and the comb is broadened to the wavelength of the Ti:Sapphire, the beat note should be apparent on the detector. One monitors for the beat note by directly connecting the input of one of the spectrum analyzers to the output of the photodiode. This is illustrated in Figure 3.18. By increasing the span of the spectrum analyzer to 100 or 200 MHz, a beat note at 100 MHz (the repetition frequency of the fs laser) should be apparent when comb radiation is on the detector. This 100 MHz beat note is the spacing between adjacent comb modes (f_{REP}). If this beat note is not visible, this means the comb radiation is not reaching the detector and the alignment to the detector should be changed by adjusting the vertical and horizontal displacement of the lens shown in Figure 3.6. Once f_{REP} is visible, the spectrum analyzer can be adjusted for a 50 MHz sweep centered at 25 MHz. When the Ti:Sapphire and comb are perfectly collinear, of the same polarization, spatially mode matched, and the comb has radiation at the same frequency as the Ti:Sapphire a beat note should be apparent. The proportion of light from the comb and the Ti:Sapphire should be balanced, by rotating the half wave-plate in between the two PBS's shown in Figure 3.6. If no beat note is apparent, the steps outlined in sections 3.2.6 through 3.2.8 should be repeated until a beat note is found.

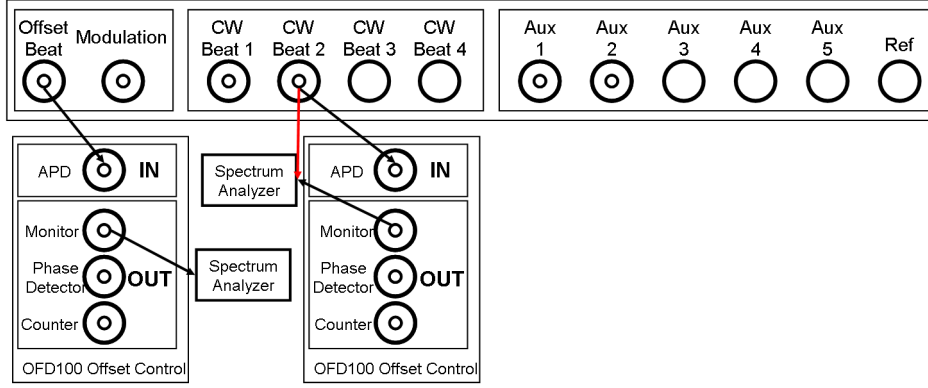


Figure 3.18: Cartoon diagramming nominal and temporary BNC connections. Normally the “CW Beat 2” from the photodiode is plugged into “APD In” of the “OFD100 Offset Control” and the monitor of the “Offset Control” is connected to the spectrum analyzer. The red line indicates that the “CW Beat Control 2” can be directly connected to the spectrum analyzer input.

3.2.9 Optimizing CW Beat Note

Once a suspected beat note is observed, it should be verified before optimization is attempted. Blocking either the input Ti:Sapphire or the comb radiation will make the beat note disappear. If blocking either radiation source does not remove the beat, probably too much power from either the Ti:Sapphire or comb is on the detector, and the balance should be adjusted with the third half wave-plate. Finally, by scanning the Ti:Sapphire at a slow speed (~ 1 MHz/s) should slowly scan the beat note across the spectrum analyzer, within the RF filters’ bandpass. Once the beat note (f_{CW}) has been verified, the signal can be optimized. The Ti:Sapphire should be scanned until the beat note is approximately centered at 20 MHz. Then the 50 MHz and 30 MHz low pass filters (Mini-Circuits BLP-50⁺, BLP-30⁺) and external bandpass filter (Mini-Circuits BBP-21.4⁺) can be inserted in-between the output of “CW Beat 2” and the APD in as shown in Figure 3.18.

Once the harmonics of f_{REP} and other noise is removed with the low-pass and bandpass filters, the input attenuation of the spectrum analyzers can be adjusted as necessary to aid in CW Beat optimization. The beat note can be adjusted by changing the parameters listed in Sections 3.2.6 through 3.2.8. Several iterations between the vertical and horizontal placement of the lens, the rotation of all three half-wave plates and collinearity mirrors shown in Figure 3.6, the XYZ stage of the non-linear PCF and the “PControl Amplifier” sliders shown in Figure 3.17 may be necessary. The XYZ stage of the PCF can be adjusted, both manually and by computer control. Initial coarse adjustment will occur manually and finer adjustment will occur using the XYZ control shown in Figure 3.17. The beat note should be optimized until a signal to noise ratio (SNR) of at least 20 is seen with 40 dB of input attenuation. Then the signs of the beat notes can be

determined.

3.3 Measurement of Ti:Sapphire laser

Once a cw beat is observed on the spectrum analyzer with a SNR of at least 20 with 40 dB of input attenuation, the absolute frequency of the cw laser can be measured. Equations 3.4 and 3.5 are used to determine the frequency of the input laser. Equation 3.4 is used for the fundamental comb (YAG input) and Equation 3.5 is used for the frequency doubled comb (Ti:Sapphire input). The values of f_{REP} , $|f_{CEO}|$ and $|f_{CW}|$ are determined directly from the frequency comb. The Offset Beat ($|f_{CEO}|$) and the CW Beat ($|f_{CW}|$) are shown on the “Counters View” screen shown in Figure 3.15. The repetition frequency (f_{REP}) is calculated from the “Downmixed Repetition Rate” (DMRR) shown in Figure 3.15 using Equation 3.6. The value of the comb mode participating with the cw laser, n , and the sign of f_{CEO} and f_{CW} must be determined before Equations 3.4 and 3.5 can be used to determine the frequency of the cw laser. The procedure for determining these values is to first determine the sign of the cw beat (f_{CW}), then the sign of the carrier envelope offset beat (f_{CEO}), and then the comb mode number n .

$$f_{YAG} = n \times f_{REP} \pm f_{CEO} \pm f_{CW} \quad (3.4)$$

$$f_{Ti:Sapphire} = n \times f_{REP} \pm 2f_{CEO} \pm f_{CW} \quad (3.5)$$

$$f_{REP} = \frac{f_{DMRR} + 980}{10} \text{MHz} \quad (3.6)$$

3.3.1 CW Beat Note Sign Determination

The sign of the CW beat note can be determined by either scanning the repetition rate of the frequency comb (as described in the MenloSystems manual [10]) while the Ti:Sapphire is fixed, or scanning the frequency of the Ti:Sapphire while the repetition rate of the frequency comb is fixed. Figure 3.19 shows an explanation of how the sign of the CW Beat is determined. Normal use of the comb will usually find the second case more intuitive. The figure shows the case of the Ti:Sapphire frequency being higher than the nearest comb mode, meaning that the beat sign is positive. When the laser frequency increases (the wavelength and reference cell piezo voltage decrease), the beat frequency increases. This can lead to the information on the left half of Figure 3.20. When the direction of travel of the reference cell piezo and the CW beat are opposite in sign,

the cw beat is positive, and when they are in the same direction, the sign is negative.

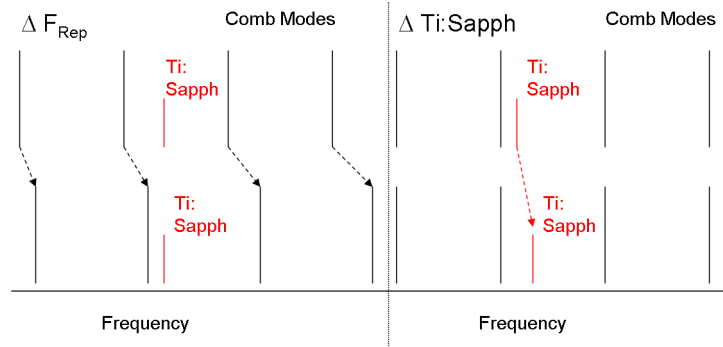


Figure 3.19: A case of a positive beat frequency. The left side of the figure shows the effect on the cw beat frequency when scanning the repetition frequency of the fs laser while the Ti:Sapphire frequency is fixed. The right side of the figure shows the effect of scanning the Ti:Sapphire frequency while the fs laser frequency is fixed.

Scan F_{Rep}	Scan Ti:Sapph			
$F_{\text{Repetition}}$ Δ Matisse Beat	$F_{\text{Ti:Sapph}}$ $\lambda_{\text{RefCellPiezo}}$ Δ Matisse Beat	Ti:Sapph Sign	Δ Offset Beat Δ Ti:Sapph	Offset Beat Sign
↑↓	↑↓	+	↓↑	+
↓↑	↓↑		↑↓	-
↑↓	↑↑	-	↓↓	+
↓↑	↓↓		↑↑	-

Figure 3.20: A chart indicating how to determining the sign of the CW beat of the Ti:Sapphire and laser the CEO beat sign of the frequency comb. The wavelength of the Ti:Sapphire corresponds to the piezo voltage of the reference cell. If the wavelength and CW beat travel in the same direction (CW beat increases with wavelength) then the sign of the CW beat is negative. If the wavelength and CW beat travel in opposite directions (CW beat decreases with wavelength) then the sign of the CW beat is positive. For a positive CW sign, if the offset frequency decreases while the CW beat of the Ti:Sapphire decreases, then the CEO beat sign is negative. For a positive CW sign, if the offset frequency increases while the CW beat of the Ti:Sapphire decreases, then the offset beat sign is positive.

3.3.2 Carrier Envelope Offset Beat Note Sign Determination

Once the sign of the cw beat note has been determined, the sign of the CEO beat can be determined. Figure 3.21 shows a visual explanation of the CEO of an optical frequency comb. When the octave spanning comb is frequency doubled, one of the red comb lines from the frequency doubled comb is heterodyned with the one of the blue comb lines of the fundamental comb. The heterodyne beat between them is measured near 20 MHz, but it matters if the frequency doubled comb mode contribution is higher in frequency (positive CEO), or lower in frequency than the fundamental comb mode contribution (negative CEO).

The sign of the f_{CEO} is determined by unlocking the offset lock (described in Sections 3.1.2 and 3.2.4) and changing f_{CEO} by adjusting the knob shown in Figure 3.13. The direction of frequency change in CEO is noted, as well as the direction of change in cw beat frequency. The chart in Figure 3.20 is consulted and

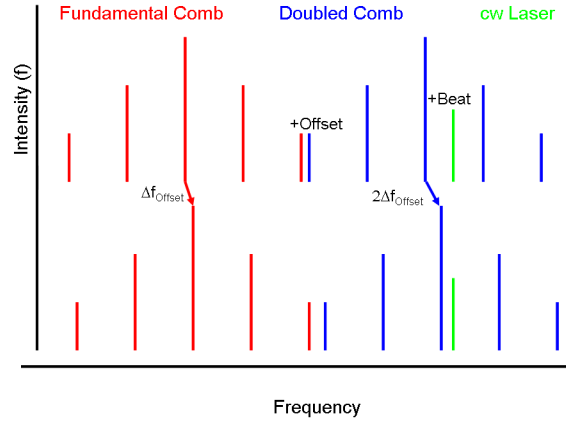


Figure 3.21: A case of a positive beat frequency and positive offset beat frequency. The top case shows the conditions before the CEO of the comb is changed. The lower chart shows the effect of increasing the offset frequency. Overall, the graphic illustrates that the cw beat frequency will decrease when the offset frequency is increased while the Ti:Sapphire frequency is fixed for a positive cw and offset beat. Understanding this figure, together with Figure 3.19 illustrates how Figure 3.20 was constructed.

the appropriate sign is determined from the chart.

3.3.3 Comb Mode Number Determination

Once the sign of the cw and CEO beats are determined, and the wavemeter is aligned, the comb mode number contributing to the beat note can be determined. Figure 3.22 shows a screenshot of a part of the LabVIEW program used to determine the cw laser's frequency. On the bottom right of the screenshot, two

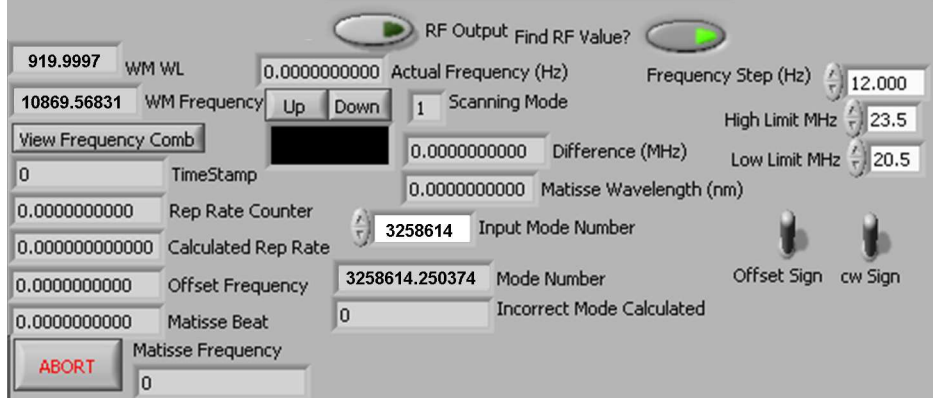


Figure 3.22: Two toggle switches at the bottom right of the screenshot are used to indicate the sign of the offset and cw beat frequencies. Pointing up means a positive sign, pointing down means a negative sign. The two boxes at the top left of the screenshot indicate the wavemeter wavelength and frequency.

toggle switches are used to indicate the sign of the offset and cw beat frequencies. These **must** be in the correct position, “up” for positive and “down” for negative. When the “View Frequency Comb” button is pressed, the computer communicates with the OFC to read out several of the values, such as the “Time Stamp”, the “Rep Rate Counter”, the “Offset Frequency” (f_{CEO}) and cw beat “Matisse Beat” (f_{CW}). The Repetition Rate (f_{REP}) is calculated from the “Rep Rate Counter” value using Equation 3.2. Now that the signs of f_{CEO} and f_{cw} are known the only unknown is the mode number n , and Equation 3.5 can be solved for the mode number using an estimation of $f_{Ti:Sapphire}$ from the wavemeter ($f_{Ti:Sapphire,wavemeter}$) as shown with Equation 3.7.

$$n_{estimate} = \frac{f_{Ti:Sapphire,wavemeter} \mp 2f_{CEO} \mp f_{CW}}{f_{REP}} \quad (3.7)$$

For unambiguous determination of the frequency comb mode contribution number (n), usually a wavemeter with accuracy better than half the repetition rate of the frequency comb is required. For a 100 MHz comb, a wavemeter with accuracy better than 50 MHz should be required. As the wavemeter used has an uncertainty of 65 MHz at 920 nm, the wavemeter may not have high enough accuracy to determine the mode number. This ambiguity was investigated and it was determined that there are circumstances when the wavemeter is precise enough to determine the comb mode number. The uncertainty of the wavemeter is

usually an offset that can change from day to day and is sometimes dependent on alignment. The precision of the offset is fairly constant through the course of the day. The offset can be determined unambiguously by scanning over the hyperfine transitions of iodine using the wavemeter. The difference between the actual transitions and the reading on the wavemeter is the offset. Once the offset is known, the wavemeter can be used to unambiguously determine the comb mode contribution number.

Alternatively the comb number contribution can also be determined without scanning over iodine first, as long as the offset of the wavemeter is less than 35 MHz. When Equation 3.7 is used, the calculated value is never an exact integer. Instead the calculated mode number has at least two digits of precision after the decimal. If the calculated number is within 0.35 of the comb mode number, it is determined unambiguously. An explanation of this principle is shown in Figure 3.23.

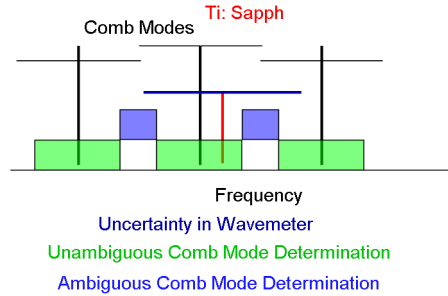


Figure 3.23: Visual explanation of how a 65 MHz accuracy wavemeter can provide unambiguous comb mode determination. The vertical black lines indicate the position of comb modes. The shorter, vertical red line illustrates the position of the Ti:Sapphire laser. The horizontal blue line represents the uncertainty of the wavemeter. The central green box represents the ± 35 MHz where the comb mode number can be unambiguously determined. The blue boxes on the sides represent the ambiguous region of comb mode determination. If the mode number calculated by Equation 3.7 is within the unambiguous region, the comb mode number is known.

Figure 3.23 illustrates that as long as the as the comb mode number is within ± 0.35 of an integer, the comb mode can be unambiguously determined without additional information. If the comb mode is outside the ± 0.35 , an iodine scan is required to determine the wavemeter offset. Once the wavemeter offset is determined, the comb mode number can be unambiguously determined.

3.3.4 Measurement of Laser Frequency

With the comb mode number accurately determined, the signs of the Offset and CW beat determined, the repetition rate, the offset beat frequency, and the CW beat frequency, all the unknowns of Equation 3.5 are known, and it can be used to determine the frequency of the Ti:Sapphire laser. Once the actual comb mode number is typed into the “Input Mode Number” field, and the correct Offset and CW signs are selected,

the software will automatically calculate the wavelength of the Ti:Sapphire as measured with the comb. If a scan is underway, the LabVIEW program will automatically save this value.

It is important to point out that the wavemeter and frequency comb measurements normally occur before any manipulation with the double-passed acoustooptic modulator (AOM), which shifts the frequency of the light by twice the frequency of the RF signal applied to the AOM. Post-signal processing is used to account for this shift. This convention was chosen for two reasons. First, the value of the frequency of the laser as determined by the frequency comb should refer to the frequency of light actually entering the frequency comb. Second, by post-signal processing, the user is aware of, and can account for, any incorrect assumptions about the sign of the shift induced by the AOM.

Once the data is read into an Igor data calibration routine, the assumption that the correct comb mode number is checked by graphing the assumed mode number (input into the program) with the calculated mode number calculated from Equation 3.7. Such a graph is shown in Figure 3.24(a). As the centroid of the Gaussian fit to the histogram (Figure 3.24(b)) is firmly within the unambiguously determined region, one can be confident that the correct mode number was chosen.

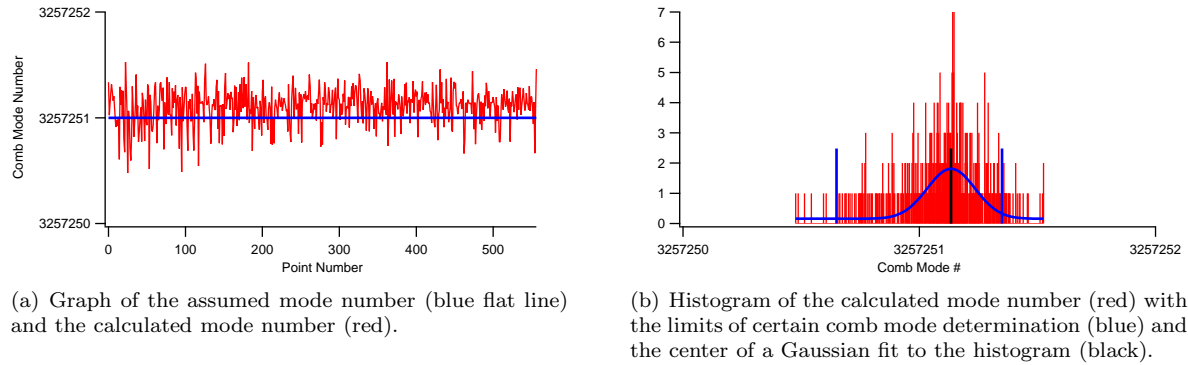


Figure 3.24: Graphs of comb scans illustrating how the assumption of the comb mode number determination was validated.

3.3.5 Recording Frequency Comb Data

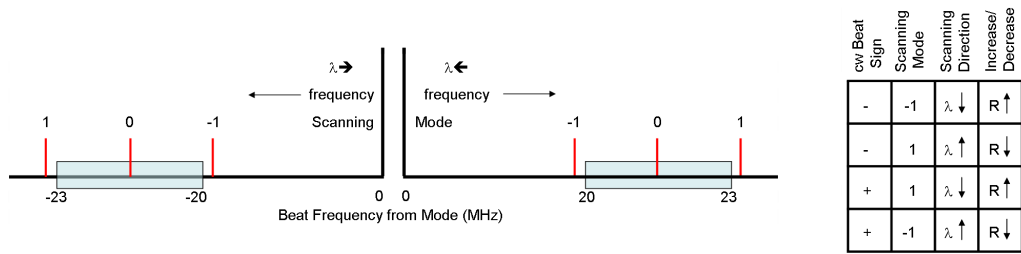
Recording the data into the LabVIEW spectroscopy program is a two-step automated process. The frequency comb program can automatically generate an XML-RPC server, if the correct setting in the setup file is selected. An example of the setup file is shown in Section B.3 of Appendix B. Once the Fiber Comb Control program is generating the XML-RPC server, it can be read by a simple Python script. LabVIEW allows Python code to run inside of LabVIEW. An example of the python code used to read the values is found in Section B.4. The LabVIEW code automatically records important values from the comb and the

wavemeter, records the user's input of the signs of the offset and CW beats and the assumed mode number, and calculates and records the frequency of the Ti:Sapphire laser unshifted by the AOM.

3.4 Scanning Comb

Precise frequency counting measurements require a narrow RF bandpass filter. The comb electronics arrived with an RF bandpass filter roughly 20.3 MHz to 23 MHz. Therefore, measurements of the cw beat of the Ti:Sapphire laser against a comb mode can only occur when the Ti:Sapphire laser is between 20.3 and 23 MHz away from the nearest comb mode. Because typical comb scans occurred over at least 600 MHz, gaps with 50 MHz spans would lose a lot of frequency calibration. Therefore, the repetition rate of the fs comb laser was incremented when the measured beat frequency approached the limits of the bandpass filters. By writing a program to integrate with the direct digital synthesizer (DDS) of the frequency comb, the repetition frequency of the fs laser was changed by 1.2 Hz every 4-5 data points. As a result, the measurement of the frequency would be made with a single comb mode during the entire scan.

Scanning was accomplished by automatically performing some calculations at each data point. The absolute value of the CW beat was compared to the low and high limits input into the program (see Figure 3.22). If the value is beneath the high limit and above the low limit, the scanning mode is set to 0 (inactive). If not, the program goes on to determine if the beat frequency should increase or decrease. The average of the low and high limit is determined. If the CW beat value is larger than the average limit, the scanning mode is set to 1 (decrease beat frequency). If the value is smaller than the average limit, the scanning mode is set to -1 (increase the beat frequency). The program takes into account whether the laser frequency is increasing or decreasing, and whether or not the CW beat frequency is positive or negative. As illustrated in Figure 3.25, f_{REP} will be increased if the laser frequency is increasing, and either the beat is too high with positive sign, or too low with negative sign. f_{REP} will be decreased if the laser frequency is decreasing, and either the beat is too high of a negative value, or too low of a positive value. A chart in Figure 3.25(b) illustrates the logic the LabVIEW program uses to determine if the frequency should be increased or decreased depending on the CW beat sign, the scanning mode, and the piezo scanning direction.



(a) A chart illustrating how to determine which direction the fs rep rate should be changed.

(b) Chart illustrating which direction to turn to change the repetition rate dependent on the scanning mode, and CW Beat sign.

Figure 3.25: Illustration of how to determine which direction to slew the optical frequency comb repetition rate.

Chapter 4

Spectroscopic Method

Three methods were used to attempt laser-based spectroscopic measurements in the SCRIBES instrument: cavity ringdown (CRDS), cavity enhanced absorption spectroscopy (CEAS), and noise immune cavity enhanced optical heterodyne modulation spectroscopy (NICE-OHMS). In the end, neither CRDS nor CEAS were able to measure the absorption signal of the ion beam, and NICE-OHMS was used to measure the dispersion signal of the ion beam. Therefore only the NICE-OHMS spectroscopy will be described.

4.1 Noise Immune Cavity Enhanced Optical Heterodyne Molecular Spectroscopy

Noise immune cavity enhanced optical heterodyne molecular spectroscopy (NICE-OHMS) was developed by Jun Ye as a highly sensitive detection technique. [81] Typical sensitive absorption techniques had previously worked on either reducing the background noise, or increasing the intrinsic absorption signal. NICE-OHMS works by doing both at the same time. NICE-OHMS is based first on frequency modulation (fm) spectroscopy, to reduce the background noise. In a sense, frequency modulation collects data from an on-resonance signal and off resonance signal and subtracts the two, thus providing a signal where there is no output unless there is some form of optical resonance. This is accomplished by using an electrooptic modulator (EOM) to add sidebands to the carrier of the laser, where one side band will collect data with on resonance and another sideband will be off resonance. An EOM is a nonlinear crystal where an electric field is applied to the crystal via electrodes. The applied electric field changes the index of refraction of the material, which changes the phase delay of a laser beam sent through the crystal. The EOMs used for frequency modulation (and NICE-OHMS) are used as phase modulators which provide a variable phase shift on a linearly polarized input beam. The RF signal induces a change in the crystal's extraordinary index of refraction and causes a phase shift in the optical signal. When an RF signal is applied to the crystal, the optical beam is frequency modulated, and some of the light at the carrier frequency is converted into sidebands at a multiple of the modulation frequency.

In addition, an optical cavity is also used in conjunction with the fm spectroscopy. In order for the carrier and sidebands to transmit through the cavity, the side band spacing must match the free spectral range (FSR) of the cavity. This configuration suppresses laser-frequency noise in the light transmitted through the cavity, and gives an enhancement factor without increased frequency noise. The sideband frequency is usually high enough that the laser source noise level approaches the shot-noise limit, thus increasing the sensitivity. The noise immunity principle arises because the sidebands are added at the cavity FSR. Any small frequency variations of the laser will still lead to amplitude fluctuations in the transmitted carrier, but the same amplitude fluctuations occur for the sidebands on adjacent cavity modes, and therefore the net signal is unaffected. Ye originally demonstrated NICE-OHMS sensitivity at $1 \times 10^{-14} \text{ cm}^{-1} \sqrt{\text{Hz}}^{-1}$ on overtone transitions of C_2H_2 , C_2HD and CO_2 at $1.064 \text{ }\mu\text{m}$. [81] Ye originally observed only sub-Doppler dispersion.

Ye demonstrated that 2 EOMs can be used to add two sets of FM sidebands to the laser. A low frequency RF component is detected as a cavity-back reflection signal to produce the cavity-dispersion locking error signal for locking the laser to the cavity. A high frequency RF component equal to the FSR of the cavity is added by the second EOM, and is demodulated from the signal observed after transmission through the cavity

4.2 Optical Setup

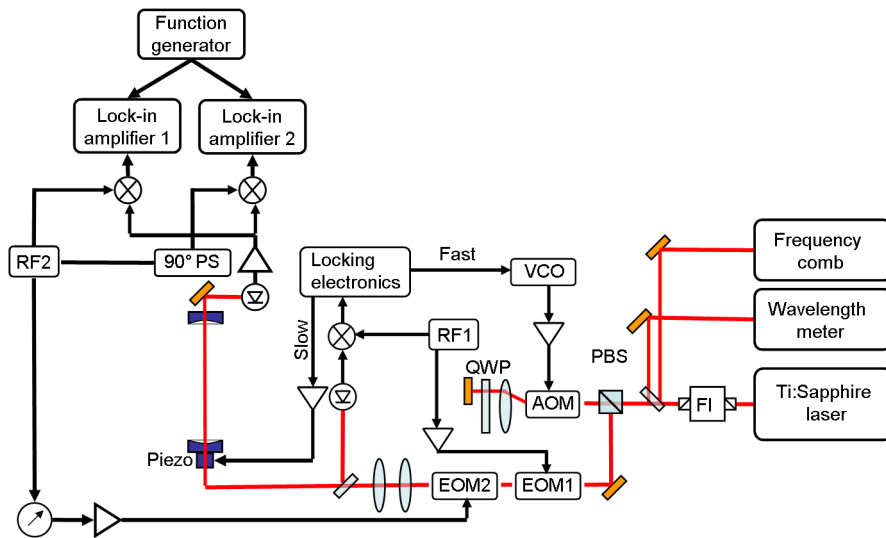


Figure 4.1: Optical and detection layout for NICE-OHMS.

An overview of the spectroscopic optical train and detection system is shown in Figure 4.1 and has been described previously. [13,46,86] The optics set of the Ti:Sapphire laser (described in Chapter 2) was switched to the long wave optics and the frequency set near 920 nm. The output of the etalon locked Ti:Sapphire laser was passed through a Faraday isolator (Optics For Research, IO-5-NIR-LP) to make sure that no back reflections from any optical surface or cavity interfere with the stability of the laser. A BK-7 window was used to pick off two reference beams, with one going to the mid-infrared wavemeter (Bristol 621A-IR), and one going to the optical frequency comb (described in Chapter 3). The wavemeter has an absolute frequency accuracy of 0.2 ppm, or 65 MHz at 920 nm (the wavelength for near-IR N_2^+ spectroscopy), 77 MHz at 780 nm (the wavelength of the Ti:Sapphire for DFG generation), and 20 MHz at 3000 nm (the wavelength of DFG laser light). The laser was then double passed through a 85 MHz resonant acousto-optic modulator (AOM) (Brimrose, TEM-85-2 (AOM) and FFA-85-B2-F2.25-X (driver)), quarter wave plate (QWP) lens and retro-reflector, so that the pointing of the laser beam would be immune to changes caused by changes in the AOM frequency. [137] An AOM is a device where the index of refraction is modulated by propagating sound waves. For this setup, the AOM induced a 170 MHz redshift to the laser light. Two sets of RF sidebands are added by two electrooptic modulators (EOM). Mode matching to the cavity was performed with two 1 m lenses. The first lens was located after the polarizing beam splitter (PBS). The first non-resonant EOM (Thorlabs EO-PM-NR-C1) was placed near the focal length of the first lens, and added sidebands at ~ 30 MHz with small modulation index. A second BK7 window was used to couple in a visible HeNe laser to aid in alignment. The laser beam then passed through the second resonant EOM (Newport 4003, Frequency spacing=113 MHz) roughly 15" before the cavity. The laser then passed through the second mode matching lens and a third BK7 window. This final BK7 window was used to reflect some of the back-reflection off of the cavity onto a detector. The output of this detector is demodulated with an RF mixer to generate an error signal. [138] An analog lockbox constructed by Mr. Brian Siller (which will be described in his dissertation) was used to lock the laser frequency to the cavity. Slow corrections were sent to the piezoelectric transducer which controls the length of the cavity. Fast corrections were sent to the voltage controlled oscillator (VCO) that drives the AOM. An RF generator (HP 8657A) was used to reference the heterodyne demodulation, and to drive the second EOM by passing the signal through a phase shifter and amplifier.

The second EOM placed sidebands on the laser at around 113 MHz, the FSR of the optical cavity. The heterodyne signal between the carrier and sidebands was detected by a fast silicon photoreceiver (New Focus 1801-FS-AC). The RF signal was attenuated (10dB) and amplified (Mini-Circuits ZFL-500LN⁺), split into two signals (Mini-Circuits ZFSC-2-4⁺), and demodulated with two separate mixers (Mini-Circuits ZFM-4⁺). The mixers were referenced to the same 113 MHz signal used to drive the second EOM. Two cables with

different lengths are used to induce a 90° relative phase shift between the reference signals of the two mixers. The overall detection phase is adjusted using an RF phase shifter (Minicircuits JSPHS-150⁺) in the line between the RF generator and the amplifier that drives the 113 MHz EOM. The phase shifter calibration data is found in Appendix C and a plot of the phase shift versus input voltage is shown in Figure 4.2. The output of the two separate mixers were put into the inputs of two separate lock-in amplifiers. The lock-in amplifiers were referenced to a function generator which drove the low frequency intracavity velocity modulation.

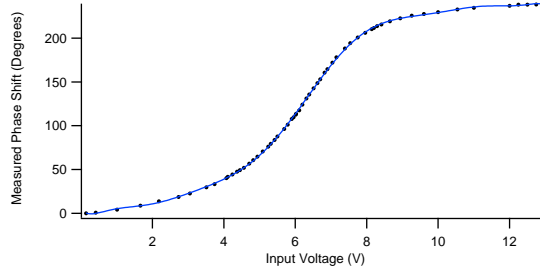


Figure 4.2: Relative phase shift of 150 MHz phase shifter with respect to input voltage.

The AOM, which allows fast corrections to the laser frequency, works by imparting a frequency shift to the laser light. One can determine the sign of the AOM frequency shift by understanding the process of how the light interacts with the AOM crystal. An 85 MHz RF signal is applied to a transducer that drives sound waves in the AOM material. The sound waves cause variations in the index of refraction of the crystal. The light will be diffracted into several beams via Brillouin scattering, with each beam being Doppler shifted by the frequency of the sound wave in the material. The diffraction angle, θ , is given by

$$\sin \theta = \frac{m \lambda_0}{2 \Lambda} \quad (4.1)$$

where Λ is the wavelength of the acoustic waves for the AOM material, λ_0 is the wavelength of the light, and m is the diffraction order of the grating which can have a positive or negative sign.

There are two types of AOMs, traveling wave and standing wave AOMs. Traveling wave AOMs induce a frequency shift to the light as it is diffracted, while standing wave AOMs do not. For our spectroscopy, a traveling wave AOM was used. Therefore, for each pass through the AOM a frequency shift (F) equal to the RF wave traveling through the AOM is imparted to the photons (with initial frequency ν_0). The resulting photon frequency (ν') is given by:

$$\nu' = \nu_0 + mF \quad (4.2)$$

Figure 4.3(a) illustrates that by observing which direction the light is deflected one can determine if the

Doppler shift is a blue or red shift. The phonons travel from the transducer through the crystal with a velocity given by the speed of sound in the crystal. If the scattered light is bent away from the transducer (*e.i.*, $\sin \theta$ is positive) it is a positive mode diffraction order corresponding to a blue shift. If it moves towards the transducer (*e.i.*, $\sin \theta$ is negative), it is a negative mode diffraction order corresponding to a red shift. The double pass setup is shown in Figure 4.3(b).

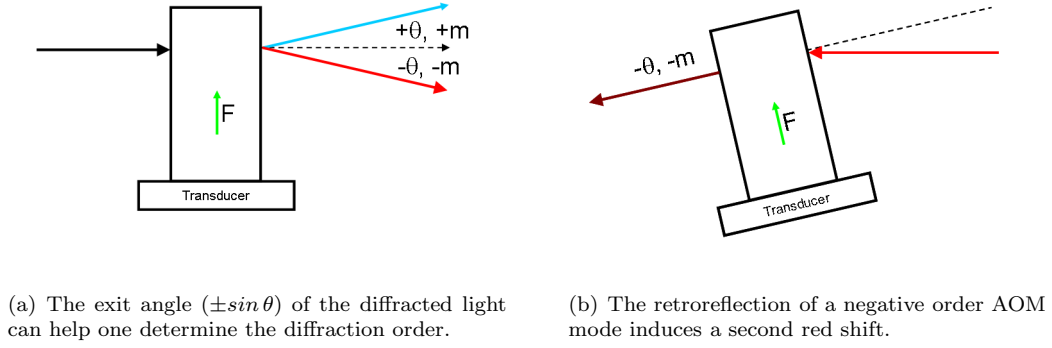


Figure 4.3: The sign of the Doppler shift of the AOM can be determined by determining the geometry of the input and output beams.

For the initial CEVMS [13] and PCEVMS [46] experiments, the AOM was set up with a positive diffraction order. For the NICE-OHMS positive column [86] and N_2^+ ion beam experiments [71], the AOM was set up with a negative diffraction order. Because the failure to properly assign the direction of the AOM shift will lead to inaccuracies of 170 MHz, it was decided that only post-signal processing would be used to account for this shift.

A cavity increases the spectroscopic path length, has a characteristic FSR range, finesse, cavity linewidth and ring-down time (should the input light be lost). The equation for calculating the finesse is given by

$$Finesse \approx \pi \sqrt{\frac{R}{1-R}} \quad (4.3)$$

where R is the effective reflectivity of the mirrors. The free spectral range ($FSR=c/2L$), where L is the length of the cavity, can be used to calculate the FWHM of the cavity resonance ($FWHM=FSR/finesse$). The cavity enhanced length for ion beam spectroscopy can be calculated by $l \times F/\pi$, where l is the sample length. Table 4.1 shows the calculated values of the sample path length, finesse, and FWHM based on the mirror reflectivity. The comparison between the DLASFIB and SCRIBES instruments shows that the finesse has increased, the sample path length has increased, and the cavity linewidth has decreased. Figure 4.4 illustrates the FWHM of the spectroscopy cavity for the SCRIBES instrument.

Reflectivity Effective %	Single Pass Path Length (m)	Cavity Enhanced Path Length (m)	Finesse	FWHM (kHz)
0.9690	0.15	5	100	1130
0.9875	0.27	22	250	451
0.9932	0.27	40	460	245

Table 4.1: Cavity parameters for the DLASFIB ($F=100$) and SCRIBES ion beam instrument $F=(250, 460)$.

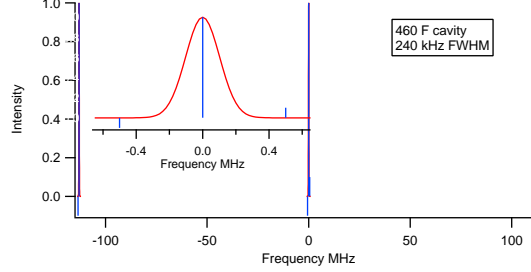


Figure 4.4: Cavity linewidth for a finesse of 450 with 113 MHz FSR and sideband spacing.

4.3 Modifications to Laser Table

Previous experiments with cavity ring-down spectroscopy with the ion beam instrument on the laser table showed that the turbo pumps induced vibrations which adversely affected the optical spectroscopy cavity. Therefore the instrument was removed from the laser table and constructed on a movable substructure. In order to have a cavity surround the ion beam instrument, breadboards were cantilevered off of the end and sides of the laser table. Figure 4.5 shows an overview of the modifications. The red boxes are the new breadboards. The blue boxes represent aluminum plates above and below the laser table. The green rectangle represents the laser table, while the black rectangles represent the 80-20 supports. Two $24 \times 12 \times 2.4$ " breadboards (Newport RG-12-2) were set on Sorbothane isolation vibration (McMaster-Carr 8514K61 70 Hardness $1/8$ ") on top of the aluminum plates and were compressed against the plates with several bar clamps (McMaster-Carr 6545A4).

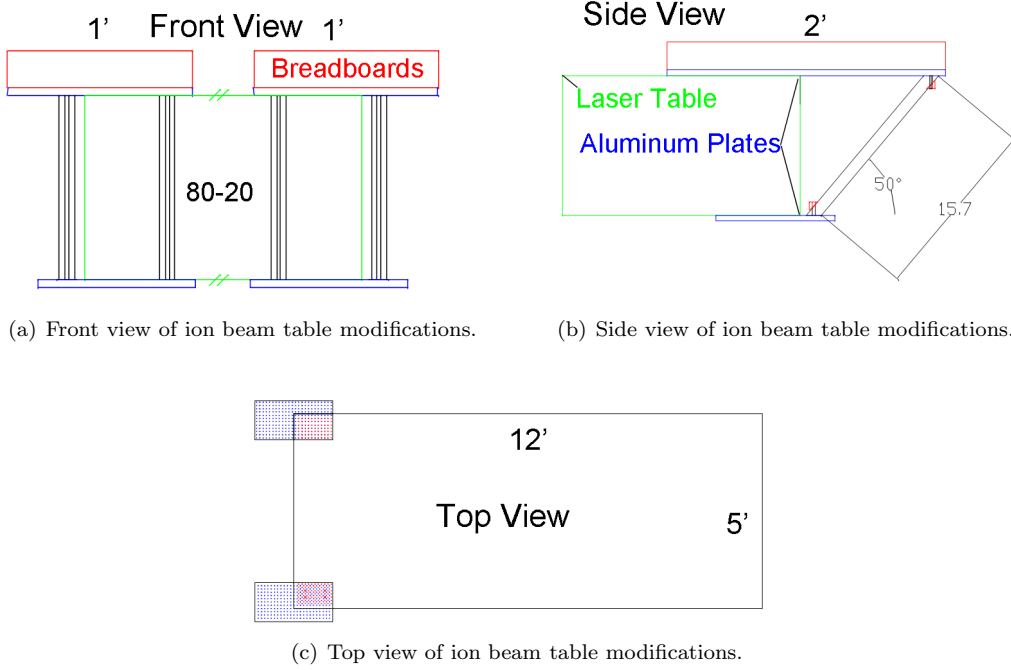


Figure 4.5: Designs for modifications to ion beam laser table.

4.4 Cavity Setup

For the rovibronic spectroscopy of N_2^+ , 1" diameter mirrors with 1 m radius of curvature and 99.6% reflectivity at 925 nm were purchased (Rainbow Research Optics).

$$w_0^2 = \frac{\lambda}{2\pi} \sqrt{d(2R - d)} \quad (4.4)$$

Equation 4.4 [139] gives the $1/e^2$ radius of a laser beam to be resonant with a cavity dependent on the wavelength of light (λ), the separation between the mirrors (d), and the radius of curvature of the mirrors (R). For the 1.32 m cavity at 920 nm, with mirror radius of 1 m, the radius of the cavity is 0.37 mm, and the expected beam diameter was 0.74 mm. Two 1 m lenses were used to approximately mode match the beam diameter to around 0.8 mm.

4.5 Cavity Mounts

Highly stable cavity mounts are essential for achieving good laser/cavity lock. Several iterations of ring-down mounts have been made in the past. In the mounts used for the N_2^+ spectroscopy, brass was used instead of stainless steel because it is much faster to machine, and it is much heavier, and thus, more stable.

An overview schematic of the cavity mounts are shown in Figure 4.6, and detailed schematic drawings are found in Section C.3. In Figure 4.6, the base plate (colored black), the back plate (green), and front plate (blue), the piezoelectric transducer or piezo dummy (red), and the mirror holders (blue) are indicated. Red lines indicate where precision (1/4-80) screws are used to push the mounts apart and align the mirrors. These mounts were set on a layer of vibration dampening Sorbothane, and the clamps which pushed the mount down were also separated from the mount with Sorbothane thus minimizing vibrations. It was determined that the mounts needed to stabilize for several days before laser locking could occur.

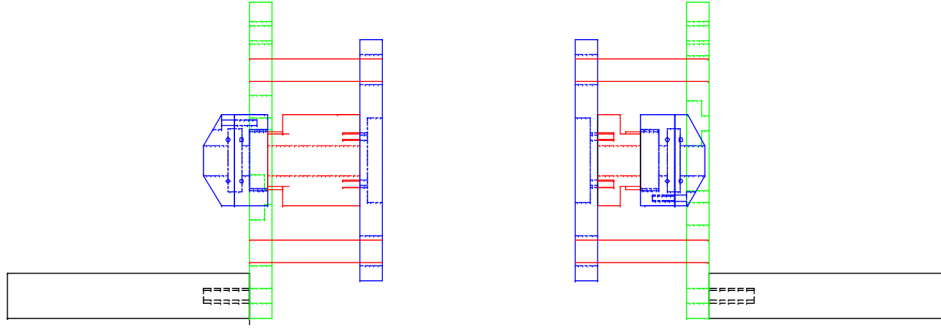


Figure 4.6: Overview of stable cavity mounts made of brass.

Another iteration of brass cavity mounts, compatible with vacuum sealing to the system is described in Section C.4 but was not implemented at the time of publication.

4.6 Line shape and Sensitivity Equations

In frequency modulation (FM) spectroscopy, the photo-detector signal is proportional to [140]

$$I_{fm}(\nu) = \frac{c \beta E_0^2}{8\pi} [(\delta_{-1} - \delta_1) \cos \theta_{fm} + (\phi_1 + \phi_{-1} - 2\phi_0) \sin \theta_{fm}] \quad (4.5)$$

where E_0 is the electric field peak amplitude of radiation impinging on the detector, β is the heterodyne modulation index, $\delta_{\pm 1}$ denotes the amplitude attenuation due to the plus and minus sidebands of the laser, and ϕ denotes the optical phase shift experienced by the plus and minus sideband, as well as the carrier component. A beat signal is only observed when $\delta_{-1} - \delta_1 \neq 0$ or when $\phi_{-1} + \phi_1 - 2\phi_0 \neq 0$. [140, 141] Because the cosine terms describe the amplitude attenuation differences experienced by the sidebands, they represents the absorption of the signal. The sine term denotes the difference in phase shift experienced by the carrier and average phase shifts experienced by the sidebands, and represents the dispersion signal. [140, 141]

The signal (in V) and line shape for frequency modulation as a function of frequency de-tuning (ν_d) and

RF detection phase (θ_{fm}) is given by [142]

$$\begin{aligned}
S^{fm}(\nu_d, \theta_{fm}) = & \eta_{fm} J_0(\beta) J_1(\beta) P_0 l c \alpha_0 \\
& \times [[\chi_{-1}^{abs}(\nu_d - \nu_{fm}) - \chi_1^{abs}(\nu_d - \nu_{fm})] \cos \theta_{fm} \\
& + [\chi_{-1}^{disp}(\nu_d - \nu_{fm}) - 2\chi_0^{disp}(\nu_d - \nu_{fm}) + \chi_{-1}^{disp}(\nu_d - \nu_{fm})] \sin \theta_{fm}]
\end{aligned} \tag{4.6}$$

where ν_d is the de-tuning of the laser from the line center ν_0 , ($\nu_d = \nu_{Carrier} - \nu_0$), η_{fm} is an instrumentation factor including the responsivity and gain of the detector, and other RF components, $J_0(\beta)J_1(\beta)$ is a factor proportional to the loss of heterodyne detection with sideband strength, P_0 is the power incident on the detector, l is the interaction length of the laser with the sample, c is the concentration of the sample, α_0 is the absorption coefficient on resonance ($\alpha_0 = S c p$, where $c p$ is the partial pressure of the analyte of interest, and S is the line strength), χ_{\pm}^{abs} is the general line shape for absorption for the + and - sideband, $\chi_{\pm,0}^{disp}$ is the general line shape for dispersion for the +,- sidebands and the carrier, and ν_{fm} is the RF frequency applied to the EOM (sideband spacing).

When frequency modulation is used with a cavity, as in NICE-OHMS, the expected NICE-OHMS signal is enhanced by a factor $\frac{2F}{\pi}$. [142] The maximum AC value of the detector (AC_{Max}) is equal to $P_0 \eta_{fm}$, and the voltage signal can be converted to a fractional signal by dividing by AC_{Max} . In the ion beam experiment, due to the fact that the Doppler splitting caused by the fast ion beam is much larger than the heterodyne frequency and signal linewidth, only one direction of the Doppler shift will be probed by the laser beam at a given frequency. This has two consequences. First, the enhancement factor becomes only $\frac{F}{\pi}$. Second, if optical saturation is present, the laser will still depopulate the lower level, but this loss of population will not be observable as a lamb dip in either dispersion or absorption, as it was with previous AC modulated cavity enhanced, and NICE-OHMS studies. [13, 46, 86] This is because Lamb dip observations require zero-velocity components, [143] and when the Doppler shift is on the order of 2-3 cm^{-1} , no zero-velocity components are observable. For an ion beam signal, it will be easier to replace ($\alpha_0 c$) with ($S\rho$), where S is the line strength (cm/ion) and ρ is the ion density (ions cm^{-3}). Therefore, the expected fractional signal is given by

$$\begin{aligned}
\left(\frac{I}{I_0}\right)^{fm}(\Delta\nu, \theta_{fm}) = & \frac{F}{\pi} J_0(\beta) J_1(\beta) L \rho S \\
& \times [[\chi^{abs}(\Delta\nu - \nu_{fm}) - \chi^{abs}(\Delta\nu - \nu_{fm})] \cos \theta_{fm} \\
& + [\chi^{disp}(\Delta\nu - \nu_{fm}) - 2\chi^{disp}(\Delta\nu - \nu_{fm}) + \chi^{disp}(\Delta\nu - \nu_{fm})] \sin \theta_{fm}]
\end{aligned} \tag{4.7}$$

where the first line contains the components of the signal strength, and the last two lines contain the Doppler

broadened FM general line shape ($\chi_{Doppler}^{fm,no}$) for absorption and dispersion.

Without the signal strength portion of this equation, the line shape becomes

$$\begin{aligned}\chi_{Doppler}^{fm,no} = & [\chi^{abs}(\nu_d - \nu_{fm}) - \chi^{abs}(\nu_d + \nu_{fm})] \sin \theta_{fm} \\ & + [\chi^{disp}(\nu_d - \nu_{fm}) - 2\chi^{disp}(\nu_d) + \chi^{disp}(\nu_d + \nu_{fm})] \cos \theta_{fm}\end{aligned}\quad (4.8)$$

where χ^{abs} and χ^{disp} represent the general line shapes for Doppler broadened absorption and dispersion.

The Doppler broadened absorption line shape for a peak-normalized Gaussian is [142]

$$\chi_G^{abs}(\nu) = e^{-4 \ln 2 (\Delta\nu / \text{FWHM})^2} \quad (4.9)$$

where FWHM is the full width at half maximum for the Gaussian profile.

The Doppler broadened dispersion line shape, derived from a peak-normalized Gaussian line shape, is given by [11, 142, 144]

$$\chi^{disp}(\nu) = -\frac{2}{\sqrt{\pi}} e^{-\gamma^2} \int_0^\gamma e^{\gamma'^2} d\gamma' \quad (4.10)$$

where $\gamma = 2\nu_d \sqrt{\ln 2} / \text{FWHM}$. This functional form is called a Dawson function, and is the same shape as a Gaussian times the imaginary error function.

Under optically saturated conditions, the absorption and dispersion lineshapes behave differently. Studies of sub-Doppler and Doppler broadened saturation features show that the absorption amplitude is reduced by a factor $1/\sqrt{1+G_j}$, where G_j is a measure of the saturation for each sideband, j , and the rest of the line shape, and the FWHM remain constant. [11] For the case of $\beta \sim 0.36$ with a sideband saturation parameter ($G_{\pm 1}^+$) of 3, the absorption loss was only up to a factor of two. [11] It is expected at higher modulation depth $\beta \sim 0.83$ (as in the case for the ion beam experiment) that there will be more of an absorption loss. Further, when the dispersion line shape follows a Doppler broadened profile, there is no change in the amplitude of the dispersion line shape; [11] it remains unaffected by saturation. When the dispersion line shape has increasing Lorentzian character, for instance when the spectroscopy is sensitive to pressure and transit time broadening, the dispersion line shape is affected by the saturation.

Because NICE-OHMS uses frequency modulation, both the absorption and dispersion signals can be detected as described earlier in Equation 4.8. [11] However, because the signals must be demodulated with an RF mixer, either a linear combination of the two signals is obtained, or the phase shift can be set so that either the dispersion or the absorption signal is extracted. Using an RF phase shifter is helpful to isolate the signals into either one mixer or the other, instead of taking a linear combination of both absorption and

dispersion. By splitting the signal with a power splitter and using two separate mixers, referenced 90° to each other, both the dispersion and the absorption signals can be observed. In that case, the dispersion and absorption signals can be given by Equations 4.11 and 4.12 respectively.

$$\chi^{disp} = \chi^{disp}(\nu_d - \nu_{fm}) - 2\chi^{disp}(\nu_d) + \chi^{disp}(\nu_d + \nu_{fm}) \quad (4.11)$$

$$\chi^{abs} = [\chi^{abs}(\nu_d - \nu_{fm}) - \chi^{abs}(\nu_d + \nu_{fm})] \quad (4.12)$$

In addition, the ions are velocity modulated, and therefore the spectroscopic signal undergoes a velocity modulation, which induces a velocity modulation splitting, whose value is smaller than the observed line width. The general line shape functions for dispersion and absorption then follow Equations 4.13 and 4.14, respectively.

$$\begin{aligned} \chi_{vm}^{disp} = & \chi^{disp}(\nu_d - \nu_{fm} - \nu_{vm}) - 2\chi^{disp}(\nu_d - \nu_{vm}) + \chi^{disp}(\nu_d + \nu_{fm} - \nu_{vm}) \\ & - \chi^{disp}(\nu_d - \nu_{fm} + \nu_{vm}) + 2\chi^{disp}(\nu_d + \nu_{vm}) - \chi^{disp}(\nu_d + \nu_{fm} + \nu_{vm}) \end{aligned} \quad (4.13)$$

$$\begin{aligned} \chi_{vm}^{abs} = & \chi^{abs}(\nu_d - \nu_{fm} - \nu_{vm}) - \chi^{abs}(\nu_d - \nu_{fm} + \nu_{vm}) \\ & - \chi^{abs}(\nu_d - \nu_{fm} - \nu_{vm}) + \chi^{abs}(\nu_d - \nu_{fm} + \nu_{vm}) \end{aligned} \quad (4.14)$$

4.7 Detector

A 125 MHz photoreceiver (New Focus 1801-FS-AC) was used to record the heterodyne signal. The photoreceiver is supposed to have a 40,000 V/A AC gain and a 1000 V/A DC gain, however it was determined that those gains were not correct. The detector was calibrated by recording the power with a New Focus power meter, and the voltage from the DC channel was recorded on an oscilloscope. For recording the AC voltage, the AOM was used to modulate the signal, and the voltage from the AC channel was recorded on the oscilloscope. The initial results of the DC and AC voltage as a function of input power are shown in Figure 4.7(a). From this graph, it is apparent that the DC response is linear over this power range, and the AC gain is linear up until $350 \mu\text{W}$. From the input power and the responsivity of the photodiode (0.51 A/W), the photocurrent can be calculated. Figure 4.7(b) shows a graph of the DC voltage as a function of the photocurrent, the slope of which gives the DC gain as 8077 V/A . Figure 4.7(c) shows a graph of the

AC voltage as a function of the photocurrent. At low input power, the AC gain was measured to be 20668 V/A. The AC gain begins to saturate after 350 μW (or 179 μA). However, it was determined that a stronger spectroscopic signal was found with higher DC levels. Therefore, the gain may not necessarily be a static value. However, the calibration data was collected by fully modulating the laser light on and off with the AOM. As much smaller AC levels are induced by the velocity modulation, it is possible that the gain of the circuit is still constant. We therefore assume that the detector is still in the linear region and note the caveat that it may not be.

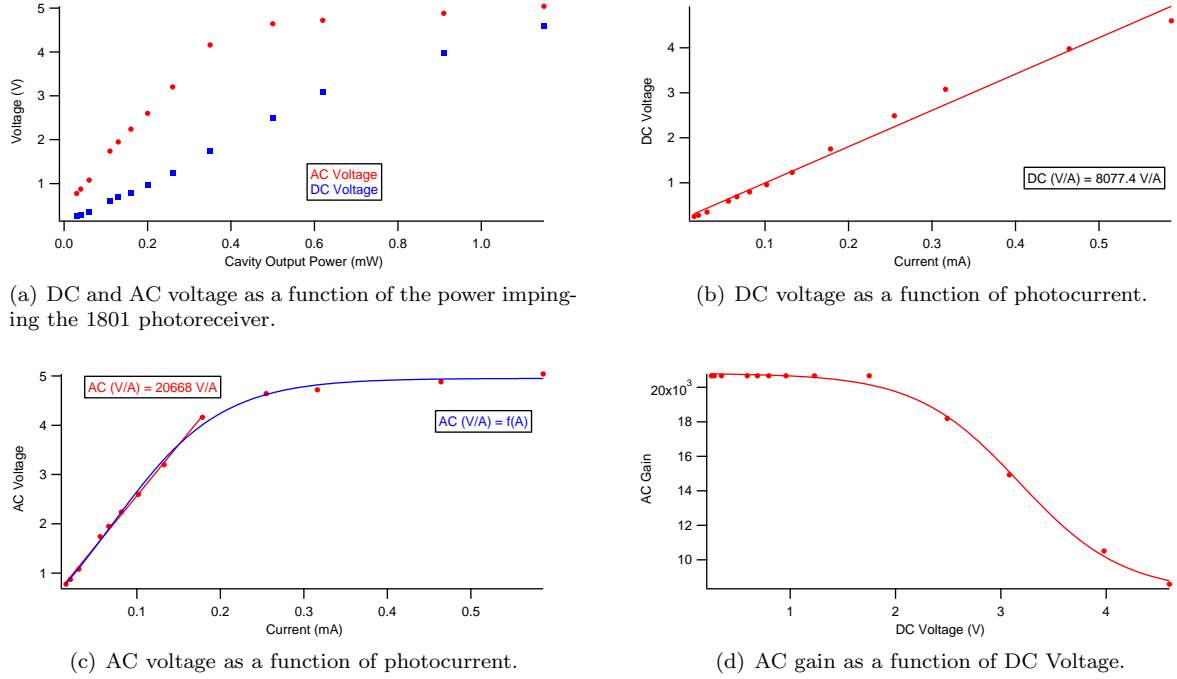


Figure 4.7: Graphs indicating detector calibration

A sigmoidal fit provides a functional form for non-linearity of the detector for future use. The functional form for a sigmoidal fit is given by

$$y = base + \frac{max}{1 + \exp(\frac{x_{half}-x}{rate})} \quad (4.15)$$

The parameters for this fit are found to be: $base=-1.89$, $max=6.838$, $x_{half}=0.527$, and $rate=0.641$ to convert the observed DC signal voltage to an AC voltage value. Alternately, the AC gain can be assumed to be the linear value shown in Figure 4.7(c) for the first nine points, and calculated for the remaining four points as shown in Figure 4.7(d). A sigmoidal fit to this curve allows the AC gain to be calculated as a function of the AC gain as a function of the DC voltage, which is helpful for data analysis. For this

fit, $base=20803$, $max=-12669$, $xhalf=3.1776$, and $rate=0.4909$. The values for the detector calibration are found in Table 4.2.

Power mW	Current mA	V DC 1 M Ω	V AC	DC Gain V/A	AC Gain V/A	AC Gain AC V/A
0.03	0.0153	0.251	0.776	8077	50719	20668
0.04	0.0204	0.278	0.872	8077	42745	20668
0.06	0.0306	0.346	1.08	8077	35294	20668
0.11	0.0561	0.591	1.74	8077	31016	20668
0.13	0.0663	0.688	1.95	8077	29412	20668
0.16	0.0816	0.795	2.24	8077	27451	20668
0.20	0.102	0.96	2.6	8077	25490	20668
0.26	0.1326	1.23	3.2	8077	24133	20668
0.35	0.1785	1.75	4.16	8077	23305	20668
0.50	0.255	2.49	4.64	8077	18196	18196
0.62	0.3162	3.08	4.72	8077	14927	14927
0.91	0.4641	3.98	4.88	8077	10515	10515
1.15	0.5865	4.6	5.04	8077	8593	8593

Table 4.2: Heterodyne detector calibration data.

4.8 Expected Line Shape

Graphical examples of the expected line shape are illustrated in this section. If an expected transition is known for a particular rest frequency, observation in a fast ion beam will induce a blue and red shift as illustrated in Figure 4.8(a). The magnitude of the shift away from the rest transition is approximately proportional to the velocity. Therefore, faster ions are shifted further away from the rest frequency to the red and blue sides. When an additional velocity modulation is applied to the ions in the ion beam, each component undergoes an additional splitting, illustrated in Figure 4.8(b). Because the highest frequency shift corresponds to the fastest beam, this will correspond to the negative portion of the function generation of the velocity modulation. Being in phase with the negative portion of the cycle is the same as being 180° out of phase with the x channel, and so the outer Doppler split component of both ν^+ and ν^- will have a negative phase with respect to the x channel of the lock-in amplifiers (indicated by the negative value).

Figure 4.9 illustrates the effect of the heterodyne on the absorption (left) and dispersion (right) for the blue component from the ion beam Doppler shift. The dotted blue line illustrates the line center of this Doppler shift. The red and blue dash-dot lines illustrate the line center of the velocity modulated components. The solid black vertical lines represent the laser sideband positions when the carrier is parked at the dash-dot positions. On the left side of the graph, only the sideband positions are shown relative to the velocity modulation splitting. On the right side, both sidebands and the carrier are illustrated by the

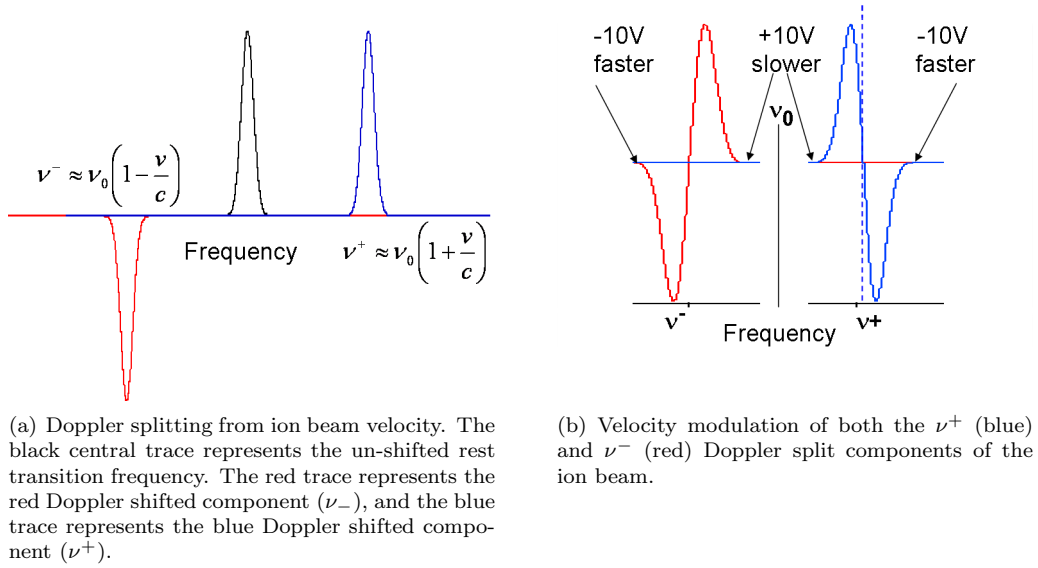


Figure 4.8: Doppler splitting due to the fast ion beam (a) and velocity modulation (b).

vertical black lines. For the absorption side, compare with Equation 4.14 of four Gaussian line shapes. For the dispersion side, compare with Equation 4.13 of six Dawson line shapes. Each of those components are convoluted together, and the resulting expected lineshapes are illustrated in Figure 4.10.

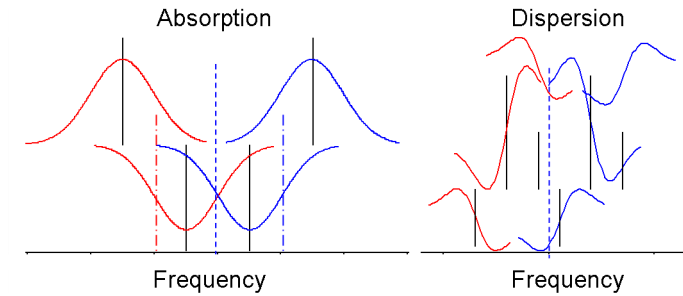


Figure 4.9: Effect of heterodyne on the absorption and dispersion signals for the blue shifted Doppler component (ν^+).

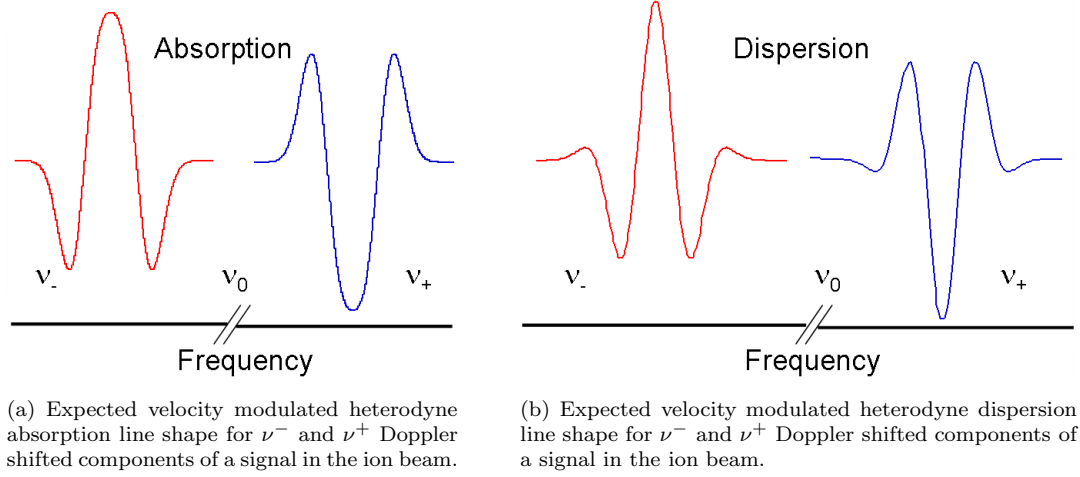


Figure 4.10: Expected velocity modulated heterodyne NICE-OHMS line shape for a) absorption and b) dispersion.

4.9 Saturation Effects

From theoretical studies on the Doppler broadened NICE-OHMS lineshapes, it is known that saturation can affect the absorption and dispersion by different amounts depending on the line shape and relaxation processes. [11] In order to quantify the effects of this saturation, it is necessary to know the modulation index of the heterodyne sidebands. An electrooptic modulator removes intensity from the carrier and imparts a phase shift, which is equivalent to a frequency shift to different sidebands. By monitoring the laser frequency mode structure after modulation, one can measure the heterodyne depth of modulation (β). An oscilloscope trace of a spectrum analyzer used to monitor the laser frequency mode structure is shown in Figure 4.11. The height of the peaks can be used to determine the ratio of intensity in the carrier and the sidebands, as illustrated in Figure 4.11(b).

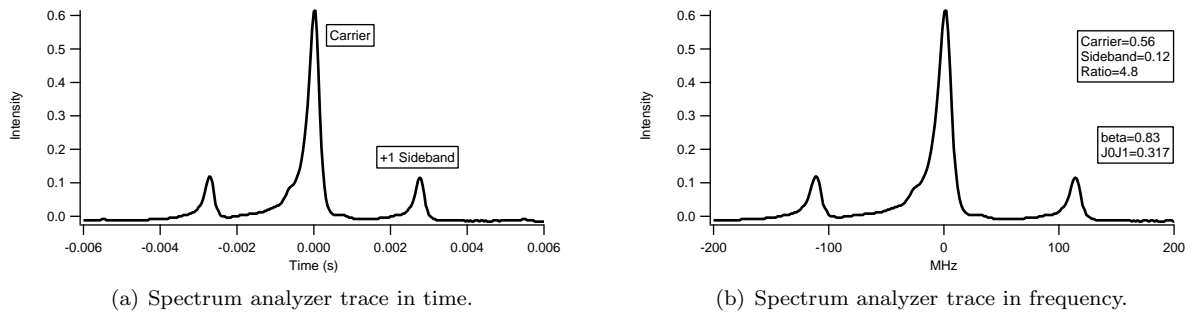


Figure 4.11: Observed spectrum analyzer trace of the frequency modulated Ti:Sapphire laser in a) time and b) frequency.

The amplitude of the frequency modulation follows the Bessel functions of the first kind, of order 0

($J_0(\beta)$) for the carrier and of order 1 ($J_1(\beta)$) for the sidebands. (Higher order sidebands ($J_2...(\beta)$) could be considered, but are omitted for this discussion because even the second order sidebands are fairly weak ($\sim 1\%$) at our modulation index ($\beta \sim 0.83$)). Figure 4.12 gives an example of the amplitude of the Bessel functions of the zeroth and first orders for a modulation index between zero and two.

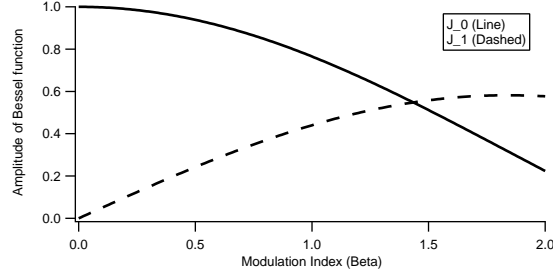
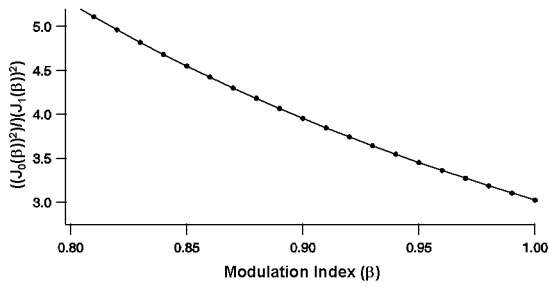
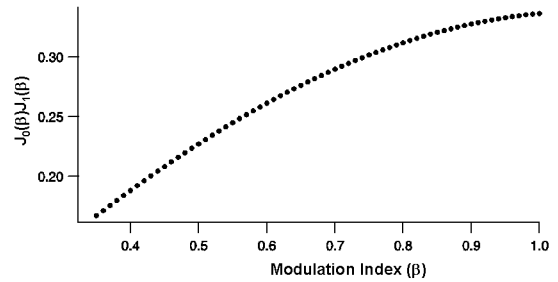


Figure 4.12: Bessel functions of the zeroth and first kind for modulation index between zero and two.

It should be remembered that the Bessel functions represent the amplitudes of the electromagnetic wave, whereas the spectrum analyzer detector measures the intensity ($\propto |E_0|^2$). Therefore, when converting from the ratio of the observed peak height of the carrier to the sidebands, one should use the ratio of the squares of the Bessel functions. Figure 4.13(a) contains calculations of the values of the Bessel functions squared ($(J_0/J_1)^2$). By finding the appropriate ratio (4.8) observed in Figure 4.11 in the y axis of Figure 4.13(a), the modulation index (β) can be found on the x axis. For the intensity calculations, the heterodyne value is determined from the product of the amplitudes of the carrier (J_0) and sideband (J_1), shown in Figure 4.13(b) ($J_0(\beta)J_1(\beta)=0.317$ for $\beta=0.83$). Furthermore, as the intensity is split into two sidebands and one carrier, the percentage of the intensity can be determined from the ratio as $I_{\pm 1}=100/(\text{ratio}+2)$ and $I_0 = 100 - 2 \times I_{\pm 1}$. In this case, $I_{\pm 1} = 14.7\%$ and $I_0 = 70.5\%$.



(a) Squared ratio of J_0 to J_1 used to determine the modulation index.



(b) Product of J_0 and J_1 used to determine the modulation loss in the sensitivity equations.

Figure 4.13: Graphs of Bessel function values used for determining modulation depth (β) and sensitivity parameters.

The general saturation dependent absorption and dispersion line shape functions for a sideband (j) and

saturation parameter (G_j) were derived by Ma et al. [11]

$$\chi_j^{abs}(\Delta\omega, G_j) = \chi^0 \frac{1}{1 + G_j} \text{Re}[w(x_j + iy_j)] \quad (4.16)$$

$$\chi_j^{disp}(\Delta\omega, G_j) = -\chi^0 \text{Im}[w(x_j + iy_j)] \quad (4.17)$$

$$y_j = y\sqrt{1 + G_j} \quad (4.18)$$

$$y = \sqrt{\ln 2} \gamma_R / \delta\omega_D \quad (4.19)$$

$$x_j = (\Delta\omega + j\omega_m) \sqrt{\ln 2} / \delta\omega_D \quad (4.20)$$

where G_j is the saturation parameter for each sideband ($j=\pm 1, 0$), $\delta\omega_D$ is the radial Doppler half-width, ω_m is the sideband spacing or fm frequency, and γ_{tt} is the relaxation half width in radial units (caused by transit time broadening). $w(x_j + iy_j)$ can be represented with $z = x_j + iy_j$ and

$$w(z) = \exp[-z^2](1 + i\text{erfi}(z)) \quad (4.21)$$

where $G_j = G^+ J_j^2(\beta)$ and G^+ is the degree of saturation given by

$$G^+ = \frac{2\mu^2 I^+}{3c\epsilon_0 \hbar^2 \gamma_{tt}^2} \quad (4.22)$$

Ma [11] simulated the effect of saturation on absorption and dispersion for $G^+ \leq 100$ and $y \leq 0.1$ and found that when $y=0$, only the absorption intensity was affected by saturation and the dispersion was completely unaffected by saturation (see Figure 4.16(e)). At higher values of y (when the relaxation rate became a non-zero percentage of the overall linewidth) the dispersion began to be affected by the saturation. The y value is influenced by the transit time broadening (γ_{tt}) and then power broadening is taken into account. Ma [11] assumed molecules passing tangentially through a Gaussian laser beam to calculate the transit time as the fastest process under observation, and gave the relaxation half-width as a function of the transit time through laser beam ($\tau=2 w/u$). The transit time broadening became:

$$\gamma_{tt, Gaussian, hw} = \frac{\pi}{2\tau_{tt}} \text{Mrad/s} \quad (4.23)$$

where w is the 1/e radius of the laser beam and u is the most probable thermal velocity of the molecules. In this case, the molecule starts to interact with the laser beam as it approaches the far-reaching Gaussian

wings of the laser beam. However, this case is not valid for a collinear ion beam/laser beam geometry.

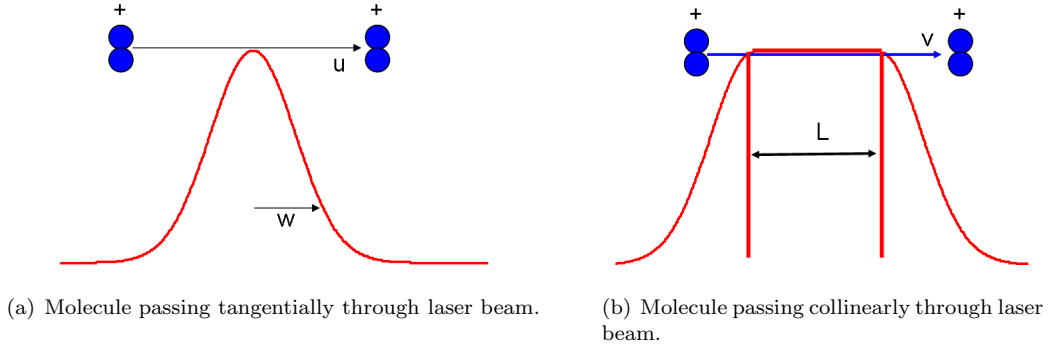


Figure 4.14: Transit time for a molecule passing a laser beam.

Instead the transit time is approximated by recognizing that the molecule starts oscillating fairly quickly as it approaches the laser beam, and stays in a constant intensity region (see Figure 4.14(b)), approximated with a rectangle, whose spectral intensity profile is given by [145]

$$I(\omega) = \frac{\sin^2[(\omega - \omega_0)\tau/2]}{(\omega - \omega_0)^2} \quad (4.24)$$

where τ is the time of the ion spent interacting with the laser and is shown in Figure 4.15.

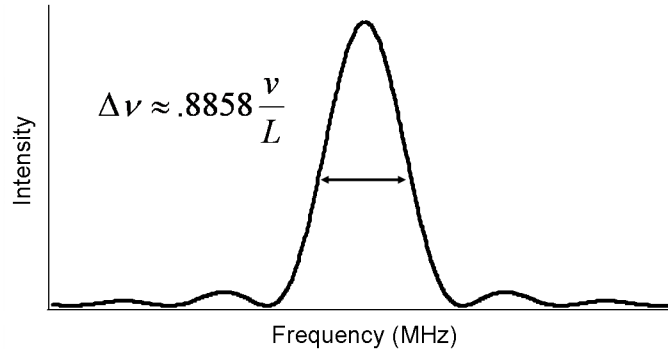


Figure 4.15: Spectral intensity profile for an ion passing collinearly through a laser beam.

Using L'Hopital's rule, the half max value is determined to be $\tau^2/4$, and numerical calculations determined the FWHM to be $\sim 0.8858/\tau$ (Hz). For the ion beam system discussed in Chapter 5, the transit time for a 4 kV beam is $1.639 \mu\text{s}$, which would correspond to a transit time broadening of 0.54 MHz (FWHM) ($\gamma_{tt,radial,hw}=1.7$ Mrad/s). Using Equation 4.19 with an observed 120 MHz linewidth (FWHM) ($\delta\omega_{D,hw}=377$ Mrad/s) gives an expected y value of 0.0038 assuming that the transit time is the fastest homogeneous broadening process.

The intensity of light in the cavity (I^+) is determined by

$$I^+ = \frac{I \times F}{\pi} \quad (4.25)$$

where F is the Finesse of the cavity and I is the intensity of light coupled into the cavity (W/m^2). For 100 mW impinging on the cavity, and a 10% coupling efficiency, approximately 10 mW enter the cavity. The beam radius supported by the cavity is 0.37 mm, corresponding to an area of $4.3 \times 10^{-7} \text{ m}^2$, and an intensity of $3.4 \text{ W}/\text{mm}^2$. Because 70% of that intensity goes into the carrier and 14.7 % goes into each sideband, the intracavity intensity of the carrier (I_{Carrier}^+) and sidebands ($I_{\text{Sidebands}}^+$) are 2.4 and 0.5 W/mm^2 . Using a 0.27 MHz transit time broadening (half width), and Equation 4.22, the carrier and sideband saturation was calculated to be 30229 (G_0^+) and 6311 ($G_{\pm 1}^+$) respectively.

A Mathematica sheet was used to run the simulations and compare them to the results of Ma. The results of the simulation are shown in Figure 4.16(a-d) and the corresponding results from Ma are shown in Figure 4.16(e); the simulations agree with one another.

Once the results of the simulation matched with the published results, the parameters of the simulation were changed to more closely resemble the experimental parameters described above. Sensitivity calculations for the observed signal (see Section 6.6) show a signal $14\times$ smaller than expected. Using the simulations with the expected saturation parameter (30229 and 6311 for the carrier and sidebands respectively) and the expected y parameter due to power broadening (0.0038), the simulated dispersion signal only shows 44% of the unsaturated signal. Simulations of the absorption signal show only 2% of the absorption signal remaining. As the S/N in most of the scans was on the order of 40, and the saturated absorption signal is a factor of 55 lower, it is not very surprising that no absorption is observed.

Overall, the fact that transit time broadening and power broadening play any role in the spectroscopy may be surprising. For instance, for a plasma discharge, one is usually limited to a Doppler broadened signal. The Doppler linewidth can be calculated from [146]

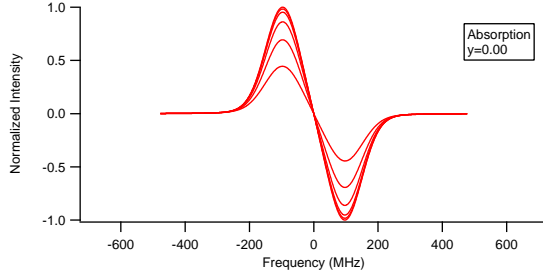
$$\Delta\nu_{D,FWHM} = \nu_0 \sqrt{\frac{8kT \ln 2}{M c^2}} \quad (4.26)$$

where k is Boltzmann's constant, T is the temperature, M is the mass of the species, ν_0 is the frequency of the transition, and c is the speed of light. For a 600 K plasma of N_2^+ at 10859 cm^{-1} , the expected Doppler-broadened line width is $\sim 1 \text{ GHz}$ (FWHM). Due to the nature of the fast ion beam (discussed in Section 5.12), this linewidth is reduced to a sub-Doppler value via kinematic compression.

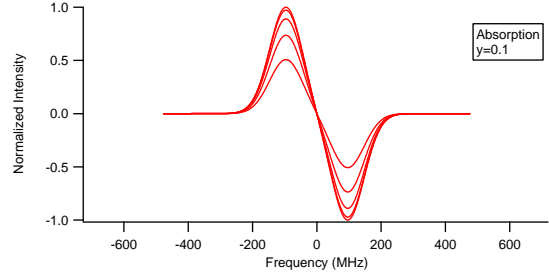
These results show important implications for the mid-IR. Assuming a 10% coupling efficiency of 500 μW

of mid IR light into a cavity whose cavity mode radius is now 0.68 mm, the intracavity carrier and sideband intensity will become 3583 and 748 W/m². Assuming a similar transit time for HN₂⁺, and a transition dipole of 0.22 Debye, [79] the saturation parameters for the carrier and sidebands become $G_0^+=15$ and $G_1^+=3$ ($G^+=21$).

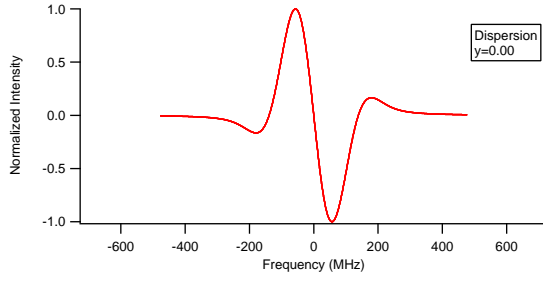
The resulting estimated y value of 0.011, coupled with the smaller saturation parameters, means there will be far less saturation losses for dispersion than absorption. Using an estimate of the y value, and the saturation parameters, more simulations were performed for the absorption and dispersion in the mid IR. These simulations are shown in Figure 4.18. For the given estimates of the parameters, the dispersion is expected to be reduced down to 96% of the unsaturated value, and the absorption is expected to be reduced down to 49% of the unsaturated value.



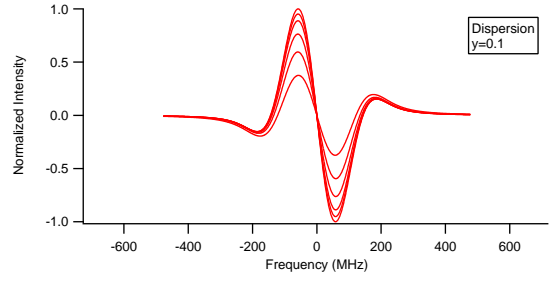
(a) Simulation for absorption with $y=0.0$.



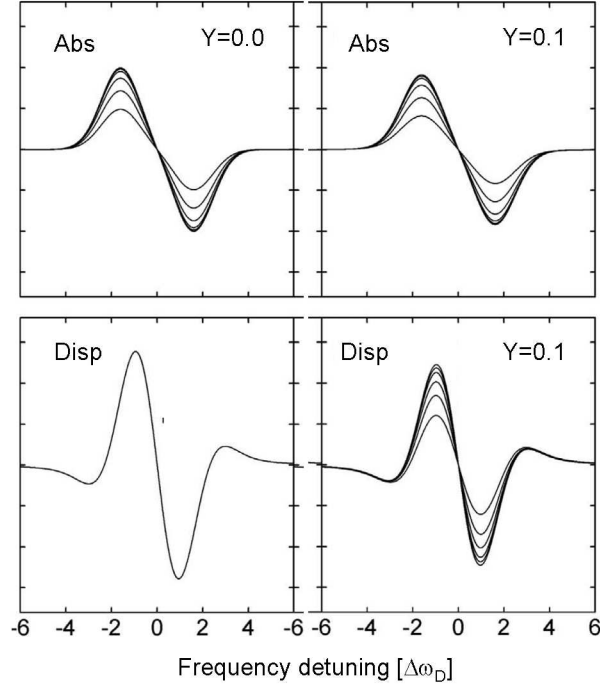
(b) Simulation for absorption with $y=0.1$.



(c) Simulation for dispersion with $y=0.0$.



(d) Simulation for dispersion with $y=0.1$.



(e) Simulation by Ma

Figure 4.16: Panels a-d, simulations of absorption and dispersion for $G^+=0, 1, 3, 10, 30, 100$ with $\Delta\nu_{Doppler,FWHM}=120$ MHz, $\omega_m=1.6\Delta_D$, $\beta=0.36$, $J_0^2=0.97$, $J_1^2=0.03$. Panel e, published simulations for comparison. [11]

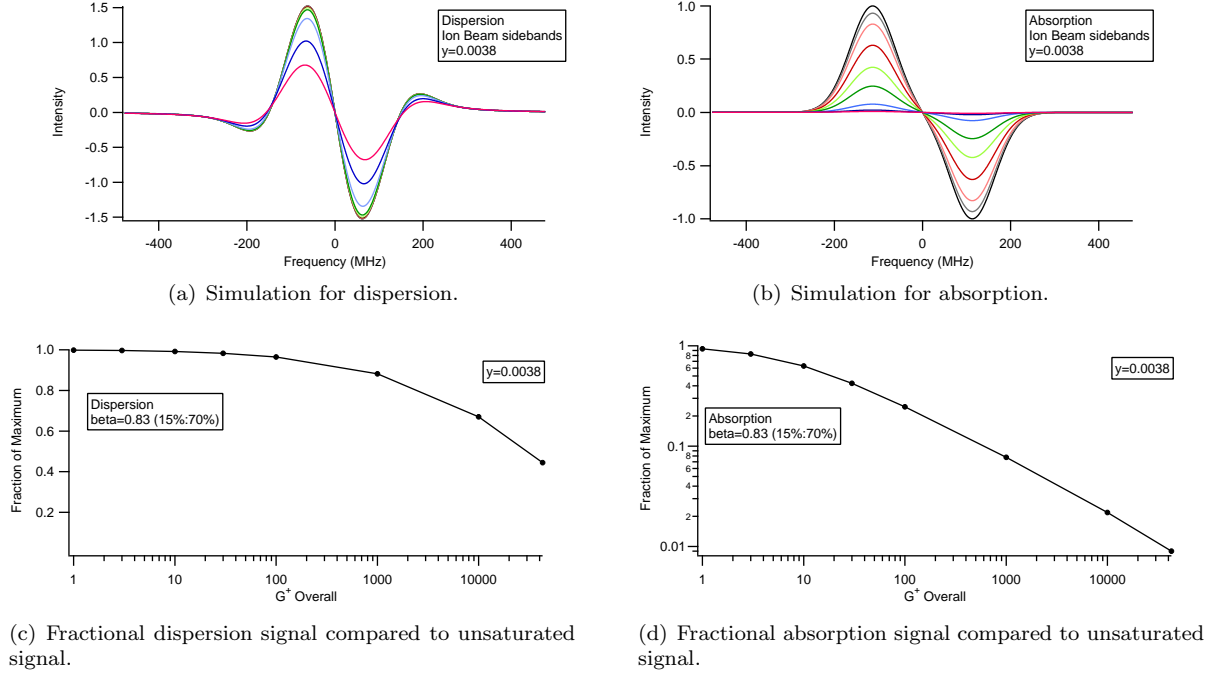


Figure 4.17: Simulations of absorption and dispersion with $y=0.0028$. Panels a-b, $G^+=0, 1, 3, 10, 30, 100, 1000, 10000, 42851$ with $\Delta\nu_{Doppler,FWHM} = 120$ MHz, $\nu_m=113$ MHz, $\beta=0.83$, $J_0^2=0.70$, $J_1^2=0.15$.

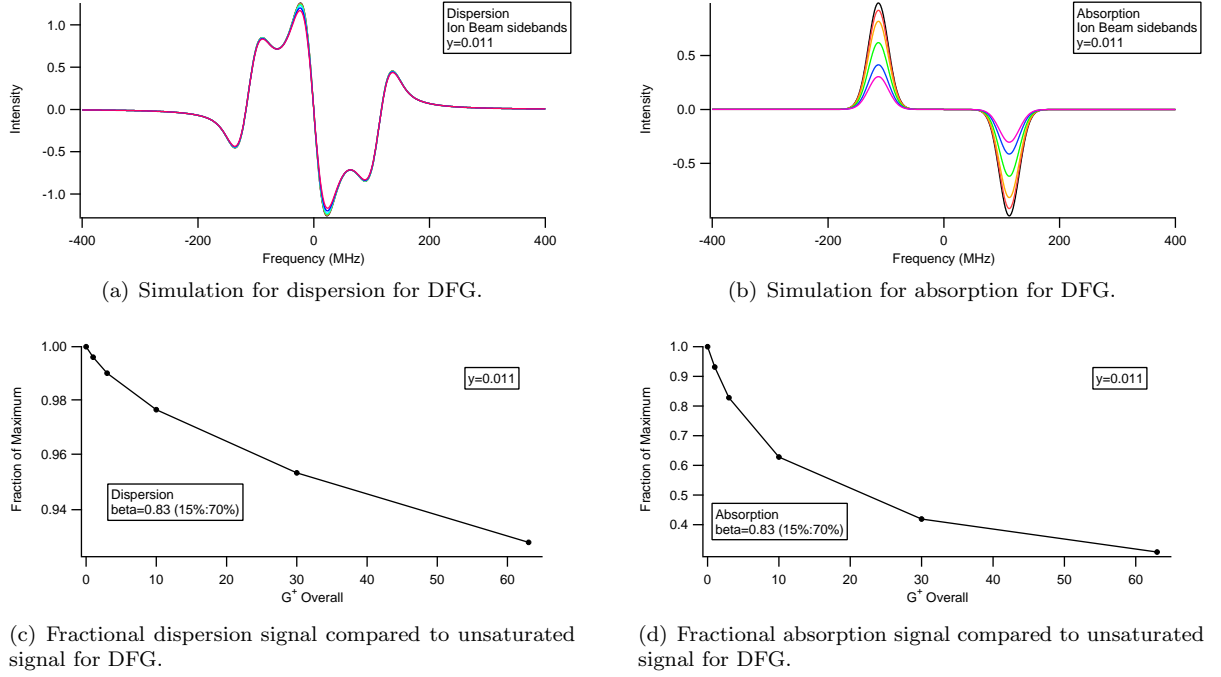


Figure 4.18: Simulations of absorption and dispersion with $y=0.011$. Panels a-b, $G^+=0, 1, 3, 10, 30, 63$ with $\Delta\nu_{Doppler,FWHM} = 40$ MHz, $\nu_m=113$ MHz, $\beta=0.83$, $J_0^2=0.70$, $J_1^2=0.15$.

Chapter 5

Fast Ion Beam System

5.1 Overall Design Approach

5.1.1 Previous Direct Absorption Measurements of Ion Beams

In 1989, Rich Saykally's group at UC Berkeley reported the first measurement of direct absorption from a fast molecular ion beam. [12] Their instrument was unique because it was the first time in which the general direct absorption process was applied to a molecular ion beam. Other ion beam techniques require specialized molecular systems that allow for pre-dissociation. Due to the high velocity of the ion beam, the recorded spectra underwent a kinematic compression, with observed line widths smaller than the Doppler width of the ions at their kinetic temperature. Another consequence of the increased velocity is a Doppler shift in the observed frequencies, which is related to the mass of the ion of interest, thus providing a mass identification of each spectral line. Some of the techniques the Saykally group used involved performing a mass analysis before the spectroscopy so that the ion beam species could be optimized. Velocity modulation was used to discriminate against the neutrals, a passive optical cavity was used to increase the sensitivity and a double balanced detector was used to reduce the noise of the spectroscopic signal. Initially, a nozzle-filament source was used to produce HF^+ from neat HF. Plate aperture ion optics were used to extract and collimate the HF^+ ions from the source. Direct current quadrupoles were used to turn the ion beam 90° to be coaxial with the laser beam and away from the neutrals created in the source. A tunable color center infrared laser beam was used to probe the ions spectroscopically. Due to stability and tuning issues, the laser was locked at a fixed frequency, while the velocity of the ions was tuned and modulated by the use of a slow ramp and fast square wave coupled onto the drift tube. A schematic of the first DLASFIB instrument is shown in Figure 5.1. Later implementations of the instruments used an uncooled cold cathode to produce HN_2^+ and HCO^+ , [78] as well as H_3O^+ and NH_4^+ , [79] whose infrared spectra and absolute IR intensities were measured. In this configuration, the first quadrupole was removed, and the ions were probed collinear to the ion production plasma. Only one quadrupole was used to turn the ions into the Wien filter mass

spectrometer.

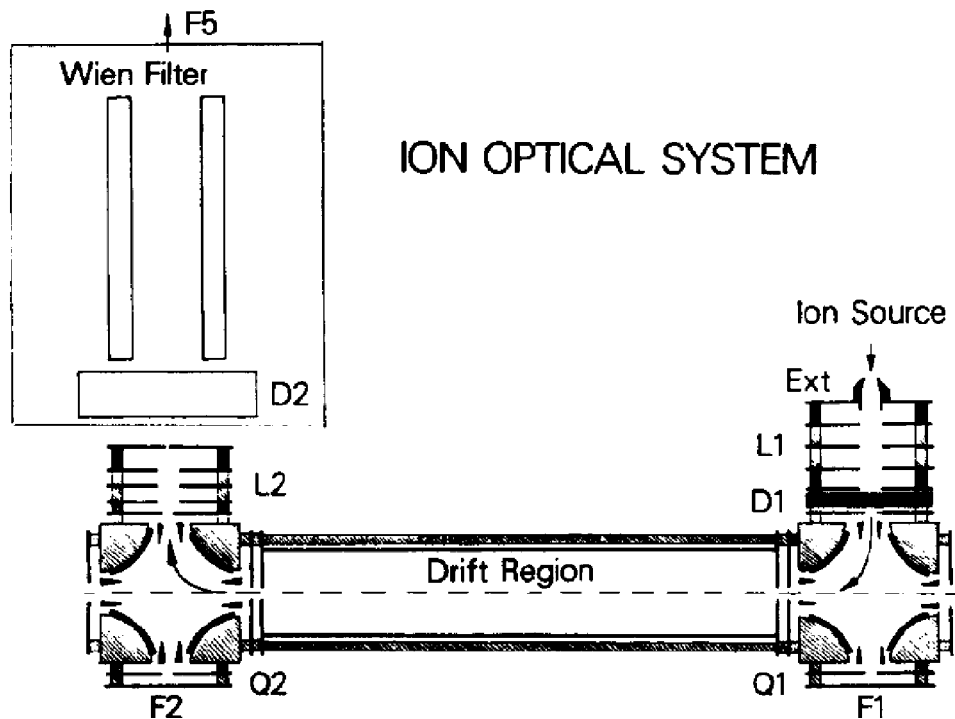


Figure 5.1: Instrumental layout of the first Direct Laser Absorption Spectroscopy Fast Ion Beam Spectrometer at UC-Berkeley.

Keim reported the rotational temperature (T_{Rot}) and vibrational temperature (T_{Vib}) of HN_2^+ ions in the DLASFIB instrument to be 600 and 500 K respectively. T_{Rot} of H_3O^+ and NH_4^+ were reported to be 525 and 400 K respectively, and T_{Vib} was assumed to be equal to T_{Rot} [79]. The increased rotational temperatures would drastically increase the spectral congestion and quantum dilution for many polyatomic ions of astrochemical interest, including many carbocations such as CH_5^+ and C_3H_3^+ . Therefore, while some small polyatomic ions could be studied with an uncooled ion beam, more interesting molecules necessitate better rotational cooling. The Saykally group tried to implement supersonic cooling, but were unable to successfully implement it.

One problem with their implementation of supersonic cooling was that all DLASFIB setups used a monolithic vacuum chamber with a single large-throughput diffusion pump (effective pumping speed = 2300 L/s). The resulting chamber pressure was on the order of between 2×10^{-4} and 3×10^{-5} Torr in the ion optical system, including the Wien filter mass spectrometer. This type of an expansion was able to produce rotational temperatures of between 78 and 166 K for HN_2^+ . Attempts to properly cool the ions rotationally with a supersonic expansion using a 2500 L/s diffusion ejector pump failed for at least two reasons. First, the pump evacuating the expansion chamber should have been backed with a 142 L/s pump while only a 47 L/s

pump was used. Second, the designs of their sources were not optimized to reduce arcing when the chamber pressure was in the glow discharge region of the Paschen curve. [147] While free jet expansions easily cool molecular beam expansions and expansion ion discharges down to 10 – 25 K, it is still unknown whether fast ion beam acceleration through an ion/neutral skimmed region will increase the rotational temperature of cooled molecular ions. [148]

5.1.2 Overview of New Ion Beam Instrument

Work in the McCall group has focused on making improvements on a direct absorption ion beam experiment in terms of the ion optics, the spectroscopy sensitivity, and the mass spectrometry. Many of the improvements in components used have been enabled by technological advancements over the last 20 years.

A schematic of our uncooled ion beam instrument is shown in Figure 5.2 and details will be given in the following sections. Modular construction was used to facilitate changes and access to the system, and allow for differential pumping to achieve lower instrument pressures. The instrument is mounted on a versatile aluminum extrusion support structure (80-20) and the entire vacuum setup can be moved on retractable heavy duty wheels. The ion source is housed in a large vacuum chamber that was dimensioned to enable high throughput pumping of continuous supersonic expansion ion sources. The rest of the ion beam instrument was housed inside various Conflat (CF) crosses, tees and nipples. After the ions are produced in an ion source, they are extracted and accelerated to ground, and focused into a beam by an electrostatic ion lens. Two sets of xy-steerers are used to vertically and horizontally translate and steer the ion beam before it passes into a cylindrical bender.

The ions are then bent by 90° and focused into the drift tube by a cylindrical electrostatic double-focusing deflector. The drift tube is a 27 cm long stainless steel tube which is used to modulate the ion velocity. The drift tube is connected to a signal generator through a vacuum feedthrough and it is electrically isolated from the vacuum chamber. Two movable, electrically isolated stainless steel apertures can be extended into the ion beam path through slits in the drift tube to optimize the overlap between the laser cavity and the ion beam. The 3 mm diameter apertures are mounted on two vertical linear motion manipulators situated 12.9 cm apart. After the drift tube region the ion beam enters the second 90° bender which guides the ions out of the laser cavity path into the mass spectrometer where the ion beam composition and energy can be analyzed *online* during spectroscopic operation, employing a time-of-flight beam modulation technique [149, 150]. A cw beam is pulsed into an ion packet whose arrival times after a flight distance of ~ 1.5 m are detected with an electron multiplier. The laser beam is coupled into the instrument using Brewster windows to reduce reflection losses and a laser cavity is built up to increase the path length and signal strength.

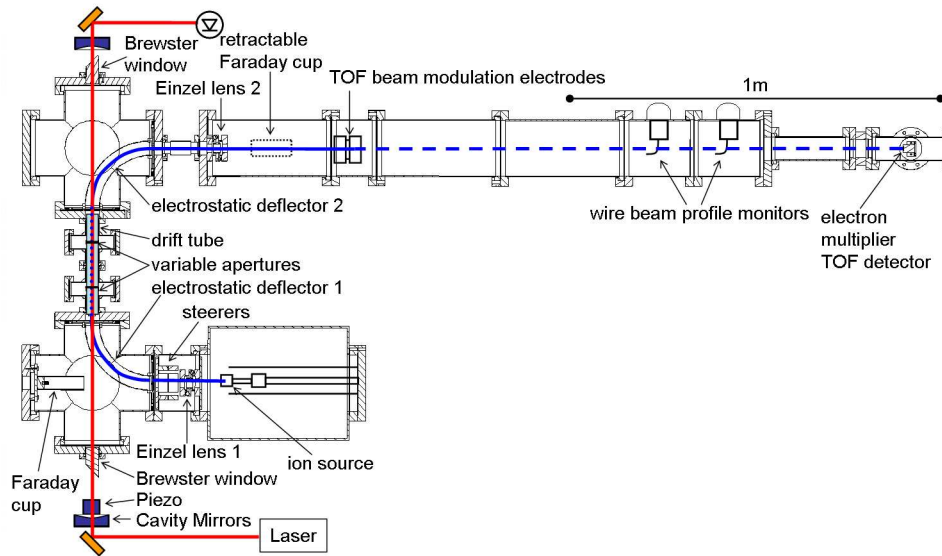


Figure 5.2: A bird's-eye schematic view of the fast ion beam portion of the SCRIBES instrument. The blue lines represent the ion beam, while the red lines represent the path of the laser beam.

5.2 Vacuum Considerations

Schematics of the existing pumping setup and future supersonic pumping setup are shown in Figures 5.3 and 5.6, respectively. The vacuum system was constructed mostly from stock CF parts (Kurt J. Lesker), with the exception of the source chamber, which was mounted with a 8" Conflat flange to connect to the ion beam and two ISO-F 250 connections, one for the source flange, and one for the turbo pump/roots pump. The first Einzel lens and steerer components are housed in a custom length 8" CF nipple. The electrostatic deflectors were housed in 8" CF 6-way crosses (C6-0800). The modulation tube was housed in 2-3/4" CF 4-way crosses (C-0275). The linear manipulators were attached on top of 2-3/4" nipples (FN-0275). After the drift region, a 2-3/4" bellows allows for some flexibility in the system between the drift region and the mass spectrometer. An 8" CF tee (T-0800) is used to house the retractable Faraday cup and the second Einzel lens. The mass spectrometer pulser plates were housed in a custom 8" CF nipple. The pulsed ion beam packet passes through two 8" CF nipples (FN-0800) and two beam profile monitors (National Electrostatics Corporation, BPM83). A 4.5" CF nipple (FN-0450), gate valve (SA0250MCCF), and 4-way cross (C-0450) are used to connect the mass spectrometer, seal the electron multiplier off from the rest of the instrument, and house the electron multiplier and turbo.

The Leybold Mag W 2200 pump provides 2000 L/s of pumping speed (for N_2) but is conductance limited by the ISO 250 flange connecting it to the chamber down to 1475 L/s. The two Varian Navigator 551 pumps provide 550 L/s of pumping speed (for N_2) but are conductance limited by the 8" CF flanges to 432 L/s beneath the 8" 6-way crosses which house the cylindrical benders. The Varian Navigator 250 pump provides 250 L/s of pumping speed (for N_2) but is conductance limited by the 4.5" CF flange of the detector cross to 143 L/s. Each turbo pump requires a mechanical rough pump. The 250 L/s pump is backed by a dedicated 1.65 L/s scroll pump (Edwards A72401906 with A50597000 exhaust silencer) located in the lab. The pressure of the forevacuum of the electron multiplier chamber turbo was measured with another thermocouple gauge (KJL 912162). The 2000 L/s and two 550 L/s pumps are backed by a 13 L/s mechanical pump (1374 Welch) located in the pump room. A 6" PVC vacuum line allows connection of the forevacuums of the three turbos to the mechanical pump through micro-maze oil traps (MMA-152-2QF). The pressure of this forevacuum lines was measured with a thermocouple gauge (KJL6000) connected to a digital readout (KJL610). The mechanical pump exhaust was modified to be vented with the exhaust fumes to remove hydrogen and hydrocarbons from the pump room. Drawings for the adapter required are found in Section D.1.

Four ion gauges can measure the pressure of the high vacuum system and determine how well the differential pumping is performing. A schematic of the vacuum measurement connections is shown in Figure 5.4. A

self contained ion gauge (IMG401 Hornet – Instrutech.com IGM401YFD with power supply cord (PS501A)) is connected directly to the source chamber. Two ion gauges (Kurt J. Lesker G100F) are connected directly above each 8" 6-way cross housing the cylindrical deflectors. Another ion gauge is connected to the 4-way cross housing the MS electron multiplier detector. The controller (Kurt J. Lesker KJL6600C) for the ion gauges only controls two ion gauges at a time, in addition to the forevacuum thermocouple gauge of the mass spectrometer forevacuum line.

Electrical connections to the source, Faraday cups, and various ion optics were made with various BNC, SHV-5 and SHV-20 feedthroughs as illustrated in Figure 5.5. The DC bias voltages for the source beam and discharge voltage were accomplished with a 2-3/4" CF 2 connector feedthrough (IFTXE021153)). The DC bias voltages for the Einzel lens and steerer assembly were accomplished with SHV-5 feedthroughs connected via a 2-3/4" CF cross, (2 4-feedthrough connectors (IFTSE041033) and a 1-feedthrough connector (IFTSE011033) feedthrough) connected to the source chamber. The Faraday cup electrode is connected to a 2-3/4" CF SHV-5 feedthrough (IFTSE011033). The DC bias voltage for the benders was supplied with two welded SHV-5 connectors welded into the sides of each 8" cross (IFTSE011031). The modulation voltage was applied to the linear manipulator iris plates and drift tube with three separate connections with 2-3/4" CF BNC feedthroughs (IFTBG012033). The DC bias for the second Einzel lens and the electrode reading of the retractable faraday cup were supplied through weldable SHV-5 feedthroughs connected into the side of the 8" tee (IFTSE011031). The pulsing bias for the mass spectrometer pulser plates was supplied through 2 of 5 feedthroughs (IFTSE011031) welded into the custom nipple.

The planned supersonic expansion source ion beam system involves adding a third electrostatic cylindrical bender, and placing the 2000 L/s pump onto another 8" Conflat cross with an adapter. The source chamber will then house the supersonic discharge source, and will connect via a bellows and reducer to the 20" stainless steel pipe that connects to a roots pump located outside of the building. The roots pump with 20" pipe provides 3200 L/s of pumping speed (for N₂) but is conductance limited by the ISO 250 flange to 2043 L/s.

With the cold cathode source in operation, the pressure in the source chamber is on the order of 1×10^{-5} Torr. The 6-way crosses with cylindrical benders normally have pressures of 1×10^{-6} Torr at deflector 1 and 1×10^{-7} Torr at cylindrical bender 2. The vacuum cross that houses the detector in the mass spectroscopy leg can be separated from the main system by a gate valve and typically has pressures on the order of 2×10^{-8} Torr.

It was determined that the turbo pumps would have a longer lifetime if water cooling was supplied. The Oerlikon MagLev pump was already set up for water-cooling, but the Varian pumps did not have adapters

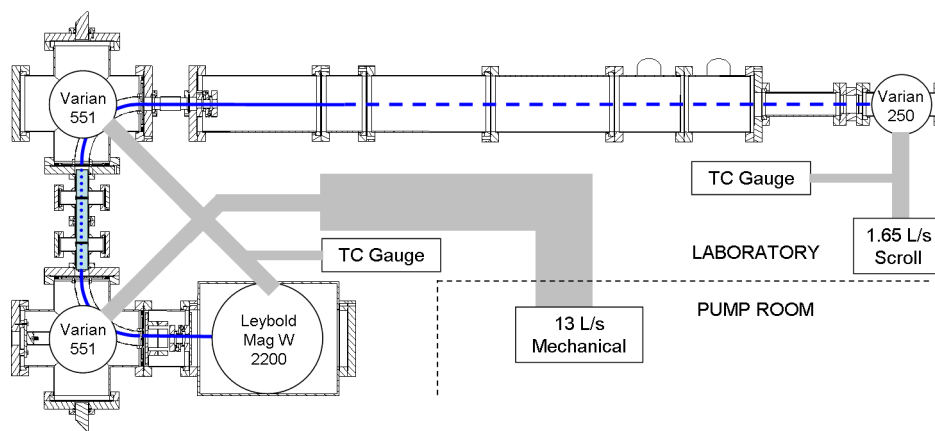


Figure 5.3: Schematic of turbos and forevacuum pumps in the uncooled ion beam system. Four turbo pumps provide ultrahigh vacuum: one on the source chamber, one below each 8" cross, and one after the electron multiplier in the mass spectrometer.

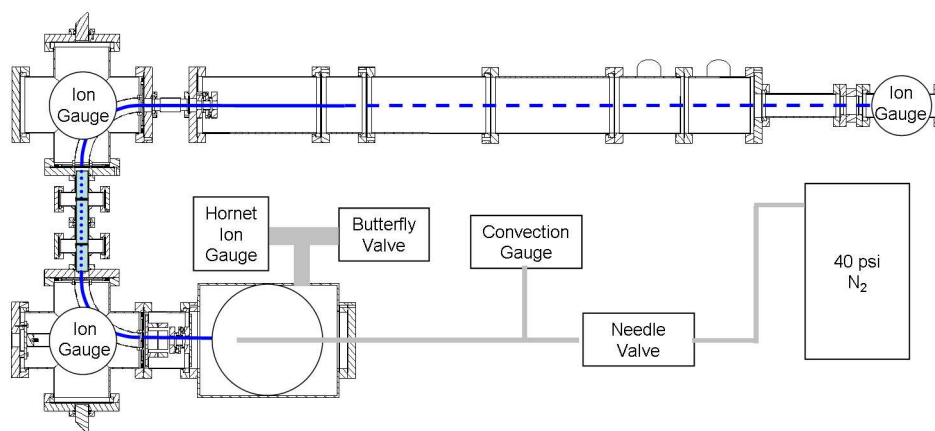


Figure 5.4: Schematic of ion gauge location in the non-supersonically cooled ion beam system. Three ion gauges from Kurt J Lesker, are located above each 8" 6-way cross, and beneath the 4.5" 4-way MS detector cross. One Hornet ion gauge is connected to the source chamber. The same 2-3/4" connection that allows for the Hornet to be connected to the ion beam chamber also has a butterfly valve that is used to vent the system after the turbos have been spun down. Sample gas is feed into the ion source from a nitrogen tank through a needle valve. The pressure after the needle valve is read through a convection gauge.

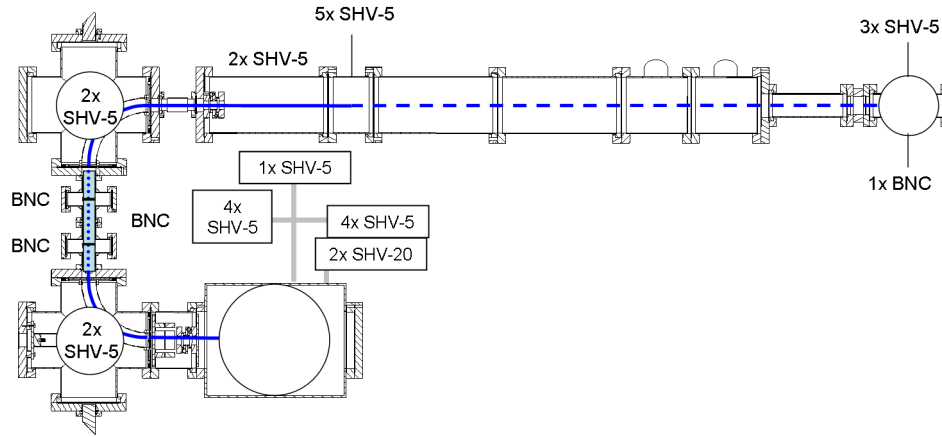


Figure 5.5: Schematic of electrical feedthroughs which bring instrumentation voltage into the ion beam system. Source voltages go through the SHV-20 connections, Einzel lens 1 and steerer voltages go through the source chamber. SHV-5 feedthroughs are welded directly into the 8" 6-way crosses, the 8" 3-way tee, and the 8" nipple. 3 SHV-5 connectors and 1 BNC were welded directly into the 4.5" CF flange that mounts the electron multiplier.

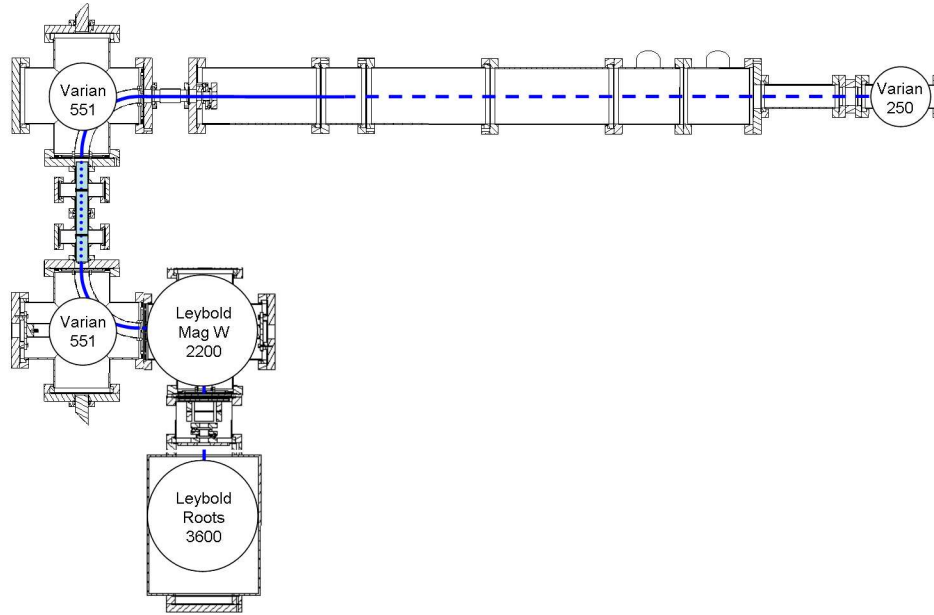


Figure 5.6: Schematic of vacuum pumps in the planned supersonic expansion cooled ion beam system. An additional high throughput pump is added to the source chamber. Two thermocouple gauges are used to measure the forevacuum pressure, one connected to the MS scroll pump, and one connected to the mechanical pump.

to the British pipe thread. Therefore, adapters for all three Varian pumps were designed and constructed out of brass. The drawings for these adapters are found in Figure D.2.

5.3 Instrument Base

Previous experiments with cavity ring-down spectroscopy with the ion beam instrument on the laser table showed that the turbo pumps induced vibrations which adversely affected the laser cavity. Therefore the instrument was removed from the laser table and constructed on a movable instrument base. That base was constructed of 80-20 aluminum extrusions, connected to each other with corner brackets and joining plates, and rests on the floor with heavy duty leveling casters (part # 2715). The leveling casters allowed the instrument to be rolled in and out of position, and raised to any reasonable height. The turbo pumps should not be spinning when the instrument is translated. A listing of the parts purchased for constructing the instrument are listed in Section D.3. An illustration of the instrument base is shown in Figure 5.7.

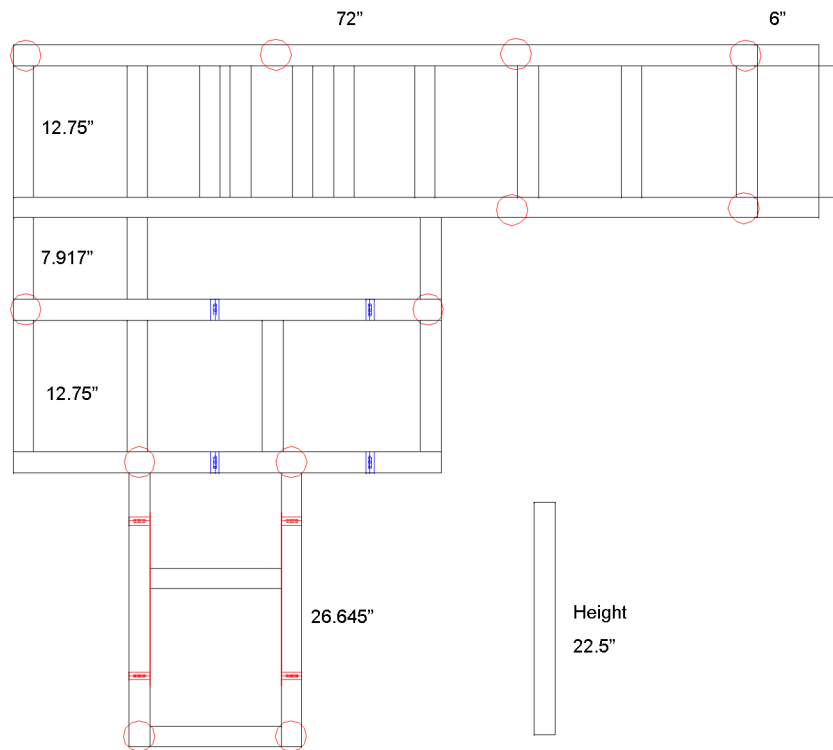


Figure 5.7: Schematic of top view of the ion beam system base. The top and bottom are essentially equivalent, with a 22.5" extrusion between them. The red circles indicate the approximate caster positions.

5.3.1 Steel Pipe Holders

As most of the ion beam instrument was constructed from round conflat parts, steel pipe holders were constructed to connect the ion beam directly to the instrument base. The drawing in Figure 5.8 illustrates how this was done. Metric grub screws (jwwinco.com 16WG30) with thrust pads (jwwinco.com 8N60G29) were used to push against the CF pipes and center them. Twenty three holders are used to support the ion beam instrument and 4 spare holders are available for future expansion of the ion beam. Construction schematics for the holders are found in Section D.4.

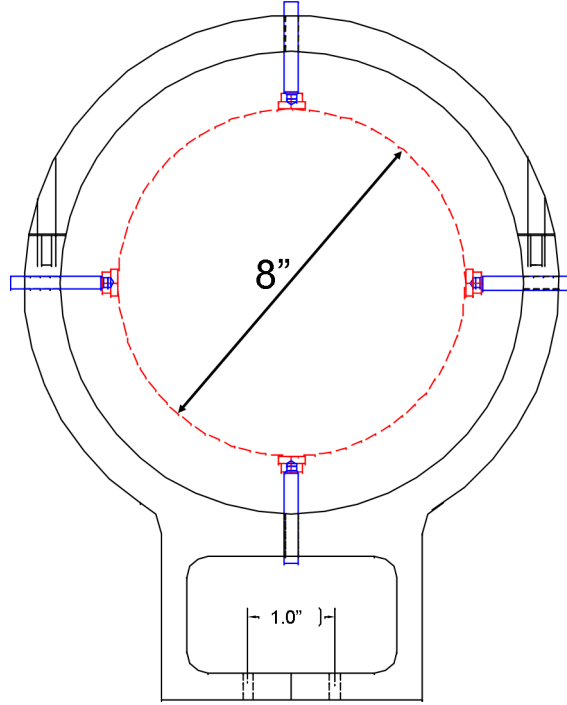


Figure 5.8: Schematic of steel pipe holders that connect the 8" CF parts (red-dashed) to the instrument base. Grub screws are used to flexibly connect the holder to the CF pipes (blue), and center the pipe.

5.4 Cold Cathode Source

Before implementation of a supersonic expansion source can be done, the initial testing and characterization of the ion beam instrument involved using an uncooled discharge ion source. An ideal ion source would produce high ion current with low beam divergence, and low gas throughput. Several ion sources are possible including corona discharge, cold cathodes and filament sources. Because of the reliability of cold cathodes, and their use in a previous fast ion beam instrument, [79] a cold cathode source was chosen.

5.4.1 Source Construction and Operation

A source with modular capabilities was designed for ease of part replacement. Our cold cathode source was made with a fused silica tube held by two electrodes, with an opening at one end for the sample gas, and another opening for the ions to leave. The electrodes were constructed using stock parts for Ultra-Torr fittings from Swagelok. A 3/8" to 3/8" Ultra-Torr straight union was used for the front electrode (SS-6-UT-6), and a 3/8" to 1/4" reducing union (SS-6-UT-6-4) was used for the back electrode and was connected to the gas line. The stock parts were modified, as illustrated in Figure 5.9. The front electrode was drilled through so that the fused silica tube could fit completely through it and approximately $\frac{1}{3}$ of the union

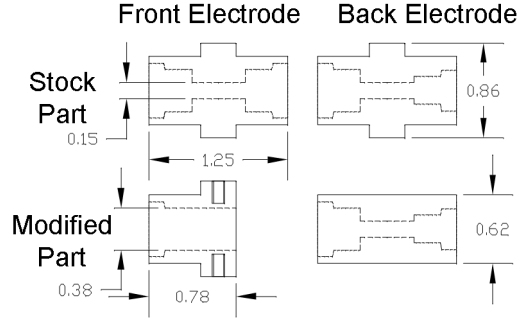


Figure 5.9: Schematic illustrating how stock Ultra-Torr fittings were modified to form the cold cathode source.

was removed. Additionally, three 4-40 blind taps were added to the central hexagonal portion of the front electrode so that the a bias voltage could be connected to the front electrode. The central hexagonal portion of the back electrode was turned down into a cylinder, so that it could fit inside of the source holder.

One of the Ultra-Torr ferrules was replaced with a custom designed ferrule to form the ion exit from the source. This ferrule has a 1 mm diameter aperture to allow the ions to escape. The front of the ferrule has a 22° angle in it to reduce the beam expansion caused by the space-charge interaction. [151,152] A schematic of the ferrule is shown in Figure D.4.

High temperature silicone O-rings (012S70 McMaster-Carr) replaced the stock Viton O-rings. A 9 mm OD \times 7 mm ID fused silica tube was cut to 3.25" lengths and the ends were ground polished. A small circle of stainless steel mesh was inserted into the back electrode to enlarge the discharge surface. An expanded view of the source parts and of the source in operation are shown in Figure 5.10. An aluminum cap holds the back electrode of the source and provides mechanical stability, allows for the connection to high voltage, and also allows for water cooling to this back electrode. The ions are extracted to a stainless steel plate with a 0.25" diameter hole in it. As the extraction plate is held at earth ground, the ions fall in potential when they traverse from the high voltage at the front electrode to the ground potential at the extraction plate. The electric potential energy (qV) is converted to kinetic energy ($1/2 Mv^2$), and the ions travel with increased velocity producing the fast ion beam (where q is the charge of an electron, V is the beam energy in Volts, M is the mass in kg and v is the velocity in m/s). When the source is assembled the front ferrule and end-cap make a smooth surface as shown in Figure 5.10(b).

The source is held in place using a homemade movable x-y stage built on an ISO-250F flange. Detailed schematics for the full assembly are not available. However schematics for the parts that actually hold the back electrode are available and shown in Figure D.5.

In order to form a fast ion beam, high voltage was applied to both electrodes, as illustrated in Figure

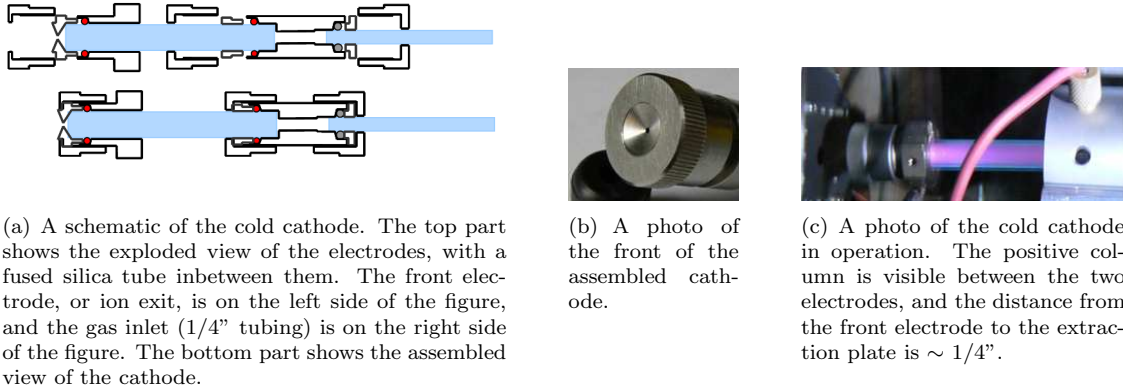


Figure 5.10: Schematic of cold cathode source.

5.11. The front electrode was connected to the “Float Power Supply” which determines the beam energy. The float power supply is also connected to the electrical common of the reversible polarity “Discharge Power Supply.” The polarity of the discharge power supply can be changed from positive to negative, but this should only be done when the float power supply is off and discharged, and the discharge power supply is disconnected.

When the discharge power supply provides a positive voltage, ions are extracted from the front electrode serving as the cathode (the least positive electrode), which generally provides ions formed by electron impact and experience few collisions. [79] When the discharge power supply provides a negative voltage, the source extracts ions from the front electrode serving as the anode (the more positive electrode), which generally provides ions formed by secondary collisions with other ions formed by electron impact, and the ions experience many collisions. This result is consistent with that reported by Keim [79]. However, for a pure nitrogenic plasma, more N_2^+ was extracted from the cathode, which is inconsistent with the effect observed by Keim [79].

Other ions, such as H_3^+ , would be better suited to anodic extraction. Whichever electrode serves as the cathode experiences heating. When the source is run from an anodic extraction, the back electrode serves as the cathode, and experiences the heating. As the back electrode is held in place by a PEEK and aluminum part, if the cathode becomes too hot, the PEEK will be damaged. Therefore, a water-cooling source was developed to cool the cathode under anodic extraction. Schematics for the water cooling are shown in Figure D.7. When the source is run extracting from the anode, normally a larger hole in the ferrule (2 mm or 3 mm) was necessary to extract the ions.

5.4.2 Source Power Supplies

The float power supply (Glassman FC120W 15kV 8mA) accelerates the fast ion beam and is connected to the front electrode and the ground of the discharge power supply. The discharge power supply (Glassman EQ1200W 6kV 0.2A reversible polarity) is used to produce ions in the positive column plasma in the source. Because the discharge power supply is floated by connecting the output of the float power supply to the ground of the discharge power supply, the discharge power supply must be electrically isolated by placing it inside a polycarbonate box. A large polycarbonate box was constructed with 4x 0.5" holes for large gauge insulated wire (for input/output) to pass through, four 3.5" holes for air circulation fans, ceramic rods to push the on/off buttons for the power supply and high voltage enable, and teflon rods that can turn the voltage and current control potentiometers. The discharge power supply is then powered through an isolation transformer.

A schematic diagram of the isolation box, source power supply layout, and source configuration is shown in Figure 5.11. Single phase 208 V AC is brought into the isolator box and connected to a custom isolation transformer providing up to 15 kV isolation from core to ground (Quality Transformers-1.2 KVA, 1 phase, 60 Hz, 208 VAC \rightarrow 120 VAC). The isolated 120 V AC output (live and neutral) is input into the discharge power supply's AC input. The output of the 15 kV power supply is brought into the isolation box and directly connected to the ground of the discharge power supply, and to a SHV-20 terminated output cable which runs to the source front plate. The output of the discharge power supply is passed through a ballast resistor (100 k Ω) to keep the net circuit resistance positive through the plasma, [147] and limit the current drawn from the power supply. After passing through the ballast resistor, the discharge output exits the isolation box through a SHV-20 terminated cable. At the source chamber, the discharge and float voltage enters via two SHV-20 feedthroughs illustrated in Figure 5.5.

On the inside of the vacuum chamber, the source bias voltages are brought to the source with 20 kV insulated wire. An electrical lug connects the 20 kV wire to the front electrode with a 4-40 screw into the tapped hole described in Section 5.4.1. The discharge voltage connects with a slightly more complicated setup. The 20 kV wire is inserted through a homemade PEEK adapter screw, illustrated in Figure D.6, and a plastic ferrule (Cole-Parmer C-01939-32). Solder was then applied at the end of the wire, and a rounded/pointed tip of solder was formed. When the PEEK 1/4-28 screw was screwed into the aluminum cap holder, the solder was eventually brought into contact with the back electrode, and the discharge power supply was connected to the back electrode. The connections were initially tested with a multimeter. If no discharge is formed, or no fast ion beam is seen, ensuring these electrical connections are connected is a good place to start.

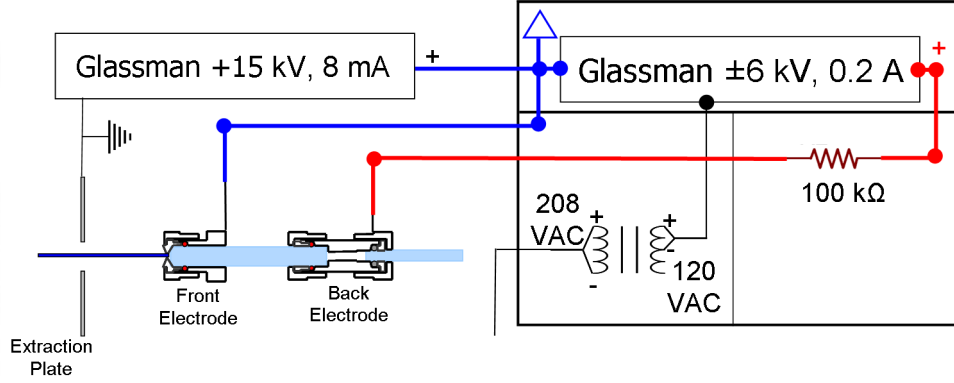


Figure 5.11: Electronics layout for power supplies driving source discharge. A schematic of the cold cathode with attached power supplies. The front electrode serves as either the cathode or the anode depending on the polarity of the discharge power supply. If the discharge power supply sources a positive voltage with respect to its common supply, ions are extracted from the cathode and undergo few collisions. If the discharge power supply sources a negative voltage with respect to its common supply, ions are extracted from the anode and undergo many collisions.

The input sample gas flow is controlled with a manual leak valve (Kurt J. Lesker – 2-3/4" CF VZLVM263R) as illustrated in Figure 5.4. The flow is not linear with respect to the knob position, and therefore a high backing pressure with the valve mostly closed provides the finest control of the pressure. The backing pressure was normally 40–45 PSI. On the output side of the leak valve, a convection gauge (KJL-912161) connected to a readout (KJL 902171) was used to measure the pressure before a ~ 4 m section of $\frac{1}{4}$ " plastic tubing.

5.5 Ion Optical System

The ion optics configuration was designed to optimize the ion density in the laser/ion overlap region between the two electrostatic deflectors. Figure 5.12 shows a Simion 3D [153,154] simulation of typical ion trajectories throughout the setup. It is apparent that the ion trajectories are relatively collimated through the drift region. All ion optical elements are electrostatic, which means that all particles with the same kinetic energy and charge state are guided on the same trajectory without discrimination against particle mass. Figure 5.13 shows a simulation of the potential energy surface. The deceleration mode of the Einzel lenses is apparent as the ions approach the biased electrodes.

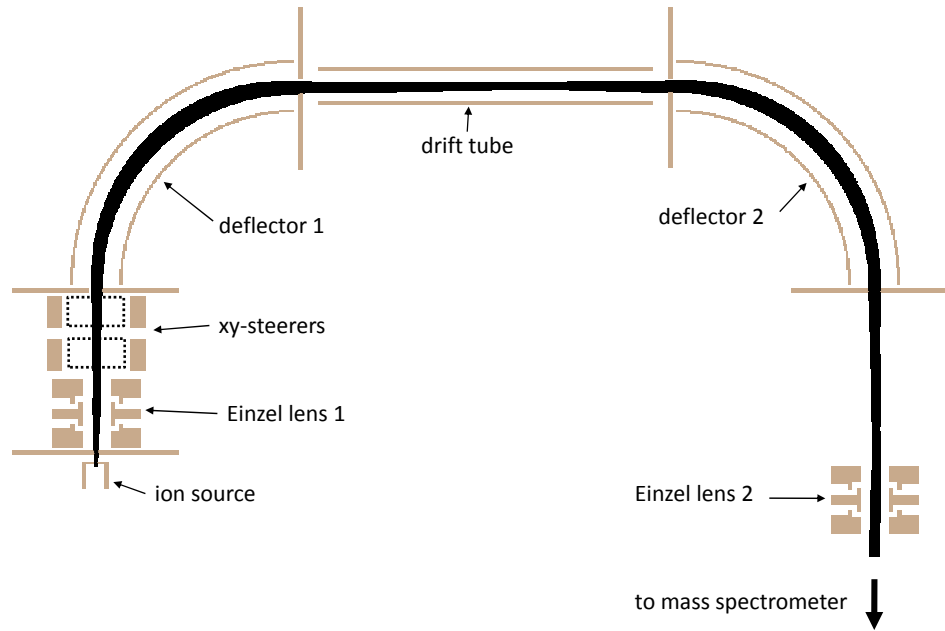


Figure 5.12: SimION 8.0 simulation of typical ion trajectories through two Einzel lenses and 2 cylindrical benders.

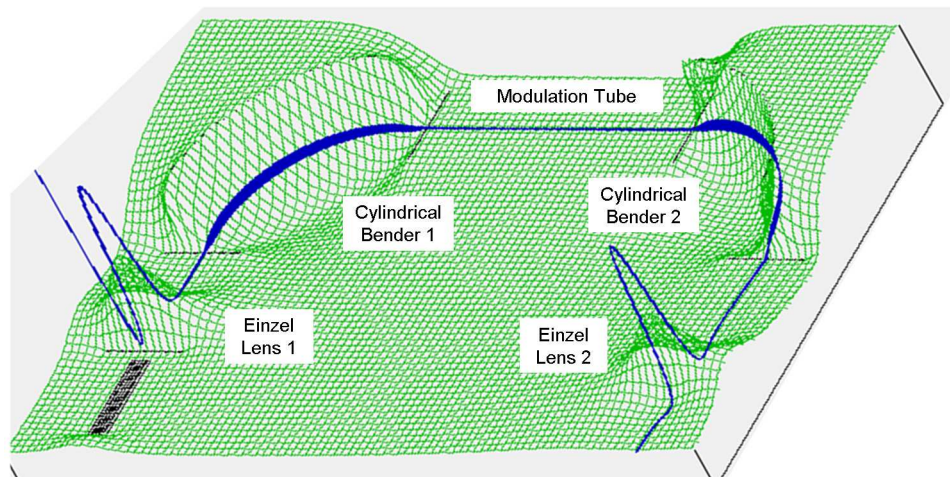


Figure 5.13: SimION 8.0 simulation of the potential energy surface of ion optical components in the fast ion beam system. The ions are birthed at 4 kV of beam energy and are accelerated to ground, collimated by the Einzel lens, and then turned 90° by the electrostatic benders into the drift region.

5.5.1 Ion Optics Power Supplies

Eight channels of a power supply provide bias voltage for the Einzel lenses, positive and negative benders. (Gamma High Voltage, RMCR5P \times 2/3P \times 3/3N/3/M*; 2 modules 0 \rightarrow +5 kV; 3 modules 0 \rightarrow +3 kV, 3 modules 0 \rightarrow -3 kV; all modules with 1 mA current). Another 8 channel Gamma power supply is used to control the horizontal and vertical steerers. (Gamma High Voltage BP1/ \times 8/DM \pm 1 kV; All modules with 500 μ A current). Both sets of ion optics power supplies can be controlled locally with a potentiometer knob or by computer control in the LabVIEW program, whose graphical user interface is shown in figure 5.14. The LabVIEW program is set to output a (\pm 10 for the 1 kV power supplies; 0 \rightarrow 10 for the 5, \pm 3 kV supplies) signal voltage which is proportional to output of the power supply. Using the LabVIEW program had the added advantage of keeping track of the ion optic voltages used for each scan. This segment of the program requires that the top “Adjust Ion Optic Voltages?” boolean control be on while the voltage is changed. The values are automatically saved during a scan, but can also be saved outside of a scan by pressing the “Save?” button. The ion optics from a previous scan (or day) can be read in by pressing the “Read?” button.

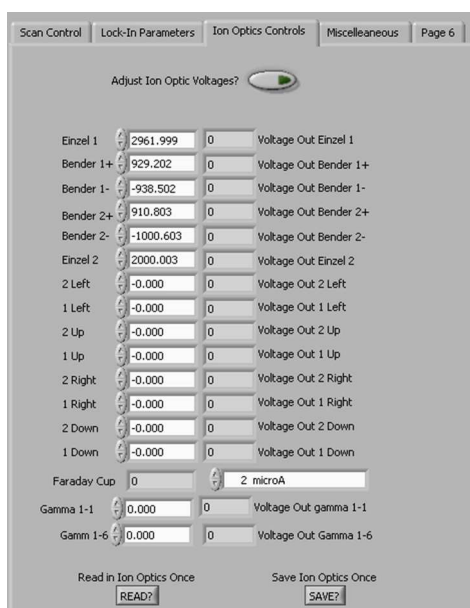


Figure 5.14: Screen shot of LabVIEW program ion optics control

5.5.2 Extraction and First Einzel Lens

The positive ions that emerge from the ion source are extracted by a stainless steel plate and focused by the first Einzel lens. Drawings for the parts that comprise the extractor plate are shown in Figure D.8a. The aperture of the extractor plate diameter can be determined by connecting a stainless steel plate with the desired aperture diameter to the extractor plate. The extractor plate typically had 0.25" diameter aperture attached (Kimball Physics, B Series, 5×5, 0.25" Round Diameter).

The ions are then collimated by an electrostatic lens. The DLASFIB instrument used traditional plate apertures for the ion optics lens. Three element lenses are usually chosen because this geometry decouples the focal properties of the lens from the ratio of the plate potentials. [155] An Einzel lens is any three-plate lens where the potential on the first plate equals the potential on the third plate. Traditionally, Einzel lenses have $(V_2 \sim V_{Cathode}) > V_1, V_3$ (also called the decelerating mode), which has greater aberrations than the accelerating mode.

Instead of following the DLASFIB design, a cylindrical lens geometry was chosen. Cylinder lenses are stronger than plate apertures for a given voltage and diameter, [155] have smaller aberration coefficients, and are easier to make and mount. Cylindrical lens are designed such that the length (A) is greater than half the diameter (D), and has gaps of less than D/10 to minimize stray electric fields. In our case D=0.94", A=0.71", and the electrode gap is 0.15". While the gap is larger than D/10, plates V_1 and V_3 have an extra ground shield to reduce the interference of stray electric fields. Details of the construction of the Einzel lens are found in Section D.6.

5.5.3 X-Y Steerers

A pair of two parallel plate steerers is used to deflect the ion beam in both horizontal and vertical direction, allowing for an adjustment of the beam angle as well as for parallel offsets to the ion beam position. Each steerer plate is supplied by an independent bipolar power supply (Gamma High Voltage, BP1/x8/DM 500 μ A S/N 38-1108) with voltages up to ± 1000 V. By applying voltages of the same sign to opposing steerer plates, it is also possible to induce additional horizontal or vertical focusing in the steerer section.

5.5.4 Cylindrical Deflectors

The cylindrical 90° deflectors follow a new design that provides control of the ion beam focusing in both dimensions. [156] Standard cylindrical benders focus an incoming ion beam only in the plane of deflection. Therefore, typically an asymmetric lens or focusing element is required to restore the circular ion beam

profile after deflection. The same principle applies to electrostatic quadrupole deflectors unless more sophisticated shim electrodes are used. Spherical deflectors focus the beam in both directions, hence an incoming parallel beam into an ideal spherical deflector is focused into a single spot after 90° deflection. However, spherical deflectors require larger vacuum chambers and are more complicated and costly to manufacture when compared to cylindrical deflectors. Our cylindrical deflectors use plates of differing plate heights to mimic the field of a spherical deflector at the ideal ion beam orbit. [156]

By equating the centripetal and electrostatic forces of the ion beam, the expected voltage required to deflect an ion beam is given by [156]

$$V = \frac{2qV_{Beam}D}{R} \quad (5.1)$$

where D is the separation between the plates, and R is the radius of curvature for the ion beam in-between the bender plates. For the experimental parameters of $R=0.158$, $D=0.036$ m, and $V_{Beam}=4$ kV, the expected voltage is ~ 1850 V. However, this approximation does not take into account the fact that the radius of curvature starts at infinity, changes to R , and then returns to infinity, thus making the potential values needed slightly higher than expected. It should be noted, that the plate voltages should be as close to symmetric as possible to avoid the re-referencing that can occur if the voltages of the ion beam as they enter the deflector. [156] Details of the construction of the cylindrical deflectors are found in Section D.8 of Appendix D.

5.6 First Faraday Cup

When neither plate of the first bender is biased, the beam passes un-deflected through the hole in the outer plate seen in Figure D.10 onto the Faraday cup. The Faraday cup current is read by a picoammeter (Keithley 6485). The ammeter produces an analog signal which can be recorded by the LabVIEW data acquisition program. Faraday cups are fairly easy to design, and the only design considerations are to make sure the length of the cup will ensure that no secondary electrons emitted escape the cup. This is accomplished by making the length of the cup at least $5\times$ the diameter of the cup, and by not having a perpendicular collector face. [157] Failure to reach this condition can make the ion current reading high by at least 30%. The initial DLASFIB instrumental papers used simple stainless steel plates instead of a properly designed Faraday cup. [79] Details of the construction of the Faraday cups are found in Section D.9. For the first Faraday cup, the electrode was six times longer in length than diameter.

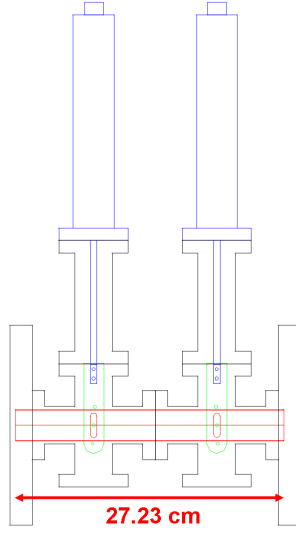


Figure 5.15: Schematic drawing of drift tube with overlap irises and linear motion manipulators.

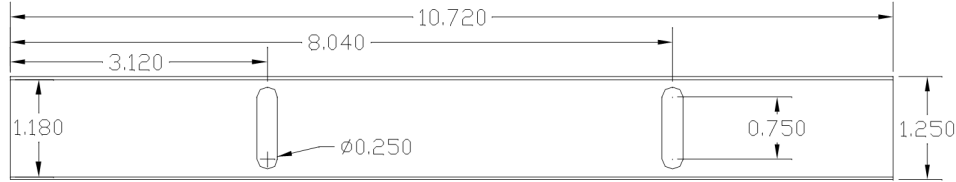


Figure 5.16: Schematic drawing of drift tube.

5.7 Achieving Ion Beam and Laser Beam Overlap

In order to ensure that the ion beam and laser beam were spatially overlapped within in the drift region, iris apertures controlled by linear motion manipulators (MDC 660010) are centered around the laser beam. The setup is shown in Figure 5.15. The 27 cm drift tube is shown in red from the vertical view with slots that allow the aperture plates to enter the ion/laser beam path. The linear manipulators are shown in blue, and the stainless steel aperture plates are shown in green. The view of the aperture plates is actually a front view, so that the reader can see the holes in the aperture plates. In reality, the plates fit into the slots indicated in the drift tube.

Details of the construction of the linear apertures are found in Section D.10. A drift tube was constructed from a 1.25" diameter 10.72" long stainless steel tube. Aperture plates were constructed and mechanically connected to the linear motion manipulators, but electrically isolated from the manipulators with polycarbonate washers. The modulation voltage is attached to the aperture plate. Each aperture plate has three holes horizontally offset from each other by 1 mm. The horizontal hole that let the laser power through over the widest vertical range was chosen. In this way, the correct horizontal spacing of the aperture could

be found to within 1 mm. Then the vertical position of the laser beam could be found by centering the manipulator hole on the laser beam. The detector signal was observed while raising and lowering the linear manipulator. The center of travel was set to the center of the laser beam. Using this method, the apertures were centered to the laser beam, and later the ion current was optimized by passing through these apertures. A simple function generator is used to drive the drift tube modulation, and the modulation voltage was measured with an oscilloscope.

5.8 Second Cylindrical Deflector

After traversing the overlap region, the ion beam is bent out of the overlap region by the second cylindrical bender and directed into the TOF mass spectrometer leg. The second cylindrical deflector is similar to the one diagrammed in Figure D.10 with the exception of the outer plate. In Figure D.10(c), two relief holes are illustrated. In the second cylindrical bender, only the 0.6" hole is retained, and the 1" hole is not included.

To collimate the ion beam, and optimize the size for mass spectrometer pulsing, another Einzel lens is used. The design of this Einzel lens is identical to the one shown in Figure D.8 with two exceptions. Four blind tap 4-40 holes were added to the exit of the Einzel lens. Additionally, the mount of the Einzel lens to the instrument follows a slightly different design. These two changes are illustrated in Figure D.14. The second Einzel lens is located directly after the second cylindrical bender and bellows, prior to the retractable Faraday cup.

A Faraday cup was designed and attached to a pneumatically controlled linear feedthrough (MDC 662006). By supplying between 60 and 80 psi of pressurized air and applying 120 VAC to the solenoid valve, the unit will insert the Faraday cup into the ion beam path and will measure the current of the ion beam passing through the apertures in the drift region. A cartoon overview of the setup of the retractable Faraday cup is shown in Figure 5.17. Design schematics for the second Faraday cup are found in Section D.12.

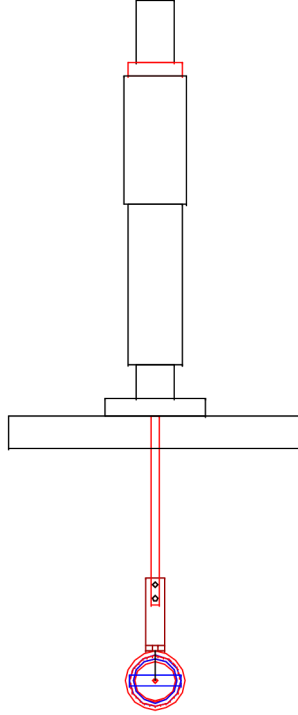


Figure 5.17: Schematic drawing of assembled pneumatic retractable Faraday cup.

5.9 Mass Spectrometer

Previous ion beam spectroscopists used a Wien velocity filter as a mass analyzer to identify the ion species and to optimize the ion current at a lower beam energy than that at which the spectroscopy was performed, [12,78,79] mainly because of the limited resolving power of a Wien filter. An example mass spectrum given by the DLASFIB Wien filter is shown in Figure 5.18. Due to the bulkiness required for suitable mass resolution, a Wien filter is seldom used as a mass analyzer by itself, but is often used in conjunction with other mass analyzers which require narrow velocity selection. [158] A linear time-of-flight mass spectrometer (TOFMS), however, has the resolving power to characterize the ion beam simultaneously with the spectroscopy.

Our linear TOFMS uses the well characterized beam modulation technique [149,150,159] to create an ion packet from a continuous ion beam. Initial attempts to theoretically describe the beam-modulation were only partially successful, because the theory [160] involved treating beams of homogeneous mass only. A first order theory [149] was eventually successfully created which describes the motion of ions, and explains the modulation technique, and allows for the description of the time-of-flight method. Essentially the cw beam passes through two deflector plates which initially deflect the beam away from the iris and detector. By quickly reversing the polarity of two plates held at equal but opposite polarity, the ion beam is swept across a $1/8''$ diameter aperture located near the detector. Two beam profilers aid in aligning the ion beam

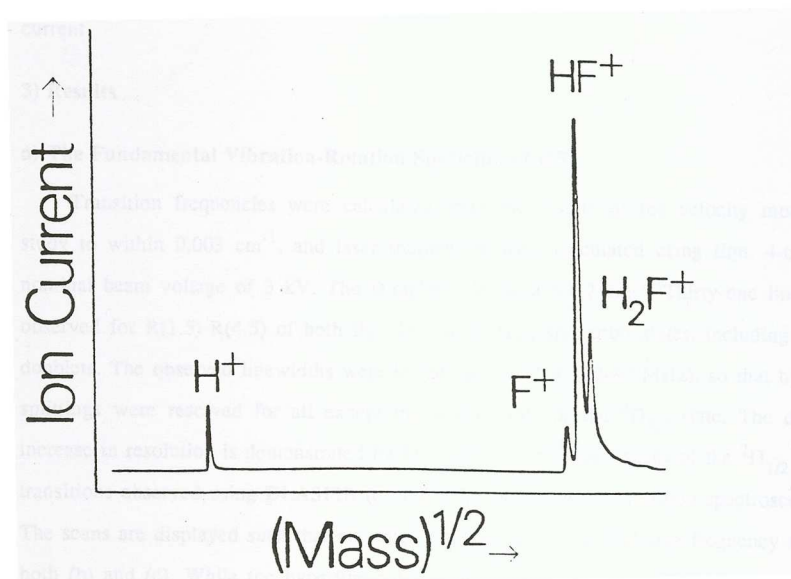


Figure 5.18: Example Wien filter mass spectrum from the DLASFIB instrument. [12]

through the 1.53 m drift tube and onto the electron multiplier detector. Some interesting aspects of the beam modulated time of flight method are that the mass resolution is independent of the mass and are proportional to the square of the flight length, and that there is no mass-dependent intensity discrimination. [149].

A schematic drawing of the pulsing plates in our mass spectrometer is shown in Figure 5.19. Five SHV-5 weldable feedthroughs were welded into a custom 8" CF nipple that was 5.75" long. An assembly of ion optics was inserted into the end closest to the cylindrical bender and 8" tee housing the second Faraday cup. The ion optics assembly consists of two pairs of plates, one vertical, and another horizontal with respect to the ion beam instrument. The horizontal assembly is closest to the cylindrical bender and the vertical plates were closest to the electron multiplier. Each ion optic plate was 1.075" long (along ion beam propagation) and 1" wide (transverse to ion beam propagation). The faces of each plate were separated by 0.5". Two orthogonal pairs of plates were designed to allow for steering, however the electrical connections to the horizontal plates (and/or) feedthroughs are grounded and cannot currently be used. Design schematics for the pulser assembly are found in Section D.13.

The pulse train is controlled by a digital delay generator (Quantum Composers QC-9518). The high voltage switching is accomplished with two pulse generators (Directed Energy PVX-4150). The pulse generators are powered by a bipolar 1 kV power supply (Gamma RMCRI -2PN/M. 2 mA). The delay generator creates a 500 Hz square wave with 0.001 s pulse widths between 0 and 5 volts. Channel A of the digital delay generator swings high at the start of the pulse and Channel B swings low. After 1 ms, the generator switches polarity, and Channel A swings low when Channel B swings high. One pulse generator is controlled

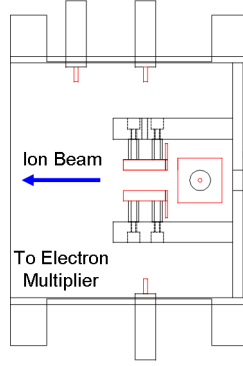
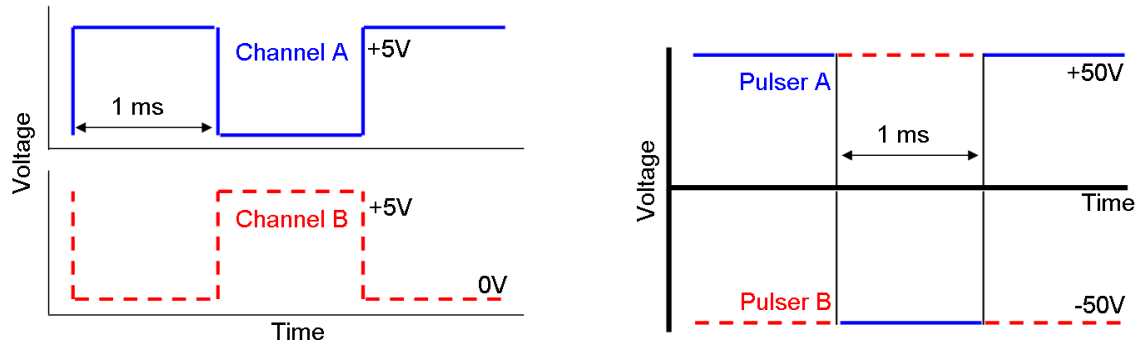


Figure 5.19: Schematic drawing of pulsing plates used to switch the cw ion beam into a pulse of ions, housed in an 8" CF nipple.



(a) Schematic of MS digital delay generator pulse train. Channel A is on top, in blue solid lines. Channel B is on the bottom in the red dashed lines.

(b) Schematic of MS pulse generator pulse train. Pulser A is the blue solid lines. Pulser B is the red dashed lines.

Figure 5.20: Schematic drawing of pulse trains.

by Channel A and the other is controlled by Channel B. Both pulse generators have \pm high voltage (HV) inputs, a trigger input, and a HV output. The outputs of the bipolar power supplies are split using SHV-5 splitters (Pasternack Enterprises PE9249) and input to the positive and negative inputs of the pulse generators. The outputs of the pulse generators are connected to the SHV feedthroughs and connected to the vertical plates of the MS pulser ion optic assembly.

The specifications for the delay generator indicate that the TTL rise time would be 3 ns, and that it should be able to drive a 50 Ω impedance. However, it was determined that the delay generator could not drive the pulse generator gate with the delay generator TTL pulse. Instead, the output was set to a variable value of 5 V. The specifications for the delay generator indicate that the rise time would be 25 ns (for 10V into 50 Ω). The specifications for the pulse generators indicate the gate rise time to be less than 20 ns. The rise and fall time of the output are specified to be less than 25 ns each.

For beam modulated time of flight mass spectrometry, the theoretical resolution for a pulsed time of

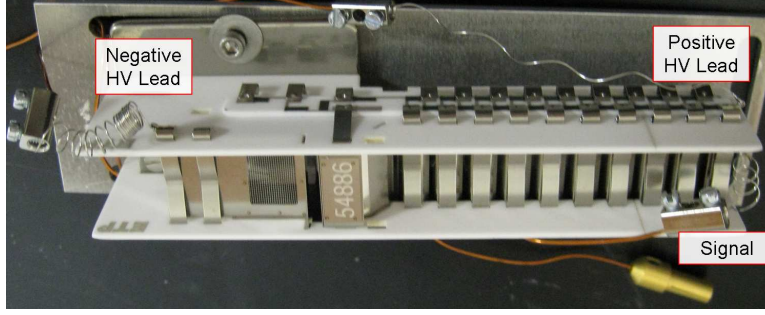


Figure 5.21: Photo of detector and plate assembly, with negative and positive high voltage leads, and signal lead.

flight instrument is given by [149]

$$\frac{M}{\Delta M} = \frac{L^2 V_0}{2DU(B+S)} \quad (5.2)$$

where L (1.44 m) is the drift length from the edge of the pulse plate to the iris over which the ions are swept, V_0 is the voltage between the plates (2×50 V), D is the separation of the plates (12.8 mm), U is the energy of the ion beam (4000 kV), S is the slit width (3 mm), and B is the size of the beam (5 mm). For the experimental parameters listed, the expected ion resolution would be 249. Design schematics for the MS iris are found in Section D.14. The iris was positioned approximately 3" before the electron multiplier. The electron multiplier (SGE Analytical Science -14820H S/N 54886) was housed inside of a 4.5" 4-way cross. The detector is connected to the flange with two home-built plates designed to center the ion beam onto the area of the detector, and to place the detector face in the center of the 4.5" cross with respect to the direction of ion beam travel. Design schematics for the detector assembly are found in Section D.15.

The detector and plate were assembled and electrical connections were made as pictured in Figure 5.21. The un-insulated detector leads were connected to Kapton (a vacuum safe insulation) coated wire, which connected to the feedthroughs on the CF flange. The negative high voltage (HV) lead is connected to a 1 mA power supply and biases the cathode. A positive HV lead is also available, but this would float the signal so normally this lead is grounded. The signal lead is connected to the BNC feedthrough. A fast non-inverting preamplifier with a gain of 200 is used on the output of the electron multiplier (VT120A Advanced Measurement Technology Inc/Ortec/Ametek).

Mass spectra were collected by using an externally 50Ω terminated 100 MHz digital oscilloscope (Tektronix DPO2014), where the time traces could be saved to a flash drive or computer. Figure 5.22(a) illustrates the original data taken from the oscilloscope in the time trace. A 166 ns time offset was subtracted from the measured time (t_{measured}) to account for the delay time of cables and the rise time of the pulsers ($t' = t_{\text{measured}} - 166\text{ns}$). The approximate beam velocity (v) was calculated using $v = d/t'$ and a distance (d)

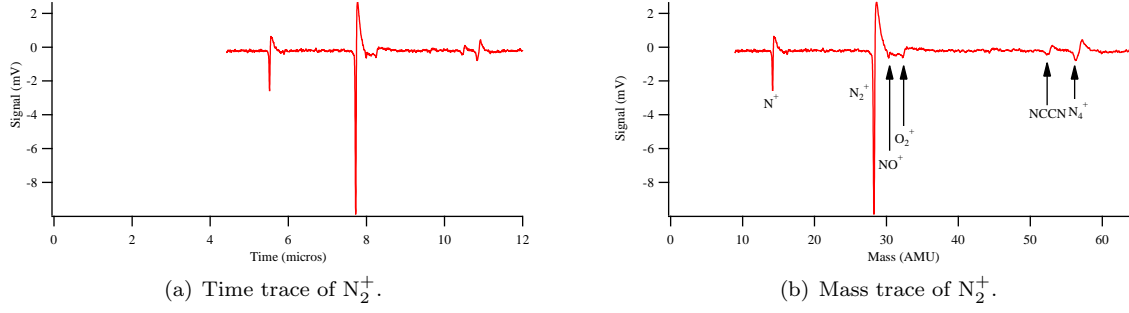


Figure 5.22: Example mass spectrum of a cathodic extraction of N_2^+ at 6 kV.

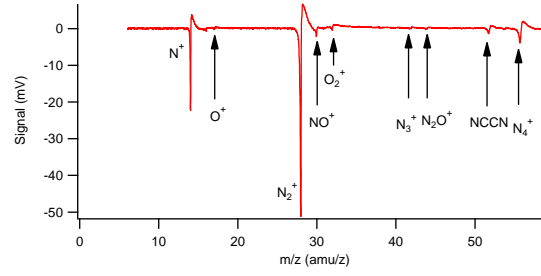


Figure 5.23: Example mass spectrum of a cathodic extraction of N_2^+ at 4 kV.

of 1.53 meters. The mass was then calculated using Equation 5.3 where q is the charge of an electron, V_{Beam} is the approximate beam voltage (5950 V for Figure 5.22 and 3840 for Figure 5.23), and N_A is Avogadro's number.

$$\left(\frac{m(\text{amu})}{z} \right) = \frac{2qV_{Beam}N_A 1000}{v^2} \quad (5.3)$$

The time trace can be fit to a Gaussian line shape in Igor

$$y_0 + Ae^{-\left(\frac{x-x_0}{width}\right)^2} \quad (5.4)$$

where x_0 is the center of the Gaussian, A is the amplitude prefactor for the Gaussian, y_0 is a vertical offset, and the $width=2\sigma^2$. Therefore, the $FWHM = 2\sqrt{\ln(2)}width$. By using Gaussian fits to each of the time arrival peaks, a central arrival time (x_0) and amplitude could be measured. The amplitudes could then be compared to determine the relative composition of the ion beam, as shown in Table 5.1.

Once the mass spectrometer was calibrated, it was possible to take single shots of mass spectra by detuning the Einzel lens and reducing the number of ions reaching the detector to the single ion regime. By collecting 200 separate mass spectra, and fitting a Gaussian to each time wave, the central time for 200

Species	Percentage of Beam
N ⁺	28.7
O ⁺	0.8
N ₂ ⁺	59.2
NO ⁺	2.4
O ₂ ⁺	1.1
N ₃ ⁺	0.3
N ₂ O ⁺	0.4
NCCN	2.0
N ₄ ⁺	5.1

Table 5.1: Percentage species within N₂⁺ ion beam.

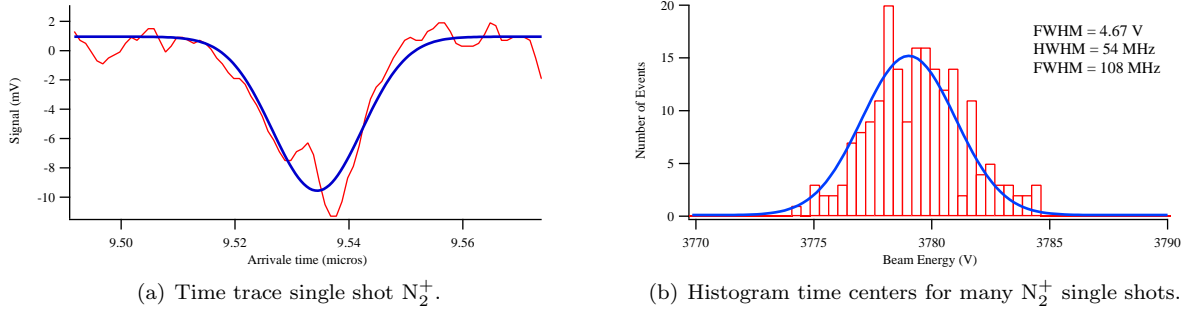


Figure 5.24: Single shot measurements of many single ion events were used to create a histogram to measure the beam energy spread of the ion beam.

single-ion events were recorded, illustrated in Figure 5.24. Given the mass of the species, Equation 5.3 can be solved for the beam energy (V_{Beam}) from the central arrival time. A histogram of the beam energies could then be produced, and a FWHM of the histogram measures the beam energy spread of the ion beam. In this case, the FWHM was 4.77 V. The effect of the beam voltage on the observed ion transition is described in Section 5.12. The effect of the beam energy spread on the linewidth can be obtained by differentiating the value of the Doppler shift (Equation 5.9) with respect to voltage and solving for $\delta\nu$. Calculating the expected linewidth from the approximation of the Doppler shift (Equation 5.9) is accurate to within 60 KHz compared to if the actual value of the Doppler shift (Equation 5.10).

$$\delta\nu \approx \frac{\nu_0 \delta V}{2} \sqrt{\frac{2q}{VMc^2}} \quad (5.5)$$

Mass spectroscopists generally compare the resolving power ($m/\Delta m$) as the figure of merit for mass spectrometers. The resolution of time of flight measurements for species shown in Figure 5.23 are shown in Table 5.2. Some values of the resolving power of spectra taken with the Wien filter (see Figure 5.18) of the Saykally DLASFIB instrument are also included. One will note that the resolution of the time of flight spectrometer is an order of magnitude higher, despite the fact that the TOFMS was operated at full beam

Species	Mass (amu)	Width (amu)	m/ Δ m	Source
N ⁺	14	0.0423	331	Illinois
N ₂ ⁺	28	0.0714	392	Illinois
N ₄ ⁺	56	0.1881	298	Illinois
F ⁺	19	—	30	Berkeley
HF ⁺	20	—	36	Berkeley

Table 5.2: Resolving power of beam modulated time of flight mass spectrometer (Illinois) compared to a Wien filter (Berkeley).

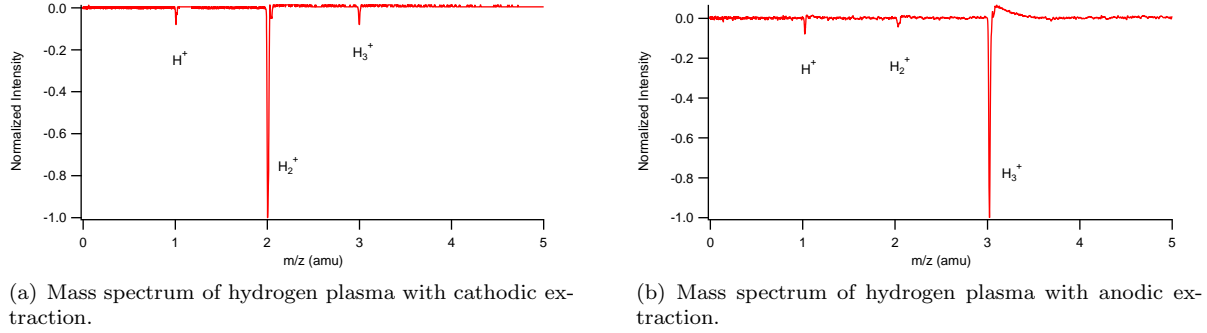


Figure 5.25: Hydrogen plasma reveals different source behavior for anodic and cathodic extraction.

voltage.

With a fully characterized time of flight mass spectrometer, investigation of source behavior was investigated. As a performance check, hydrogen gas was discharged and an ion beam from a hydrogenic plasma was extracted from the cathode. A time-of-flight analysis revealed that only H₂⁺ was being formed. This was highly interesting because the H₂⁺ protonation reaction



is a fast reaction, known to occur with almost every collision to produce H₃⁺. [161]

The charge of the species contributes to the reactivity. For instance the recombination rate of H₂⁺ with an electron is $7 \times 10^{-9} \text{ cm}^3/\text{s}$, [162,163] while the protonation reaction has a reaction rate of $2 \times 10^{-9} \text{ cm}^3/\text{s}$, [164] which is a factor of 3.5 smaller. The fast reaction rate for the protonation (compared to neutral-neutral reactions) is due to the charge-induced dipole attraction which has no activation barrier. Therefore, a mass spectrum of pure H₂⁺ indicated that no collisions were occurring with the cathodic extraction. The fact that a cathodic extraction would produce mostly electron impact ions is consistent with results obtained earlier. [79] However, for a 3:1 H₂ to N₂ gas mixture, the resulting HN₂⁺ beam was found to be strongest under an anodic extraction. [79] The strongest ion beam for a pure N₂ discharge results from a cathodic extraction. Example spectra of the hydrogenic plasmas are found in Figure 5.25.

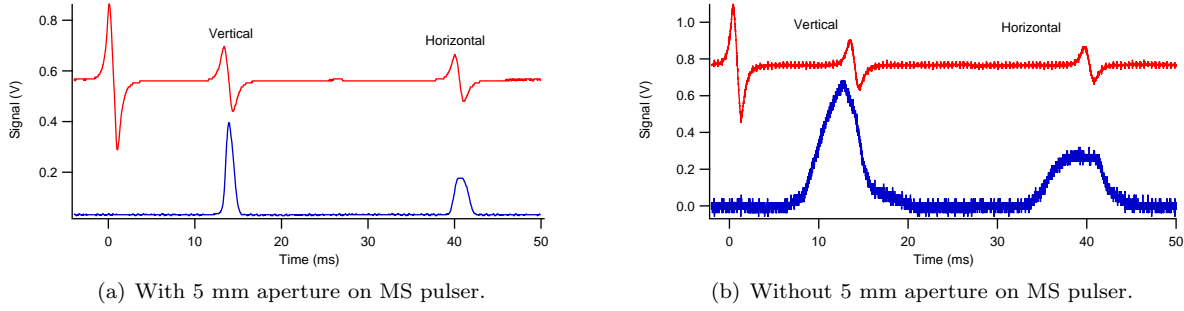


Figure 5.26: Beam profile monitor traces for ion beam at ~ 4 kV beam voltage on the bottom, fiducial traces on the top. The extra noise without the aperture is a function of a different BPM being used, rather than the state of the aperture. The width of the ion beam, however, is much larger in graph b.

5.10 Beam Profile Monitors

Commercially available beam profile monitors (BPM) work by scanning a molybdenum wire through the path of an ion beam and collecting the subsequent secondary electron emission. Magnets located on the rotating spindle are used to produce a reference signal (fiducial) when the wire passes through the vertical and horizontal parts of the beam. By comparing the secondary electron signal as a function of time with the fiducial time, the position of the ion beam with respect to the center of the CF tube can be determined.

As the center of the mass spectrometer electron multiplier was radially centered in the CF tubes, in order for the electron multiplier to see a signal, the un-deflected ion beam should pass through the radial center near the detector. In order to aid in alignment, the beam profile monitors were used to adjust the cylindrical deflectors and center the ion signal on the fiducial (reference) produced by the beam profile monitors.

Figure 5.26 demonstrates several traces of the BPM output on the oscilloscope. The center of the signal in the vertical and horizontal positions is shown by the fiducial trace. The ion beam is centered in those directions when the center of the BPM trace is near the center of the fiducial trace. There will be a large vertical offset on the BPM signals if the ion beam is hitting the side of BPM collector, or if the ion beam is over/defocused.

5.11 Brewster Windows

From previous, unpublished ion beam experiments attempting cavity ring-down spectroscopy, it was determined that fast neutrals produced by interactions with the residual background ground gas were formed. [84] The neutrals are unaffected by the ion optics, and can smash into and damage the ring-down mirrors. It was decided that for the cavity enhanced and NICE-OHMS spectroscopy, only a medium Finesse cavity would be formed by spoiling the cavity with either Brewster windows, or anti-reflection (AR) coated windows, as



Figure 5.27: Schematic illustrating vertical offset due to Brewster windows.

these would be less likely than ring-down mirrors to be damaged, and are not as costly to replace. However, it was determined that placing planar AR coated windows within the cavity caused an etalon effect which interfered with locking to the cavity, so Brewster windows were used instead. While several groups separate back-reflections from cavities from the incident beams using circularly polarized light with a quarter wave plate (QWP) and polarizing beam splitter (PBS) pair, the use of a Brewster window requires p-polarized light. Therefore, no QWP/PBS pair could be used, and instead a simple beam splitter catches a portion of the back-reflection and reflects it to a detector.

Eventually, mid-IR light will be used, therefore Brewster windows made from IR transmissive CaF_2 were designed. The index of refraction of CaF_2 at mid-IR wavelengths is nominally 1.43. Brewster's angle (θ_B) is given by $\theta_B = \arctan(n_2/n_1)$ where n_2 and n_1 are indices of refraction for CaF_2 and air/vacuum respectively. For CaF_2 , Brewster's angle was 54.8° and the complimentary angle was 35.2° . The SCS machine shop was able to machine the angle to within 0.1 of a degree. A schematic for the Brewster window holder is shown in Figure D.19. Un-coated CaF_2 windows were obtained (Thorlabs WG51050 1" diameter - 5 mm thick) and glued onto the window holders using 5 minute epoxy. The optical thickness of the windows offsets the laser beam from its incoming trajectory. As the light that approaches the cavity is vertically polarized, the correct geometry of the windows for p-polarized light is either reflecting up or down, inducing a vertical offset. Usually the best configuration for the ion beam is to have the windows pointing up, which lowers the laser beam inside of the cavity. This means that the instrument does not have to be lifted up as far. However, some amount of light is still lost, which is reflected upwards. The user, therefore, must be careful to block this reflection for eye safety.

5.12 Spectroscopic Applications

The ion beam is accelerated to the energy of the float voltage (V), and the potential energy of the ions is converted to kinetic energy $qV = 1/2Mv^2$ (where q is the charge of an electron, M is the mass of an ion and v is the velocity of the accelerated ion) such that $v = \sqrt{2qV/M}$. When the ions are created at a high potential, there is still a thermal spread of velocities produced within the plasma, which can be

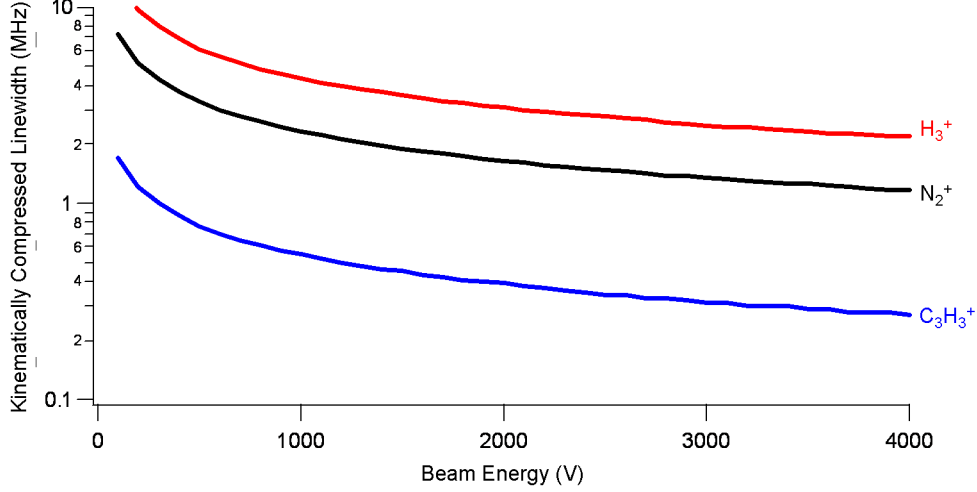


Figure 5.28: Graph illustrating the fast ion beam kinematic compression.

approximated by the Boltzmann spread, $\frac{\nu_0}{c} \sqrt{\frac{2kT}{M}}$. When the ions are accelerated, the absolute energy of the ions is increased, but the spread remains constant. [165] By adding the energy of the ion beam to the average velocity, the observed spectroscopic linewidth is decreased by the factor $\sqrt{\frac{kT}{4qV}}$ shown in Equation 5.7, [51] where ν_0 is the original frequency, k is Boltzmann's constant and T is the temperature of ions in the plasma. Inspection of Equation 5.7 shows that for a given T and V , the line width will decrease with increasing mass of ions. Further, for a given M and T , the line width will decrease most dramatically with beam voltage (V) for the first 1000 V of beam energy, and only minimally after that. A graph of the simulated kinematically compressed linewidth for H_3^+ , N_2^+ and C_3H_3^+ at $T=1000$, 600, and 1000 K, respectively, are shown in Figure 5.28. For the test molecule N_2^+ , the minimum linewidth due to kinematic compression would be 1, 1.2 or 1.7 MHz for a 6, 4 or 2 kV beam respectively. These values are all safely above the minimum transit time limited linewidth values of 100, 80, and 70 kHz for a 27 cm overlap, where the transform limited linewidth is given by Equation 5.8. The kinematic compression linewidth is also smaller than the observed spectroscopic line width as discussed in Section 6.2.

$$\delta\nu_{Kinematic}(\text{Hz}) = \frac{\nu_0}{c} \sqrt{\frac{kT}{4qV}} \sqrt{\frac{2kT}{M}} \quad (5.7)$$

$$\delta\nu_{Transform}(\text{Hz}) = \frac{1}{2\pi L} \sqrt{\frac{2qV}{M}} \quad (5.8)$$

Once the laser was made collinear with the ion beam, spectroscopy could be performed. Due to the increased velocity of an ion beam, the observed frequency transitions will occur with a Doppler shift dependent

on the velocity. Saykally's group used the approximation [6]

$$\frac{\nu'}{\nu_0} \approx 1 \pm \frac{v}{c} \quad (5.9)$$

which is only accurate to 50 MHz at this frequency to the true values. The sub-MHz accuracy of frequency determination using the frequency comb requires that Equation 5.10 be used instead, [6]

$$\frac{\nu'}{\nu_0} = \sqrt{\frac{1 \mp v/c}{1 \pm v/c}} \quad (5.10)$$

where ν' is the Doppler shifted frequency, ν_0 is the rest frequency, and v is the velocity of the ions, given by

$$v = \sqrt{\frac{2qV'}{M}} \quad (5.11)$$

Chapter 6

N_2^+ in the Ion Beam

The initial proof of concept system studied with this instrument was the fundamental band of the $A^2\Pi_u - X^2\Sigma_g^+$ system of N_2^+ . N_2^+ is an important species in atmospheric aurorae and electrical nitrogen discharges. [82] Several bands were observed in auroral storms by Meinel in 1950 [166], [167], and the 1–0 band was recorded in the laboratory by Benesh et al. in 1979 with a resolution of 1800 MHz. [168] The frequencies of many of the transitions in the fundamental band of this system have been measured at the Doppler-limit to 60 MHz precision and 150 MHz accuracy. [82] These studies all relied on unmodulated sources, either DC positive column discharges or hollow cathodes. Other workers investigated higher vibrational levels by using velocity modulation [169], [170], [171]. Additionally, N_2^+ is a fairly simple molecule to produce in a plasma discharge and the mass spectrum of our ion beam has been previously shown to contain mostly N_2^+ and N^+ (see Section 5.9). Thus N_2^+ served as an easily understood benchmark of the capabilities of our fast ion beam spectrometer.

As discussed in the introduction, recent results with cavity enhanced (cavity enhanced absorption or NICE-OHMS spectroscopy) velocity modulation show some ion/neutral discrimination when the VMS is demodulated at twice the modulation frequency (2f). This is done by choosing a plasma-frequency demodulation phase that minimizes the neutral signal. An example of the ion neutral discrimination is shown in Figure 6.1, where a five-fold enhancement in the strength of the neutral signal is still apparent. [20] The lock-in phase necessary to minimize neutral absorption is dependent on the modulation frequency and the pressure of the cell. It is also possible that multiple neutral absorbing species will have different plasma phase separations. While there is definitely an ion/neutral discrimination, it is not a rigorous discrimination. Additionally, as the introduction pointed out, plasma discharge asymmetries and charge exchange reactions remove the rigorous ion/neutral discrimination in traditional (1f) demodulation VMS.

These initial results with N_2^+ in an ion beam showcase the ability of an ion beam to have rigorous ion/neutral discrimination. This is because, instead of merely modulating a plasma, the fast ion beam of ions is velocity modulated. As the fast ion beam is spatially separated from the background neutrals, there is a rigorous ion/neutral discrimination. As continuous wave and pulsed supersonic expansion discharge

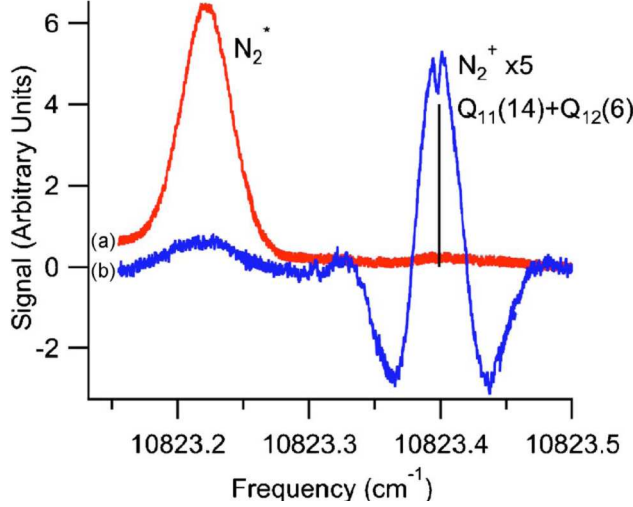


Figure 6.1: Spectroscopic signal of N_2^+ (blue) and N_2^* (red) of a positive column using cavity enhanced velocity modulation. [13]

experiments do not provide any ion/neutral discrimination, often absorption spectra are complicated by interfering neutrals, excited radicals and Rydberg neutrals. Using a spatial separation with a fast ion beam, and velocity modulation, gives rigorous ion/neutral discrimination against neutral absorbing species. These results also highlight the mass identifying capability of every line in the spectroscopy, which will remove the ambiguity of the contributing species discussed in Chapter 1.

6.1 Daily Experimental Procedure

The instrumental setup has been described in Chapters 2, 3, 4, and 5. Daily experimental preparation consisted of: warming up the wavemeter, maximizing the laser power, aligning the ion beam apertures to the laser cavity, having the ion beam instrument under vacuum, turning on the source and maximizing ion current through the laser apertures. The laser was then scanned across the expected line positions, and the dispersion signal was recorded. The remainder of this section represents a step-by-step guide to daily operation.

Step 1. Turn on the wavemeter, and allow for a 30 minute warm-up period before spectroscopic wavelength measurements are made.

Step 2. Peak the Ti:Sapphire power daily by adjusting M1, M3, M4, flashing and peaking the thick etalon, and weekly by checking the reference cell alignment.

Step 3. Lock the Ti:Sapphire to the correct wavelength. Begin by scanning the BiFi and reading the wavelength on the wavemeter. Position the BiFi in the center of a mode closest to the wavelength of interest.

Perform a thin etalon scan and use the wavemeter to position the thin etalon motor position closest to the wavelength of interest. “Set” the parabola position near the bottom of the parabola of the thin etalon reflux; the piezo-etalon control (PZETL) should now be active. Engage the reference thin etalon control. Set the slow piezo lockpoint at 0.35 and engage the lock control. Slowly decrease the slow piezo lock-point (while monitoring the lock) to 0.2 in 0.01 increments.

Step 4. Once the laser is locked to the reference cell at the wavelength of interest, the apertures inside the ion beam can be centered to the laser beam. The apertures are horizontally aligned with the laser by choosing the hole that allows the longest vertical travel of the linear manipulators without spoiling the cavity finesse. The apertures are aligned vertically by centering the transmission of the aperture on the laser beam. The height was approximately 39 mm for manipulator 1 and 41 mm for manipulator 2.

Step 5. Ensure the ion source is in good operating condition. Once the ion current extracted from the source begins falling off, or once the source begins arcing during operation, the source will need to be regenerated. If the source has been open to atmosphere for some time, the source will also need to be replaced. Often source maintenance will involve vapor-blasting the source ferrule, cap, and extraction plate in the SCS machine shop, while replacing the fused silica tube and silicone O-rings. Sometimes the metal mesh needs to be replaced. The source is reassembled by connecting the back electrode to the plastic gas inlet tube on the 1/4” side, and to the fused silica tube on the 3/8” side. The aluminum cap is then screwed onto the PEEK source holder and holds the back electrode in place. The front electrode, with vapor-blasted ferrule and cap, is then connected to the end of the glass tube. The vapor-blasted extraction plate is replaced. The electrical connection to the back electrode is made by screwing the connection into the aluminum cap. If the source is to be used in the anodic extraction, the water cooling adapter is also screwed into the aluminum cap and the water cooling cold sink is connected to the adapter. The source is positioned between 1/4” to 1/2” away from the extraction plate and the PMMA window of the source chamber is replaced.

Step 6. Starting the turbo pumps: Once all vacuum connections are closed (including checking the vents on the two 550 L/s pumps, source chamber vent butterfly valve, source window, and gas-inlet Ultra-Torr connection), the butterfly valves connecting the forevacuum to the 2000 L/s turbo, and two turbo pumps can be opened. Once the chamber pressure reads less than one Torr on the digital thermocouple gauge (KJL610, Figure 5.3), the turbo pumps may be started, but it is safest to wait until the pressure is less than 300 mTorr to make sure no connection is open or loose (the biggest culprit is often the Ultratorr where the nitrogen gas is supplied on the outside of the instrument). The cooling water to all four turbo pumps should be running before the turbo pumps are started. Once the vacuum chamber pressure is below 300 mTorr with the rough pumps, the 2000 L/s pump can be turned on. Normally the pump is left in the “on” position,

but the pump is stopped. The pump is engaged by pressing the green start button. The start-up time for the 550 L/s pumps is about 1/3 of that of the 2000 L/s pump, so waiting 2-3 minutes before turning them on is recommended. The 550 L/s pumps can be turned on by pressing their respective “start” buttons. It takes 7-8 minutes before all turbos have spun up. If the system has been open for longer than 30 minutes, it is generally helpful to leave the system under turbo vacuum for several hours to remove the residual water adsorbed to the chamber walls. It is helpful during this “cleaning” stage to degas the ion gauges. The Hornet can be degassed independently, but only one of the ion gauges controlled by the KJL6600C ion gauge controller can be degassed at a time. Degassing involves heating the element to remove the water from the element, leading to a more accurate pressure reading. By monitoring the base pressure of the chamber over time, one can see when the rate of pressure decrease starts to level out, indicating either a leak or that base pressure is attained, dependent on the absolute levels attained. (For comparison, see the example pressures indicated in Section 5.2).

Step 7. Ion beam optimization: Once the system has reached vacuum base pressure, the source can be ignited. The leak valve is opened until the convection gauge reads about 500 mTorr of N₂. The float power supply is turned on and the high voltage is enabled. (Usually the float voltage is only turned down when necessary). The discharge power supply is turned on and the high voltage is enabled at 3.5 kV. The pressure is slowly increased. Usually between 1 and 3 Torr, depending on the size (and age) of the source aperture, the source will ignite. The discharge power supply can be turned down to 2 kV, but the effect of the discharge voltage on the spectroscopic results has not been investigated, and most spectra were obtained at 3.5 kV. Most of the previous cold cathode experiments with an ion beam used a 3.5 kV discharge voltage. [79]

For N₂⁺, the highest ion current was observed with a cathodic extraction. In this configuration, the plasma was a dim purple, and the ions are mostly created by electron impact. Usually the lowest pressure extended the lifetime of the source. With the first cylindrical bender unbiased, the picoammeter could be physically connected to the first Faraday cup. It is **essential** that the picoammeter be off when connections to the ammeter are changed, otherwise the high voltage possibly built up on Faraday cups will damage the ammeter, requiring costly re-calibration. The ion optics for the steerers should then be set to 0 V, so that minimal deflection is occurring. Then the source, mounted on the ISO-F-250 flange at the back of the source chamber, can be translated horizontally and vertically to maximum the ion current. The picoammeter (after being turned off) can be connected to the second, retractable Faraday cup. The current on the Faraday cup was maximized by changing the voltages of bender 1 and 2, the vertical and horizontal steerers, and Einzel lens 1 iteratively until the current was maximized. Ideally, the current should be larger than 1 μ A passing through the apertures at 4 kV beam energy, greater than 0.7 μ A at 2kV beam energy, and greater than 2

μA at 6 kV beam energy.

Once the ions are collinear to the laser, the laser is locked near an absorption/dispersion feature, a voltage modulation signal is provided to the drift tube, and the detectors and lock-in amplifiers are set up as described in Chapter 4, the program can be scanned over the expected absorption features.

6.2 Data Analysis

Data analysis was performed using an Igor procedure file included and annotated in Appendix E. The program reads in all the columns of data, names the columns with a description of the wave and a user-supplied suffix (often the same as the scan number). Figure 6.2(a) displays the raw data as recorded by the LabVIEW program. The Igor program then multiplies the data by a user defined scaling value dependent on the sensitivity of the lock-in amplifier. The scaling factor is equal to the sensitivity (often $50 \mu\text{V}$) setting divided by 10. Figure 6.2(b) shows the spectrum multiplied by the scaling value.

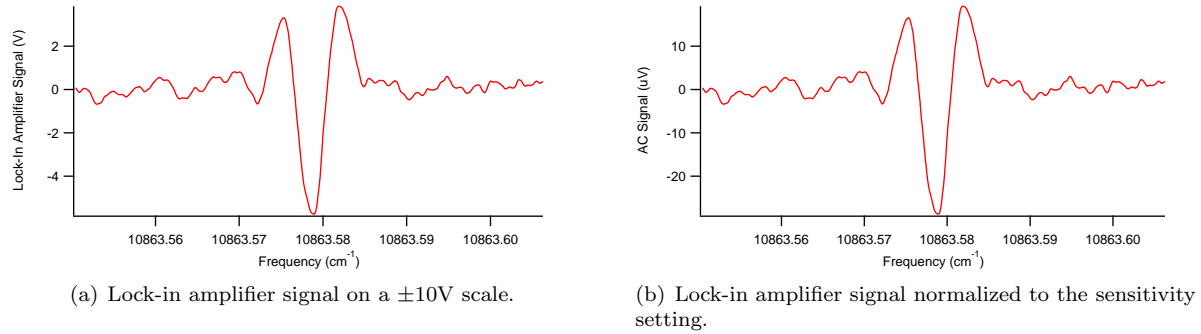


Figure 6.2: Example spectroscopic signal of N_2^+ with 2 kV beam voltage.

The DC level of the detector is plotted in Figure 6.3(a) with a quartic polynomial fit to smooth out the noise. The DC level of the detector can be converted to the maximum AC level using Equation 6.1 and is shown in Figure 6.3(b).

$$AC_{Voltage, MAX} = \frac{DC G_{RF} G_{AC}}{G_{DC}} \quad (6.1)$$

where the measured RF gain (G_{RF}) was 7.798, the measured DC gain (G_{DC}) was 8077 V/A, and the measured AC gain (G_{AC}) was 20668 V/A (see Section 4.7). (G_{RF}) can be estimated using Equation 6.2 where L_{Mixer} is the insertion loss of the mixer (2.317), L_{PS} is the insertion loss of the power splitter (1.496), RF_{Amp} is the gain of the RF amplifier (25.704), and L_{Att} is the 10 dB attenuator used before the RF amplifier which was not always used. The RF gain (without the 10 dB attenuator) was measured to be 7.798, fairly

close to the estimated gain value of 7.413. The 10 dB attenuator is expected to reduce the measured gain by a factor of 3.162 to 2.466.

$$RF_{Gain} = \frac{RF_{Amp}}{L_{PS}L_{Mixer}(L_{Att})} \quad (6.2)$$

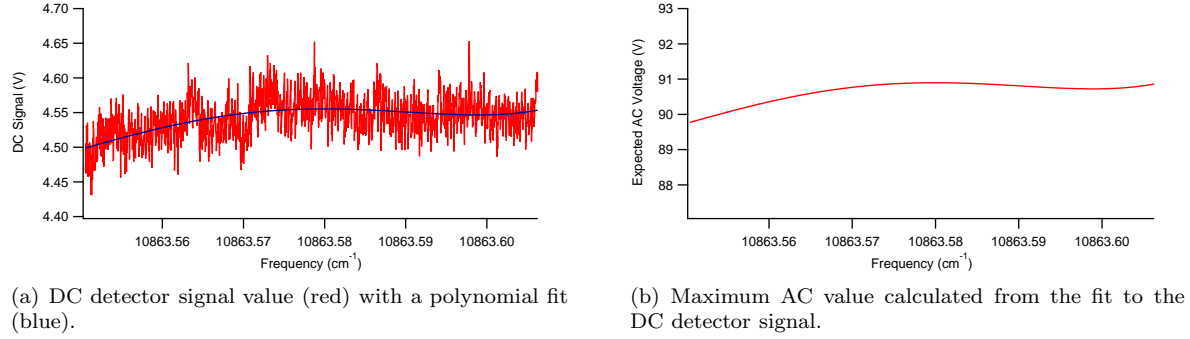


Figure 6.3: Example spectroscopic signal detector DC baseline and corresponding AC signal.

The fractional signal can be calculated by dividing the actual voltage observed (Figure 6.2)(b) by the maximum AC signal (Figure 6.3(b)). Figure 6.4a shows the observed fractional signal. Figure 6.4b shows the observed fractional signal with the location of the velocity modulated signal splittings.

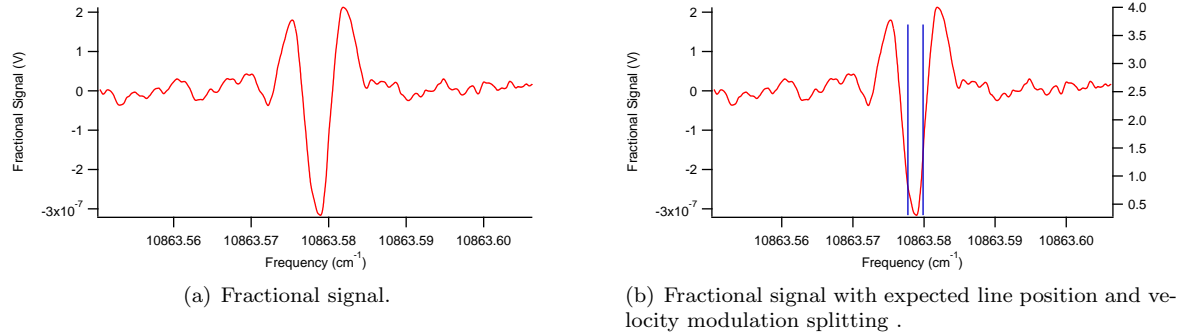


Figure 6.4: Example spectroscopic fractional signal of N₂⁺ with 2 kV beam voltage.

The current of the ion beam passing through the linear apertures is plotted in Figure 6.5 with a quartic polynomial fit to smooth out the noise. The ion density probed by the laser beam was calculated using Equation 6.3, where I_{Avg} is the average current during the scan in μA , q is the charge of an electron, r is the radius of the apertures (0.0015 m), and V_{Beam} is the energy of the ion beam. For the graph shown in Figure 6.5, the average ion current was 0.7 μA with a beam energy of 1985 V, which produces an ion density of 1×10^7 ions/cm⁻³. In order to compare the current we receive with other experiments, it is helpful to compare the same source type, the same molecule, and the same instrumental layout. Unfortunately there is little overlap between the two instruments. The first DLASFIB instrument used two bending elements

before the current was measured, while the source was a hot filament source with HF^+ being produced. The second DLASFIB instrument had the source collinear to the laser, and only one bending element was used after the drift region, with a cold cathode producing HN_2^+ , HCO^+ and NH_4^+ . Additionally, for these iterations, the Faraday cup design was incorrect, and the currents measured were at least 30% too high. However they quote their ion density to be $1 \times 10^7 \text{ ion cm}^{-3}$ for HN_2^+ . With the use of cavity enhanced spectroscopies, and the future use of supersonic expansions, it is not possible to place the source directly inline with the laser. Ultimately, the emittance of the ion source will limit the ion density of ions probed.

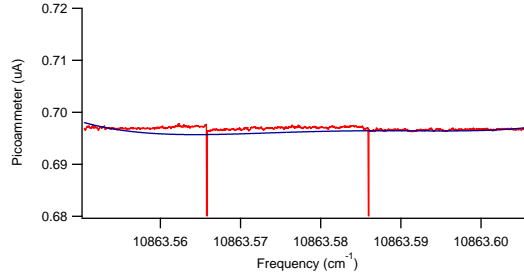


Figure 6.5: Example picoammeter readings N_2^+ at 2 kV.

$$\text{IonDensity} = \frac{I_{Avg}}{1 \times 10^6 q (\pi r^2) v} \quad (6.3)$$

For several float voltages, the average ion current passing through the apertures during a scan was calculated. The results of the ion current are shown in Figure 6.6(a). Using Equation 6.3, the ion density was calculated and is plotted in Figure 6.6(b).

The maximum space charge limited ion current which can be extracted from a diode system (parallel plates, formed between the extraction plate and the source) can be estimated by the Child's/Langmuir Equation (6.4), where J is the current density (A/mm^2), M is the mass of the ion (kg) and d is the separation between the plates (mm). [172, 173]

$$J = \frac{4\epsilon_0}{9} \sqrt{\frac{2q}{M}} \frac{V^{1.5}}{d^2} \quad (6.4)$$

Applied to the ion beam, the Child's equation estimates the maximum current that can be extracted out of the source and through the extractor plate. When the ion beam is vignettted through the irises used to make the laser beam and ion beam collinear, only a fraction of the the extracted current will be retained, and the extracted current is now proportional to the extraction voltage.

$$I = kV^{1.5} \quad (6.5)$$

For Figure 6.6, a generic fit following Equation 6.5 is used to illustrate that the current increases with float voltage as $V^{1.5}$ (Figure 6.6(a)). Because the velocity decreases as $V^{0.5}$, the overall density should increase linearly with V , which is shown experimentally in Figure 6.6(b).

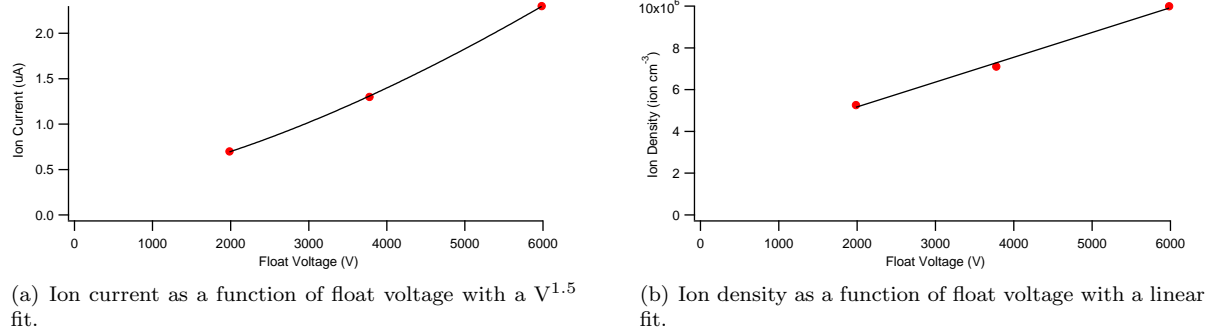


Figure 6.6: Example ion current and ion density of N_2^+ as a function of beam voltage.

For three different float voltages, the data were fit to the expected line shape function (See Equation 4.13 in Section 4.6), and the full width at half maximum (FWHM) was determined. The results for the line width are shown in Figure 6.7(a). The equation for the linewidth as a function of the energy spread of the ion beam is found in Equation 6.6, where ν_0 is the rest frequency, $\delta\nu$ is the line width, and ΔV is the voltage spread. This equation can be rearranged for ΔV as shown in Equation 6.7 and used to calculate ΔV from the $\delta\nu$ as plotted in Figure 6.7(b). While neither Equations 6.6 nor 6.7 are linear functions, over the voltage range of 2-6 kV they are fairly linear. A linear regression of $\sqrt{1/V}$ (Equation 6.6) over the 2-6 kV range has a correlation coefficient of 0.94, and a linear regression of \sqrt{V} (Equation 6.7) over the 2-6 kV range has a correlation coefficient of 0.99. The slope of the linear regression of the points in Figure 6.7(b) gives the float voltage uncertainty as a percentage of the beam voltage. The measured slope is 0.133%. This value is much higher than the static voltage regulation specified for the power supply (0.005% + 0.5 mV/mA). The specified voltage uncertainty corresponds to less than 1 V for the 15 kV power supply at 2 mA. The specified voltage ripple for the power supply was less than 0.02% of the rated voltage + 0.3 V, which amounted to 3 V at maximum output. As the observed beam energy spread was larger than the power supplies rated ripple and stability, the increase in beam energy spread and linewidth cannot be attributed to the power supply.

$$\frac{\delta\nu}{\nu_0} = \frac{\Delta V}{2} \sqrt{\frac{2q}{VMc^2}} \quad (6.6)$$

$$\Delta V = \frac{2\delta\nu}{\nu_0} \sqrt{\frac{VMc^2}{2q}} \quad (6.7)$$

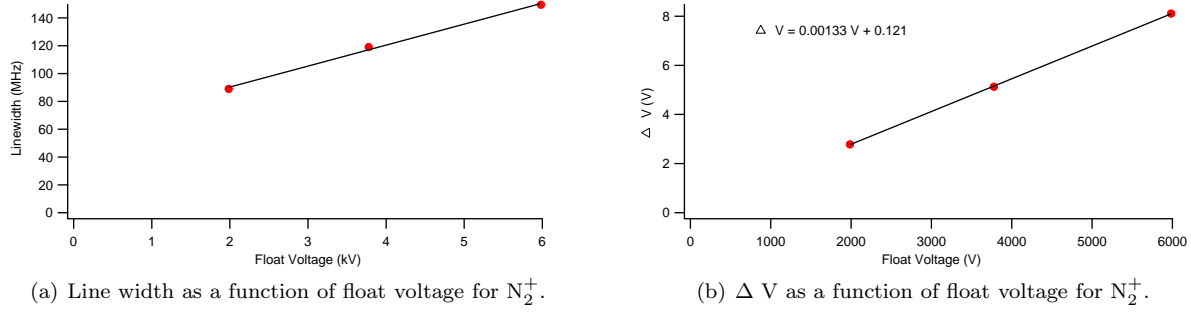


Figure 6.7: Linewidth and ΔV as a function of float voltage.

Further support of this hypothesis is shown in Figure 6.8. A voltage divider was used to measure the output beam voltage with a Keithley source meter. Although the ultimate accuracy of this method is not very high, the relative precision of the measurements should be quite good. Figure 6.8(a) contains the raw data multiplied by 1000. Once the average beam voltage is subtracted out (Figure 6.8(b)), a measure of the ripple of the power supply could be measured. The peak to peak variation of the residual was 0.9 Volts with a standard deviation of 0.11 V. Therefore, it is quite unlikely that power supply variations are leading to the beam energy spread. Instead it is possible that the penetration of the ground voltage from the extraction plate into the cathode aperture is a complex function of the beam voltage, as illustrated in Figure 1.4. The width of the extraction sheath depends on the float voltage, a result consistent with the work of other ion beam experiments. [12, 174]

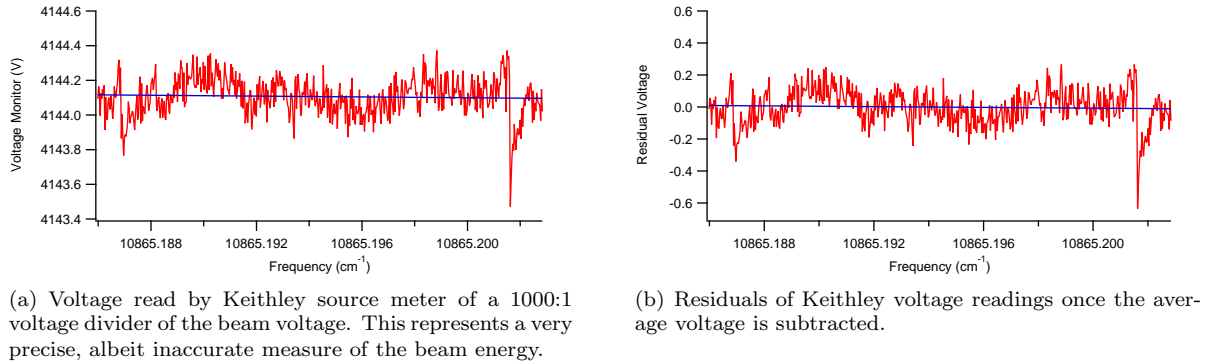


Figure 6.8: Beam voltage monitor read by Keithley source meter.

6.3 Doppler Split Examples

As described in Section 4.6, both absorption and dispersion can be present and can be observed by using two RF mixers referenced 90° out of phase to one another. Figure 6.9 illustrates the fractional signal coming

from the two lock-in simplifiers demodulating the different phases. The lock-in time-constants are the same, however the digital lock-in has a higher filter slope, which removes more of the noise. The graph shows that the signal is mostly confined to the first (digital) lock-in amplifier.

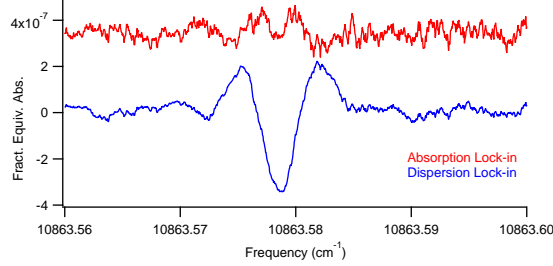


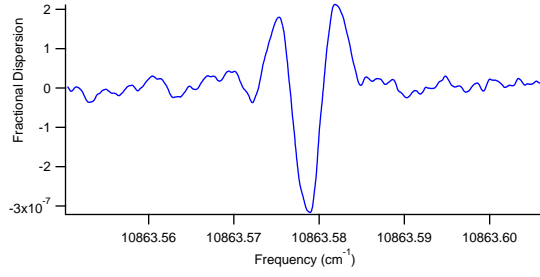
Figure 6.9: Spectroscopic data of both lock-in amplifiers. Top trace (red) digital lock-in amplifier, bottom trace (blue) analog lock-in amplifier.

The experimental line shapes are in line with the expected line shape function discussed in Chapter 4 as Equation 4.13. In order to verify that only dispersion is observed, attempts to fit the data to the full NICE-OHMS signal (velocity modulated dispersion and absorption) were made with Equation 6.8 with the line center, ν_{fm} , and ν_{vm} fixed. Figure 6.10(a) shows the raw data. Only Gaussian type line shapes were used, as previous ion beam experiments indicate the line shapes are primarily Gaussian in nature. [78] Figure 6.10b shows a fit with θ_{fm} floating. Figures 6.10(c) and (d) show fits with θ_{fm} set to the dispersion and absorption phase, respectively. The FWHM of the fits in graphs b and c were allowed to float, however when an absorption fit was attempted the FWHM ballooned to 160 MHz. The fit was still bad. Therefore, the absorption has been considered fully saturated and unobserved, and the observed spectrum is believed to be dispersion.

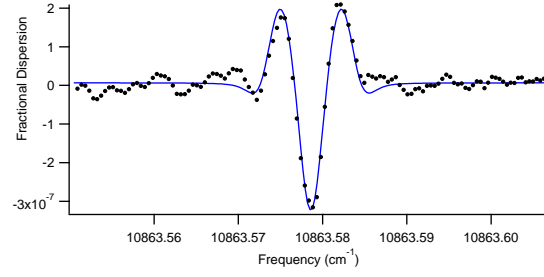
$$\begin{aligned}
& [\chi^{disp}(\nu_d - \nu_{fm} - \nu_{vm}) - 2\chi^{disp}(\nu_d - \nu_{vm}) + \chi^{disp}(\nu_d + \nu_{fm} - \nu_{vm}) \\
& - \chi^{disp}(\nu_d - \nu_{fm} + \nu_{vm}) + 2\chi^{disp}(\nu_d + \nu_{vm}) - \chi^{disp}(\nu_d + \nu_{fm} + \nu_{vm})] \cos\theta_{fm} \\
& [\chi^{abs}(\nu_d - \nu_{fm} - \nu_{vm}) - \chi^{abs}(\nu_d - \nu_{fm} + \nu_{vm}) - \chi^{abs}(\nu_d - \nu_{vm}) + \chi^{abs}(\nu_d - \nu_{fm} + \nu_{vm})] \sin\theta_{fm}
\end{aligned} \tag{6.8}$$

Examples of the red and blue Doppler shifted components of the $Q_{22}(14.5)$ line of N_2^+ are shown in Figure 6.11.

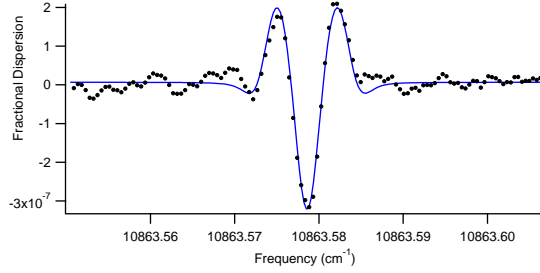
A comparison of the $Q_{22}(14.5)$ line of N_2^+ taken from the positive column and the ion beam are shown in Figure 6.12.



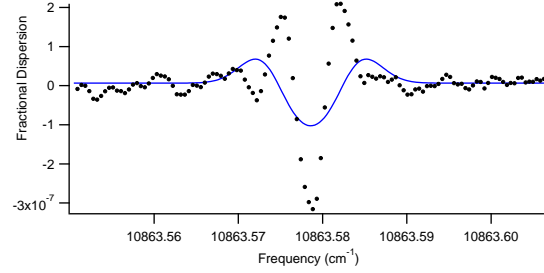
(a) Example spectra of N_2^+ at 2 kV beam voltage.



(b) A fit to Equation 6.8 which allows θ_{fm} to float



(c) A fit to Equation 6.8 with θ_{fm} set at 0° (dispersion). float.

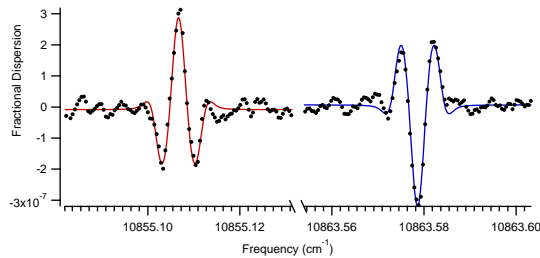


(d) A fit to Equation 6.8 with θ_{fm} set at 90° (absorption)

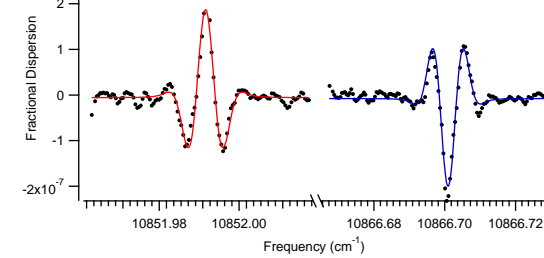
Figure 6.10: Fractional data (a); fit with θ_{fm} : (b) floating; (c) set to 0° ; (d) set to 90° . For clarity, graphs b-d have only 1 in every 15 data points is plotted.

Parameter	θ_{fm} Floating	θ_{fm} =Dispersion	θ_{fm} =Absorption	Units
x_0	10863.4786	10863.5786	10873.5786	cm^{-1}
Amplitude	1.24E-7	1.24E-7	1.35E-7	Fractional
FWHM	0.00289	0.00294	0.00635	cm^{-1}
FWHM	87	88	190	MHz
Het_Split	0.003787	0.003787	0.003787	cm^{-1}
VM_Split	0.00107	0.00107	0.00107	cm^{-1}
Theta	3	0	90	$^\circ$

Table 6.1: Line fit data for determining if the signal is dispersion or absorption.

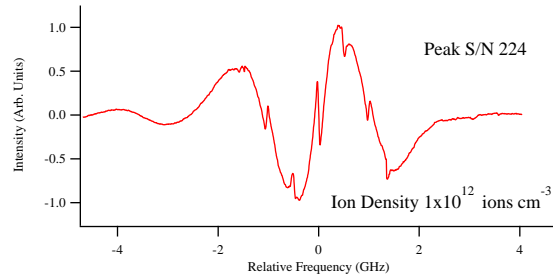


(a) Example spectra of N_2^+ at 2 kV beam voltage.

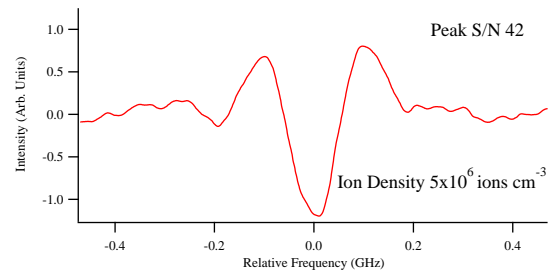


(b) Example spectra of N_2^+ at 6 kV beam voltage

Figure 6.11: Red and blue split components of the $Q_{22}(14.5)$ line of N_2^+ . Experimental data is shown by black dots, and fits to the general lineshape are shown in red and blue. For clarity, only 1 in every 15 data points is included in the graph.



(a) Example spectra of N_2^+ in the positive column taken with a 1 s time constant.



(b) Example spectra of N_2^+ in the ion beam taken with a 10 s time constant.

Figure 6.12: Comparison of N_2^+ line taken in a positive column with 1 s time constant, and of the ion beam with a 10 s time constant.

6.4 Comb Calibrated Spectra

Examples of the red and blue Doppler shifted components of the $Q_{22}(14.5)$ line of N_2^+ , calibrated with the frequency comb, are shown in Figure 6.13. A “dragging” effect, an artifact that the effective time constant of the lock-in amplifiers (100 s) was larger than the delay time of the measurement (1 s) is apparent. Therefore, scans were recorded both increasing and decreasing the laser frequency. Fits to Equation 4.13 were used, and the line centers for the scan up and scan down were averaged to determine the line center of the red and blue Doppler shifted lines. The geometric mean of the line centers of the red and blue Doppler shifted lines was then calculated as the absolute line center of the transition.

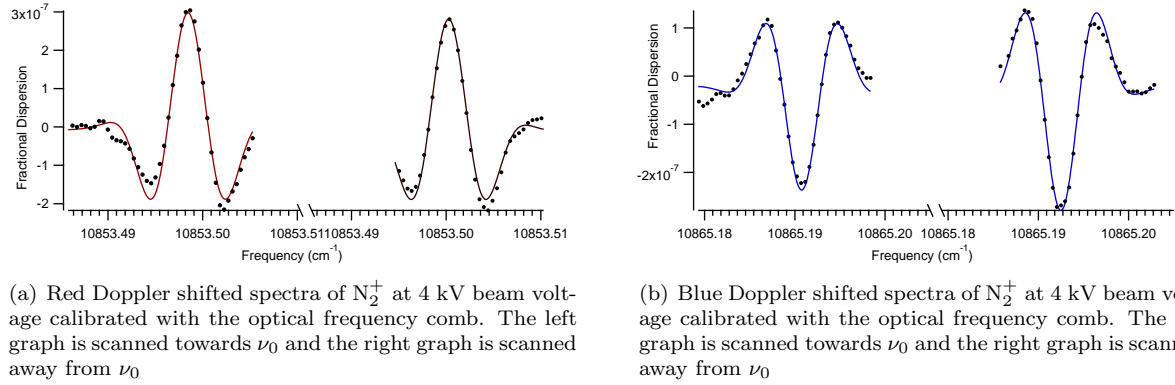


Figure 6.13: Red and blue split components of the $Q_{22}(14.5)$ line of N_2^+ calibrated with the frequency comb.

The frequencies for Doppler shifted transitions can be calculated from

$$\frac{\nu'}{\nu_0} = \sqrt{\frac{1 \mp v/c}{1 \pm v/c}} \quad (6.9)$$

where ν' is the Doppler shifted frequency, ν_0 is the rest frequency, and v is the velocity of the ions, given by

$$v = \sqrt{\frac{2qV'}{M}} \quad (6.10)$$

From Equation 6.9, the frequency of the red shifted component $(\nu_-) = (\nu_0) \sqrt{(1 - v/c)/(1 + v/c)}$, and the frequency of the blue shifted component $(\nu_+) = (\nu_0) \sqrt{(1 + v/c)/(1 - v/c)}$ can be calculated. The geometric mean of the red and blue shifted components, $\sqrt{(\nu_-)(\nu_+)}$ can be shown to be equal to ν_0 if the energy of the ion beam does not change.

If the inexact approximation is used $\frac{\nu'}{\nu_0} \approx 1 \pm \frac{v}{c}$, and the line centers are calculated by taking the arithmetic mean $(\nu_+ + \nu_-)/2$, the line calculated line centers will be off by several tens of MHz. For N_2^+

over a range of beam energies, the difference between the exact analysis with the geometric mean and the approximate arithmetic mean is 25, 50 and 75 MHz for 2, 4, and 6 kV respectively. Previous ion beam experiments accuracy were limited by their frequency calibration at 100 MHz, [12] so this wasn't much of an issue for them. [12, 78, 79]

In this measurement, the geometric mean of the blue-shifted transitions was $10865.19163 \text{ cm}^{-1}$ and the geometric mean of the red-shifted transitions was found to be $10853.49936 \text{ cm}^{-1}$. The geometric mean of these two mean values gives a rest transition frequency of $10859.34392 \text{ cm}^{-1}$, which is within 8 MHz of the positive column measured rest frequency of $10859.34418 \text{ cm}^{-1}$. [86]

6.5 Boltzmann Analysis

A Boltzmann analysis can be performed when the intensity of a transition, the degeneracy of the state, the transition probability and energy of the lower state is known. [175] The intensity of the transition is scaled by the degeneracy and transition probability, then plotted against the lower energy states of the line. The slope of that line is proportional to $-1/kT$. In order to obtain a rotational temperature, spectra of the ${}^qQ_{22}(J)$ lines (with $J=4.5, 7.5, 10.5, 14.5$ and 21.5) with lower energies ranging from 60 to 970 cm^{-1} were collected, and the fractional dispersion signal was calculated from the DC level of the detector. The spectra were fit to Equation 4.13 to obtain the intensities. The intensities were normalized to the strength of the transition (comprising the degeneracy and the transition probability), which were obtained along with the lower state energies from PGopher [176] using constants from Reference 82.

The values for the fit frequency, fit amplitude, E_{lower} , line strength, and normalized intensity are shown in Table 6.2, and the resulting Boltzmann distribution plot is shown in Figure 6.14. A linear regression of the points determines the slope to be 0.00191 cm . The reciprocal of the slope divided by Boltzmann's constant ($0.695 \text{ cm}^{-1}/\text{K}$) yields the rotational temperature of $753 \pm 45 \text{ K}$.

J"	PGopher Frequency	Fit Frequency	Fit Amplitude	$E_{\text{lower}} (\text{cm}^{-1})$	Strength	$\ln(A/S)$
4.5	10912.9236	10918.8680	-5.601E-07	57.6	0.88	-14.27
4.5	10912.9236	10918.8690	-5.810E-07	57.6	0.88	-14.23
7.5	10900.5453	10906.4829	-1.724E-06	138.3	3.08	-14.39
7.5	10900.5453	10906.4818	-1.660E-06	138.3	3.08	-14.43
10.5	10885.0316	10890.9616	-1.324E-06	253.6	2.28	-14.36
10.5	10885.0316	10890.9625	-1.232E-06	253.6	2.28	-14.43
14.5	10859.3419	10865.2589	-1.191E-06	461.0	3.36	-14.85
14.5	10859.3419	10865.2576	-1.305E-06	461.0	3.36	-14.76
21.5	10800.1377	10806.0206	-1.212E-06	971.1	10.77	-16.00
21.5	10800.1377	10806.0216	-1.255E-06	971.1	10.77	-16.00

Table 6.2: Data for calculating the rotational temperature of N_2^+ in the ion beam.

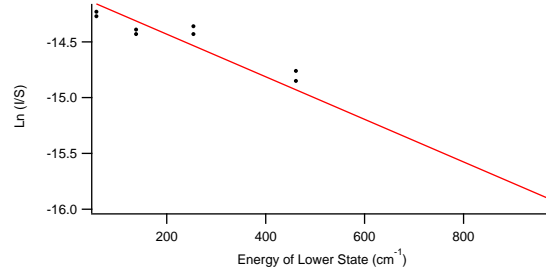


Figure 6.14: Boltzmann plot for temperature analysis.

Initially, Owrutsky reported rotational temperatures for HN_2^+ and HCO^+ to be 420 K with an uncooled cathode source extracted from the anode. [78]. Further, a vibrational temperature of 500 K was reported. Later, Keim reported the rotational temperatures of HN_2^+ as 600 K, and attribute that to the higher source pressure used in the later work [79] compared to the earlier [78]. Keim reports the rotational temperature of HCO^+ as 560 K and NH_4^+ as 400 K. The rotational temperatures observed in this work are higher and may be attributed to the higher pressure applied to the source. Additionally, the ions observed in this work were extracted from the cathode, are formed by electron impact and lack collisions with other ions. The collisions found in the anodic source help to thermalize the rotational populations.

6.6 Sensitivity

Based off of the NICE-OHMS sensitivity from Equation 4.6, the expected ion beam absorption equivalent signal is given by [142]

$$\text{Voltage} = \frac{F}{\pi} \frac{1}{2} \rho S l \frac{DC G_{RF} G_{AC}}{G_{DC}} J_0(\beta) J_1(\beta) \frac{2c}{\text{FWHM}} \sqrt{\frac{\ln(2)}{\pi}} \quad (6.11)$$

where the cavity enhancement factor $\frac{2F}{\pi}$ is reduced to the number of round trip passes in the cavity $\frac{F}{\pi}$ due to the large Doppler shift associated with the fast ion beam. Due to the velocity modulation, a factor of $\frac{1}{2}$ is added. The ion density (ρ , ions cm^{-3}), line strength (S cm ion $^{-1}$), the interaction length (l cm) describe the Beer's law absorption. The DC detector voltage level (DC), along with the RF gain (7.798 V/V), AC gain (20668 V/A) and DC gain (8077 V/A) form the power on the detector. The heterodyne modulation depth is calculated to be ($J_0(\beta)J_1(\beta) \sim 0.317$). The final term is the peak value of an area normalized Gaussian function.

The area of a peak normalized Gaussian is given by Equation 6.12.

$$\int_{-\infty}^{\infty} a e^{-(\frac{x^2}{2c^2})} dx = ac\sqrt{2\pi} \quad (6.12)$$

Therefore, for the peak normalized Gaussian lineshape [142]

$$\chi_G^{abs}(\nu) = e^{-4 \ln 2 (\Delta\nu/\text{FWHM})^2} \quad (6.13)$$

the area would be

$$\text{Area} = \text{FWHM} \sqrt{\frac{\pi}{4 \ln(2)}} \quad (6.14)$$

which has units of Hz. Inversion of the area and multiplication by the speed of light (c) gives the conversion to have a dimensional unit (cm), as is needed for the Beer's law unit analysis shown in Equation 6.15, and is consistent with the value given in

$$\left(\frac{\Delta I}{I_0}\right) = \rho \left(\frac{\text{ion}}{\text{cm}^3}\right) L(\text{cm}) S\left(\frac{\text{cm}}{\text{ion}}\right) \text{LWF}(\text{cm}) \quad (6.15)$$

Therefore, the linewidth factor is given in Equation 6.16 and the derivation is consistent with the value given by [177].

$$\text{LWF} = \frac{2c}{\text{FWHM}} \sqrt{\frac{\ln(2)}{\pi}} \quad (6.16)$$

The expected absorption equivalent fractional signal is given by dividing the expected signal in voltage (see Equation 6.11) by the maximum AC voltage possible ($DC \times G_{RF} \times G_{AC}/G_{DC}$ yielding Equation 6.17.

$$\frac{\Delta I}{I_0} = \frac{F}{\pi} \frac{1}{2} \rho S L J_0(\beta) J_1(\beta) \frac{2c}{\text{FWHM}} \sqrt{\frac{\ln(2)}{\pi}} \quad (6.17)$$

Using the equations presented above, the following constants, and the experimental parameters found in Table 6.3, the expected signal strength can be calculated and compared to the observed signal strength. For N_2^+ , the molecular mass is 28. The rotational temperature was measured to be 750 K. 3 mm diameter apertures were used to produce ion overlap leading to 0.071 cm^2 area apertures. Finesse was 450, the overlap length is 27.23 cm, and the line strength is assumed to be $3.87 \times 10^{-18} \text{ cm/ion}$ for the $\text{Q}_{22}(14.5)$ line at this temperature.

There is a large difference between the scans that did and that did not have the 10 dB attenuator before the amplifier. While performing scans with the ion beam, a large RAM peak was observed at the detector.

Data Point	Time Constant (s)	10 dB Attenuation	RF Gain and Sidebands	Beam Voltage (V)	Velocity (cm/s)	Current (μ A)	Ion Density ion/cm	Detector DC Voltage (V)
1	3	N	6.33	5987	20311511	2.31	1.00E7	4.11
2	3	N	6.33	5981	20301331	2.28	9.94E6	4.12
3	3	N	6.33	1985	11695475	0.70	5.26E6	4.54
4	3	N	6.33	1985	11695475	0.70	5.26E6	4.70
5	10	Y	2.00	3777	16132850	0.75	4.13E6	2.91
6	10	Y	2.00	3777	16132850	0.71	3.87E6	2.83
7	10	Y	2.00	3777	16132850	0.59	3.23E6	3.44
8	10	Y	2.00	3777	16132850	0.83	4.56E6	2.72

Data Point	Max AC Voltage (V)	Line Width (MHz)	Line Width Factor	Expected Signal Voltage	Observed Signal Voltage	Expected Fractional Signal	Observed Fractional Signal	Factor Off
1	82	150	188	3.71E-04	9.80E-06	4.52E-06	1.19E-07	38
2	82	150	188	3.68E-04	-9.78E-06	4.47E-06	1.19E-07	37
3	91	90	313	3.57E-04	1.13E-05	3.94E-06	1.25E-07	32
4	94	90	313	3.70E-04	-1.05E-05	3.95E-06	1.12E-07	35
5	19	120	235	4.27E-05	-3.48E-06	2.32E-06	-1.86E-07	12
6	18	120	235	3.88E-05	-3.10E-06	2.18E-06	-1.73E-07	13
7	22	120	235	3.94E-05	2.86E-06	1.82E-06	1.32E-07	14
8	17	120	235	4.40E-05	2.58E-06	2.56E-06	1.49E-07	17

Table 6.3: Expected and observed signal strengths for several representative scans of the ion beam.

The RAM peak was believed to be saturating the amplifier. This was tested by adding a 6 and 12 dB attenuators before the amplifier and observing the loss in signal strength. The results of the attenuation insertion is shown in Figure 6.15. The conversion factor for voltage to dB is shown in Equation 6.18, and for 6 dB of attenuation would decrease the voltage by a factor of ~ 2 (0.501) (see the transfer function equation to convert dB into a power level in Equation 6.18).

$$\frac{V_{out}}{V_{in}} = 10^{-\frac{dB}{20}} \quad (6.18)$$

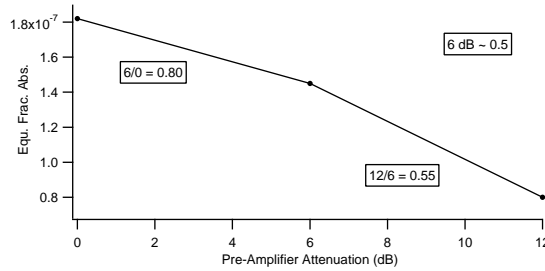


Figure 6.15: Testing amplifier saturation by adding RF attenuation.

As shown in Figure 6.15, the first 6 dB of attenuation only decreases the voltage by 1.25. Adding the

second 6 dB of attenuation, the signal voltage decreased by almost a factor of 2. Therefore, it was determined that the RAM peak is saturating the amplifier, and more representative values can be obtained with a 10 dB attenuator in place. Another factor of 2.3 can be explained as being due to the high saturation parameter, as explained in Section 4.9. As a weaker transition will be probed with less laser power in the mid-IR, it is expected that the saturation losses will be smaller in the mid-IR.

6.7 Noise

The average thermal noise of a detector is given by [141]

$$I_{\text{Thermal,Average}} = \sqrt{\frac{4kT\Delta f}{R}} \quad (6.19)$$

where k is Boltzmann's constant, T is the temperature, Δf is the bandwidth of the detector, and R is the input impedance.

For frequency modulation spectroscopy, the shot noise is given by [141]

$$I_{\text{Shot,Average}} = \sqrt{2g^2q^2\eta\frac{P_0}{h\nu}\Delta f} \quad (6.20)$$

where g is the gain of the detector, q is the charge of an electron, η is the quantum efficiency of the detector, P_0 is the power incident on the detector, Δf is the bandwidth of detection, h is Planck's constant, and ν is the frequency of the light.

For frequency modulation spectroscopy, the signal to noise ratio is given by [141]

$$\frac{S}{N} = \frac{\frac{1}{2}g^2q^2\eta^2\left(\frac{P_0}{h\nu}\right)^2\Delta\delta^2\beta^2}{2g^2q^2\eta\frac{P_0}{h\nu}\Delta f + \frac{4kT\Delta f}{R}} \quad (6.21)$$

where $\Delta\delta$ is the change in absorption, and β is the sideband modulation index. It is therefore, always advantageous to increase the laser power, the modulation index, to have a high η , and to work with small bandwidth detectors.

The shot noise for NICE-OHMS is given by [81]

$$\sigma_{\text{shot noise}} = \frac{\pi}{F \times l} \sqrt{\frac{qB}{\eta P_0} \frac{1}{J_0(\beta)J_1(\beta)}} \quad (6.22)$$

where l is the interaction length (27 cm), F is the finesse (460), η is the responsivity of the detector, P_0 is the power on the detector, and $J_0(\beta)J_1(\beta)$ is the modulation depth of the sidebands. For the NIR detector

($\eta=0.51$ A/W) and 1.10 mW power coming out of the cavity, the fractional shot noise limit is 2×10^{-12} . For a mid-IR detector (1 A/W) and 50 μ W power coming out of the cavity, the fractional shot noise limit is one order of magnitude higher, at 1×10^{-11} . The noise of a scan shown in Figure 6.11(a) was measured by calculating the standard deviation of the baseline. This value was 3×10^{-12} which shows that the technique is near the shot noise limit.

Chapter 7

Future Work and Conclusions

In Chapter 6, our sensitive spectroscopy coupled with our fast ion beam spectrometer allowed us to demonstrate complete and rigorous ion/neutral discrimination, sub-Doppler (kinematically compressed) line widths (see Figure 6.7), of a high rotational-temperature ion source (see Section 6.5). The use of the fast ion beam allowed for a mass spectrometer to monitor the optimization of plasma conditions to maximize the ion of interest (see Section 5.9). Additionally, the ability to determine the mass identification for every spectral line has been demonstrated (see Sections 6.4 and 4.8). This dissertation represents the return of ion spectroscopy to using ion beams for sample formation. Finally, sensitive enough spectroscopic methods allow for the low ion density of an ion beam to be probed directly via frequency modulation spectroscopy. This dissertation also details the first direct spectroscopic measurement of an electronic transition in an ion beam.

7.1 Mid-IR NICE-OHMS DFG Laser

By demonstrating these advantages with this newly developed spectroscopy in the NIR on N_2^+ , it is now possible to employ this same technique in the mid-IR by constructing a DFG laser capable of performing NICE-OHMS. A schematic of the DFG laser capable of performing NICE-OHMS in the mid-IR is shown in Figure 7.1.

Using the NIR NICE-OHMS spectrometer, it was determined that the some residual amplitude modulation (RAM) was present and adversely affected the laser/cavity lock. This RAM is frequency dependent and would change as the Ti:Sapphire laser was scanned. Because of the additional level of modulation, this RAM doesn't adversely affect the spectroscopic signal, but it does adversely affect the laser/cavity lock. It was suggested, that placing the locking sidebands on a fixed frequency laser would at least make the RAM constant. For this iteration of the NICE-OHMS spectroscopy, both EOMs were placed on the YAG laser. As the output of the YAG is still elliptically polarized, the quarter waveplate (QWP) is placed directly after the Faraday isolator. It was determined that a Faraday isolator was needed before the periodically poled lithium niobate (PPLN) crystal. The sum harmonic generation (SHG) PPLN crystal was used to double

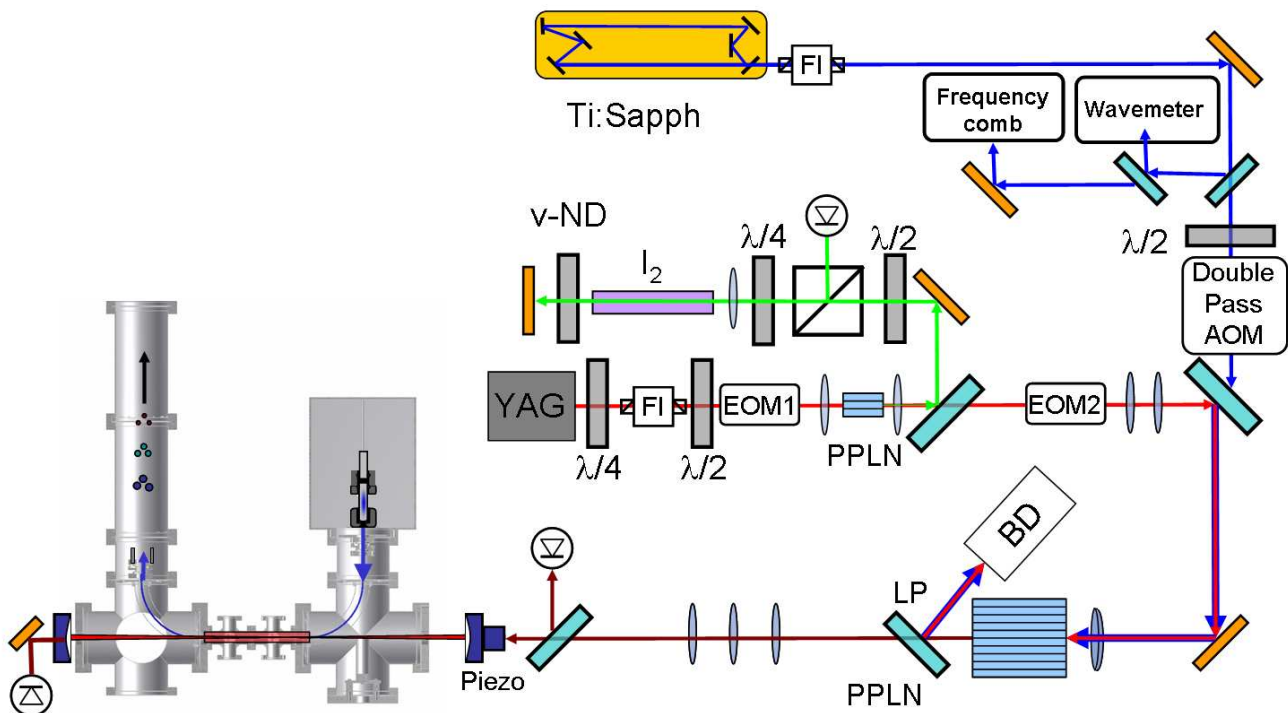


Figure 7.1: Optical layout for NICE-OHMS compatible DFG layout.

the frequency of the YAG laser, which could then be used to lock the laser to an iodine line, as discussed in Section 2.2. Heterodyne sidebands at the free spectral range of the cavity (~ 113 MHz) were added using a second EOM. The YAG was then mode matched to be the same mode size as the Ti:Sapphire laser and was overlapped spatially. DFG light was produced as described in Section 2.3. The output DFG light was mode-matched to the optical cavity. Once the DFG light is successfully locked to the cavity, several molecules can be studied in the mid-IR.

7.2 Indirect Terahertz Spectroscopy of HN_2^+

By observing spectra in the mid-IR it is expected that the observed linewidth will be reduced, that the absorption and dispersion signals will be less saturated, and the full sensitivity of the mid-IR instrument can be characterized. One molecule which is fairly simple to produce with our cold-cathode source is HN_2^+ . The first assignment to HN_2^+ was the rotational $J = 1 \rightarrow 0$ transition of 93.1 GHz by Thaddeus in 1974 using astronomical data. [178] Thaddeus showed that HN_2^+ had a predicted rotational constant of 92.2 GHz, and assigned the transition at 93.1 GHz to HN_2^+ ($B_0=1.55$). The first laboratory measurement of HN_2^+ was in 1976 when the $J = 1 \leftarrow 0$ HN_2^+ transition was split into a hyperfine multiplet and the line

centers for the multiplet were measured in the microwave. [3] The deuterium isotopologue was measured the next year. [179] In 1981, the $J=1 \rightarrow 2$, $2 \rightarrow 3$, $3 \rightarrow 4$ and $4 \rightarrow 5$ transitions were measured, and the spectral constants B_{000} and D_{000} were measured for HN_2^+ to be $1.5539705 \text{ cm}^{-1}$ and $2.919 \times 10^{-6} \text{ cm}^{-1}$, respectively. [4] These rotational constants provided accuracy to within 1 kHz of the measured $J=0$ line. In 1982, the $J=10 \rightarrow 11$ transition of HN_2^+ was measured and used to increase the accuracy of the spectral constants. [5] In 1983, using velocity modulation spectroscopy, 43 IR transitions of the ν_1 band of HN_2^+ were collected under Doppler broadened conditions to $\pm 100 \text{ MHz}$ accuracy by Gudeman [1], giving $\nu_0=3233.9538$, $B_{000}=1.554049$, $B_{100}=1.541429$, $D_{000}=3.11 \times 10^{-6}$, and $D_{100}=3.07 \times 10^{-6} \text{ cm}^{-1}$. In 1985, 41 additional transitions were used, and in conjunction with the microwave data, new "higher accuracy" constants were obtained: [2] $\nu_0=3233.9530$, $B_{100}=1.533971$, $B_{000}=1.541357$, $D_{100}=2.928 \times 10^{-6}$, and $D_{000}=2.901 \times 10^{-6} \text{ cm}^{-1}$. In addition, the equilibrium distance of the N-H and N-N bond were determined to be 1.03359 \AA and 1.092766 \AA , respectively. Figure 7.2(a) contains a simulation using the most accurate rotational constants determined by Owrutsky [2] at 30, 600, and 1000 K normalized to 30 K. The fraction of band for 30, 300, 600, and 1000 K is shown in Figure 7.3. Figure 7.2(b) shows the simulation at 600 K with units of cm ion^{-1} .

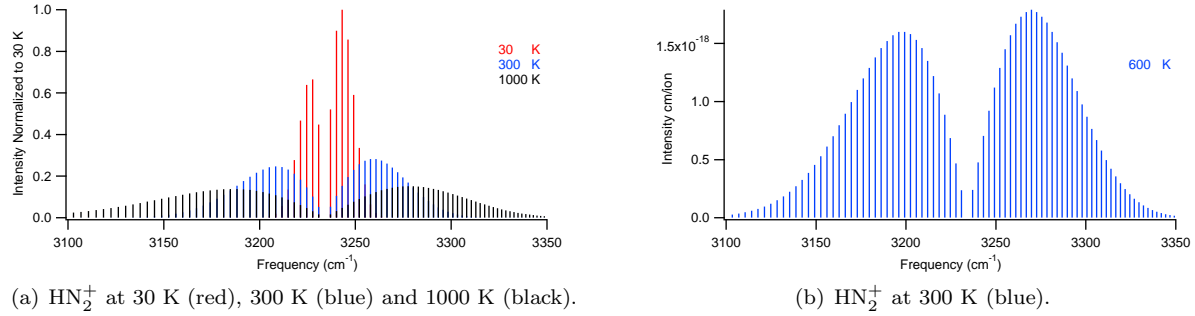


Figure 7.2: Spectra of HN_2^+ .

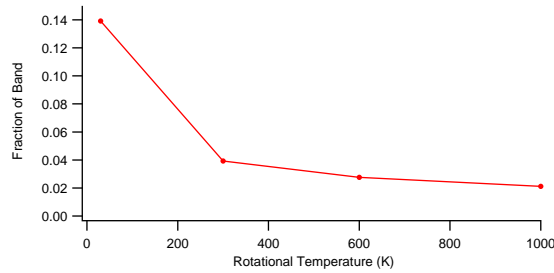


Figure 7.3: Fraction of band for HN_2^+ as a function of rotational temperature.

Table 7.1 shows the frequencies for the constants obtained by Gudeman [1] and Owrutsky [2]. Because the Owrutsky constants include the weighted microwave values, they are believed to be more accurate. However,

the Gudeman constants have been observed at transitions between P(20) and R(19). Two transitions listed in Gudeman include the R(3) and the P(20) transitions. The R(3) transition is correctly predicted by both sets of rotational constants. However, only the Gudeman constants correctly predict the frequency of observed P(20) transition. Additionally the R(9) line was observed by Owrutsky in a fast ion beam [78], and was observed closer to the Gudeman values [1] than the Owrutsky values [2]. For the purposes of finding more lines, it is expected that the Gudeman values should be used first.

Once these IR transitions are observed, combination differences can be taken. Observations of two transitions with a common upper or lower level can be used to obtain the energy difference between the lower or upper states, respectively. For example, subtracting the two transitions frequencies that have the same upper state (say the R(0) and the P(2) states), will yield the energy difference between the lower level energies of the J=0 and J=2 states, as illustrated on the left side of Figure 7.4. Combination differences can then be used to build up the energy differences between the even or the odd states. However, as the $J=1 \leftarrow 0$ transition has been measured to high accuracy, it can be used to convert between the even and odd differences. By subtracting the $1 \leftarrow 0$ transition from the $2 \leftarrow 0$ combination difference will yield the $2 \leftarrow 1$ transition. Subtracting the $2 \leftarrow 1$ transition from the $3 \leftarrow 1$ combination difference will yield the $3 \leftarrow 2$ transition. This process can be continued until all of the rotational transitions have been measured. Table 7.2 illustrates this reconstruction process with the data taken from a positive column (± 100 MHz accuracy and Doppler broadened linewidth) [1] and compares that to the data taken from the pure rotational spectrum. [3–5]

Inspection of the table, indicates a difference between the reconstruction and the rotational spectrum. It is apparent that for low values of J (< 20), that the accuracy of the reconstruction is within the accuracy of the mid-IR measurements. By increasing the accuracy of the measurements by calibrating the frequencies with a frequency comb, the accuracy of the reconstruction should improve as well. This process should be tested. The HN_2^+ lines should be observed and calibrated with the frequency comb. Then the rotational spectrum can be reconstructed. Once the performance of the system has been measured, the same technique can be performed on other linear polyatomic molecules.

	Owrutsky	Gudeman	Difference		Owrutsky	Gudeman	Difference
P(50)	3063.01	3049.425	13.585	R(0)	3237.0209	3237.0367	-0.0158
P(49)	3066.744	3053.6596	13.0844	R(1)	3240.074	3240.0942	-0.0202
P(48)	3070.4658	3057.8738	12.592	R(2)	3243.1122	3243.1264	-0.0142
P(47)	3074.1755	3062.0673	12.1082	R(3)	3246.1354	3246.133	0.0024
P(46)	3077.8729	3066.2402	11.6327	R(4)	3249.1435	3249.1142	0.0293
P(45)	3081.5582	3070.3922	11.166	R(5)	3252.1365	3252.0698	0.0667
P(44)	3085.2311	3074.5234	10.7077	R(6)	3255.1143	3254.9997	0.1146
P(43)	3088.8917	3078.6334	10.2583	R(7)	3258.0768	3257.9038	0.173
P(42)	3092.54	3082.7223	9.8177	R(8)	3261.024	3260.7822	0.2418
P(41)	3096.1758	3086.79	9.3858	R(9)	3263.9557	3263.6347	0.321
P(40)	3099.7992	3090.8362	8.963	R(10)	3266.872	3266.4612	0.4108
P(39)	3103.4101	3094.861	8.5491	R(11)	3269.7726	3269.2618	0.5108
P(38)	3107.0085	3098.8641	8.1444	R(12)	3272.6576	3272.0363	0.6213
P(37)	3110.5943	3102.8455	7.7488	R(13)	3275.5269	3274.7846	0.7423
P(36)	3114.1675	3106.805	7.3625	R(14)	3278.3804	3277.5068	0.8736
P(35)	3117.728	3110.7426	6.9854	R(15)	3281.2179	3280.2028	1.0151
P(34)	3121.2757	3114.6582	6.6175	R(16)	3284.0395	3282.8724	1.1671
P(33)	3124.8107	3118.5515	6.2592	R(17)	3286.845	3285.5157	1.3293
P(32)	3128.3329	3122.4227	5.9102	R(18)	3289.6344	3288.1325	1.5019
P(31)	3131.8422	3126.2714	5.5708	R(19)	3292.4076	3290.7229	1.6847
P(30)	3135.3386	3130.0976	5.241	R(20)	3295.1644	3293.2868	1.8776
P(29)	3138.8221	3133.9013	4.9208	R(21)	3297.9049	3295.824	2.0809
P(28)	3142.2925	3137.6823	4.6102	R(22)	3300.6289	3298.3347	2.2942
P(27)	3145.7498	3141.4405	4.3093	R(23)	3303.3364	3300.8186	2.5178
P(26)	3149.1941	3145.1758	4.0183	R(24)	3306.0272	3303.2758	2.7514
P(25)	3152.6251	3148.8882	3.7369	R(25)	3308.7013	3305.7062	2.9951
P(24)	3156.043	3152.5774	3.4656	R(26)	3311.3586	3308.1098	3.2488
P(23)	3159.4475	3156.2435	3.204	R(27)	3313.999	3310.4864	3.5126
P(22)	3162.8388	3159.8862	2.9526	R(28)	3316.6224	3312.8362	3.7862
P(21)	3166.2166	3163.5056	2.711	R(29)	3319.2288	3315.1589	4.0699
P(20)	3169.581	3167.1016	2.4794	R(30)	3321.818	3317.4546	4.3634
P(19)	3172.9319	3170.6739	2.258	R(31)	3324.3899	3319.7232	4.6667
P(18)	3176.2692	3174.2226	2.0466	R(32)	3326.9445	3321.9647	4.9798
P(17)	3179.5929	3177.7476	1.8453	R(33)	3329.4816	3324.1791	5.3025
P(16)	3182.9029	3181.2487	1.6542	R(34)	3332.0012	3326.3662	5.635
P(15)	3186.1992	3184.7259	1.4733	R(35)	3334.5033	3328.5261	5.9772
P(14)	3189.4817	3188.1791	1.3026	R(36)	3336.9876	3330.6587	6.3289
P(13)	3192.7503	3191.6081	1.1422	R(37)	3339.454	3332.764	6.69
P(12)	3196.0051	3195.013	0.9921	R(38)	3341.9026	3334.8419	7.0607
P(11)	3199.2458	3198.3936	0.8522	R(39)	3344.3332	3336.8924	7.4408
P(10)	3202.4725	3201.7498	0.7227	R(40)	3346.7458	3338.9154	7.8304
P(9)	3205.6851	3205.0816	0.6035	R(41)	3349.1401	3340.911	8.2291
P(8)	3208.8835	3208.3888	0.4947	R(42)	3351.5161	3342.8791	8.637
P(7)	3212.0677	3211.6714	0.3963	R(43)	3353.8738	3344.8197	9.0541
P(6)	3215.2376	3214.9294	0.3082	R(44)	3356.213	3346.7326	9.4804
P(5)	3218.3931	3218.1625	0.2306	R(45)	3358.5336	3348.618	9.9156
P(4)	3221.5343	3221.3708	0.1635	R(46)	3360.8356	3350.4757	10.3599
P(3)	3224.6609	3224.5542	0.1067	R(47)	3363.1187	3352.3058	10.8129
P(2)	3227.7729	3227.7125	0.0604	R(48)	3365.383	3354.1082	11.2748
P(1)	3230.8703	3230.8457	0.0246	R(49)	3367.6283	3355.8828	11.7455

Table 7.1: Transitions of HN_2^+ (cm^{-1}) calculated with constants from Gudeman [1] and Owrutsky [2]. Listed (observed) transitions are in **bold**.

J Lower	Reconstruction	Terahertz	Difference
0	GHz	GHz	MHz
1	186.36	186.34	14
2	279.52	279.51	7
3	372.70	372.67	25
4	465.84	465.82	12
5	559.00	558.97	31
6	652.12	652.10	20
7	745.24	745.21	34
8	838	838	18
9	931	931	35
10	1024	1024	14
11	1118	1117	27
12	1210	1210	8
13	1303	1303	13
14	1396	1396	9
15	1489	1489	5
16	1582	1582	32
17	1675	1675	33
18	1768	1768	64
19	1861	1861	74
20	1953	1953	106
21	2046	2046	120
22	2139	2139	160
23	2231	2231	177
24	2324	2324	224
25	2416	2416	249
26	2508	2509	301
27	2601	2601	334
28	2693	2693	394
29	2785	2786	433
30	2877	2878	499
31	2969	2970	547
32	3061	3062	622
33	3153	3154	677
34	3245	3246	763
35	3337	3338	825
36	3429	3430	921
37	3520	3521	991
38	3612	3613	1099
39	3703	3704	1177
40	3795	3796	1295
41	3886	3887	1386
42	3977	3979	1512
43	4068	4070	1618
44	4159	4161	1749
45	4250	4252	1871
46	4341	4343	2011
47	4431	4433	2147

Table 7.2: Reconstructed rotational spectrum of HN_2^+ as calculated with the rotational constants from Gudeman [1] compared with the measured rotational spectrum. The first rotational point is from [3]. The next four rotational points are from [4], and the remaining rotational transitions until $J=21$ are from [5]. The remaining rotational transitions are calculated using the rotational constants ($B=1.553971411 \text{ cm}^{-1}$ and $D=0.0000029324 \text{ cm}^{-1}$).

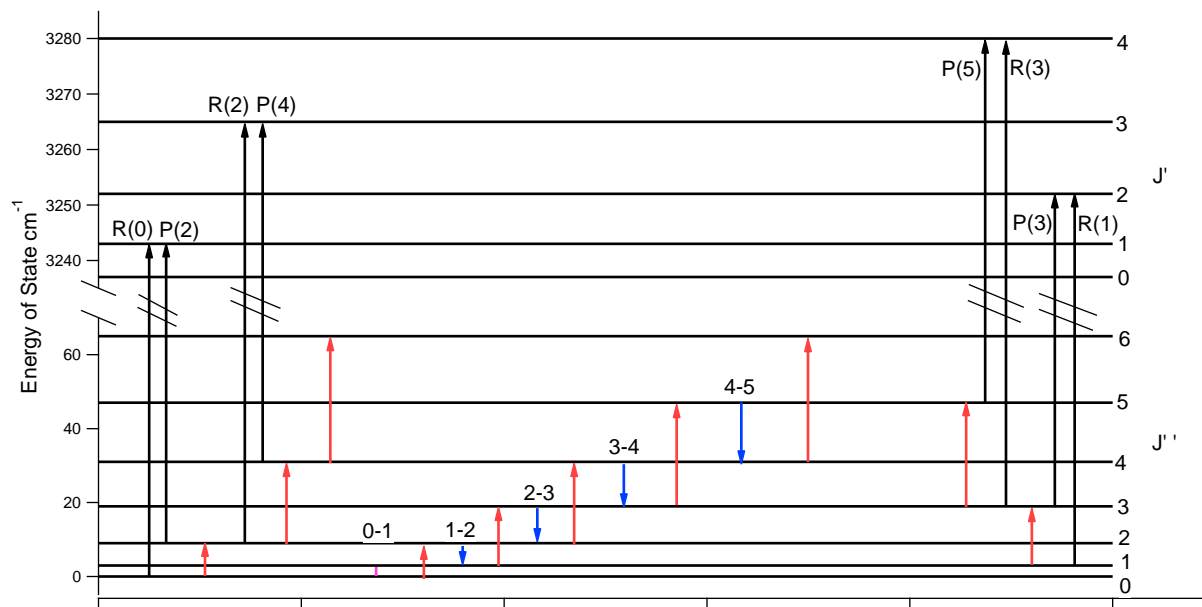


Figure 7.4: HN_2^+ energy level diagram for the lower and upper vibrational states. IR transitions are shown in black, and combination differences are shown by the red arrows. The $J=1 \leftarrow 0$ transition is indicated by the pink line. And the reconstructed rotational spectrum is shown by the blue arrows.

7.3 Indirect Terahertz Spectroscopy of Molecular Ions

Because the rotational spectrum of HN_2^+ has been measured up to $J=21$, we can benchmark the fast ion beam indirect terahertz spectroscopy with the actual rotational spectrum with this molecule. Once the limits of accuracy have been determined using this benchmark molecule, we can use this technique for molecules whose rotational spectrum has not been measured. Based on the sensitivity of the mid-IR system, it is expected that the rotational spectrum of HCS^+ , HOC^+ , HCO^+ , CO^+ , CH^+ , and HCNH^+ can be measured.

7.3.1 Indirect Terahertz Spectroscopy of CH^+

CH^+ was one of the first molecular species observed in the interstellar medium, though most spectroscopic information comes from electronic bands. The $J = 1 \leftarrow 0$ rotational transition of CH^+ was reported at 835.07895 GHz. [180]. CH^+ is extremely reactive especially with H_2 which form complex hydrocarbons. As the 835 GHz frequency is difficult to synthesize, alternate routes of obtaining rotational spectral information would be quite helpful.

While the rotational dipole of CH^+ is quite large 1.62 D. [181], the vibrational transition dipole moment is much smaller. The Einstein A coefficient of for the vibrational mode of CH^+ is calculated to be 1.63 s^{-1} , [182]. The Einstein A coefficient can be converted into the transition dipole moment using Equation

7.1

$$\mu^2 = \frac{3hc^3 A_{ij}}{64\pi^4 \nu^3} \quad (7.1)$$

where μ is the dipole moment in electrostatic units (esu), h is Planck's constant in erg s, c is the speed of light in cm/s, ν is the frequency of the transition in Hz, and A_{ij} is the Einstein A coefficient in Hz. Recognizing that $1 \text{ esu} = 1 \times 10^{18} \text{ Debye}$, can convert esu to Debye. Using the Einstein A coefficient of CH^+ , the transition dipole for vibrational spectroscopy of CH^+ can be calculated as 0.016 Debye. In addition to the weak transition dipole moment, CH^+ may prove difficult to study because it reactions to form hydrocarbons.

From the electronic work which has been performed previously, [183] the band origin was measured to be 2739.65 cm^{-1} , and the rotational constants have been determined to be $B_0=13.9302$, $D_0=0.001365$, and $H_0=4 \times 10^{-8}$, $B_1=13.4407$, $D_1=0.001342$, and $H_1=4 \times 10^{-8}$.

Based on the electronic transitions previously measured, a simulated spectrum is shown in Figure 7.5, and the fraction of band is shown as a function of rotational temperature between 30 and 1000 K in Figure 7.6. A list of the transition frequencies is shown in Table 7.3.

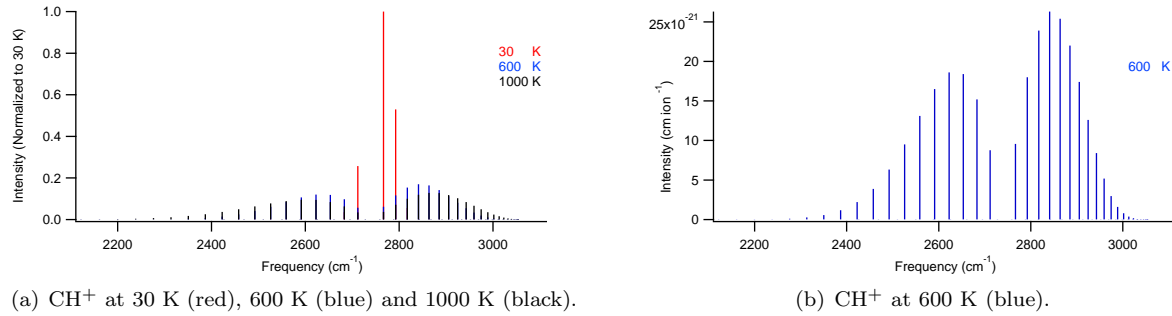


Figure 7.5: Spectra of CH^+ .

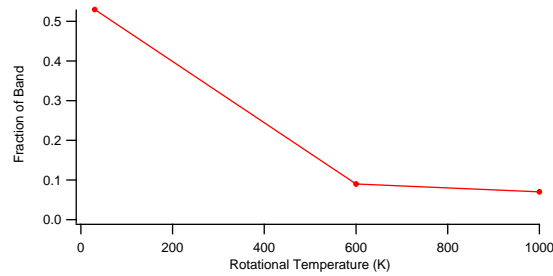


Figure 7.6: Fraction of band for CH^+ as a function of rotational temperature.

Table 7.3: Rovibrational spectrum of CH⁺ calculated with PGo-
pher.

Frequency cm ⁻¹	Intensity cm ion ⁻¹	E upper cm ⁻¹	E lower cm ⁻¹	Strength	Transition
892.9025	5.81E-44	28202.255	27309.3525	43.74	P(50)
924.9803	3.88E-43	27448.8028	26523.8225	42.8652	P(49)
957.7686	2.62E-42	26690.9916	25733.223	41.9904	P(48)
991.2423	1.78E-41	25929.8366	24938.5943	41.1156	P(47)
1025.375	1.22E-40	25166.3529	24140.978	40.2408	P(46)
1060.1397	8.42E-40	24401.5549	23341.4152	39.366	P(45)
1095.5086	5.8E-39	23636.4543	22540.9457	38.4912	P(44)
1131.4533	3.99E-38	22872.0593	21740.606	37.6164	P(43)
1167.9444	2.73E-37	22109.373	20941.4286	36.7416	P(42)
1204.9521	1.86E-36	21349.3926	20144.4405	35.8668	P(41)
1242.4457	1.26E-35	20593.1074	19350.6618	34.992	P(40)
1280.394	8.38E-35	19841.4987	18561.1046	34.1172	P(39)
1318.7653	5.52E-34	19095.5375	17776.7722	33.2424	P(38)
1357.5271	3.57E-33	18356.1844	16998.6573	32.3676	P(37)
1396.6465	2.27E-32	17624.3878	16227.7413	31.4928	P(36)
1436.0901	1.41E-31	16901.0832	15464.993	30.618	P(35)
1475.8239	8.6E-31	16187.1918	14711.3679	29.7432	P(34)
1515.8136	5.1E-30	15483.62	13967.8065	28.8684	P(33)
1556.0243	2.94E-29	14791.2582	13235.2339	27.9936	P(32)
1596.4208	1.65E-28	14110.9795	12514.5587	27.1188	P(31)
1636.9675	8.92E-28	13443.6393	11806.6718	26.244	P(30)
1677.6286	4.67E-27	12790.0742	11112.4456	25.3692	P(29)
1718.3678	2.36E-26	12151.1011	10432.7333	24.4944	P(28)
1759.1486	1.14E-25	11527.5164	9768.3678	23.6196	P(27)
1799.9341	5.33E-25	10920.095	9120.1609	22.7448	P(26)
1840.6875	2.38E-24	10329.59	8488.9025	21.87	P(25)
1881.3715	1.02E-23	9756.7315	7875.36	20.9952	P(24)
1921.9488	4.15E-23	9202.2261	7280.2773	20.1204	P(23)
1962.3818	1.61E-22	8666.756	6704.3742	19.2456	P(22)
2002.6329	5.96E-22	8150.9787	6148.3458	18.3708	P(21)
2042.6646	2.09E-21	7655.5261	5612.8615	17.496	P(20)
2082.4389	6.96E-21	7181.0038	5098.5649	16.6212	P(19)
2121.9182	2.19E-20	6727.9908	4606.0726	15.7464	P(18)
2161.0647	6.5E-20	6297.0388	4135.9742	14.8716	P(17)
2199.8406	1.82E-19	5888.6718	3688.8312	13.9968	P(16)
2238.2083	4.79E-19	5503.3852	3265.177	13.122	P(15)
2276.1302	1.19E-18	5141.6461	2865.5159	12.2472	P(14)
2313.5689	2.75E-18	4803.8921	2490.3233	11.3724	P(13)
2350.487	5.98E-18	4490.5314	2140.0444	10.4976	P(12)
2386.8474	1.21E-17	4201.942	1815.0946	9.6228	P(11)
2422.6132	2.29E-17	3938.472	1515.8587	8.748	P(10)
2426.5125	1.04E-42	28950.335	26523.8225	43.74	R(49)
2457.7477	4.03E-17	3700.4384	1242.6907	7.8732	P(9)
2469.032	6.89E-42	28202.255	25733.223	42.8652	R(48)
2492.2145	6.57E-17	3488.1277	995.9132	6.9984	P(8)
2510.2085	4.62E-41	27448.8028	24938.5943	41.9904	R(47)

Continued on next page...

Table 7.3 continued.

Frequency cm ⁻¹	Intensity cm ion ⁻¹	E upper cm ⁻¹	E lower cm ⁻¹	Strength	Transition
2525.9775	9.87E-17	3301.7951	775.8176	6.1236	P(7)
2550.0137	3.11E-40	26690.9916	24140.978	41.1156	R(46)
2559.0008	1.36E-16	3141.6643	582.6635	5.2488	P(6)
2588.4214	2.1E-39	25929.8366	23341.4152	40.2408	R(45)
2591.2489	1.71E-16	3007.9275	416.6786	4.374	P(5)
2622.6869	1.93E-16	2900.7452	278.0583	3.4992	P(4)
2625.4072	1.42E-38	25166.3529	22540.9457	39.366	R(44)
2653.28	1.91E-16	2820.2459	166.9659	2.6244	P(3)
2660.9489	9.6E-38	24401.5549	21740.606	38.4912	R(43)
2682.994	1.58E-16	2766.526	83.5321	1.7496	P(2)
2695.0256	6.46E-37	23636.4543	20941.4286	37.6164	R(42)
2711.7951	9.1E-17	2739.65	27.8549	0.8748	P(1)
2727.6188	4.32E-36	22872.0593	20144.4405	36.7416	R(41)
2758.7113	2.86E-35	22109.373	19350.6618	35.8668	R(40)
2766.526	9.92E-17	2766.526	0	0.8748	R(0)
2788.2879	1.87E-34	21349.3926	18561.1046	34.992	R(39)
2792.391	1.87E-16	2820.2459	27.8549	1.7496	R(1)
2816.3352	1.21E-33	20593.1074	17776.7722	34.1172	R(38)
2817.2132	2.48E-16	2900.7452	83.5321	2.6244	R(2)
2840.9616	2.73E-16	3007.9275	166.9659	3.4992	R(3)
2842.8414	7.68E-33	19841.4987	16998.6573	33.2424	R(37)
2863.606	2.64E-16	3141.6643	278.0583	4.374	R(4)
2867.7962	4.79E-32	19095.5375	16227.7413	32.3676	R(36)
2885.1165	2.29E-16	3301.7951	416.6786	5.2488	R(5)
2891.1914	2.93E-31	18356.1844	15464.993	31.4928	R(35)
2905.4642	1.8E-16	3488.1277	582.6635	6.1236	R(6)
2913.02	1.75E-30	17624.3878	14711.3679	30.618	R(34)
2924.6208	1.31E-16	3700.4384	775.8176	6.9984	R(7)
2933.2767	1.02E-29	16901.0832	13967.8065	29.7432	R(33)
2942.5588	8.72E-17	3938.472	995.9132	7.8732	R(8)
2951.9579	5.75E-29	16187.1918	13235.2339	28.8684	R(32)
2959.2514	5.39E-17	4201.942	1242.6907	8.748	R(9)
2969.0613	3.16E-28	15483.62	12514.5587	27.9936	R(31)
2974.6727	3.1E-17	4490.5314	1515.8587	9.6228	R(10)
2984.5864	1.68E-27	14791.2582	11806.6718	27.1188	R(30)
2988.7975	1.66E-17	4803.8921	1815.0946	10.4976	R(11)
2998.5339	8.63E-27	14110.9795	11112.4456	26.244	R(29)
3001.6017	8.27E-18	5141.6461	2140.0444	11.3724	R(12)
3010.906	4.28E-26	13443.6393	10432.7333	25.3692	R(28)
3013.062	3.86E-18	5503.3852	2490.3233	12.2472	R(13)
3021.7064	2.04E-25	12790.0742	9768.3678	24.4944	R(27)
3023.1558	1.69E-18	5888.6718	2865.5159	13.122	R(14)
3030.9403	9.33E-25	12151.1011	9120.1609	23.6196	R(26)
3031.8619	6.92E-19	6297.0388	3265.177	13.9968	R(15)
3038.6139	4.09E-24	11527.5164	8488.9025	22.7448	R(25)
3039.1596	2.67E-19	6727.9908	3688.8312	14.8716	R(16)
3044.735	1.72E-23	10920.095	7875.36	21.87	R(24)
3045.0296	9.69E-20	7181.0038	4135.9742	15.7464	R(17)
3049.3127	6.88E-23	10329.59	7280.2773	20.9952	R(23)
3049.4535	3.32E-20	7655.5261	4606.0726	16.6212	R(18)

Continued on next page...

Table 7.3 continued.

Frequency cm ⁻¹	Intensity cm ion ⁻¹	E upper cm ⁻¹	E lower cm ⁻¹	Strength	Transition
3052.3573	2.62E-22	9756.7315	6704.3742	20.1204	R(22)
3052.4138	1.07E-20	8150.9787	5098.5649	17.496	R(19)
3053.8803	9.53E-22	9202.2261	6148.3458	19.2456	R(21)
3053.8945	3.28E-21	8666.756	5612.8615	18.3708	R(20)

7.3.2 Indirect Terahertz Spectroscopy of CO⁺

CO⁺ has been an important ion used to study the interstellar medium, and to further advance ion spectroscopy. It has quite a large permanent dipole in the microwave (~ 2.5 D [22], 2.771 D [184]), but the infrared transition dipole moment is about a factor of 100 times weaker than HCO⁺. The pure rotational transition of CO⁺ was reported at 117.69255 GHz and 118.10199 GHz for the $J = 1/2 \rightarrow 1/2$ and $J = 1/2 \rightarrow 3/2$ transitions, respectively. [22]. Additionally, the J=15/2 line was measured to be 1061.0059 GHz [185] and shows that the rotational constants determined by Dixon [22] are quite good for CO⁺.

The infrared transition strength of CO⁺ was calculated to be 33 km/mol. [186] Using Equation 7.2,

$$S = 2.5066\nu\mu^2 \quad (7.2)$$

where S is the band strength in km/mol, ν is the transition frequency in cm⁻¹, and μ is the transition dipole moment in Debye, the band strength can be converted to a transition dipole moment. The factor 2.5066 is a constant, given by Equation 7.3

$$Constant = \frac{8\pi^3}{3h N_A c} \frac{1 \times 10^{-36}}{10000} \quad (7.3)$$

where h is Planck's constant in ergs, N_A is Avogadro's number, and c is the speed of light in cm/s. Using Equation 7.2, the calculated band strength is 0.074 Debye.

From the rovibrational work which has been performed previously at 30 MHz accuracy, [187] the band origin was measured to be 2183.9193 cm⁻¹, and the rotational constants have been determined to be $B_0=1.9674624$, $D_0=6.324 \times 10^{-6}$, and $\gamma=9.107 \times 10^{-3}$, $B_1=1.948438$, $D_1=6.324 \times 10^{-6}$, and $\gamma=9.049 \times 10^{-3}$ cm⁻¹.

Based on the rovibrational transitions previously measured, a simulated spectrum is shown in Figure 7.7, and the fraction of band is shown as a function of rotational temperature between 30 and 1000 K in Figure 7.8. A list of the transition frequencies is shown in Table 7.4.

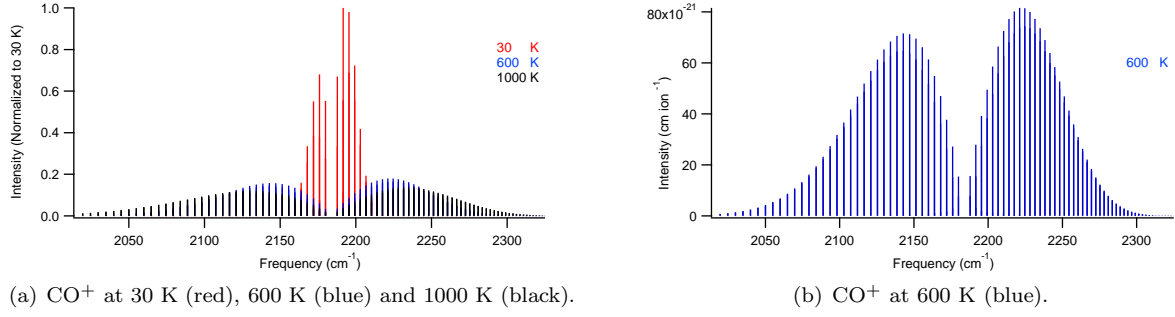


Figure 7.7: Spectra of CO⁺.

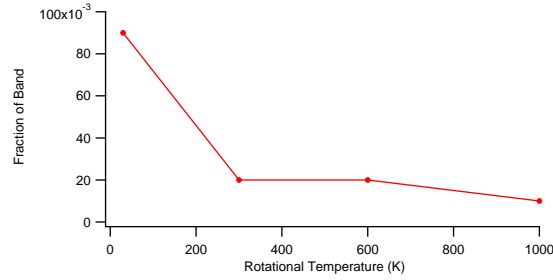


Figure 7.8: Fraction of band for CO⁺ as a function of rotational temperature.

Table 7.4: Rovibrational spectrum of CO⁺ calculated with PGo-pher.

Frequency cm ⁻¹	Intensity cm ion ⁻¹	E upper cm ⁻¹	E lower cm ⁻¹	Strength	Transition
1943.7313	2.41E-22	6919.4064	4975.6751	0.0903448	pP2(49.5)
1944.1792	4.86E-26	6919.8543	4975.6751	0.00001826	pQ12(49.5)
1949.3327	3.19E-22	6731.8789	4782.5462	0.0903448	pP1(49.5)
1949.3446	3.12E-22	6731.44	4782.0954	0.0885193	pP2(48.5)
1949.7835	6.58E-26	6731.8789	4782.0954	0.00001863	pQ12(48.5)
1954.9155	4.11E-22	6547.6219	4592.7064	0.0885193	pP1(48.5)
1954.9273	4.03E-22	6547.192	4592.2647	0.0866937	pP2(47.5)
1955.3572	8.85E-26	6547.6219	4592.2647	0.00001902	pQ12(47.5)
1960.4675	5.28E-22	6367.0905	4406.623	0.0866937	pP1(47.5)
1960.4793	5.17E-22	6366.6697	4406.1904	0.0848682	pP2(46.5)
1960.9001	1.18E-25	6367.0905	4406.1904	0.00001942	pQ12(46.5)
1965.9886	6.74E-22	6190.2919	4224.3033	0.0848682	pP1(46.5)
1966.0004	6.6E-22	6189.8801	4223.8798	0.0830426	pP2(45.5)
1966.4121	1.58E-25	6190.2919	4223.8798	0.00001984	pQ12(45.5)
1971.4786	8.55E-22	6017.233	4045.7544	0.0830426	pP1(45.5)
1971.4903	8.37E-22	6016.8303	4045.34	0.0812171	pP2(44.5)
1971.893	2.09E-25	6017.233	4045.34	0.00002028	pQ12(44.5)
1976.9375	1.08E-21	5847.9208	3870.9833	0.0812171	pP1(44.5)
1976.9491	1.05E-21	5847.5271	3870.578	0.0793915	pP2(43.5)
1977.3427	2.76E-25	5847.9208	3870.578	0.00002075	pQ12(43.5)
1982.3649	1.35E-21	5682.3618	3699.9969	0.0793915	pP1(43.5)

Continued on next page...

Table 7.4 continued.

Frequency cm ⁻¹	Intensity cm ion ⁻¹	E upper cm ⁻¹	E lower cm ⁻¹	Strength	Transition
1982.3765	1.32E-21	5681.9772	3699.6007	0.0775659	pP2(42.5)
1982.7611	3.62E-25	5682.3618	3699.6007	0.00002123	pQ12(42.5)
1987.7608	1.68E-21	5520.5626	3532.8018	0.0775659	pP1(42.5)
1987.7723	1.65E-21	5520.1871	3532.4147	0.0757403	pP2(41.5)
1988.1479	4.72E-25	5520.5626	3532.4147	0.00002173	pQ12(41.5)
1993.1251	2.09E-21	5362.5296	3369.4045	0.0757403	pP1(41.5)
1993.1365	2.04E-21	5362.1631	3369.0265	0.0739147	pP2(40.5)
1993.503	6.14E-25	5362.5296	3369.0265	0.00002226	pQ12(40.5)
1998.4575	2.57E-21	5208.2689	3209.8114	0.0739147	pP1(40.5)
1998.4689	2.51E-21	5207.9115	3209.4426	0.0720891	pP2(39.5)
1998.8263	7.94E-25	5208.2689	3209.4426	0.00002282	pQ12(39.5)
2003.7579	3.14E-21	5057.7868	3054.0288	0.0720891	pP1(39.5)
2003.7693	3.06E-21	5057.4384	3053.6691	0.0702635	pP2(38.5)
2004.1177	1.02E-24	5057.7868	3053.6691	0.00002341	pQ12(38.5)
2009.0263	3.82E-21	4911.089	2902.0628	0.0702635	pP1(38.5)
2009.0375	3.72E-21	4910.7497	2901.7121	0.0684378	pP2(37.5)
2009.3769	1.31E-24	4911.089	2901.7121	0.00002402	pQ12(37.5)
2014.2623	4.62E-21	4768.1814	2753.9191	0.0684378	pP1(37.5)
2014.2735	4.5E-21	4767.8511	2753.5776	0.0666122	pP2(36.5)
2014.6038	1.67E-24	4768.1814	2753.5776	0.00002467	pQ12(36.5)
2019.4659	5.55E-21	4629.0696	2609.6037	0.0666122	pP1(36.5)
2019.4771	5.4E-21	4628.7483	2609.2712	0.0647865	pP2(35.5)
2019.7983	2.11E-24	4629.0696	2609.2712	0.00002536	pQ12(35.5)
2024.6369	6.62E-21	4493.7589	2469.122	0.0647865	pP1(35.5)
2024.648	6.44E-21	4493.4467	2468.7987	0.0629608	pP2(34.5)
2024.9602	2.67E-24	4493.7589	2468.7987	0.00002608	pQ12(34.5)
2029.7752	7.85E-21	4362.2549	2332.4797	0.0629608	pP1(34.5)
2029.7863	7.63E-21	4361.9517	2332.1655	0.061135	pP2(33.5)
2030.0894	3.35E-24	4362.2549	2332.1655	0.00002685	pQ12(33.5)
2034.8806	9.25E-21	4234.5625	2199.6819	0.061135	pP1(33.5)
2034.8916	8.98E-21	4234.2684	2199.3768	0.0593093	pP2(32.5)
2035.1857	4.19E-24	4234.5625	2199.3768	0.00002766	pQ12(32.5)
2039.9529	1.08E-20	4110.6868	2070.7339	0.0593093	pP1(32.5)
2039.9639	1.05E-20	4110.4018	2070.4379	0.0574835	pP2(31.5)
2040.2489	5.21E-24	4110.6868	2070.4379	0.00002853	pQ12(31.5)
2044.9921	1.26E-20	3990.6327	1945.6406	0.0574835	pP1(31.5)
2045.003	1.22E-20	3990.3568	1945.3538	0.0556577	pP2(30.5)
2045.279	6.46E-24	3990.6327	1945.3538	0.00002945	pQ12(30.5)
2049.9979	1.46E-20	3874.4049	1824.407	0.0556577	pP1(30.5)
2050.0087	1.41E-20	3874.138	1824.1292	0.0538319	pP2(29.5)
2050.2757	7.97E-24	3874.4049	1824.1292	0.00003043	pQ12(29.5)
2054.9702	1.67E-20	3762.008	1707.0377	0.0538319	pP1(29.5)
2054.981	1.62E-20	3761.7501	1706.769	0.052006	pP2(28.5)
2055.2389	9.78E-24	3762.008	1706.769	0.00003148	pQ12(28.5)
2059.9089	1.91E-20	3653.4462	1593.5373	0.052006	pP1(28.5)
2059.9196	1.84E-20	3653.1973	1593.2777	0.0501801	pP2(27.5)
2060.1685	1.2E-23	3653.4462	1593.2777	0.00003261	pQ12(27.5)
2064.8138	2.16E-20	3548.7239	1483.9101	0.0501801	pP1(27.5)
2064.8244	2.08E-20	3548.4841	1483.6597	0.0483541	pP2(26.5)
2065.0642	1.46E-23	3548.7239	1483.6597	0.00003381	pQ12(26.5)

Continued on next page...

Table 7.4 continued.

Frequency cm ⁻¹	Intensity cm ion ⁻¹	E upper cm ⁻¹	E lower cm ⁻¹	Strength	Transition
2069.6847	2.43E-20	3447.8452	1378.1605	0.0483541	pP1(26.5)
2069.6953	2.34E-20	3447.6145	1377.9192	0.0465281	pP2(25.5)
2069.9261	1.76E-23	3447.8452	1377.9192	0.00003512	pQ12(25.5)
2074.5215	2.71E-20	3350.814	1276.2925	0.0465281	pP1(25.5)
2074.5321	2.61E-20	3350.5923	1276.0603	0.044702	pP2(24.5)
2074.7538	2.13E-23	3350.814	1276.0603	0.00003652	pQ12(24.5)
2079.3241	3.01E-20	3257.6342	1178.3101	0.044702	pP1(24.5)
2079.3346	2.88E-20	3257.4215	1178.087	0.0428759	pP2(23.5)
2079.5472	2.56E-23	3257.6342	1178.087	0.00003804	pQ12(23.5)
2084.0923	3.31E-20	3168.3093	1084.217	0.0428759	pP1(23.5)
2084.1027	3.17E-20	3168.1057	1084.003	0.0410497	pP2(22.5)
2084.3063	3.06E-23	3168.3093	1084.003	0.0000397	pQ12(22.5)
2088.8259	3.61E-20	3082.8429	994.017	0.0410497	pP1(22.5)
2088.8362	3.45E-20	3082.6483	993.8121	0.0392234	pP2(21.5)
2089.0308	3.66E-23	3082.8429	993.8121	0.00004151	pQ12(21.5)
2093.5248	3.92E-20	3001.2382	907.7134	0.0392234	pP1(21.5)
2093.5351	3.74E-20	3001.0527	907.5176	0.0373971	pP2(20.5)
2093.7206	4.35E-23	3001.2382	907.5176	0.00004348	pQ12(20.5)
2098.1888	4.22E-20	2923.4985	825.3097	0.0373971	pP1(20.5)
2098.199	4.01E-20	2923.3221	825.123	0.0355706	pP2(19.5)
2098.3755	5.15E-23	2923.4985	825.123	0.00004566	pQ12(19.5)
2102.8178	4.5E-20	2849.6269	746.809	0.0355706	pP1(19.5)
2102.828	4.27E-20	2849.4595	746.6315	0.033744	pP2(18.5)
2102.9954	6.08E-23	2849.6269	746.6315	0.00004807	pQ12(18.5)
2107.4117	4.76E-20	2779.6261	672.2144	0.033744	pP1(18.5)
2107.4218	4.51E-20	2779.4677	672.0459	0.0319173	pP2(17.5)
2107.5801	7.16E-23	2779.6261	672.0459	0.00005074	pQ12(17.5)
2111.9702	5E-20	2713.499	601.5287	0.0319173	pP1(17.5)
2111.9803	4.71E-20	2713.3496	601.3694	0.0300903	pP2(16.5)
2112.1296	8.42E-23	2713.499	601.3694	0.00005373	pQ12(16.5)
2116.4933	5.2E-20	2651.248	534.7548	0.0300903	pP1(16.5)
2116.5033	4.88E-20	2651.1078	534.6045	0.0282632	pP2(15.5)
2116.6435	9.87E-23	2651.248	534.6045	0.0000571	pQ12(15.5)
2120.9807	5.36E-20	2592.8757	471.895	0.0282632	pP1(15.5)
2120.9907	5.01E-20	2592.7445	471.7539	0.0264359	pP2(14.5)
2121.1219	1.15E-22	2592.8757	471.7539	0.00006091	pQ12(14.5)
2125.4324	5.46E-20	2538.3844	412.952	0.0264359	pP1(14.5)
2125.4423	5.09E-20	2538.2622	412.8199	0.0246082	pP2(13.5)
2125.5644	1.35E-22	2538.3844	412.8199	0.00006527	pQ12(13.5)
2129.8481	5.52E-20	2487.776	357.9279	0.0246082	pP1(13.5)
2129.858	5.11E-20	2487.6629	357.8049	0.0227802	pP2(12.5)
2129.9711	1.58E-22	2487.776	357.8049	0.00007031	pQ12(12.5)
2134.2278	5.51E-20	2441.0527	306.8249	0.0227802	pP1(12.5)
2134.2376	5.07E-20	2440.9486	306.711	0.0209517	pP2(11.5)
2134.3417	1.84E-22	2441.0527	306.711	0.00007619	pQ12(11.5)
2138.5713	5.43E-20	2398.2162	259.6449	0.0209517	pP1(11.5)
2138.581	4.96E-20	2398.1212	259.5402	0.0191225	pP2(10.5)
2138.676	2.16E-22	2398.2162	259.5402	0.00008314	pQ12(10.5)
2142.8783	5.29E-20	2359.2682	216.3899	0.0191225	pP1(10.5)
2142.888	4.78E-20	2359.1823	216.2943	0.0172926	pP2(9.5)

Continued on next page...

Table 7.4 continued.

Frequency cm ⁻¹	Intensity cm ion ⁻¹	E upper cm ⁻¹	E lower cm ⁻¹	Strength	Transition
2142.974	2.53E-22	2359.2682	216.2943	0.0000915	pQ12(9.5)
2147.1489	5.07E-20	2324.2102	177.0614	0.0172926	pP1(9.5)
2147.1585	4.53E-20	2324.1333	176.9749	0.0154616	pP2(8.5)
2147.2354	2.98E-22	2324.2102	176.9749	0.0001017	pQ12(8.5)
2151.3827	4.78E-20	2293.0437	141.6609	0.0154616	pP1(8.5)
2151.3923	4.21E-20	2292.9758	141.5835	0.0136292	pP2(7.5)
2151.4601	3.54E-22	2293.0437	141.5835	0.0001145	pQ12(7.5)
2155.5798	4.42E-20	2265.7697	110.1899	0.0136292	pP1(7.5)
2155.5892	3.82E-20	2265.7109	110.1216	0.0117945	pP2(6.5)
2155.6481	4.25E-22	2265.7697	110.1216	0.000131	pQ12(6.5)
2159.7398	3.98E-20	2242.3894	82.6496	0.0117945	pP1(6.5)
2159.7492	3.36E-20	2242.3396	82.5904	0.0099564	pP2(5.5)
2159.799	5.18E-22	2242.3894	82.5904	0.0001532	pQ12(5.5)
2163.8627	3.49E-20	2222.9036	59.0409	0.0099564	pP1(5.5)
2163.872	2.84E-20	2222.8629	58.9909	0.0081126	pP2(4.5)
2163.9128	6.46E-22	2222.9036	58.9909	0.0001844	pQ12(4.5)
2167.9483	2.93E-20	2207.3132	39.3649	0.0081126	pP1(4.5)
2167.9576	2.26E-20	2207.2815	39.324	0.0062583	pP2(3.5)
2167.9893	8.37E-22	2207.3132	39.324	0.0002318	pQ12(3.5)
2171.9965	2.31E-20	2195.6187	23.6223	0.0062583	pP1(3.5)
2172.0057	1.62E-20	2195.5961	23.5904	0.0043808	pP2(2.5)
2172.0283	1.16E-21	2195.6187	23.5904	0.0003129	pQ12(2.5)
2176.007	1.65E-20	2187.8207	11.8137	0.0043808	pP1(2.5)
2176.0162	9.17E-21	2187.8071	11.7909	0.0024338	pP2(1.5)
2176.0298	1.83E-21	2187.8207	11.7909	0.0004868	pQ12(1.5)
2179.9798	9.29E-21	2183.9193	3.9395	0.0024338	pP1(1.5)
2179.9935	4.65E-21	2183.9193	3.9258	0.0012169	pQ12(0.5)
2187.8071	4.69E-21	2187.8071	0	0.0012169	rQ21(0.5)
2187.8207	9.38E-21	2187.8207	0	0.0024338	rR1(0.5)
2191.6567	1.87E-21	2195.5961	3.9395	0.0004868	rQ21(1.5)
2191.6703	9.34E-21	2195.5961	3.9258	0.0024338	rR2(0.5)
2191.6793	1.68E-20	2195.6187	3.9395	0.0043808	rR1(1.5)
2195.4679	1.19E-21	2207.2815	11.8137	0.0003129	rQ21(2.5)
2195.4907	1.67E-20	2207.2815	11.7909	0.0043808	rR2(1.5)
2195.4996	2.38E-20	2207.3132	11.8137	0.0062583	rR1(2.5)
2199.2406	8.68E-22	2222.8629	23.6223	0.0002318	rQ21(3.5)
2199.2725	2.34E-20	2222.8629	23.5904	0.0062583	rR2(2.5)
2199.2813	3.04E-20	2222.9036	23.6223	0.0081126	rR1(3.5)
2202.9747	6.76E-22	2242.3396	39.3649	0.0001844	rQ21(4.5)
2203.0157	2.98E-20	2242.3396	39.324	0.0081126	rR2(3.5)
2203.0244	3.65E-20	2242.3894	39.3649	0.0099564	rR1(4.5)
2206.6699	5.47E-22	2265.7109	59.0409	0.0001532	rQ21(5.5)
2206.72	3.56E-20	2265.7109	58.9909	0.0099564	rR2(4.5)
2206.7287	4.21E-20	2265.7697	59.0409	0.0117945	rR1(5.5)
2210.3262	4.53E-22	2292.9758	82.6496	0.000131	rQ21(6.5)
2210.3854	4.08E-20	2292.9758	82.5904	0.0117945	rR2(5.5)
2210.3941	4.71E-20	2293.0437	82.6496	0.0136292	rR1(6.5)
2213.9434	3.81E-22	2324.1333	110.1899	0.0001145	rQ21(7.5)
2214.0117	4.54E-20	2324.1333	110.1216	0.0136292	rR2(6.5)
2214.0203	5.15E-20	2324.2102	110.1899	0.0154616	rR1(7.5)

Continued on next page...

Table 7.4 continued.

Frequency cm ⁻¹	Intensity cm ion ⁻¹	E upper cm ⁻¹	E lower cm ⁻¹	Strength	Transition
2217.5213	3.24E-22	2359.1823	141.6609	0.0001017	rQ21(8.5)
2217.5987	4.93E-20	2359.1823	141.5835	0.0154616	rR2(7.5)
2217.6073	5.51E-20	2359.2682	141.6609	0.0172926	rR1(8.5)
2221.0598	2.77E-22	2398.1212	177.0614	0.0000915	rQ21(9.5)
2221.1463	5.25E-20	2398.1212	176.9749	0.0172926	rR2(8.5)
2221.1548	5.8E-20	2398.2162	177.0614	0.0191225	rR1(9.5)
2224.5588	2.39E-22	2440.9486	216.3899	0.00008314	rQ21(10.5)
2224.6544	5.49E-20	2440.9486	216.2943	0.0191225	rR2(9.5)
2224.6628	6.01E-20	2441.0527	216.3899	0.0209517	rR1(10.5)
2228.018	2.06E-22	2487.6629	259.6449	0.00007619	rQ21(11.5)
2228.1227	5.66E-20	2487.6629	259.5402	0.0209517	rR2(10.5)
2228.1311	6.15E-20	2487.776	259.6449	0.0227802	rR1(11.5)
2231.4373	1.78E-22	2538.2622	306.8249	0.00007031	rQ21(12.5)
2231.5512	5.76E-20	2538.2622	306.711	0.0227802	rR2(11.5)
2231.5595	6.22E-20	2538.3844	306.8249	0.0246082	rR1(12.5)
2234.8166	1.54E-22	2592.7445	357.9279	0.00006527	rQ21(13.5)
2234.9396	5.79E-20	2592.7445	357.8049	0.0246082	rR2(12.5)
2234.9479	6.22E-20	2592.8757	357.9279	0.0264359	rR1(13.5)
2238.1558	1.33E-22	2651.1078	412.952	0.00006091	rQ21(14.5)
2238.2879	5.76E-20	2651.1078	412.8199	0.0264359	rR2(13.5)
2238.2961	6.15E-20	2651.248	412.952	0.0282632	rR1(14.5)
2241.4546	1.14E-22	2713.3496	471.895	0.0000571	rQ21(15.5)
2241.5958	5.66E-20	2713.3496	471.7539	0.0282632	rR2(14.5)
2241.6039	6.03E-20	2713.499	471.895	0.0300903	rR1(15.5)
2244.713	9.84E-23	2779.4677	534.7548	0.00005373	rQ21(16.5)
2244.8632	5.51E-20	2779.4677	534.6045	0.0300903	rR2(15.5)
2244.8713	5.85E-20	2779.6261	534.7548	0.0319173	rR1(16.5)
2247.9307	8.46E-23	2849.4595	601.5287	0.00005074	rQ21(17.5)
2248.0901	5.32E-20	2849.4595	601.3694	0.0319173	rR2(16.5)
2248.0981	5.62E-20	2849.6269	601.5287	0.033744	rR1(17.5)
2251.1076	7.25E-23	2923.3221	672.2144	0.00004807	rQ21(18.5)
2251.2761	5.09E-20	2923.3221	672.0459	0.033744	rR2(17.5)
2251.2841	5.36E-20	2923.4985	672.2144	0.0355706	rR1(18.5)
2254.2436	6.19E-23	3001.0527	746.809	0.00004566	rQ21(19.5)
2254.4212	4.83E-20	3001.0527	746.6315	0.0355706	rR2(18.5)
2254.4292	5.07E-20	3001.2382	746.809	0.0373971	rR1(19.5)
2257.3386	5.27E-23	3082.6483	825.3097	0.00004348	rQ21(20.5)
2257.5253	4.54E-20	3082.6483	825.123	0.0373971	rR2(19.5)
2257.5331	4.76E-20	3082.8429	825.3097	0.0392234	rR1(20.5)
2260.3923	4.48E-23	3168.1057	907.7134	0.00004151	rQ21(21.5)
2260.5881	4.23E-20	3168.1057	907.5176	0.0392234	rR2(20.5)
2260.5959	4.43E-20	3168.3093	907.7134	0.0410497	rR1(21.5)
2263.4046	3.79E-23	3257.4215	994.017	0.0000397	rQ21(22.5)
2263.6095	3.92E-20	3257.4215	993.8121	0.0410497	rR2(21.5)
2263.6172	4.09E-20	3257.6342	994.017	0.0428759	rR1(22.5)
2266.3753	3.19E-23	3350.5923	1084.217	0.00003804	rQ21(23.5)
2266.5893	3.6E-20	3350.5923	1084.003	0.0428759	rR2(22.5)
2266.597	3.75E-20	3350.814	1084.217	0.044702	rR1(23.5)
2269.3044	2.68E-23	3447.6145	1178.3101	0.00003652	rQ21(24.5)
2269.5275	3.28E-20	3447.6145	1178.087	0.044702	rR2(23.5)

Continued on next page...

Table 7.4 continued.

Frequency cm ⁻¹	Intensity cm ion ⁻¹	E upper cm ⁻¹	E lower cm ⁻¹	Strength	Transition
2269.5351	3.41E-20	3447.8452	1178.3101	0.0465281	rR1(24.5)
2272.1916	2.24E-23	3548.4841	1276.2925	0.00003512	rQ21(25.5)
2272.4238	2.97E-20	3548.4841	1276.0603	0.0465281	rR2(24.5)
2272.4314	3.09E-20	3548.7239	1276.2925	0.0483541	rR1(25.5)
2275.0368	1.87E-23	3653.1973	1378.1605	0.00003381	rQ21(26.5)
2275.2782	2.67E-20	3653.1973	1377.9192	0.0483541	rR2(25.5)
2275.2857	2.77E-20	3653.4462	1378.1605	0.0501801	rR1(26.5)
2277.8399	1.55E-23	3761.7501	1483.9101	0.00003261	rQ21(27.5)
2278.0904	2.38E-20	3761.7501	1483.6597	0.0501801	rR2(26.5)
2278.0978	2.47E-20	3762.008	1483.9101	0.052006	rR1(27.5)
2280.6007	1.28E-23	3874.138	1593.5373	0.00003148	rQ21(28.5)
2280.8603	2.11E-20	3874.138	1593.2777	0.052006	rR2(27.5)
2280.8677	2.18E-20	3874.4049	1593.5373	0.0538319	rR1(28.5)
2283.319	1.05E-23	3990.3568	1707.0377	0.00003043	rQ21(29.5)
2283.5877	1.86E-20	3990.3568	1706.769	0.0538319	rR2(28.5)
2283.595	1.92E-20	3990.6327	1707.0377	0.0556577	rR1(29.5)
2285.9948	8.59E-24	4110.4018	1824.407	0.00002945	rQ21(30.5)
2286.2725	1.62E-20	4110.4018	1824.1292	0.0556577	rR2(29.5)
2286.2798	1.68E-20	4110.6868	1824.407	0.0574835	rR1(30.5)
2288.6278	7E-24	4234.2684	1945.6406	0.00002853	rQ21(31.5)
2288.9146	1.41E-20	4234.2684	1945.3538	0.0574835	rR2(30.5)
2288.9219	1.46E-20	4234.5625	1945.6406	0.0593093	rR1(31.5)
2291.2178	5.68E-24	4361.9517	2070.7339	0.00002766	rQ21(32.5)
2291.5138	1.22E-20	4361.9517	2070.4379	0.0593093	rR2(31.5)
2291.521	1.25E-20	4362.2549	2070.7339	0.061135	rR1(32.5)
2293.7649	4.58E-24	4493.4467	2199.6819	0.00002685	rQ21(33.5)
2294.0699	1.04E-20	4493.4467	2199.3768	0.061135	rR2(32.5)
2294.077	1.07E-20	4493.7589	2199.6819	0.0629608	rR1(33.5)
2296.2687	3.68E-24	4628.7483	2332.4797	0.00002608	rQ21(34.5)
2296.5828	8.89E-21	4628.7483	2332.1655	0.0629608	rR2(33.5)
2296.5899	9.14E-21	4629.0696	2332.4797	0.0647865	rR1(34.5)
2298.7291	2.94E-24	4767.8511	2469.122	0.00002536	rQ21(35.5)
2299.0524	7.52E-21	4767.8511	2468.7987	0.0647865	rR2(34.5)
2299.0594	7.73E-21	4768.1814	2469.122	0.0666122	rR1(35.5)
2301.146	2.34E-24	4910.7497	2609.6037	0.00002467	rQ21(36.5)
2301.4784	6.33E-21	4910.7497	2609.2712	0.0666122	rR2(35.5)
2301.4854	6.5E-21	4911.089	2609.6037	0.0684378	rR1(36.5)
2303.5193	1.85E-24	5057.4384	2753.9191	0.00002402	rQ21(37.5)
2303.8608	5.29E-21	5057.4384	2753.5776	0.0684378	rR2(36.5)
2303.8677	5.42E-21	5057.7868	2753.9191	0.0702635	rR1(37.5)
2305.8488	1.46E-24	5207.9115	2902.0628	0.00002341	rQ21(38.5)
2306.1994	4.39E-21	5207.9115	2901.7121	0.0702635	rR2(37.5)
2306.2062	4.5E-21	5208.2689	2902.0628	0.0720891	rR1(38.5)
2308.1342	1.15E-24	5362.1631	3054.0288	0.00002282	rQ21(39.5)
2308.494	3.62E-21	5362.1631	3053.6691	0.0720891	rR2(38.5)
2308.5007	3.71E-21	5362.5296	3054.0288	0.0739147	rR1(39.5)
2310.3756	8.94E-25	5520.1871	3209.8114	0.00002226	rQ21(40.5)
2310.7444	2.97E-21	5520.1871	3209.4426	0.0739147	rR2(39.5)
2310.7511	3.04E-21	5520.5626	3209.8114	0.0757403	rR1(40.5)
2312.5727	6.95E-25	5681.9772	3369.4045	0.00002173	rQ21(41.5)

Continued on next page...

Table 7.4 continued.

Frequency cm ⁻¹	Intensity cm ion ⁻¹	E upper cm ⁻¹	E lower cm ⁻¹	Strength	Transition
2312.9506	2.42E-21	5681.9772	3369.0265	0.0757403	rR2(40.5)
2312.9573	2.48E-21	5682.3618	3369.4045	0.0775659	rR1(41.5)
2314.7254	5.37E-25	5847.5271	3532.8018	0.00002123	rQ21(42.5)
2315.1124	1.96E-21	5847.5271	3532.4147	0.0775659	rR2(41.5)
2315.119	2.01E-21	5847.9208	3532.8018	0.0793915	rR1(42.5)
2316.8335	4.13E-25	6016.8303	3699.9969	0.00002075	rQ21(43.5)
2317.2296	1.58E-21	6016.8303	3699.6007	0.0793915	rR2(42.5)
2317.2361	1.62E-21	6017.233	3699.9969	0.0812171	rR1(43.5)
2318.8968	3.16E-25	6189.8801	3870.9833	0.00002028	rQ21(44.5)
2319.3021	1.27E-21	6189.8801	3870.578	0.0812171	rR2(43.5)
2319.3086	1.29E-21	6190.2919	3870.9833	0.0830426	rR1(44.5)
2320.9153	2.41E-25	6366.6697	4045.7544	0.00001984	rQ21(45.5)
2321.3297	1.01E-21	6366.6697	4045.34	0.0830426	rR2(44.5)
2321.3361	1.03E-21	6367.0905	4045.7544	0.0848682	rR1(45.5)
2322.8888	1.82E-25	6547.192	4224.3033	0.00001942	rQ21(46.5)
2323.3123	7.97E-22	6547.192	4223.8798	0.0848682	rR2(45.5)
2323.3186	8.14E-22	6547.6219	4224.3033	0.0866937	rR1(46.5)
2324.8171	1.37E-25	6731.44	4406.623	0.00001902	rQ21(47.5)
2325.2496	6.27E-22	6731.44	4406.1904	0.0866937	rR2(46.5)
2325.2559	6.4E-22	6731.8789	4406.623	0.0885193	rR1(47.5)
2326.7	1.03E-25	6919.4064	4592.7064	0.00001863	rQ21(48.5)
2327.1417	4.9E-22	6919.4064	4592.2647	0.0885193	rR2(47.5)
2327.1479	5E-22	6919.8543	4592.7064	0.0903448	rR1(48.5)
2328.5374	7.69E-26	7111.0836	4782.5462	0.00001826	rQ21(49.5)
2328.9882	3.81E-22	7111.0836	4782.0954	0.0903448	rR2(48.5)

7.3.3 Indirect Terahertz Spectroscopy of HCO⁺

In the initial demonstration of velocity modulation spectroscopy, Gudeman measured the ν_1 band origin to be 3088.727 cm⁻¹, [20] however, only R-branch transitions were measured. Later, Amano confirmed the assignments of the J values made by Gudeman and determined that the band origin was 0.012 cm⁻¹ higher. Since then, HCO⁺ has been studied by numerous investigators. [185, 188–196]

For our purposes, the $J = 0 \rightarrow 1$ transition was originally measured to be near 89.188545 GHz. [23]. More accurate measurements of the rotational constant yield the $J = 0 \rightarrow 1$ transition to be 89.188542 GHz. [195]. The infrared transition strength of HCO⁺ was calculated to be between 0.168 Debye [197] and 0.215 Debye. [198]

From the rovibrational work which has been performed previously at 30 MHz accuracy, [192] the band origin was measured to be 3088.73951 cm⁻¹. The rotational constants used for this analysis kept the ground state constants fixed to the microwave values of $B_0=1.487509736$, $D_0=2.74823 \times 10^{-6}$. [199] and the upper state constants were allowed to float, and were determined to be $B_1=1.475699$ and $D_1=2.68 \times 10^{-6}$. [192]

Based on the rovibrational transitions previously measured, a simulated spectrum is shown in Figure 7.9, and the fraction of band is shown as a function of rotational temperature between 30 and 1000 K in Figure 7.10. A list of the transition frequencies is shown in Table 7.5.

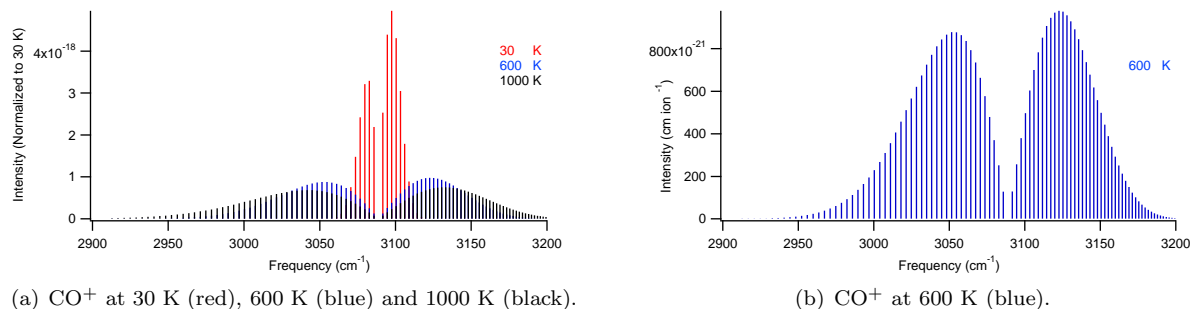


Figure 7.9: Spectra of HCO^+ .

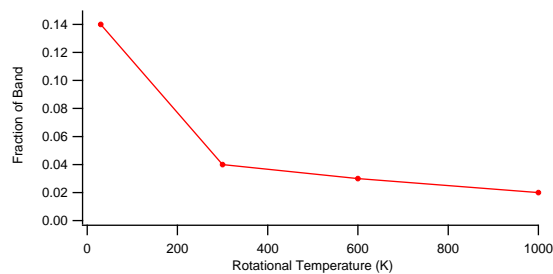


Figure 7.10: Fraction of band for HCO^+ as a function of rotational temperature.

Table 7.5: Rovibrational spectrum of HCO^+ calculated with PGo-pher.

Frequency cm^{-1}	Intensity cm ion^{-1}	E upper cm^{-1}	E lower cm^{-1}	Strength	Transition
2912.8359	7.13E-22	6688.1154	3775.2795	0.4704	P(50)
2916.8555	9.96E-22	6544.7581	3627.9026	0.460992	P(49)
2920.8565	1.38E-21	6404.2765	3483.42	0.451584	P(48)
2924.839	1.9E-21	6266.6738	3341.8347	0.442176	P(47)
2928.8028	2.6E-21	6131.9529	3203.1502	0.432768	P(46)
2932.7476	3.53E-21	6000.1169	3067.3693	0.42336	P(45)
2936.6734	4.75E-21	5871.1685	2934.4951	0.413952	P(44)
2940.58	6.35E-21	5745.1107	2804.5307	0.404544	P(43)
2944.4674	8.42E-21	5621.9462	2677.4789	0.395136	P(42)
2948.3353	1.11E-20	5501.6777	2553.3425	0.385728	P(41)
2952.1836	1.45E-20	5384.3079	2432.1243	0.37632	P(40)
2956.0122	1.88E-20	5269.8393	2313.8271	0.366912	P(39)
2959.821	2.41E-20	5158.2744	2198.4534	0.357504	P(38)
2963.6098	3.08E-20	5049.6157	2086.0059	0.348096	P(37)

Continued on next page...

Table 7.5 continued.

Frequency cm ⁻¹	Intensity cm ion ⁻¹	E upper cm ⁻¹	E lower cm ⁻¹	Strength	Transition
2967.3785	3.9E-20	4943.8655	1976.487	0.338688	P(36)
2971.127	4.91E-20	4841.0262	1869.8992	0.32928	P(35)
2974.8552	6.12E-20	4741.1	1766.2448	0.319872	P(34)
2978.5629	7.57E-20	4644.0891	1665.5262	0.310464	P(33)
2982.25	9.3E-20	4549.9956	1567.7456	0.301056	P(32)
2985.9164	1.13E-19	4458.8216	1472.9052	0.291648	P(31)
2989.562	1.37E-19	4370.5691	1381.0071	0.28224	P(30)
2993.1867	1.64E-19	4285.2401	1292.0533	0.272832	P(29)
2996.7904	1.95E-19	4202.8362	1206.0459	0.263424	P(28)
3000.3728	2.29E-19	4123.3595	1122.9866	0.254016	P(27)
3003.9341	2.68E-19	4046.8116	1042.8775	0.244608	P(26)
3007.4739	3.1E-19	3973.1941	965.7202	0.2352	P(25)
3010.9923	3.56E-19	3902.5088	891.5165	0.225792	P(24)
3014.489	4.06E-19	3834.757	820.268	0.216384	P(23)
3017.9641	4.57E-19	3769.9404	751.9763	0.206976	P(22)
3021.4174	5.11E-19	3708.0603	686.6429	0.197568	P(21)
3024.8488	5.66E-19	3649.1181	624.2693	0.18816	P(20)
3028.2582	6.21E-19	3593.1151	564.8569	0.178752	P(19)
3031.6456	6.74E-19	3540.0525	508.4069	0.169344	P(18)
3035.0107	7.25E-19	3489.9314	454.9206	0.159936	P(17)
3038.3536	7.71E-19	3442.7529	404.3993	0.150528	P(16)
3041.6741	8.11E-19	3398.5181	356.844	0.14112	P(15)
3044.9721	8.43E-19	3357.228	312.2558	0.131712	P(14)
3048.2476	8.66E-19	3318.8833	270.6357	0.122304	P(13)
3051.5004	8.78E-19	3283.4851	231.9846	0.112896	P(12)
3054.7306	8.77E-19	3251.034	196.3034	0.103488	P(11)
3057.9379	8.64E-19	3221.5307	163.5928	0.09408	P(10)
3061.1223	8.36E-19	3194.9759	133.8536	0.084672	P(9)
3064.2838	7.93E-19	3171.3702	107.0865	0.075264	P(8)
3067.4222	7.35E-19	3150.7141	83.2919	0.065856	P(7)
3070.5375	6.63E-19	3133.0081	62.4706	0.056448	P(6)
3073.6296	5.77E-19	3118.2524	44.6228	0.04704	P(5)
3076.6984	4.79E-19	3106.4475	29.7491	0.037632	P(4)
3079.7439	3.7E-19	3097.5936	17.8497	0.028224	P(3)
3082.7659	2.52E-19	3091.6909	8.925	0.018816	P(2)
3085.7645	1.28E-19	3088.7395	2.975	0.009408	P(1)
3091.6909	1.29E-19	3091.6909	0	0.009408	R(0)
3094.6186	2.57E-19	3097.5936	2.975	0.018816	R(1)
3097.5226	3.8E-19	3106.4475	8.925	0.028224	R(2)
3100.4027	4.97E-19	3118.2524	17.8497	0.037632	R(3)
3103.259	6.04E-19	3133.0081	29.7491	0.04704	R(4)
3106.0913	7E-19	3150.7141	44.6228	0.056448	R(5)
3108.8997	7.83E-19	3171.3702	62.4706	0.065856	R(6)
3111.684	8.52E-19	3194.9759	83.2919	0.075264	R(7)
3114.4443	9.07E-19	3221.5307	107.0865	0.084672	R(8)
3117.1804	9.45E-19	3251.034	133.8536	0.09408	R(9)
3119.8923	9.69E-19	3283.4851	163.5928	0.103488	R(10)
3122.5799	9.78E-19	3318.8833	196.3034	0.112896	R(11)
3125.2433	9.74E-19	3357.228	231.9846	0.122304	R(12)
3127.8824	9.57E-19	3398.5181	270.6357	0.131712	R(13)

Continued on next page...

Table 7.5 continued.

Frequency cm ⁻¹	Intensity cm ion ⁻¹	E upper cm ⁻¹	E lower cm ⁻¹	Strength	Transition
3130.4971	9.29E-19	3442.7529	312.2558	0.14112	R(14)
3133.0873	8.91E-19	3489.9314	356.844	0.150528	R(15)
3135.6531	8.45E-19	3540.0525	404.3993	0.159936	R(16)
3138.1945	7.93E-19	3593.1151	454.9206	0.169344	R(17)
3140.7113	7.37E-19	3649.1181	508.4069	0.178752	R(18)
3143.2035	6.78E-19	3708.0603	564.8569	0.18816	R(19)
3145.6711	6.18E-19	3769.9404	624.2693	0.197568	R(20)
3148.1141	5.58E-19	3834.757	686.6429	0.206976	R(21)
3150.5325	4.99E-19	3902.5088	751.9763	0.216384	R(22)
3152.9261	4.43E-19	3973.1941	820.268	0.225792	R(23)
3155.2951	3.89E-19	4046.8116	891.5165	0.2352	R(24)
3157.6393	3.39E-19	4123.3595	965.7202	0.244608	R(25)
3159.9587	2.93E-19	4202.8362	1042.8775	0.254016	R(26)
3162.2534	2.51E-19	4285.2401	1122.9866	0.263424	R(27)
3164.5233	2.13E-19	4370.5691	1206.0459	0.272832	R(28)
3166.7683	1.79E-19	4458.8216	1292.0533	0.28224	R(29)
3168.9885	1.5E-19	4549.9956	1381.0071	0.291648	R(30)
3171.1839	1.24E-19	4644.0891	1472.9052	0.301056	R(31)
3173.3543	1.02E-19	4741.1	1567.7456	0.310464	R(32)
3175.5	8.32E-20	4841.0262	1665.5262	0.319872	R(33)
3177.6207	6.73E-20	4943.8655	1766.2448	0.32928	R(34)
3179.7165	5.4E-20	5049.6157	1869.8992	0.338688	R(35)
3181.7874	4.3E-20	5158.2744	1976.487	0.348096	R(36)
3183.8334	3.4E-20	5269.8393	2086.0059	0.357504	R(37)
3185.8545	2.67E-20	5384.3079	2198.4534	0.366912	R(38)
3187.8506	2.08E-20	5501.6777	2313.8271	0.37632	R(39)
3189.8219	1.6E-20	5621.9462	2432.1243	0.385728	R(40)
3191.7682	1.23E-20	5745.1107	2553.3425	0.395136	R(41)
3193.6897	9.35E-21	5871.1685	2677.4789	0.404544	R(42)
3195.5862	7.06E-21	6000.1169	2804.5307	0.413952	R(43)
3197.4578	5.29E-21	6131.9529	2934.4951	0.42336	R(44)
3199.3045	3.93E-21	6266.6738	3067.3693	0.432768	R(45)
3201.1263	2.9E-21	6404.2765	3203.1502	0.442176	R(46)
3202.9233	2.13E-21	6544.7581	3341.8347	0.451584	R(47)
3204.6954	1.55E-21	6688.1154	3483.42	0.460992	R(48)
3206.4427	1.12E-21	6834.3453	3627.9026	0.4704	R(49)

7.3.4 Indirect Terahertz Spectroscopy of HCNH⁺ and HCS⁺

Similar simulations and analysis can be performed for HOC⁺, [197, 198, 200, 201] HCNH⁺, [188] and HCS⁺ [202].

7.4 Infrared Spectrum of $\text{C}_3\text{H}_3^{+1}$

After the mid-infrared linewidth and sensitivity has been fully characterized, supersonic cooling should be implemented. Supersonic cooling will involve using a supersonic expansion discharge source, the roots blower connected to the source chamber, a skimmer floated to the beam energy, and an additional cylindrical bender. Once the ion beam is in working order, it will probably be easiest to measure the rotational temperature with HN_2^+ . After a cold ion beam is produced, more complex molecules, like C_3H_3^+ can be studied.

The cyclopropenyl cation ($\text{c-C}_3\text{H}_3^+$) is the smallest of Hückel's aromatics ($4n+2$ π electrons, $n = 0$), and therefore is of great interest to physical organic chemists. In combustion chemistry, it is the dominant cation in both acetylene and benzene flames, [204, 205] representing about 80% of the ion signal. In the context of astrochemistry, the Giotto spacecraft mission to Halley's comet made a probable mass-spectrometric detection of C_3H_3^+ in 1986, [206] an emission line from Jupiter's aurora has been tentatively assigned to $\text{c-C}_3\text{H}_3^+$, [207] and $\text{c-C}_3\text{H}_3^+$ is widely believed to be the precursor to $\text{c-C}_3\text{H}_2$, a ubiquitous molecule in both dense [208] and diffuse [209, 210] interstellar clouds.

Because of the importance of this molecular ion, significant efforts have been undertaken to record its rovibrational spectrum. Low resolution Raman (SO_2 solution) and IR scans (polycrystalline) were first recorded by Craig et al. [211] and this was followed by a Ne matrix spectrum by Maier et al. [212] Infrared photodissociation spectra of complexes between C_3H_3^+ and N_2 were obtained by Dopfer and colleagues; [213, 214] in their experiment the doubly degenerate ν_4 band of $\text{c-C}_3\text{H}_3^+$ was split into two components at 3094 and 3129 cm^{-1} by the presence of the N_2 ligand.

Calculations of the ground and excited vibrational states of the molecule yield the rotational constants. Anharmonic calculations give the band center, and new calculations yield the coriolis constant. The band center for the ν_4 mode was calculated to be 3122.9 cm^{-1} . The rotational constants were determined to be $B_0 = 1.02096 \text{ cm}^{-1}$ and $C_0 = 0.51048 \text{ cm}^{-1}$ for the ground state, and $B_1 = 1.02182 \text{ cm}^{-1}$ and $C_1 = 0.51091 \text{ cm}^{-1}$ for the vibrationally excited state. The coriolis constant for this mode is $\zeta_{44} = -0.0078$. Using these values a spectrum could be simulated using Pgopher at 25K, [176] and is shown in Figure 7.11.

When different rotational temperatures were used, the number of lines above a minimum intensity increased from 780 to 2685 lines. Consequently, the fraction of band for the strongest line decreased from 0.0384 to 0.0023, illustrating the loss of signal strength for spectroscopy resulting from rotationally excited ions. Figure 7.12 illustrates this loss in signal strength with resulting increase in complexity.

Figure 7.13 shows the spectrum in finer detail at the band origin. Different k stacks are vertically offset. The $k=0$ state is missing the even levels, as is predicted by the nuclear spin for a D_{3H} molecule. Comparing

¹Much of this section is adapted from Mills et al. 2012. [203]

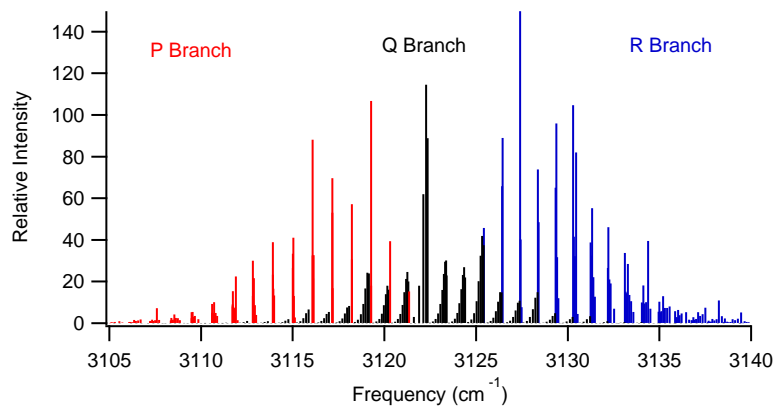


Figure 7.11: The simulated rovibrational spectra of $c\text{-C}_3\text{H}_3^+$ at 25 K.

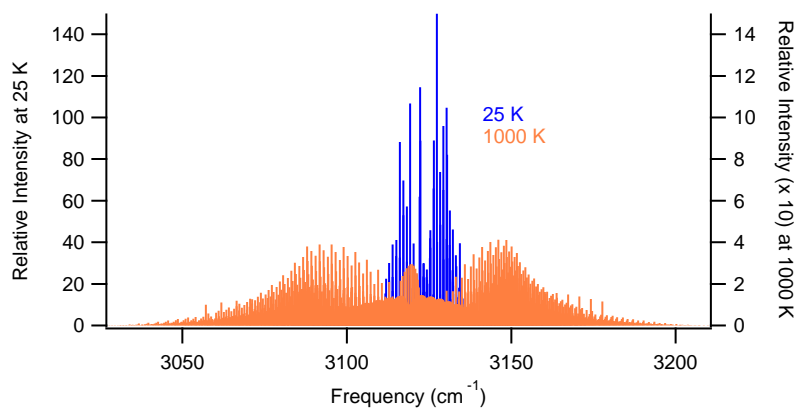


Figure 7.12: Spectra at 25 and 1000 K illustrate the need for thermal relaxation to enable spectroscopy.

the different K stacks, the 4:2:2 intensity alternation between the $k=0$, $k=1$, and $k=3$ stacks is seen.

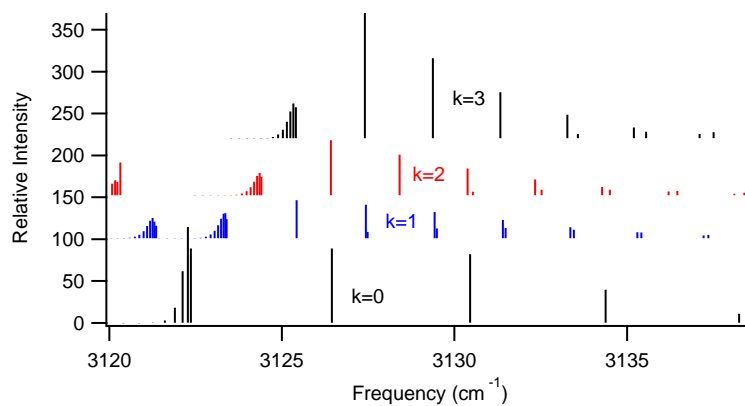


Figure 7.13: Zoom in of band origin. Nuclear spin intensity alternations expected between the $k=0$, $k=1$, and $k=2 \dots$ lines for the same J . Missing even J states expected for $k=0$.

Appendix A

Appendix for Laser Drawings

A.1 Neutral Density Filter Wheels

Schematics for the construction of neutral density filter wheel mounts compatible with the Matisse Ti:Sapphire ring laser are shown in Figure A.1.

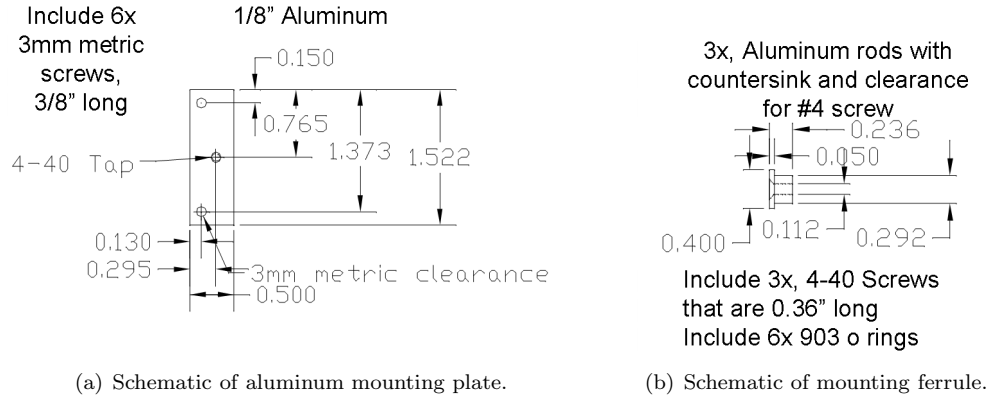
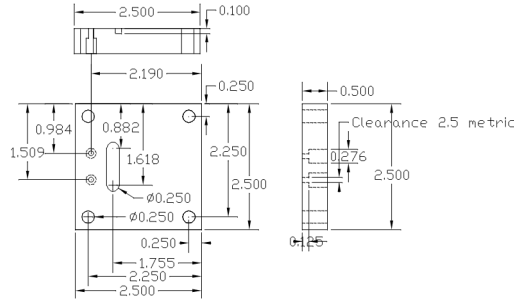


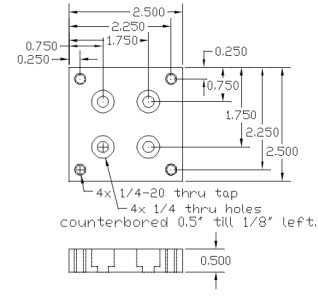
Figure A.1: Neutral density filter wheel assembly.

A.2 SHG Oven Mount

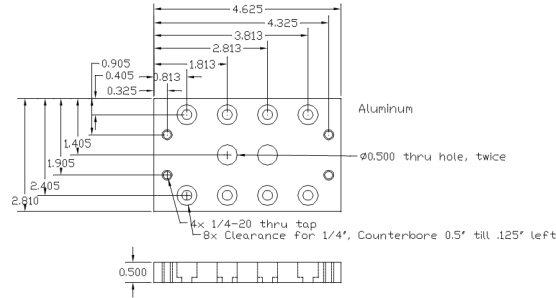
The sum harmonic generation (SHG) PPLN oven was connected to a 3 axis stage (New Focus 9082) using an adapter plate shown in Figure A.2(a). The 3 axis stage was connected to a 1 axis stage (New Focus 9063-COM) with the adapter plate shown in Figure A.2(b). The 1 axis translation stage was connected to another 1 axis translation stage (Thorlabs PT1) with an adapter plate shown in Figure A.2(c). This oven layout allowed for precise alignment of the SHG crystal to the laser beam, in the direction of the laser propagation, transverse horizontally, and transverse vertically allowing for full alignment of the crystal to the optimum position for SHG conversion.



(a) Schematic of SHG top adapter plate.



(b) Schematic of SHG middle adapter plate.



(c) Schematic of SHG bottom adapter plate.

Figure A.2: Mounts for SHG oven interface.

A.3 Frequency Tripler

A frequency tripler, used for third harmonic locking the SHG YAG radiation to an iodine line, was designed and constructed by Jim Wentz of the SCS Electrical Shop. A schematic diagram of the circuit is shown in Figure A.3. The circuit is designed to frequency triple a 10 kHz signal to a 30 kHz reference signal.

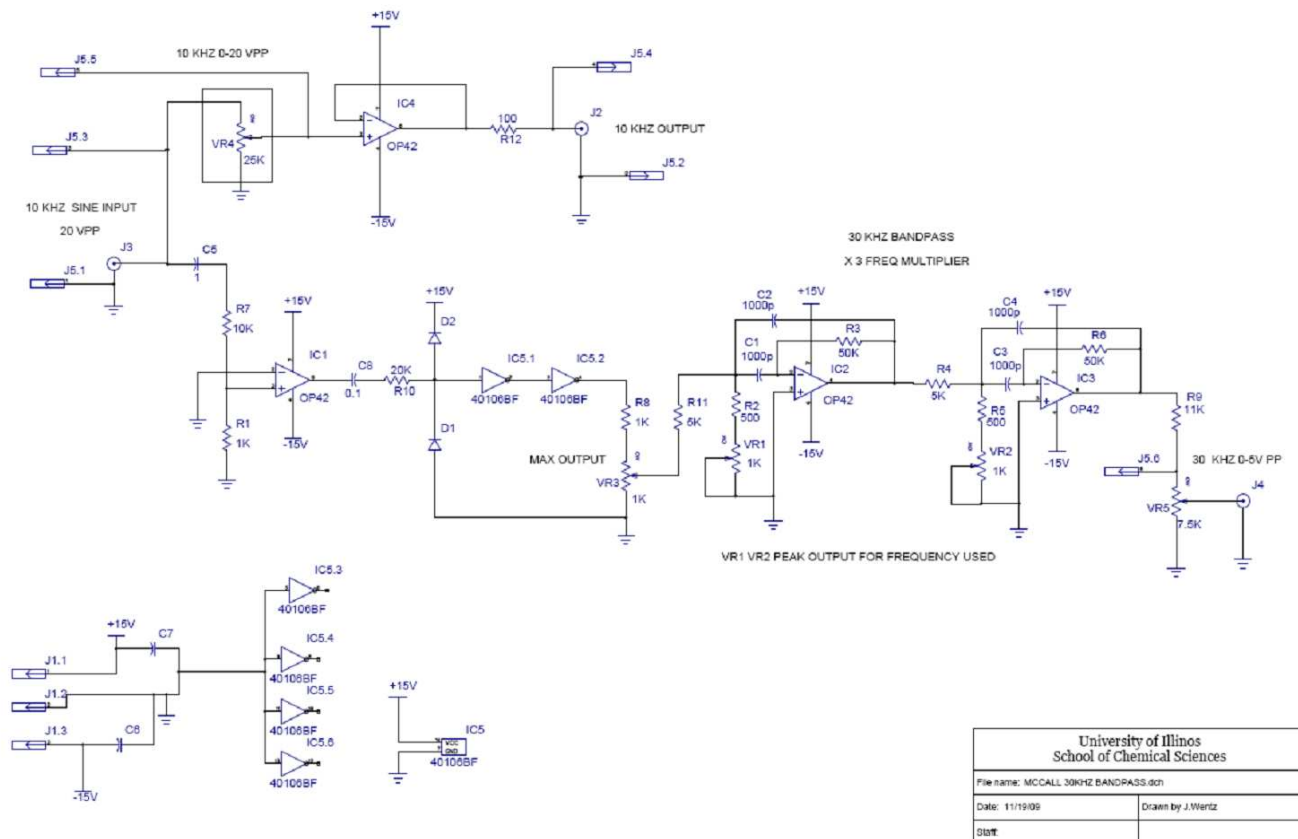
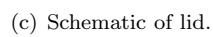
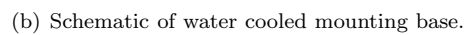
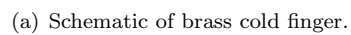


Figure A.3: Electrical schematic for circuit provide a frequency tripler at 10 kHz.

A.4 Peltier Cooling

The Peltier device (CUI Inc CP60333; Digikey 102-1674-ND) is sandwiched between a brass cold finger and the lid of the water cooling with thermal grease on both sides. A 1/8" diameter O-ring (#268) was used to seal the water cooling base to the lid, and NPT fittings were used to connect Swagelok fittings to the water cooling base. A 10A power supply (MG Electronics - PS10AD) was used to power the Peltier device. Schematics for the water cooling parts are shown in Figure A.4. The peltier device has a voltage and current limit of 15 V and 3 A respectively, but the voltage seldom needed to exceed 10 V.



158

A.5 LabWindows Temperature Controller Program

```
\#include <formatio.h>
\#include <cvirte.h>
\#include <rs232.h>
\#include <utility.h>
\#include <userint.h>
\#include "temperature.h"
\#include <string.h>
\#include <stdlib.h>
\#include <stdio.h>
int panel_handle,
    comport = 4,
    baudrate = 115200,
    portindex, // portindex = comport - 1
    parity = 0,
    databits = 8,
    stopbits = 1,
    inputq = 512,
    outputq = 512,
    xmode = 0,
    ctsmode = 0,
    stringsize,
    bytes_sent,
    bytes_read,
    RS232Error,
    config_flag,
    breakstatus,
    port_open,
    com_status,
    send_mode,
    send_byte,
    send_term_index,
    read_term_index,
    read_term = '\r',
    inqlen,          /* Stores result from GetInQLen */
    outqlen,         /* Stores result from GetOutQLen */
stop = 0;
short read_cnt = 1000;
double timeout = 5.0,
    tset;
char devicename[30], // Global Variables are bad for you.
    send_data[500],
    read_data[2000],
//    read_data1[2000],
    tbox_read_data[2000],
    com_msg[500],
    msg[100],
    arg[100];
char status_byte;
/* Internal function prototypes */
void DisplayRS232Error (void);
```

```

void enableComPort (void);
int ProcessEvent (int *stopPtr);
void UpdatePID (void);
void Offset (void);
void BegTMAX (void);
void FirstTemp (void); // Actual Temp
void SetToNormal (void);
void AllDisable (void);
void BegTset (void);
/* This is the application's entry-point. */
int main (int argc, char *argv[])
{
    if (InitCVIRTE (0, argv, 0) == 0)
        return -1;
    if ((panel_handle = LoadPanel (0, "temperature.uir", PANEL)) < 0)
        return -1;
    DisplayPanel (panel_handle);
    enableComPort();
    Delay(0.2);
    FirstTemp();
    AllDisable();
    SetToNormal();
    BegTMAX ();
    BegTset();
    Offset ();
    UpdatePID ();
    RunUserInterface ();
    DiscardPanel (panel_handle);
    return 0;
}
/* Display error information to the user. */
void DisplayRS232Error (void)
{
    char ErrorMessage[200];
    switch (RS232Error)
    {
        default :
            if (RS232Error < 0)
            {
                Fmt (ErrorMessage, "%s<RS232 error number %i", RS232Error);
                MessagePopup ("RS232 Message", ErrorMessage);
            }
            break;
        case 0 :
            MessagePopup ("RS232 Message", "No errors.");
            break;
        case -2 :
            Fmt (ErrorMessage, "%s", "Invalid port number (must be in the "
                "range 1 to 8).");
            MessagePopup ("RS232 Message", ErrorMessage);
            break;
        case -3 :
            Fmt (ErrorMessage, "%s", "No port is open.\n"

```

```

        "Check COM Port setting in Configure.");
        MessagePopup ("RS232 Message", ErrorMessage);
        break;
    case -99 :
        Fmt (ErrorMessage, "%s", "Timeout error.\n\n"
            "Either increase timeout value,\n"
            "        check COM Port setting, or\n"
            "        check device.");
        MessagePopup ("RS232 Message", ErrorMessage);
        break;
    }
}

void enableComPort (void)
{
    SuspendTimerCallbacks();
    port_open = 0; /* initialize flag to 0 - unopened */
    //GetConfigParms ();
    DisableBreakOnLibraryErrors ();
    RS232Error = OpenComConfig (comport, devicename, baudrate, parity,
                                databits, stopbits, inputq, outputq);
    EnableBreakOnLibraryErrors ();
    if (RS232Error) DisplayRS232Error ();
    if (RS232Error == 0) {
        port_open = 1;
        SetXMode (comport, xmode);
        SetCTSMMode (comport, ctsmode);
    }
    send_data[0] = '\r';
    send_data[1] = '\0';
    stringsize = StringLength(send_data);
    bytes_sent = ComWrt (comport, send_data, stringsize);
    FlushInQ(comport);
    FlushOutQ(comport);
    ResumeTimerCallbacks();
}

int ProcessEvent (int *stopPtr){
    *stopPtr = stop;
    return ProcessSystemEvents();
}

int CVICALLBACK QuitProgram (int panel, int control, int event,
    void *callbackData, int eventData1, int eventData2)
{
    SuspendTimerCallbacks();
    Delay(0.1);
    switch (event)
    {
        case EVENT_COMMIT :
            if (port_open){
                FlushOutQ(comport);
                RS232Error = CloseCom (comport);
                if (RS232Error)
                    DisplayRS232Error ();
            }
    }
}

```



```

        QuitUserInterface (0);
        break;
    case EVENT_RIGHT_CLICK :
        //DisplayHelp (QuitHelp);
        break;
    }
    ResumeTimerCallbacks();
    return 0;
}

int CVICALLBACK SetNormal (int panel, int control, int event,
void *callbackData, int eventData1, int eventData2)
{
    switch (event)
    {
    case EVENT_COMMIT:
        SetCtrlAttribute (panel_handle, PANEL_CycleTempSet, ATTR_DIMMED, 1);    // 1 means dimmed
        SetCtrlAttribute (panel_handle, PANEL_Speed, ATTR_DIMMED, 1);
        SetCtrlAttribute (panel_handle, PANEL_Direction, ATTR_DIMMED, 1);
        SetCtrlAttribute (panel_handle, PANEL_CycleStart, ATTR_DIMMED, 1);
        SetCtrlAttribute (panel_handle, PANEL_CycleStop, ATTR_DIMMED, 1);

        SetCtrlAttribute (panel_handle, PANEL_NormalTempSet, ATTR_DIMMED, 0); // 0 means not dimmed
        SetCtrlAttribute (panel_handle, PANEL_NormalEnable, ATTR_DIMMED, 0);
        SetCtrlAttribute (panel_handle, PANEL_NormalDisable, ATTR_DIMMED, 0);
        SetCtrlAttribute (panel_handle, PANEL_Tune, ATTR_DIMMED, 1);
        Delay(0.1);
        FlushInQ(comport);
        FlushOutQ(comport);
        send_data[0] = '\0';    // Read Actual Temperature, set to temp set value.
        strcat(send_data, "tact?\r");
        stringsize = StringLength(send_data);
        bytes_sent = ComWrt (comport, send_data, stringsize);    // send data
        read_data[0] = '\0';    // discard first line, which is ""
        bytes_read = ComRdTerm (comport, read_data, read_cnt, read_term);
        read_data[0] = '\0'; // read second line, which is response from com port
        bytes_read = ComRdTerm (comport, read_data, read_cnt, read_term);
        Delay(0.2);
        FlushInQ(comport);
        FlushOutQ(comport);
        SetCtrlVal (panel_handle, PANEL_NormalTempSet, atof(read_data));
        SetCtrlVal (panel_handle, PANEL_TempSet, atof(read_data));
        SetCtrlVal (panel_handle, PANEL_CURTEMP, atof(read_data));    // Thermometer
        SetCtrlVal (panel_handle, PANEL_newtemp, atof(read_data));    // Indicator below Thermometer
        // check if enabled, dim correct button (enable versus disabled).
        Delay(0.2);
        FlushInQ(comport);
        FlushOutQ(comport);
        strcpy(send_data, "stat?\r"); // get status
        stringsize = StringLength(send_data);
        bytes_sent = ComWrt (comport, send_data, stringsize);
        read_data[0] = '\0'; // read status
        bytes_read = ComRdTerm (comport, read_data, read_cnt, read_term);
        read_data[0] = '\0';

```

```

bytes_read = ComRdTerm (comport, read_data, 2, read_term);
status_byte = 0x10*read_data[0] + read_data[1];
Delay(0.2);
if((status_byte & 0x01) == 0){    // dim the disable, bcz the unit is disabled
SetCtrlAttribute (panel_handle, PANEL_NormalDisable, ATTR_DIMMED, 1);
SetCtrlAttribute (panel_handle, PANEL_Tune, ATTR_DIMMED, 1);
}
else {
// dim the enable, bcz the unit is enabled
//(Won't happen on startup, because there is a automatic disable on startup).
SetCtrlAttribute (panel_handle, PANEL_NormalEnable, ATTR_DIMMED, 1);
SetCtrlAttribute (panel_handle, PANEL_Tune, ATTR_DIMMED, 0);
}
Delay(0.2);
FlushInQ(comport);
FlushOutQ(comport);
// Read offset, set button to on
//(so it can only be detuned) if the instrument has an offset.
send_data[0] = '\0';
strcat(send_data, "tune?\r");
stringsize = StringLength(send_data);
bytes_sent = ComWrt (comport, send_data, stringsize);    // send data
Delay(0.2);
read_data[0] = '\0';    // read response
bytes_read = ComRdTerm (comport, read_data, read_cnt, read_term);
Delay(0.2);
read_data[0] = '\0';    // discard first line, which is "tune?"
bytes_read = ComRdTerm (comport, read_data, read_cnt, read_term);
// read second line, which is response from com port
Delay(0.2);
SetCtrlVal (panel_handle, PANEL_Offset, atof(read_data));
// display Tuning Offset in the main panel,
Delay(0.2);
if (atof(read_data)==0) {
SetCtrlVal (panel_handle, PANEL_Tune, 1);
}
break;
}
return 0;
}

int CVICALLBACK NormalEnable (int panel, int control, int event,
void *callbackData, int eventData1, int eventData2)
{
SuspendTimerCallbacks();
switch (event)
{
case EVENT_COMMIT:
SetCtrlAttribute (panel_handle, PANEL_NormalEnable, ATTR_DIMMED, 1);
SetCtrlAttribute (panel_handle, PANEL_NormalDisable, ATTR_DIMMED, 0);
// Read set temperature and enable the heater.
GetCtrlVal (panel_handle, PANEL_NormalTempSet, &tset);
FlushInQ(comport);
FlushOutQ(comport);

```

```

send_data[0] = '\0';
arg[0] = '\0';
strcat(send_data, "tset=");
sprintf(arg, "%.1f", tset);
strcat(send_data, arg);
strcat(send_data, "\r");
stringsize = StringLength(send_data);
bytes_sent = ComWrt (comport, send_data, stringsize);
Delay(0.2);
// Enable heater
FlushInQ(comport);
FlushOutQ(comport);
strcpy(send_data, "stat?\r");
stringsize = StringLength(send_data);
bytes_sent = ComWrt (comport, send_data, stringsize);
read_data[0] = '\0';
bytes_read = ComRdTerm (comport, read_data, read_cnt, read_term);
read_data[0] = '\0';
bytes_read = ComRdTerm (comport, read_data, 2, read_term);
status_byte = 0x10*read_data[0] + read_data[1];
Delay(0.2);
if((status_byte & 0x01) == 0){
FlushInQ(comport);
FlushOutQ(comport);
strcpy(send_data, "ens\r");
stringsize = StringLength(send_data);
bytes_sent = ComWrt (comport, send_data, stringsize);
SetCtrlAttribute (panel_handle, PANEL_Tune, ATTR_DIMMED, 0);
}

break;
}
ResumeTimerCallbacks();
return 0;
}

int CVICALLBACK NormalDisable (int panel, int control, int event,
void *callbackData, int eventData1, int eventData2)
{
SuspendTimerCallbacks();
switch (event)
{
case EVENT_COMMIT:
SetCtrlAttribute (panel_handle, PANEL_NormalEnable, ATTR_DIMMED, 0);
SetCtrlAttribute (panel_handle, PANEL_NormalDisable, ATTR_DIMMED, 1);

// Disable the heater.
FlushInQ(comport);
FlushOutQ(comport);
strcpy(send_data, "stat?\r");
stringsize = StringLength(send_data);
bytes_sent = ComWrt (comport, send_data, stringsize);
read_data[0] = '\0';
bytes_read = ComRdTerm (comport, read_data, read_cnt, read_term);

```

```

read_data[0] = '\0';
bytes_read = ComRdTerm (comport, read_data, 2, read_term);
status_byte = 0x10*read_data[0] + read_data[1];
Delay(0.2);
if((status_byte & 0x01) != 0){
FlushInQ(comport);
FlushOutQ(comport);
strcpy(send_data, "ens\r");
stringsize = StringLength(send_data);
bytes_sent = ComWrt (comport, send_data, stringsize);
SetCtrlAttribute (panel_handle, PANEL_Tune, ATTR_DIMMED, 1);
}
break;
}
ResumeTimerCallbacks();
return 0;
}

int CVICALLBACK Tune (int panel, int control, int event,
void *callbackData, int eventData1, int eventData2)
{
SuspendTimerCallbacks();
switch (event)
{
case EVENT_COMMIT:
Delay(0.2);
FlushInQ(comport); // flush any leftovers from previous operations
FlushOutQ(comport);
send_data[0] = '\0';
strcpy(send_data, "tune\r");
stringsize = StringLength(send_data);
bytes_sent = ComWrt (comport, send_data, stringsize); // send data
Delay(0.2);
break;
}
ResumeTimerCallbacks();
return 0;
}

int CVICALLBACK Cycle (int panel, int control, int event,
void *callbackData, int eventData1, int eventData2)
{
SuspendTimerCallbacks();
switch (event)
{
case EVENT_COMMIT:
SetCtrlAttribute (panel_handle, PANEL_CycleTempSet, ATTR_DIMMED, 0);
SetCtrlAttribute (panel_handle, PANEL_Speed, ATTR_DIMMED, 0);
SetCtrlAttribute (panel_handle, PANEL_Direction, ATTR_DIMMED, 0);
SetCtrlAttribute (panel_handle, PANEL_CycleStart, ATTR_DIMMED, 0);
SetCtrlAttribute (panel_handle, PANEL_NormalTempSet, ATTR_DIMMED, 1);
SetCtrlAttribute (panel_handle, PANEL_NormalEnable, ATTR_DIMMED, 1);
SetCtrlAttribute (panel_handle, PANEL_NormalDisable, ATTR_DIMMED, 1);
SetCtrlAttribute (panel_handle, PANEL_Tune, ATTR_DIMMED, 1);
break;
}
}

```

```

}
ResumeTimerCallbacks();
return 0;
}
int CVICALLBACK CycleStart (int panel, int control, int event,
void *callbackData, int eventData1, int eventData2)
{
double Direction;
double settemp;
double curtemp;
double speed;
double increment; // per second
double cursettemp;
char arg[100];
double curstep, numsteps, l;
double current_temp, previous_temp;
SuspendTimerCallbacks();
switch (event)
{
case EVENT_COMMIT:
GetCtrlVal (panel_handle, PANEL_CycleTempSet, &settemp); // Read cycle set temp,
GetCtrlVal (panel_handle, PANEL_Direction, &Direction); // Read Direction
Delay(0.2);
FlushInQ(comport);
FlushOutQ(comport);
send_data[0] = '\0'; // get current temperature value.
strcat(send_data, "tact?\r");
stringsize = StringLength(send_data);
bytes_sent = ComWrt (comport, send_data, stringsize);
read_data[0] = '\0'; // read first line of response
bytes_read = ComRdTerm (comport, read_data, read_cnt, read_term);
read_data[0] = '\0'; // discard first line, which is "tact?"
bytes_read = ComRdTerm (comport, read_data, read_cnt, read_term);
// read second line, which is response from com port
curtemp = atof(read_data);
cursettemp = curtemp;
GetCtrlVal (panel_handle, PANEL_Speed, &speed); // Read cycle speed.
increment = speed / 60 * Direction; // * Direction
FlushInQ(comport);
FlushOutQ(comport);
send_data[0] = '\0'; // set initial temperature
arg[0] = '\0';
strcat(send_data, "tset=");
sprintf(arg, "%.1f", curtemp);
strcat(send_data, arg);
strcat(send_data, "\r");
stringsize = StringLength(send_data);
bytes_sent = ComWrt (comport, send_data, stringsize);
// Enable heater
Delay(0.2);
FlushInQ(comport);
FlushOutQ(comport);
send_data[0]='\0';

```

```

strcpy(send_data, "stat?\r"); // find out if heater is on
stringsize = StringLength(send_data);
bytes_sent = ComWrt (comport, send_data, stringsize);
Delay (0.2);
read_data[0] = '\0';
bytes_read = ComRdTerm (comport, read_data, read_cnt, read_term);
read_data[0] = '\0';
bytes_read = ComRdTerm (comport, read_data, read_cnt, read_term);
read_data[0] = '\0';
bytes_read = ComRdTerm (comport, read_data, 2, read_term);
status_byte = 0x10*((int)read_data[0]-'0') + ((int)read_data[1]-'0');
// This part of the code isn't working right.
//status_byte = 10*read_data[0] + read_data[1];
// This part of the code isn't working right.
if((status_byte & 0x01) == 0){
FlushInQ(comport);
FlushOutQ(comport);
strcpy(send_data, "ens\r");
stringsize = StringLength(send_data);
bytes_sent = ComWrt (comport, send_data, stringsize);
}
Delay(.2);
SetCtrlAttribute (panel_handle, PANEL_CycleStop, ATTR_DIMMED, 0);
SetCtrlAttribute (panel_handle, PANEL_CycleStart, ATTR_DIMMED, 1);
curstep = 0;
numsteps = (settemp - cursettemp)/increment;
SetCtrlAttribute (panel_handle, PANEL_Normal, ATTR_DIMMED, 1);
SetCtrlAttribute (panel_handle, PANEL_CycleTempSet, ATTR_DIMMED, 1);
SetCtrlAttribute (panel_handle, PANEL_Speed, ATTR_DIMMED, 1);
SetCtrlAttribute (panel_handle, PANEL_Direction, ATTR_DIMMED, 1);
SetCtrlAttribute (panel_handle, PANEL_Quit, ATTR_DIMMED, 1);
SetCtrlAttribute (panel_handle, PANEL_TMAXSETTING, ATTR_DIMMED, 1);
SetCtrlAttribute (panel_handle, PANEL_getTmax, ATTR_DIMMED, 1);
SetCtrlAttribute (panel_handle, PANEL_GetOffset, ATTR_DIMMED, 1);
SetCtrlAttribute (panel_handle, PANEL_PIDUpdate, ATTR_DIMMED, 1);
SetCtrlAttribute (panel_handle, PANEL_Proportional, ATTR_DIMMED, 1);
SetCtrlAttribute (panel_handle, PANEL_Integral, ATTR_DIMMED, 1);
SetCtrlAttribute (panel_handle, PANEL_Derivative, ATTR_DIMMED, 1);
SetCtrlAttribute (panel_handle, PANEL_GetTemp, ATTR_DIMMED, 1);
SetCtrlAttribute (panel_handle, PANEL_TempNow, ATTR_DIMMED, 1);
while(curstep < numsteps && !stop){
//while ((cursettemp <= settemp) && !stop){
cursettemp += increment;
curstep++;
Delay(0.3); // This is the major delay change
FlushInQ(comport); // flush any leftovers from previous operations
FlushOutQ(comport);
send_data[0] = '\0';
arg[0] = '\0';
strcat(send_data, "tset=");
sprintf(arg, "%.1f", cursettemp);
strcat(send_data, arg);
strcat(send_data, "\r");

```

```

stringsize = StringLength(send_data);
bytes_sent = ComWrt (comport, send_data, stringsize);
Delay(0.3);
SetCtrlVal (panel_handle, PANEL_TempSet, cursettemp);
SetCtrlVal (panel_handle, PANEL_NormalTempSet, cursettemp);
// read current temperature
FlushInQ(comport); // flush any leftovers from previous operations
FlushOutQ(comport);
send_data[0] = '\0';
strcat(send_data, "tact?\r");
stringsize = StringLength(send_data);
bytes_sent = ComWrt (comport, send_data, stringsize); // send data
// read response
read_data[0] = '\0'; // discard first line, which is ""
bytes_read = ComRdTerm (comport, read_data, read_cnt, read_term);
read_data[0] = '\0'; // read second line, which is response from com port
bytes_read = ComRdTerm (comport, read_data, read_cnt, read_term);
// flush any leftovers
Delay(0.3);
// display Current Temperature in the main panel, in double form
SetCtrlVal (panel_handle, PANEL_CURTEMP, atof(read_data));
// Thermometer
SetCtrlVal (panel_handle, PANEL_newtemp, atof(read_data));
// Indicator below Thermometer

ProcessEvent(&stop);
}
stop = 0;
Delay (0.5);
//Delay(600.0); // end of cycle delay
// read current temperature
FlushInQ(comport); // flush any leftovers from previous operations
FlushOutQ(comport);
send_data[0] = '\0';
strcat(send_data, "tact?\r");
stringsize = StringLength(send_data);
bytes_sent = ComWrt (comport, send_data, stringsize); // send data
// read response
read_data[0] = '\0'; // discard first line, which is ""
bytes_read = ComRdTerm (comport, read_data, read_cnt, read_term);
read_data[0] = '\0'; // read second line, which is response from com port
bytes_read = ComRdTerm (comport, read_data, read_cnt, read_term);
// flush any leftovers
Delay(0.3);
// display Current Temperature in the main panel, in double form
SetCtrlVal (panel_handle, PANEL_CURTEMP, atof(read_data));
// Thermometer
SetCtrlVal (panel_handle, PANEL_newtemp, atof(read_data));
// Indicator below Thermometer
current_temp = atof(read_data);
if(Direction > 0)
Delay(10.0);
else

```

```

Delay(30.0);
do {
// read current temperature
FlushInQ(comport); // flush any leftovers from previous operations
FlushOutQ(comport);
send_data[0] = '\0';
strcat(send_data, "tact?\r");
stringsize = StringLength(send_data);
bytes_sent = ComWrt (comport, send_data, stringsize); // send data
// read response
read_data[0] = '\0'; // discard first line, which is ""
bytes_read = ComRdTerm (comport, read_data, read_cnt, read_term);
read_data[0] = '\0'; // read second line, which is response from com port
bytes_read = ComRdTerm (comport, read_data, read_cnt, read_term);
// flush any leftovers
Delay(0.3);
// display Current Temperature in the main panel, in double form
SetCtrlVal (panel_handle, PANEL_CURTEMP, atof(read_data));
// Thermometer
SetCtrlVal (panel_handle, PANEL_newtemp, atof(read_data));
// Indicator below Thermometer
previous_temp = current_temp;
current_temp = atof(read_data);
if(Direction > 0)
Delay(10.0);
else
Delay(30.0);
} while((current_temp >= previous_temp + 0.05) || (current_temp <= previous_temp - 0.05));
Delay(0.2);
FlushInQ(comport); // flush any leftovers from previous operations
FlushOutQ(comport);
send_data[0] = '\0';
strcat(send_data, "tact?\r");
stringsize = StringLength(send_data);
bytes_sent = ComWrt (comport, send_data, stringsize); // send data
// read response
read_data[0] = '\0'; // discard first line, which is ""
bytes_read = ComRdTerm (comport, read_data, read_cnt, read_term);
read_data[0] = '\0'; // read second line, which is response from com port
bytes_read = ComRdTerm (comport, read_data, read_cnt, read_term);
SetCtrlAttribute (panel_handle, PANEL_Normal, ATTR_DIMMED, 0);
SetCtrlAttribute (panel_handle, PANEL_CycleTempSet, ATTR_DIMMED, 0);
SetCtrlAttribute (panel_handle, PANEL_Speed, ATTR_DIMMED, 0);
SetCtrlAttribute (panel_handle, PANEL_Direction, ATTR_DIMMED, 0);
SetCtrlAttribute (panel_handle, PANEL_Quit, ATTR_DIMMED, 0);
SetCtrlAttribute (panel_handle, PANEL_TMAXSETTING, ATTR_DIMMED, 0);
SetCtrlAttribute (panel_handle, PANEL_getTmax, ATTR_DIMMED, 0);
SetCtrlAttribute (panel_handle, PANEL_GetOffset, ATTR_DIMMED, 0);
SetCtrlAttribute (panel_handle, PANEL_PIDUpdate, ATTR_DIMMED, 0);
SetCtrlAttribute (panel_handle, PANEL_Proportional, ATTR_DIMMED, 0);
SetCtrlAttribute (panel_handle, PANEL_Integral, ATTR_DIMMED, 0);
SetCtrlAttribute (panel_handle, PANEL_Derivative, ATTR_DIMMED, 0);
SetCtrlAttribute (panel_handle, PANEL_GetTemp, ATTR_DIMMED, 0);

```



```

SetCtrlAttribute (panel_handle, PANEL_TempNow, ATTR_DIMMED, 0);
if(atof(read_data)>50){
SetCtrlVal (panel_handle, PANEL_CycleTempSet, settemp);
SetCtrlAttribute (panel_handle, PANEL_CycleTempSet, ATTR_DIMMED, 1);
SetCtrlAttribute (panel_handle, PANEL_Speed, ATTR_DIMMED, 1);
SetCtrlAttribute (panel_handle, PANEL_Direction, ATTR_DIMMED, 1);
SetCtrlAttribute (panel_handle, PANEL_CycleStart, ATTR_DIMMED, 1);
SetCtrlAttribute (panel_handle, PANEL_CycleStop, ATTR_DIMMED, 1);
SetCtrlAttribute (panel_handle, PANEL_NormalTempSet, ATTR_DIMMED, 0);
SetCtrlAttribute (panel_handle, PANEL_NormalEnable, ATTR_DIMMED, 0);
SetCtrlAttribute (panel_handle, PANEL_NormalDisable, ATTR_DIMMED, 0);
SetCtrlAttribute (panel_handle, PANEL_Tune, ATTR_DIMMED, 0);
SetCtrlAttribute (panel_handle, PANEL_NormalEnable, ATTR_DIMMED, 1);
SetCtrlAttribute (panel_handle, PANEL_NormalDisable, ATTR_DIMMED, 0);
}
else {
Delay(0.2);
FlushInQ(comport);
FlushOutQ(comport);
strcpy(send_data, "stat?\r");
stringsize = StringLength(send_data);
bytes_sent = ComWrt (comport, send_data, stringsize);
read_data[0] = '\0';
bytes_read = ComRdTerm (comport, read_data, read_cnt, read_term);
read_data[0] = '\0';
bytes_read = ComRdTerm (comport, read_data, 2, read_term);
status_byte = 0x10*read_data[0] + read_data[1];
Delay(0.2);
if((status_byte & 0x01) != 0){
FlushInQ(comport);
FlushOutQ(comport);
strcpy(send_data, "ens\r");
stringsize = StringLength(send_data);
bytes_sent = ComWrt (comport, send_data, stringsize);
}
SetCtrlAttribute (panel_handle, PANEL_CycleTempSet, ATTR_DIMMED, 1);
SetCtrlAttribute (panel_handle, PANEL_Speed, ATTR_DIMMED, 1);
SetCtrlAttribute (panel_handle, PANEL_Direction, ATTR_DIMMED, 1);
SetCtrlAttribute (panel_handle, PANEL_CycleStart, ATTR_DIMMED, 1);
SetCtrlAttribute (panel_handle, PANEL_CycleStop, ATTR_DIMMED, 1);

SetCtrlAttribute (panel_handle, PANEL_NormalTempSet, ATTR_DIMMED, 0);
SetCtrlAttribute (panel_handle, PANEL_NormalEnable, ATTR_DIMMED, 0);
SetCtrlAttribute (panel_handle, PANEL_NormalDisable, ATTR_DIMMED, 1);
SetCtrlAttribute (panel_handle, PANEL_Tune, ATTR_DIMMED, 1);
}
break;
}
ResumeTimerCallbacks();
return 0;
}

int CVICALLBACK CycleStop (int panel, int control, int event,
void *callbackData, int eventData1, int eventData2)

```

```

{
SuspendTimerCallbacks();
switch (event)
{
case EVENT_COMMIT:
stop = 1; // Stop cycle and turn to normal mode.
break;
}
ResumeTimerCallbacks();
return 0;
}

int CVICALLBACK getTmax (int panel, int control, int event,
void *callbackData, int eventData1, int eventData2)
{
SuspendTimerCallbacks();
switch (event)
{
case EVENT_COMMIT:
// flush any leftovers from previous operations
Delay(0.2);
FlushInQ(comport);
FlushOutQ(comport);
// send data
send_data[0] = '\0';
strcat(send_data, "tmax?\r");
stringsize = StringLength(send_data);
bytes_sent = ComWrt (comport, send_data, stringsize);
// read response
// discard first line, which is "tmax?"
read_data[0] = '\0';
bytes_read = ComRdTerm (comport, read_data, read_cnt, read_term);
// read second line, which is response from com port
read_data[0] = '\0';
bytes_read = ComRdTerm (comport, read_data, read_cnt, read_term);
// flush any leftovers
Delay(0.2);
FlushInQ(comport);
FlushOutQ(comport);
// display tmax in the main panel, in both string and double forms
//SetCtrlVal (panel_handle, PANEL_tmax, read_data);
SetCtrlVal (panel_handle, PANEL_tmaxF, atof(read_data));
break;
}
ResumeTimerCallbacks();
return 0;
}

int CVICALLBACK SetTMax (int panel, int control, int event,
void *callbackData, int eventData1, int eventData2)
{
double tmax;
char arg[100];
SuspendTimerCallbacks();
switch (event)

```

```

{
case EVENT_COMMIT:
Delay(0.2);
FlushInQ(comport);
// flush any leftovers from previous operations
FlushOutQ(comport);
GetCtrlVal (panel_handle, PANEL_TMAXSETTING, &tmax);
send_data[0] = '\0';
arg[0] = '\0';
strcat(send_data, "tmax=");
sprintf(arg, "%.1f", tmax);
strcat(send_data, arg);
strcat(send_data, "\r");
stringsize = StringLength(send_data);
bytes_sent = ComWrt (comport, send_data, stringsize);
Delay(0.2);
FlushInQ(comport);
FlushOutQ(comport);
SetCtrlVal (panel_handle, PANEL_tmaxF, tmax);
break;
}
ResumeTimerCallbacks();
return 0;
}
/* int CVICALLBACK TimerTick (int panel, int control, int event,
void *callbackData, int eventData1, int eventData2)
{
char send_timer_data[100] = "tact?\r";
char read_data_timer[1000];
int stringsize_timer = StringLength(send_timer_data);
int bytes_sent_timer, bytes_read_timer;
switch (event){
case EVENT_TIMER_TICK:
if(GetComStat(comport) == 0 && GetInQLen(comport) == 0 && GetOutQLen(comport) == 0){
// if it's not busy
FlushInQ(comport); // flush leftover input/output
FlushOutQ(comport);
bytes_sent_timer = ComWrt (comport, send_timer_data, stringsize_timer);
read_data_timer[0] = '\0';
bytes_read_timer = ComRdTerm (comport, read_data_timer, read_cnt, read_term);
read_data_timer[0] = '\0';
bytes_read_timer = ComRdTerm (comport, read_data_timer, read_cnt, read_term);
SetCtrlVal (panel_handle, PANEL_CURTEMP, atof(read_data_timer));
}
break;
}
return 0;
}*/
int CVICALLBACK GetTemp (int panel, int control, int event,
void *callbackData, int eventData1, int eventData2)
{
SuspendTimerCallbacks();
switch (event)

```

```

{
case EVENT_COMMIT:
// flush any leftovers from previous operations
Delay(0.2);
FlushInQ(comport);
FlushOutQ(comport);
// send data
send_data[0] = '\0';
strcat(send_data, "tset?\r");
stringsize = StringLength(send_data);
bytes_sent = ComWrt (comport, send_data, stringsize);
// read response
// discard first line, which is ""
read_data[0] = '\0';
bytes_read = ComRdTerm (comport, read_data, read_cnt, read_term);
// read second line, which is response from com port
read_data[0] = '\0';
bytes_read = ComRdTerm (comport, read_data, read_cnt, read_term);
// flush any leftovers
FlushInQ(comport);
FlushOutQ(comport);
// display tmax in the main panel, in both string and double forms
//SetCtrlVal (panel_handle, PANEL_tmax, read_data);
SetCtrlVal (panel_handle, PANEL_TempSet, atof(read_data));
break;
}
ResumeTimerCallbacks();
return 0;
}

int CVICALLBACK TempNow (int panel, int control, int event,
void *callbackData, int eventData1, int eventData2)
{
switch (event)
{
case EVENT_COMMIT:
FlushInQ(comport); // flush any leftovers from previous operations
FlushOutQ(comport);
send_data[0] = '\0';
strcat(send_data, "tact?\r");
stringsize = StringLength(send_data);
bytes_sent = ComWrt (comport, send_data, stringsize); // send data
// read response
read_data[0] = '\0'; // discard first line, which is ""
bytes_read = ComRdTerm (comport, read_data, read_cnt, read_term);
read_data[0] = '\0'; // read second line, which is response from com port
bytes_read = ComRdTerm (comport, read_data, read_cnt, read_term);
// flush any leftovers
FlushInQ(comport);
FlushOutQ(comport);
// display Current Temperature in the main panel, in double form
SetCtrlVal (panel_handle, PANEL_CURTEMP, atof(read_data));
// Thermometer
SetCtrlVal (panel_handle, PANEL_newtemp, atof(read_data));

```

```

// Indicator below Thermometer
break;
}
return 0;
}
int CVICALLBACK GetOffset (int panel, int control, int event,
void *callbackData, int eventData1, int eventData2)
{
switch (event)
{
case EVENT_COMMIT:
FlushInQ(comport); // flush any leftovers from previous operations
FlushOutQ(comport);
send_data[0] = '\0';
strcat(send_data, "tune?\r");
stringsize = StringLength(send_data);
bytes_sent = ComWrt (comport, send_data, stringsize); // send data
// read response
read_data[0] = '\0'; // discard first line, which is ""
bytes_read = ComRdTerm (comport, read_data, read_cnt, read_term);
read_data[0] = '\0'; // read second line, which is response from com port
bytes_read = ComRdTerm (comport, read_data, read_cnt, read_term);
FlushInQ(comport); // flush any leftovers
FlushOutQ(comport);
// display Tuning Offset in the main panel, in double form
SetCtrlVal (panel_handle, PANEL_Offset, atof(read_data)); // Offset
break;
}
return 0;
}
int CVICALLBACK PID (int panel, int control, int event,
void *callbackData, int eventData1, int eventData2)
{
switch (event)
{
case EVENT_COMMIT:
UpdatePID();
break;
}
return 0;
}
int CVICALLBACK Proportional (int panel, int control, int event,
void *callbackData, int eventData1, int eventData2)
{
int pset;
char prop[30] = "";
switch (event)
{
case EVENT_COMMIT:
GetCtrlVal (panel_handle, PANEL_Proportional, &pset);
// read desired pid value
sprintf( prop, "%i", pset );
// convert to double with no decimal points

```

```

//SetCtrlVal (panel_handle, PANEL_string, prop);
// display string
FlushInQ(comport); // flush any leftovers from previous operations
FlushOutQ(comport);
send_data[0] = '\0'; // setup to send proportional settings
strcat(send_data, "pgain=");
strcat(send_data, prop);
strcat(send_data, "\r");
stringsize = StringLength(send_data);
bytes_sent = ComWrt (comport, send_data, stringsize);
// send data
break;
}
return 0;
}

int CVICALLBACK Integral (int panel, int control, int event,
void *callbackData, int eventData1, int eventData2)
{
int iset;
char integ[30] = "";

switch (event)
{
case EVENT_COMMIT:
GetCtrlVal (panel_handle, PANEL_Integral, &iset);
// read desired pid value
sprintf( integ, "%i", iset );
// convert to double with no decimal points
//SetCtrlVal (panel_handle, PANEL_string, integ);
// display string
FlushInQ(comport);
// flush any leftovers from previous operations
FlushOutQ(comport);
send_data[0] = '\0';
// setup to send proportional settings
strcat(send_data, "igain=");
strcat(send_data, integ);
strcat(send_data, "\r");
stringsize = StringLength(send_data);
bytes_sent = ComWrt (comport, send_data, stringsize);
// send data
break;
}
return 0;
}

int CVICALLBACK Derivative (int panel, int control, int event,
void *callbackData, int eventData1, int eventData2)
{
int dset;
char deriv[30] = "";
switch (event)
{
case EVENT_COMMIT:

```

```

GetCtrlVal (panel_handle, PANEL_Derivative, &dset);
// read desired pid value
sprintf( deriv, "%i", dset );
// convert to double with no decimal points
//SetCtrlVal (panel_handle, PANEL_string, deriv);
// display string
FlushInQ(comport); // flush any leftovers from previous operations
FlushOutQ(comport);
send_data[0] = '\0'; // setup to send proportional settings
strcat(send_data, "dgain=");
strcat(send_data, deriv);
strcat(send_data, "\r");
stringsize = StringLength(send_data);
bytes_sent = ComWrt (comport, send_data, stringsize);
// send data
break;
}
return 0;
}

int CVICALLBACK NormalTempSet (int panel, int control, int event,
void *callbackData, int eventData1, int eventData2)
{
switch (event)
{
case EVENT_COMMIT:
// Read set temperature and enable the heater.
Delay(0.2);
FlushInQ(comport);
FlushOutQ(comport);
GetCtrlVal (panel_handle, PANEL_NormalTempSet, &tset);
send_data[0] = '\0';
arg[0] = '\0';
strcat(send_data, "tset=");
sprintf(arg, "%.1f", tset);
strcat(send_data, arg);
strcat(send_data, "\r");
stringsize = StringLength(send_data);
bytes_sent = ComWrt (comport, send_data, stringsize);
SetCtrlVal (panel_handle, PANEL_TempSet, tset);
Delay(0.2);
break;
}
return 0;
}

void UpdatePID (void){
int i = 0; // old pid
int j; // old pid
int offset;
char PGAIN[100] = "", IGAIN[100] = "", DGAIN[100] = "";
FlushInQ(comport); // flush any leftovers from previous operations
FlushOutQ(comport);
send_data[0] = '\0'; // setup to request pid settings
strcat(send_data, "pid?\r");

```

```

stringsize = StringLength(send_data);
bytes_sent = ComWrt (comport, send_data, stringsize); // send data
read_data[0] = '\0'; // read response
bytes_read = ComRdTerm (comport, read_data, read_cnt, read_term);
read_data[0] = '\0'; // discard first line, which is "pid?"
for(j = 0; j < 2000; j++)
read_data[j] = '\0';
bytes_read = ComRdTerm (comport, read_data, read_cnt, read_term);
// read second line, which is response from com port
PGAIN[0] = '\0'; // Initialize PID strings to null
IGAIN[0] = '\0';
DGAIN[0] = '\0';
i = 0;
while(read_data[i] >= '0' && read_data[i] <='9'){
PGAIN[i] = read_data[i];
i++;
}
PGAIN[i] = '\0';
i++;
offset = i;
while(read_data[i] >= '0' && read_data[i] <='9'){
IGAIN[i-offset] = read_data[i];
i++;
}
IGAIN[i] = '\0';
i++;
offset = i;
while(read_data[i] >= '0' && read_data[i] <='9'){
DGAIN[i-offset] = read_data[i];
i++;
}
DGAIN[i] = '\0';
Delay(.1);
FlushInQ(comport); // flush any leftovers
FlushOutQ(comport);
SetCtrlVal (panel_handle, PANEL_Proportional, atoi(PGAIN));
// Set Control to match values.
SetCtrlVal (panel_handle, PANEL_Integral, atoi(IGAIN));
SetCtrlVal (panel_handle, PANEL_Derivative, atoi(DGAIN));
}

void Offset (void){
Delay(0.2);
FlushInQ(comport); // flush any leftovers from previous operations
FlushOutQ(comport);
send_data[0] = '\0';
strcat(send_data, "tune?\r");
stringsize = StringLength(send_data);
bytes_sent = ComWrt (comport, send_data, stringsize); // send data
Delay(0.2);
read_data[0] = '\0'; // read response
bytes_read = ComRdTerm (comport, read_data, read_cnt, read_term);
Delay(0.2);
read_data[0] = '\0'; // discard first line, which is "tune?"

```



```

bytes_read = ComRdTerm (comport, read_data, read_cnt, read_term);
// read second line, which is response from com port
Delay(0.2);
SetCtrlVal (panel_handle, PANEL_Offset, atof(read_data));
// display Tuning Offset in the main panel,
Delay(0.2);
}

void BegTMAX (void){ // Read TMAX to Interface
Delay(0.2);
FlushInQ(comport); // flush any leftovers from previous operations
FlushOutQ(comport);
send_data[0] = '\0';
strcat(send_data, "tmax?\r");
stringsize = StringLength(send_data);
bytes_sent = ComWrt (comport, send_data, stringsize);
read_data[0] = '\0'; // discard first line, which is ""
bytes_read = ComRdTerm (comport, read_data, read_cnt, read_term);
read_data[0] = '\0'; // read second line, which is response from com port
bytes_read = ComRdTerm (comport, read_data, read_cnt, read_term);
SetCtrlVal (panel_handle, PANEL_tmaxF, atof(read_data));
// display tmax in the main panel, in double form
SetCtrlVal (panel_handle, PANEL_TMAXSETTING, atof(read_data));
// display tmax in control box
Delay(0.2);
}

void FirstTemp (void){
Delay(0.2);
FlushInQ(comport);
FlushOutQ(comport);
send_data[0] = '\0';
strcat(send_data, "tact?\r");
stringsize = StringLength(send_data);
bytes_sent = ComWrt (comport, send_data, stringsize);
// send data
read_data[0] = '\0'; // discard first line, which is ""
bytes_read = ComRdTerm (comport, read_data, read_cnt, read_term);
read_data[0] = '\0'; // read second line, which is response from com port
bytes_read = ComRdTerm (comport, read_data, read_cnt, read_term);
SetCtrlVal (panel_handle, PANEL_CURTEMP, atof(read_data));
// Thermometer
SetCtrlVal (panel_handle, PANEL_newtemp, atof(read_data));
// Indicator below Thermometer
Delay(0.2);
}

void SetToNormal (void){
Delay(0.2);
FlushInQ(comport);
FlushOutQ(comport);
send_data[0] = '\0';
strcpy(send_data, "mode=normal\r");
stringsize = StringLength(send_data);
bytes_sent = ComWrt (comport, send_data, stringsize);
Delay(0.2);
}

```

```

FlushInQ(comport);
FlushOutQ(comport);
}
void AllEnable (void){
Delay(0.2);
FlushInQ(comport);
FlushOutQ(comport);
strcpy(send_data, "stat?\r");
stringsize = StringLength(send_data);
bytes_sent = ComWrt (comport, send_data, stringsize);
read_data[0] = '\0';
bytes_read = ComRdTerm (comport, read_data, read_cnt, read_term);
read_data[0] = '\0';
bytes_read = ComRdTerm (comport, read_data, 2, read_term);
status_byte = 0x10*read_data[0] + read_data[1];
Delay(0.2);
if((status_byte & 0x01) == 0){
FlushInQ(comport);
FlushOutQ(comport);
strcpy(send_data, "ens\r");
stringsize = StringLength(send_data);
bytes_sent = ComWrt (comport, send_data, stringsize);
}
}
void AllDisable (void){
Delay(0.2);
FlushInQ(comport);
FlushOutQ(comport);
strcpy(send_data, "stat?\r");
stringsize = StringLength(send_data);
bytes_sent = ComWrt (comport, send_data, stringsize);
read_data[0] = '\0';
bytes_read = ComRdTerm (comport, read_data, read_cnt, read_term);
read_data[0] = '\0';
bytes_read = ComRdTerm (comport, read_data, 2, read_term);
status_byte = 0x10*read_data[0] + read_data[1];
Delay(0.2);
if((status_byte & 0x01) != 0){
FlushInQ(comport);
FlushOutQ(comport);
strcpy(send_data, "ens\r");
stringsize = StringLength(send_data);
bytes_sent = ComWrt (comport, send_data, stringsize);
}
}
void BegTset (void){
Delay(0.2);
FlushInQ(comport);
FlushOutQ(comport);
send_data[0] = '\0'; // send data
strcat(send_data, "tset?\r");
stringsize = StringLength(send_data);
bytes_sent = ComWrt (comport, send_data, stringsize);
}

```

```

// read response
// discard first line, which is ""
read_data[0] = '\0';
bytes_read = ComRdTerm (comport, read_data, read_cnt, read_term);
// read second line, which is response from com port
read_data[0] = '\0';
bytes_read = ComRdTerm (comport, read_data, read_cnt, read_term);
// flush any leftovers
Delay(0.2);
FlushInQ(comport);
FlushOutQ(comport);
SetCtrlVal (panel_handle, PANEL_TempSet, atof(read_data));
}

```

A.6 Sellmeier Curve Solving Program

The following is an Igor procedure file used to solve the temperatures for quasi phase matching for the PPLN for difference frequency generation.

```

#pragma rtGlobals=1 // Use modern global access method.
// Main program to solve the temperature for the entire range of wavelengths. function Wavelength-
sAux(IRwavelength, Period)
variable Period
variable IRwavelength
variable TiSapph
variable YAG=1.064
variable c=299792458
variable Temperature
TiSapph=(c/((c/(IRwavelength*0.000001))+c/(YAG/1000000)))*1000000
make/N=4/O coeffs=IRwavelength, TiSapph, YAG, Period
findRoots/Q /L=50000 /H=150000 Solver,coeffs
Temperature=.5*(-546.32+Sqrt(546.32^2+4*(546.32*24.5+V_Root)))
//make /O/D/N=(2000,13) TemperatureArray=Wavelengths(2.8+.001*x, 20+.25*y)
//make /O/N=2000 XWave=2.5+.001*x
return Temperature
end
// Solves temperature for individual wavelength
function Solver(dummyS, f)
wave dummyS // dummyS[0] = lambdaIR, dummyS[1] = lambdaT, dummyS[2] = LambdaY, dummyS[3] = Period
variable f
wave coeffIR
wave coeffT
wave coeffY
make /N=1/O coeffIR=dummyS[0]
make /N=1/O coeffT=dummyS[1]
make /N=1/O coeffY=dummyS[2]
return 1/(n(coeffT,f)/dummyS[1] - n(coeffY,f)/dummyS[2] - n(coeffIR,f)/dummyS[0])-dummyS[3]
end
// Determines the index of refraction
function n (dummy, f)

```

```

wave dummy //dummyT[0]=lambdaT
variable f
wave wave1
return Sqrt(wave1[0] + wave1[6]*f+(wave1[1]+wave1[7]*f)/(dummy[0]^ -(wave1[2]+wave1[8]*f)^ 2)+(wave1[3]
+wave1[9]*f)/(dummy[0]^ 2-wave1[4]^ 2)-wave1[5]*dummy[0]^ 2)
end
// Sets up temperature array
function Wavelengths(IRwavelength, Period)
variable IRwavelength
variable Period
variable i
variable j
make /O/D/N=(2500, 13) TemperatureArray
make /O/N=2500 XWave
for(i = 0; i < 2500; i = i + 1)
XWave[i] = IRwavelength + i*0.001
for(j = 0; j < 13; j = j + 1)
TemperatureArray[i][j] = WavelengthsAux(IRwavelength + i*0.001, Period + j*0.25)
endfor
endfor
end

```

A.7 Sellmeier DFG Temperature Lookup Table

Table A.1: PPLN Temperature for DFG quasi phase matching per poling period.

Pump λ (nm)	Idler $\bar{\nu}$ (cm ⁻¹)	Idler λ (μm)	Poling Period (μm)											
			20	20.25	20.5	20.75	21	21.25	21.5	21.75	22	22.25	22.5	22.75
763.231	3703.7	2.7												
764.028	3690.0	2.71												
764.82	3676.5	2.72												
765.609	3663.0	2.73												
766.393	3649.6	2.74												
767.174	3636.4	2.75												
767.95	3623.2	2.76												
768.722	3610.1	2.77												
769.49	3597.1	2.78												
770.254	3584.2	2.79	108.2											
771.014	3571.4	2.8	119.4											
771.771	3558.7	2.81	130.1											
772.523	3546.1	2.82	140.5											
773.272	3533.6	2.83	150.6											
774.016	3521.1	2.84	160.4											
774.757	3508.8	2.85	170	110										
775.494	3496.5	2.86	179.3	120.4										
776.228	3484.3	2.87	188.3	130.5										
776.957	3472.2	2.88	197.2	140.3										
777.683	3460.2	2.89		149.9										
778.406	3448.3	2.9		159.1										

Continued on next page...

Table A.1 continued.

Pump λ (nm)	Idler $\bar{\nu}$ (cm ⁻¹)	Idler λ (μ m)	Poling Period (μ m)											
			20	20.25	20.5	20.75	21	21.25	21.5	21.75	22	22.25	22.5	22.75
779.124	3436.4	2.91		168.1	108.1									
779.839	3424.7	2.92		176.9	117.9									
780.551	3413.0	2.93		185.4	127.5									
781.259	3401.4	2.94		193.8	136.8									
781.963	3389.8	2.95			145.8									
782.664	3378.4	2.96			154.5									
783.361	3367.0	2.97			163.1	102.5								
784.055	3355.7	2.98			171.4	111.9								
784.746	3344.5	2.99			179.5	120.9								
785.433	3333.3	3			187.4	129.8								
786.117	3322.3	3.01			195.1	138.3								
786.797	3311.3	3.02				146.7								
787.474	3300.3	3.03				154.8								
788.148	3289.5	3.04				162.7	102.1							
788.819	3278.7	3.05				170.4	110.8							
789.486	3268.0	3.06				178	119.3							
790.15	3257.3	3.07				185.3	127.5							
790.811	3246.8	3.08				192.5	135.5							
791.468	3236.3	3.09				199.5	143.2							
792.123	3225.8	3.1					150.8							
792.774	3215.4	3.11					158.2							
793.423	3205.1	3.12					165.3	105.1						
794.068	3194.9	3.13					172.4	113						
794.71	3184.7	3.14					179.2	120.7						
795.349	3174.6	3.15					185.9	128.1						
795.985	3164.6	3.16					192.5	135.4						
796.618	3154.6	3.17					198.9	142.5						
797.248	3144.7	3.18						149.4						
797.875	3134.8	3.19						156.1						
798.499	3125.0	3.2						162.6	102					
799.12	3115.3	3.21						169.1	109.2					
799.739	3105.6	3.22						175.3	116.2					
800.354	3096.0	3.23						181.5	123.1					
801.089	3084.5	3.242						188.6	131					
801.698	3075.0	3.252						194.4	137.4					
802.304	3065.6	3.262							143.7					
802.908	3056.2	3.272							149.9					
803.509	3046.9	3.282							155.9					
804.107	3037.7	3.292							161.7	100.7				
804.702	3028.5	3.302							167.5	107.2				
805.294	3019.3	3.312							173	113.4				
805.884	3010.2	3.322							178.5	119.5				
806.471	3001.2	3.332							183.8	125.5				
807.056	2992.2	3.342							189.1	131.3				
807.638	2983.3	3.352							194.2	136.9				
808.217	2974.4	3.362							199.2	142.4				
808.794	2965.6	3.372								147.8				
809.368	2956.8	3.382								153.1				
809.939	2948.1	3.392								158.2				
810.508	2939.5	3.402								163.2	102			
811.074	2930.8	3.412								168.1	107.6			
811.638	2922.3	3.422								172.9	112.9			
812.199	2913.8	3.432								177.6	118.1			
812.758	2905.3	3.442								182.1	123.2			
813.314	2896.9	3.452								186.6	128.2			

Continued on next page...

Table A.1 continued.

Pump λ (nm)	Idler $\bar{\nu}$ (cm ⁻¹)	Idler λ (μ m)	Poling Period (μ m)											
			20	20.25	20.5	20.75	21	21.25	21.5	21.75	22	22.25	22.5	22.75
813.868	2888.5	3.462								191	133			
814.42	2880.2	3.472								195.3	137.7			
814.969	2871.9	3.482								199.5	142.3			
815.515	2863.7	3.492									146.8			
816.06	2855.5	3.502									151.2			
816.601	2847.4	3.512									155.5			
817.141	2839.3	3.522									159.7			
817.678	2831.3	3.532									163.8	102.1		
818.213	2823.3	3.542									167.8	106.6		
818.745	2815.3	3.552									171.7	110.9		
819.275	2807.4	3.562									175.5	115.2		
819.803	2799.6	3.572									179.2	119.3		
820.329	2791.7	3.582									182.8	123.3		
820.852	2784.0	3.592									186.4	127.2		
821.373	2776.2	3.602									189.9	131.1		
821.892	2768.6	3.612									193.2	134.8		
822.409	2760.9	3.622									196.6	138.4		
822.923	2753.3	3.632									199.8	142		
823.436	2745.7	3.642										145.4		
823.946	2738.2	3.652										148.8		
824.454	2730.8	3.662										152.1		
824.959	2723.3	3.672										155.3		
825.463	2715.9	3.682										158.4		
825.965	2708.6	3.692										161.4		
826.464	2701.2	3.702										164.4	101.8	
826.961	2694.0	3.712										167.3	105	
827.457	2686.7	3.722										170.1	108.1	
827.95	2679.5	3.732										172.8	111.1	
828.441	2672.4	3.742										175.5	114.1	
828.93	2665.3	3.752										178.1	116.9	
829.417	2658.2	3.762										180.6	119.7	
829.902	2651.1	3.772										183	122.4	
830.385	2644.1	3.782										185.4	125	
830.867	2637.1	3.792										187.7	127.5	
831.346	2630.2	3.802										190	130	
831.823	2623.3	3.812										192.2	132.4	
832.298	2616.4	3.822										194.3	134.7	
832.771	2609.6	3.832										196.4	136.9	
833.243	2602.8	3.842										198.4	139.1	
833.712	2596.1	3.852											141.2	
834.179	2589.3	3.862											143.2	
834.645	2582.6	3.872											145.2	
835.109	2576.0	3.882											147	
835.571	2569.4	3.892											148.9	
836.031	2562.8	3.902											150.6	
836.489	2556.2	3.912											152.3	
836.945	2549.7	3.922											154	
837.4	2543.2	3.932											155.5	
837.852	2536.8	3.942											157	
838.303	2530.4	3.952											158.5	
838.752	2524.0	3.962											159.9	
839.199	2517.6	3.972											161.2	
839.645	2511.3	3.982											162.5	
840.089	2505.0	3.992											163.7	
840.531	2498.8	4.002											164.8	

Continued on next page...

Table A.1 continued.

Pump λ (nm)	Idler $\bar{\nu}$ (cm ⁻¹)	Idler λ (μ m)	Poling Period (μ m)											
			20	20.25	20.5	20.75	21	21.25	21.5	21.75	22	22.25	22.5	22.75
840.971	2492.5	4.012											165.9	101.1
841.409	2486.3	4.022											167	102.2
841.846	2480.2	4.032											167.9	103.2
842.281	2474.0	4.042											168.9	104.2
842.715	2467.9	4.052											169.7	105.1
843.146	2461.8	4.062											170.6	105.9
843.576	2455.8	4.072											171.3	106.7
844.005	2449.8	4.082											172	107.4
844.431	2443.8	4.092											172.7	108
844.856	2437.8	4.102											173.2	108.6
845.28	2431.9	4.112											173.8	109.2
845.702	2426.0	4.122											174.3	109.6
846.122	2420.1	4.132											174.7	110
846.54	2414.3	4.142											175.1	110.3
846.957	2408.5	4.152											175.4	110.6
847.372	2402.7	4.162											175.7	110.8
847.786	2396.9	4.172											175.9	111
848.198	2391.2	4.182											176.1	111.1
848.609	2385.5	4.192											176.2	111.1
849.018	2379.8	4.202											176.3	111.1
849.425	2374.2	4.212											176.3	111
849.831	2368.6	4.222											176.2	110.9
850.236	2363.0	4.232											176.2	110.7
850.639	2357.4	4.242											176	110.4
851.04	2351.8	4.252											175.8	110.1
851.44	2346.3	4.262											175.6	109.7
851.838	2340.8	4.272											175.3	109.3
852.235	2335.4	4.282											175	108.8
852.63	2329.9	4.292											174.6	108.2
853.024	2324.5	4.302											174.1	107.6
853.417	2319.1	4.312											173.6	106.9
853.808	2313.7	4.322											173.1	106.2
854.197	2308.4	4.332											172.5	105.4
854.585	2303.1	4.342											171.8	104.5
854.972	2297.8	4.352											171.1	103.6
855.357	2292.5	4.362											170.3	102.6
855.741	2287.3	4.372											169.5	101.5
856.123	2282.1	4.382											168.7	100.4
856.504	2276.9	4.392											167.7	
856.884	2271.7	4.402											166.8	
857.262	2266.6	4.412											165.8	
857.639	2261.4	4.422											164.7	
858.015	2256.3	4.432											163.6	
858.389	2251.2	4.442											162.4	
858.761	2246.2	4.452											161.1	
859.133	2241.2	4.462											159.8	
859.503	2236.1	4.472											158.5	
859.872	2231.2	4.482											157.1	
860.239	2226.2	4.492											155.6	
860.605	2221.2	4.502											154.1	
860.97	2216.3	4.512											152.5	
861.333	2211.4	4.522											150.9	
861.695	2206.5	4.532											149.2	
862.056	2201.7	4.542											147.5	
862.416	2196.8	4.552											145.7	

Continued on next page...

Table A.1 continued.

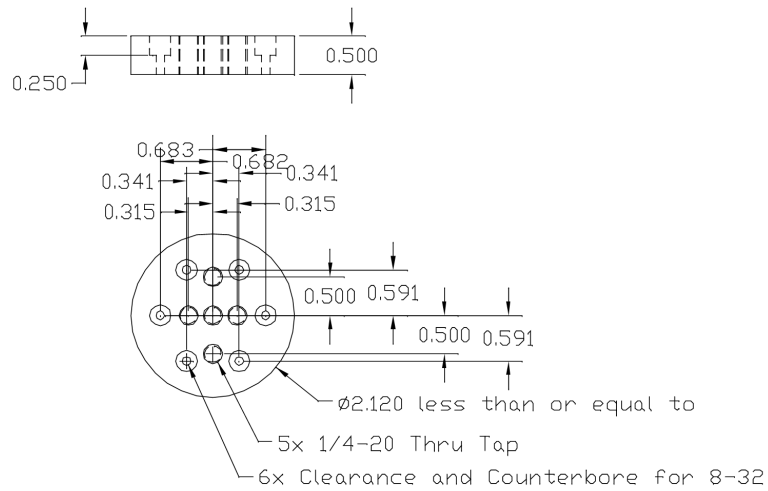
Pump λ (nm)	Idler $\bar{\nu}$ (cm ⁻¹)	Idler λ (μ m)	Poling Period (μ m)											
			20	20.25	20.5	20.75	21	21.25	21.5	21.75	22	22.25	22.5	22.75
862.774	2192.0	4.562												143.8
863.131	2187.2	4.572												141.9
863.487	2182.5	4.582												139.9
863.842	2177.7	4.592												137.9
864.195	2173.0	4.602												135.8
864.547	2168.3	4.612												133.6
864.898	2163.6	4.622									198.2	131.4		
865.247	2158.9	4.632									196.3	129.1		
865.596	2154.2	4.642									194.3	126.7		
865.943	2149.6	4.652									192.3	124.3		
866.289	2145.0	4.662									190.2	121.8		
866.633	2140.4	4.672									188	119.2		
866.977	2135.8	4.682									185.8	116.6		
867.319	2131.3	4.692									183.6	113.9		
867.66	2126.8	4.702									181.3	111.1		
868	2122.2	4.712									178.9	108.2		
868.339	2117.8	4.722									176.5	105.3		
868.676	2113.3	4.732									174	102.3		
869.013	2108.8	4.742									171.5			
869.348	2104.4	4.752									168.9			
869.682	2100.0	4.762									166.2			
870.015	2095.6	4.772									163.5			
870.347	2091.2	4.782									160.7			
870.678	2086.8	4.792									157.8			
871.007	2082.5	4.802									154.9			
871.336	2078.1	4.812									151.9			
871.663	2073.8	4.822									148.8			
871.989	2069.5	4.832									145.7			
872.314	2065.3	4.842									142.5			
872.638	2061.0	4.852									139.2			
872.961	2056.8	4.862									135.8			
873.283	2052.6	4.872									132.4			
873.604	2048.3	4.882								198.8	128.9			
873.923	2044.2	4.892								195.8	125.3			
874.242	2040.0	4.902								192.7	121.6			
874.56	2035.8	4.912								189.6	117.8			
874.876	2031.7	4.922								186.3	114			
875.191	2027.6	4.932								183.1	110			
875.506	2023.5	4.942								179.7	106			
875.819	2019.4	4.952								176.3	101.9			
876.131	2015.3	4.962								172.8				
876.443	2011.3	4.972								169.2				
876.753	2007.2	4.982								165.6				
877.062	2003.2	4.992								161.9				
877.37	1999.2	5.002								158.1				
877.739	1994.4	5.014								153.5				
878.045	1990.5	5.024								149.5				
878.35	1986.5	5.034								145.5				
878.654	1982.6	5.044								141.3				
878.957	1978.6	5.054								137.1				
879.258	1974.7	5.064								132.8				
879.559	1970.8	5.074								128.4				
879.859	1967.0	5.084								196.9	123.9			
880.158	1963.1	5.094								193.1	119.3			
880.457	1959.3	5.104								189.1	114.6			

Continued on next page...

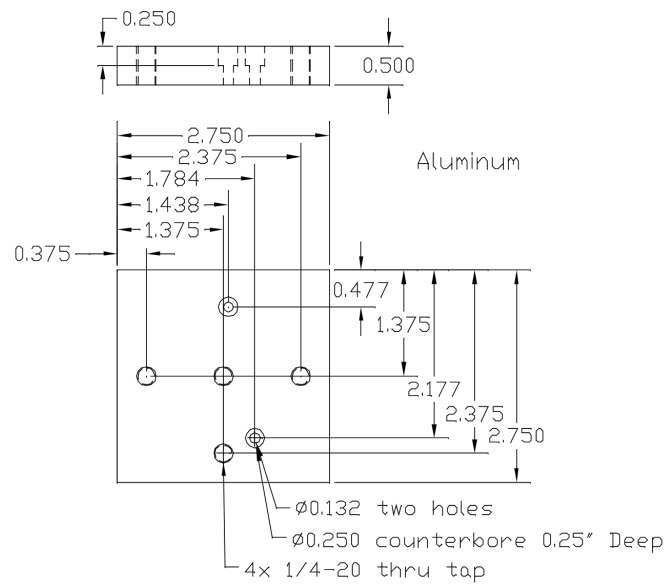
Table A.1 continued.

Pump λ (nm)	Idler $\bar{\nu}$ (cm ⁻¹)	Idler λ (μm)	Poling Period (μm)											
			20	20.25	20.5	20.75	21	21.25	21.5	21.75	22	22.25	22.5	22.75
880.754	1955.4	5.114								185.1	109.8			
881.05	1951.6	5.124								181	104.9			
881.345	1947.8	5.134								176.9				
881.639	1944.0	5.144								172.6				
881.932	1940.2	5.154								168.3				
882.225	1936.5	5.164								163.9				
882.516	1932.7	5.174								159.4				
883.096	1925.3	5.194								150.1				

A.8 NICE-OHMS Optics Mounts



(a) EOM 1 mount adapter plate.



(b) EOM 1 mount adapter plate.

Figure A.5: Adapter plates for mounting the 1st and 2nd EOM's to rotation stages.

Appendix B

Appendix for Optical Frequency Comb

B.1 Resetting Mode Lock

In most cases the mode-lock should be fairly stable and self-sustaining. And in most cases, if the fs laser is turned off, when turned on again it will return to the same mode locked state. However, sometimes power outages will cause changes in the fs laser which require a new mode-locked state to be found. If the laser does not automatically achieve mode lock (as indicated by a triple beep and the indicator light turning on – see Figure B.1) after about 5 minutes of trying, a new mode lock state will probably need to be attempted. First ensure that the values of the PControl laser sliders have been written down. Then attempt to correct the values back to the most recent “good” mode-lock state. Then try moving the sliders by 5 clicks in either direction to see if the mode lock space just shifted around a bit.

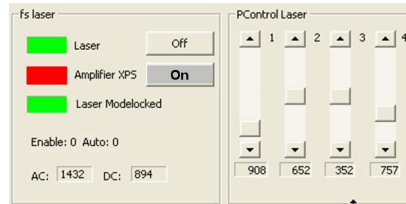


Figure B.1: Mode-lock indicator and “PControl Laser” sliders. A green indicator means that the control is active. For instance, the “laser” indicator being illuminated green means that the fs laser is being pumped. A green indicator on the “mode-locked” indicator means the mode-lock state has been achieved. The “PControl Laser” sliders indicate the positions of intracavity wedge controllers that change the polarization state of the fiber laser.

If no mode-lock is achieved by returning to the laser “good” values and the values near them, it may be necessary to start a scramble. Under the drop down menus for the main Fiber-comb program, choose the setup menu, and select fiber-laser. The “scrambler” dialogue (see Figure B.2) will then open. Pressing the “Reset” button discards the current mode locked state (if available) and starts searching for the next one. The “Halt” button disables the scrambling and auto-scrambling. The “Auto-ON”/“Auto OFF” buttons determine if the unit automatically scrambles when mode-lock is lost. Therefore “Auto ON” should seldom be pushed. “Enable ON” and “Enable OFF” turns the scrambler unit on and off, respectively. Therefore, sometimes one should press “Reset”, and if the unit does not begin searching, press “Enable On” as well. The unit should stop once it finds a good mode locked space.

Write down those values, as well as the AC and DC values. Then go through the Offset beat section to see if a strong offset beat is formed. If the AC level is not above 1400, the DC value is not above 850, or there is not a strong offset beat formed, the mode-lock state will not work well, and a new mode-lock state should be searched for. Through experience, one will find that the sliders will ultimately be in approximately the same place in order to get the best mode-lock state, but sometimes a scramble is required to find those values. Just keep nudging the directions towards where it used to be. For further instructions, please refer to the “Femtosecond Fiber Laser User Manual”. [10]

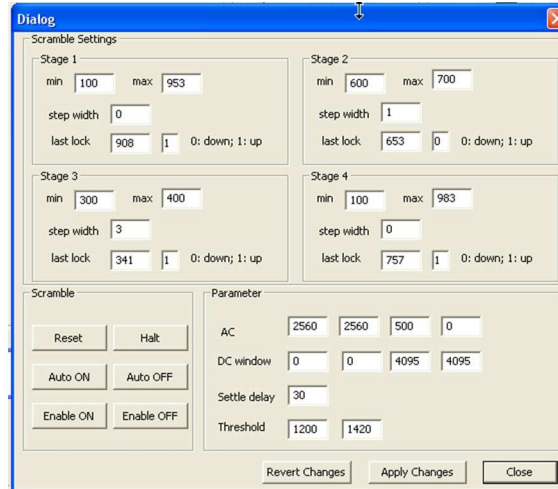


Figure B.2: “Scramble Dialogue” with the controls for starting a scramble (reset) stopping a scramble (halt). One should not press “Auto ON”, and one may press “Enable ON” or “Enable OFF” as needed.

B.2 Photonic Crystal Fiber XYZ Stage Alignment

Often the output light from the frequency doubling SHG crystal is well collimated through the fiber. When large movements are made to the comb, or disastrous mechanical motion to the oven photonic crystal fiber (PCF) stage is made, one will need to realign the XYZ stage. Begin by ensuring that approximately 80 mW of SHG light is exiting the SHG stage and entering the XYZ stage area by using the Thorlabs power meter as described in Section 3.2.5. Place a white business card where the output of the PCF fiber should be visible and view the card with the IR viewer. If very small manual adjustments of the XYZ stage do not bring light through the fiber, you will probably need to remove the microscope objective. Center the XYZ computer control of the XYZ stages by pressing the “38 V” button on the CW Beat Control 1. Translate the output objective very far from the PCF so that it is not damaged when the objective is removed. Once the objective is removed, light exiting the PCF may be visible with the IR viewer. If the beam passing through is very small, it means that the input light is focused into the cladding. Adjust the X and Y micrometers until the light going through is very bright and the beam is very large. A large beam means that the light is coupled into the core of the fiber, which is only 2 μm in diameter. Sometimes it is helpful to move the XYZ stage away from the input lens by two turns because by de-focusing the light, it is easier to get some light through

the core. This is accomplished by turning the micrometer for the Z direction counter-clockwise (when viewed from the end of the micrometer). Once the X and Y directions have been optimized, the Z direction can be returned to its original value and optimized. The light is fully optimized when it is as bright, and as white, as possible. The objective should be inspected, and cleaned with the drag and drop method as needed. The objective is then inserted (when physically removed from the fiber) and moved inward until the output beam is collimated at large distances. The XYZ stage is then optimized further manually with the micrometers, and using computer control for the brightest, whitest spot.

B.3 Enabling XML-RPC Server

In order for the LabVIEW spectroscopy program to be able to read the values from the frequency comb, the MenloSystems Fiber Comb Control (V4.21) must have the correct value in the setup file. Below is an example of the setup file, with the modified code to enable the XML-RPC server located at the end in bold. The filename is Fibercomb.setup and is located at “C:\Program Files\MenloSystems\FiberComb\etc” on the frequency comb computer (IP 130.126.226.73). Note that the pound sign (#) is the comment character for this type of file.

```
[global]
# In the global section, specify
# - ConfigRevision : should state date and fibercomb version, for documentation
# - ProjectID : for internal use
# - Synthesizer : name of the section defining synthesizer hardware
ConfigRevision = 20080527-0.4.15
ProjectID = 9210
Synthesizer = DDS
# Debug= on
[DAQmx]
NI6220 = Dev2
NI6703 = Dev1
[GuiHints]
optional (defaults to 'WinSize = Auto')
WinSize = Auto
Compact
Large
[TC1550]
# required (defaults to Channel =
serial://COM1/ baud=115200)
# specify communication channel for TC1550 control unit
# (use 'Channel = none' to deactivate)
Channel = serial://COM2/ baud=115200, timeout=500
[FXM50]
# optional
# specify options for FXM counter
# in production systems, AutoSimulate should be turned off!
Channel = serial://COM3/ baud=38400
Devices = 1

AutoSimulate = no
[BeatCalc]
FrequencyDRO = 980000000.000
ReprateHarmonic = 10
CWBeatChannels = 2
CWBeat0.Name = VIS
CWBeat0.Harmonic = 2
CWBeat1.Name = IR
[AC1550]
# optional
# specify Device Name for DDS control unit
# (use 'Channel = none' to deactivate)
DeviceName = AC1550 A
[DDS]
# optional
# specify Device Name for DDS frequency synthesizer
DeviceName = DDS
#[LockboxReprate]
# optional
#BreakOutBox_NI_6221::LB1
[ActuatorReprate]
Device = TC1550
motor = 6
[BeatControlXPS]
# required
# by default, Lockbox is LB2
AmplifierSwitch = AC1550::LDMV_I
BeatSignal = OffsetBeatSignal
SqueezerAmp = SqueezerOffset
#Lockbox = LockboxOffsetBeat
Actuator = ActuatorOffsetBeat
[OffsetBeatSignal]
```

```

Channel = BreakOutBox_NI_6221::RFDET
[SqueezerOffset]
Device = TC1550
[ActuatorOffsetBeat]
Device = TC1550
motor = 4
#[LockboxOffsetBeat]
# optional
#BreakOutBox_NI_6221::LB2
[BeatControlCW1]
# Aux channel is optional
# specify Squeezers as required
# lockbox and actuator are optional
Name = CW Beat Control 1
AmplifierSwitch = AC1550::LDMV_II
BeatSignal = BeatSignalCW1
#Wavelength = VIS
BeatSignalAux = BeatSignalCW2
WavelengthAux = 1064 nm
SqueezerAmp = SqueezerAmpCW1
SqueezerXyz = SqueezerXyzCW1
Waveplate = WaveplateCW1
#Lockbox = LockboxCW1
#Actuator = ActuatorCW1
[BeatSignalCW1]
Channel = BreakOutBox_NI_6221::AI1
#Valid.Min = 0.0
[BeatSignalCW2]
Channel = BreakOutBox_NI_6221::AI2
#Valid.Min = 0.0
[SqueezerAmpCW1]
Device = HVA75
Channel1 = BreakOutBox_NI_6703::AO0
Channel2 = BreakOutBox_NI_6703::AO1
Channel3 = BreakOutBox_NI_6703::AO2
[SqueezerXyzCW1]
Device = HVA75
Channel1 = BreakOutBox_NI_6703::AO3
Channel2 = BreakOutBox_NI_6703::AO4
Channel3 = BreakOutBox_NI_6703::AO5
[WaveplateCW1]
Device = TC1550
motor = 7
Limits = off
#[LockboxCW1]
# optional
#BreakOutBox_NI_6221::LB2
[DataSave]

[XmlRpcServer]
enable = true
port = 8123
verbosity = 1
login = comb
password = system

```

```

Channel0 = true
Channel1 = true
Channel2 = true
Channel3 = true
Channel4 = no
Channel5 = no
Channel6 = no
Channel7 = no
Time = false
TimeStamp = true
Counter = true
Phase = false
Frequency = false
BeatSignal = false
SystemLocked = false
MotorPosition = false
SqueezerXPS = false
SqueezerSHG1 = false
SqueezerSHG2 = false
Latency = false
Interlock = false
LockBoxVoltage = false
Synthesizer = false
[DataLog]
Channel0 = true
Channel1 = true
Channel2 = true
Channel3 = true
Channel4 = no
Channel5 = no
Channel6 = no
Channel7 = no
Time = true
TimeStamp = true
Counter = true
Phase = false
Frequency = true
BeatSignal = true
SystemLocked = true
MotorPosition = true
SqueezerXPS = yes
SqueezerSHG1 = yes
SqueezerSHG2 = yes
Latency = true
Interlock = true
LockBoxVoltage = true
Synthesizer = true

```

B.4 Reading Comb Values from XML server

A python script code was written inside of LabVIEW which queries the XML server to obtain the values necessary for using Equation 3.3 to determine the frequency of the laser. The text of this code is shown in Figure B.3.



```
import xmlrpclib
import time

server_url = 'http://comb:system@fcomb:8123/RPC2';
server = xmlrpclib.ServerProxy(server_url);
SoftwareVersion = server.hello()
myDataChannels=['timestamp.abs',
                'counter0.freq',
                'counter1.freq',
                'counter2.freq',
                'counter3.freq',
                'replate.freq',
                'replate.freqref',
                'timestamp.abs.day',
                'timestamp.abs.time']
timestamp= server.data.last_timestamp()
timestampstring=str(timestamp+1)+'00000'
notdone=1
while notdone:
    data= server.data.query(timestamp-0.0,myDataChannels)
    if (type(data).__name__=='dict'):
        notdone=0
    output0=data[timestampstring][myDataChannels[0]]
    output1=data[timestampstring][myDataChannels[1]]
    output2=data[timestampstring][myDataChannels[2]]
    output3=data[timestampstring][myDataChannels[3]]
    output4=data[timestampstring][myDataChannels[4]]
    output5=data[timestampstring][myDataChannels[5]]
    output6=data[timestampstring][myDataChannels[6]]
    output7=data[timestampstring][myDataChannels[7]]
    output8=data[timestampstring][myDataChannels[8]]
```

Figure B.3: Python script used to extract frequency comb values from XML server.

B.5 List of Python Commands

A list of important python commands used in the script shown in Figure B.3 is shown in Table B.1. A list of the remaining python commands used are shown in Table B.2.

Command	Description	Unit	Type
counter0.freq	Counter channel 0 frequency (DMRR)	Hz	double
counter1.freq	Counter channel 1 frequency (Offset)	Hz	double
counter2.freq	Counter channel 2 frequency (Ti:Sapphire Beat)	Hz	double
counter3.freq	Counter channel 3 frequency (YAG Beat)	Hz	double
retrate.freq	The actual repetition rate of the comb (calculated from counter0)	Hz	double
retrate.freqref	Reference Frequency for Rep Rate (98,000,000 Hz)	Hz	double
timestamp.abs	Time of data taking in Unix Time	s	double
timestamp.abs.day	Day of data taking in format YYYY-MM-DD		string
timestamp.abs.time	Time of data taking in format HH:MM:SS (one second resolution)		string

Table B.1: Important command set for XML-RPC in Fiber Comb Control v0.4.25.

Table B.2: Remaining command set for XML-RPC in Fiber Comb Control v0.4.25.

Command	Description	Unit	Type
system.interlock	System interlock status		boolean
system.locked	All relevant and active lockboxes are locked		boolean
CW2.freq	Optical frequency of CW source 2 - depends on correct beat signs!	Hz	double
aux0	Analog input source "aux0"	V	double
aux1	Analog input source "aux1"	V	double
aux2	Analog input source "aux2"	V	double
aux3	Analog input source "aux3"	V	double
beat1.act.pos	Position of CW-beat-1 Actuator	V	double
beat1.lb.mon	Monitor output of CW-beat-1 LockBox	V	double
beat1.squeezer.x	Position of CW-beat-1 beat amplifier polarization control (x)	V	double
beat1.squeezer.y	Position of CW-beat-1 beat amplifier polarization control (y)	V	double
beat1.squeezer.z	Position of CW-beat-1 beat amplifier polarization control (z)	V	double
beat1.stage.x	Position of CW-beat-1 M-VIS stage (x)	V	double
beat1.stage.y	Position of CW-beat-1 M-VIS stage (y)	V	double
beat1.stage.z	Position of CW-beat-1 M-VIS stage (z)	V	double
beat1.waveplate	Position of CW-beat-1 beat waveplate actuator		double
beat2.act.pos	Position of CW-beat-2 Actuator	V	double
beat2.lb.mon	Monitor output of CW-beat-2 LockBox	V	double
beat2.squeezer.x	Position of CW-beat-2 beat amplifier polarization control (x)	V	double
beat2.squeezer.y	Position of CW-beat-2 beat amplifier polarization control (y)	V	double
beat2.squeezer.z	Position of CW-beat-2 beat amplifier polarization control (z)	V	double
beat2.stage.x	Position of CW-beat-2 M-VIS stage (x)	V	double
beat2.stage.y	Position of CW-beat-2 M-VIS stage (y)	V	double
beat2.stage.z	Position of CW-beat-2 M-VIS stage (z)	V	double
beat2.waveplate	Position of CW-beat-2 beat waveplate actuator		double
beat3.act.pos	Position of CW-beat-3 Actuator	V	double
beat3.lb.mon	Monitor output of CW-beat-3 LockBox	V	double
beat3.squeezer.x	Position of CW-beat-3 beat amplifier polarization control (x)	V	double
beat3.squeezer.y	Position of CW-beat-3 beat amplifier polarization control (y)	V	double
beat3.squeezer.z	Position of CW-beat-3 beat amplifier polarization control (z)	V	double
beat3.stage.x	Position of CW-beat-3 M-VIS stage (x)	V	double
beat3.stage.y	Position of CW-beat-3 M-VIS stage (y)	V	double
beat3.stage.z	Position of CW-beat-3 M-VIS stage (z)	V	double
beat3.waveplate	Position of CW-beat-3 beat waveplate actuator	V	double
beat4.act.pos	Position of CW-beat-4 Actuator	V	double
beat4.lb.mon	Monitor output of CW-beat-4 LockBox	V	double

Continued on next page. . .

Table B.2 continued.

Command	Description	Unit	Type
beat4.squeezer.x	Position of CW-beat-4 beat amplifier polarization control (x)	V	double
beat4.squeezer.y	Position of CW-beat-4 beat amplifier polarization control (y)	V	double
beat4.squeezer.z	Position of CW-beat-4 beat amplifier polarization control (z)	V	double
beat4.stage.x	Position of CW-beat-4 M-VIS stage (x)	V	double
beat4.stage.y	Position of CW-beat-4 M-VIS stage (y)	V	double
beat4.stage.z	Position of CW-beat-4 M-VIS stage (z)	V	double
beat4.waveplate	Position of CW-beat-4 beat waveplate actuator	V	double
counter.gatetime	Counter gate time	s	double
counter0.freqref	Reference frequency for replate stabilization	Hz	double
counter2.signal	Signal strength of counter channel 2 input	V	double
counter1.freqref	Reference frequency for offset beat stabilization		double
counter1.signal	Signal strength of counter channel 1 input	V	double
counter3.signal	Signal strength of counter channel 3 input	V	double
lb1.mon	Monitor output of LockBox 1 (Offset beat)	V	double
lb2.mon	Monitor output of LockBox 2 (Replate)	V	double
lb3.mon	Monitor output of LockBox 3 (CW beat 1)	V	double
lb4.mon	Monitor output of LockBox 4 (CW beat 2)	V	double
offset.freq	Offset beat frequency (see counter1)	V	double
offset.freqref	Reference frequency for offset beat stabilization	Hz	double
offset.squeezer.x	Position of XPS amplifier polarization control (x)	V	double
offset.squeezer.y	Position of XPS amplifier polarization control (y)	V	double
offset.squeezer.z	Position of XPS amplifier polarization control (z)	V	double
offset.stage	Position for long term shift compensator in offset beat stabilization		double
replate.stage	Position for long term shift compensator in repetition rate stabilization		double
system.latency	data acquisition execution time (Should be well below 1)	s	double
counter.channels	Number of available counter channels (numbered starting with 0)		int
beat1.lb.status	Status of CW-beat-1 LockBox (0 off, 1 unlocked, 2 locked)		int
beat2.lb.status	Status of CW-beat-2 LockBox (0 off, 1 unlocked, 2 locked)		int
beat3.lb.status	Status of CW-beat-3 LockBox (0 off, 1 unlocked, 2 locked)		int
beat4.lb.status	Status of CW-beat-4 LockBox (0 off, 1 unlocked, 2 locked)		int
lb1.status	Status of LockBox 1 (Offset beat) (0 off, 1 unlocked, 2 locked)		int
lb2.status	Status of LockBox 2 (Replate) (0 off, 1 unlocked, 2 locked)		int
lb3.status	Status of LockBox 3 (CW beat 1) (0 off, 1 unlocked, 2 locked)		int
lb4.status	Status of LockBox 4 (CW beat 2) (0 off, 1 unlocked, 2 locked)		int

Appendix C

Appendix for Spectroscopic Methods

C.1 Phase Shifter Calibration

The 150 MHz RF phase shifter was calibrated by recording the change in relative phase shift between an RF signal at 113 MHz passing through the RF phase shifter and a reference line, and is shown in Table C.1.

Voltage	ϕ	Voltage	ϕ	Voltage	ϕ
0.14	0	5.31	79.3	7.39	188.2
0.41	0.7	5.42	83.7	7.54	194.3
1.01	4.2	5.50	87.7	7.75	200.7
1.66	8.7	5.69	96.2	7.96	206.2
2.18	13.7	5.79	101.2	8.14	210.4
2.73	18.7	5.90	107.7	8.20	211.7
3.05	22.7	5.95	109.7	8.29	213.8
3.51	29.7	6.01	112.7	8.41	215.7
3.74	33.3	6.02	113.7	8.65	219.3
4.07	40.2	6.11	117.7	8.94	222.7
4.11	41.6	6.2	124	9.26	225.7
4.24	44.3	6.31	131.2	9.6	227.7
4.37	47.6	6.39	135.7	10	229.7
4.45	49.3	6.51	142.7	10.54	232.8
4.56	51.94	6.62	148.7	11	234.7
4.71	56.7	6.7	153	12	236.9
4.82	60.7	6.82	160.7	12.25	238.272
4.94	64.7	6.9	164.7	12.5	238.372
5.09	70.5	7.04	172	12.75	238.472
5.24	76.2	7.15	178.1	13	238.572

Table C.1: Phase shifter calibration data with the phase shift (ϕ) as a function of voltage.

The data was fit to a thirteen order polynomial in the voltage (V) applied to the phase shifter.

$$\phi = a + bV + cV^2 + dV^3 + eV^4 + fV^5 + gV^6 + hV^7 + hV^8 + iV^9 + jV^{10} + kV^{11} + lV^{12} \quad (\text{C.1})$$

With the coefficients being 4.0262, -40.223, 115.87, -132.86, 83.014, -30.927, 7.2506, -1.096, 0.10717, -0.0066355, 0.00024496, -4.6813e-06, 3.1141e-08. Using that fit function, a lookup table was constructed which indicates what phase shift corresponds to what voltage and is found in Table C.2.

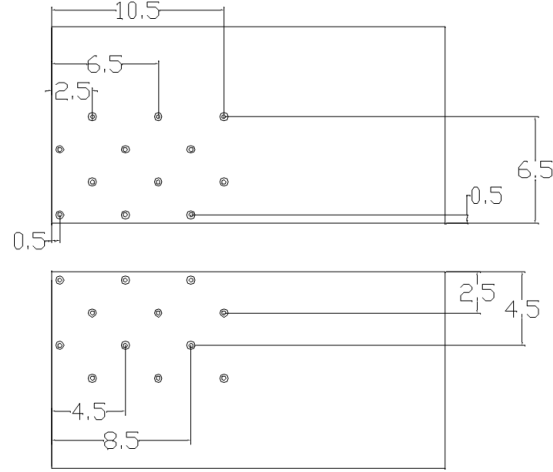
Voltage	ϕ	Voltage	ϕ	Voltage	ϕ	Voltage	ϕ
0	0.2	3	12	6	117	9	224.7
0.1	0.2	3.1	14	6.1	122	9.1	226.1
0.2	0.2	3.2	15	6.2	127	9.2	227.4
0.3	0.3	3.3	17	6.3	132	9.3	228.6
0.4	0.3	3.4	19	6.4	137	9.4	229.7
0.5	0.4	3.5	21	6.5	142	9.5	230.6
0.6	0.4	3.6	23	6.6	147	9.6	231.5
0.7	0.5	3.7	25	6.7	152	9.7	232.3
0.8	0.6	3.8	28	6.8	157	9.8	233.0
0.9	0.7	3.9	30	6.9	161	9.9	233.7
1	0.9	4	33	7	166	10	234.2
1.1	1.0	4.1	36	7.1	170	10.1	234.7
1.2	1.2	4.2	39	7.2	175	10.2	235.2
1.3	1.4	4.3	42	7.3	179	10.3	235.6
1.4	1.6	4.4	45	7.4	183	10.4	236.0
1.5	1.8	4.5	49	7.5	186	10.5	236.3
1.6	2.1	4.6	53	7.6	190	10.6	236.6
1.7	2.5	4.7	57	7.7	194	10.7	236.8
1.8	2.8	4.8	61	7.8	197	10.8	237.0
1.9	3.2	4.9	65	7.9	200	10.9	237.2
2	3.7	5	69	8	203	11	237.4
2.1	4.2	5.1	73	8.1	206	11.1	237.5
2.2	4.8	5.2	78	8.2	209	11.2	237.6
2.3	5.5	5.3	83	8.3	211	11.3	237.8
2.4	6.2	5.4	87	8.4	214	11.4	237.8
2.5	7.0	5.5	92	8.5	216	11.5	237.9
2.6	7.9	5.6	97	8.6	218	11.6	238.0
2.7	8.9	5.7	102	8.7	220	11.7	238.0
2.8	10.0	5.8	107	8.8	222	11.8	238.1
2.9	11.2	5.9	112	8.9	223	11.9	238.1

Table C.2: Phase shifter lookup table.

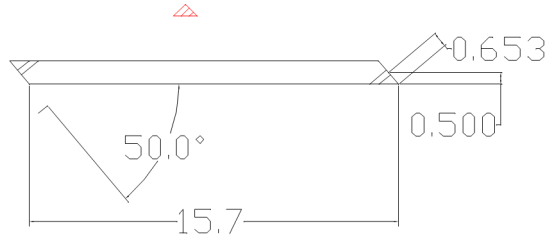
C.2 Laser Table Modifications

As the ion beam instrument was built on a separate base structure, the laser table needed to be extended to build a cavity around the instrument. Therefore, additional breadboards were cantilevered off of the end sides of the laser table. An overview of the modifications was given in Section 4.3. This section includes the details of how the laser table was modified. The SCS machine shop constructed four types of parts to modify the laser table: 1) top aluminum plates, 2) bottom aluminum plates, 3) angle washers, and 4) 80-20 supports to connect the top and bottom plates and keep them from vibrating. Schematic diagrams for these parts are shown in Figure C.1. The top aluminum plates are shown in part Figure C.1(a). The parts are 24" long by 12" tall and were rough cut. The two parts are essentially mirror images of one another, and are drilled with 12 1/4"-clearance holes countersunk to 1/2" diameter for 0.3" deep. The bottom aluminum plates are two 1/2"-thick, 8"x8" plates. The 8x angle washers are constructed from a 1/2" aluminum rod that has a loose 1/4" clearance hole drilled through it. Then the part is cut at a 45°

angle. An example of the angle bracket is shown in red in Figure C.1(b). Four 1"x1" 80-20 extrusions were cut to 15.7" long with a 50° bevel on each end, as illustrated in Figure C.1(b). Then a 1/4" clearance hole was drilled perpendicular to the cut.



(a) Schematic for 1/2" top aluminum plates.



(b) Schematic for 80-20 supports and instructions for bottom aluminum plates, and angle washers.

Figure C.1: Designs for modifications to ion beam laser table.

Once the parts were constructed, the bottom aluminum plates were attached to the laser table by drilling and tapping the bottom of the laser table, and drilling through the aluminum plates, and connecting them with screws. The top aluminum plates were connected directly to the laser table. Tapped holes were drilled into the top and bottom aluminum plates that could be connected by the 80-20 supports. The angle washers were used to account for the angle between the support and the angle of the tap into the aluminum plates.

C.3 Brass Cavity Mounts I

This iteration of brass cavity mounts is not vacuum compatible. The detailed machining schematics are shown in Figure C.2. The mounts are composed of a back plate (C.2(a)) which are attached with screws to the base plate (C.2(c)). Precision screws separate the front plate (C.2(b)) from the back plate (C.2(a)) and rest on sapphire jewels

glued into the front plate. A piezo electric transducer (Piezomechanik HPSt 150/20-15/12 VS35) or dummy (C.2(d)) is mounted with 4 metric screws to the front plate. High reflectivity mirrors are mounted in their holders (C.2(e) and C.2(f) for 1" and .8" mirrors, respectively). The recesses for the sapphire jewels are apparent on the "back view" of the front piece (C.2(b)). The "ring" recess is prepared by using a 0.5" end mill 0.05" deep, and then using a 0.255" end mill for an additional 0.05". The "disk" recess is prepared by using a 0.5" end mill 0.075" deep, and then using a 0.255" end mill for an additional 0.092". The "rods" recesses are prepared by first using a 0.5" end mill 0.092" deep, and then cutting 2 channels. The channels are 0.062" wide channels, 0.011" deep and 0.26" long. The center of each channel is separated from the center of the hole by 0.07". Four 1/8" diameter stainless steel (SS) rods 0.5" long are machined, and four springs (McMaster-Carr 9654K108) were purchased. The mirror holders are constructed out of aluminum because it is lighter than brass, and is therefore easier for the piezo to dither. The mirror holders have a top and a bottom piece. The top piece has one O-ring groove to protect the low reflectivity side of the mirror. The bottom piece has two O-ring grooves, one to protect the high reflectivity side of the mirror, and the other one to enable a vacuum seal in future implementations of cavity mounts. In all cases a 114 O-ring was used with standard channel width, but the depth was only 0.05" deep to ensure the high reflectivity mirrors are not scratched.

Several sapphire jewels (2 olive rings, 2 sapphire disks, and 4 sapphire rods) are purchased from Swiss Jewel Company (R318.0 – olive ring 0.05" thick, ID 0.125" OD 0.25" – quantity 2) (SP-28 – 0.245" long sapphire rod – quantity 4) (Sapphire Disk, 0.0898" tall 0.249" diameter – quantity 2). Once the brass parts have been machined, the sapphire jewels are glued into place with 5-minute epoxy. Six precision mounting screws (Newport 9303) are placed in-between the back and front plates and are tightened. The springs are placed in-between the front and back plates and are held in place with the 1/8" SS rods. The springs hold the mount together, and the precision screws push the mount apart, and change the tilt of the mirrors.

In addition to the actual cavity mounts, several alignment tools were also produced. Figure C.3 illustrates the schematic diagram for a long tube, in part Figure C.3(a), and alignment jigs, in Figure C.3(b). The long tube is made from aluminum and has internal M22 threads at one end, and external M22 threads at the other. It can be used to get the laser beam passing through the center of the first jig by alternately adding and removing the piece, to get a short and long distance and centering up the laser each time. The jigs in Figure C.3(b) are even more important. A small plastic (poly-methyl-methacrylate(PMMA)) insert is press fit into an aluminum mount that has internal M22 threads. The plastic insert has a 2 mm hole in it, so the laser beam can be centered to the jig on either end of the cavity.

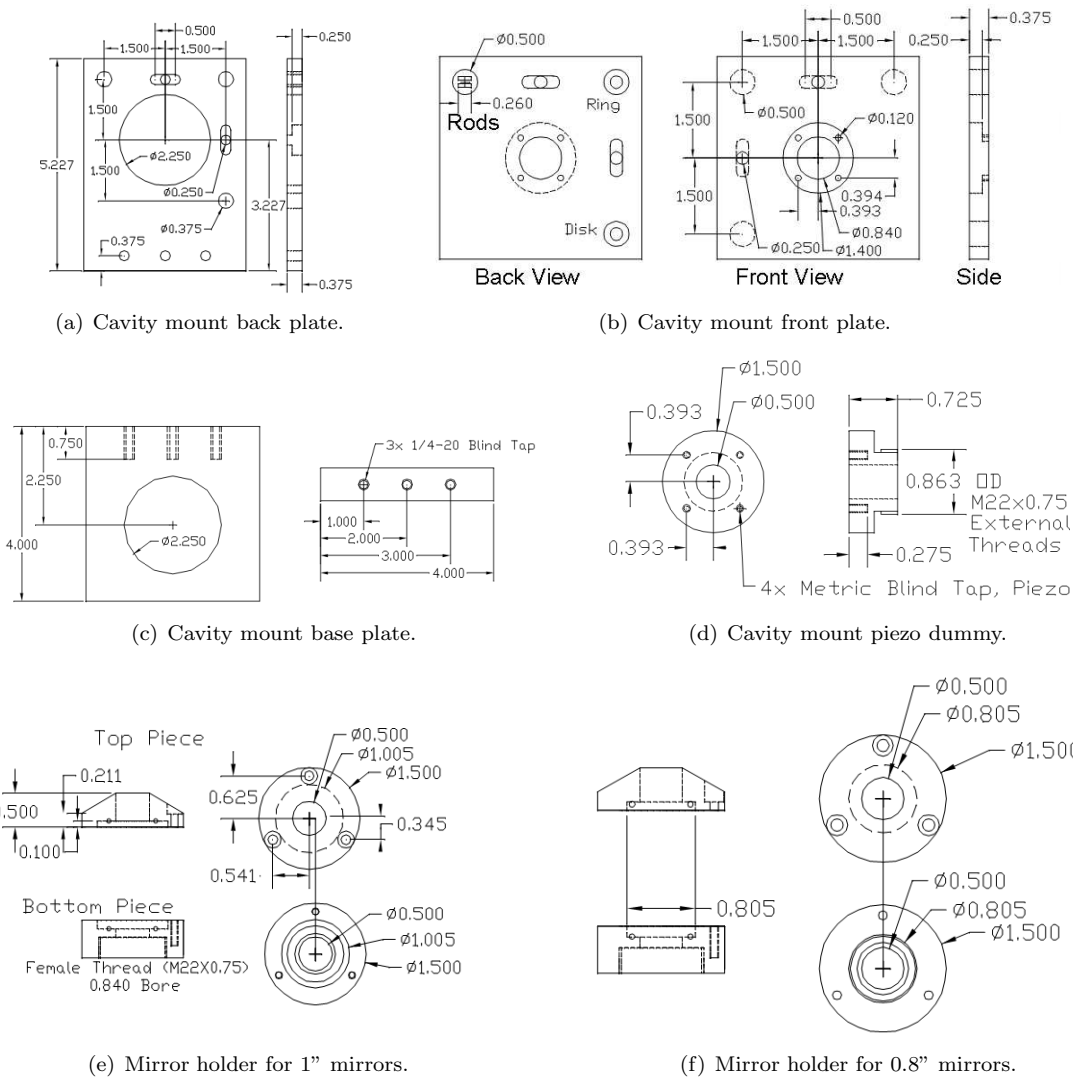


Figure C.2: Schematics for non-vacuum compatible brass cavity mount designs.

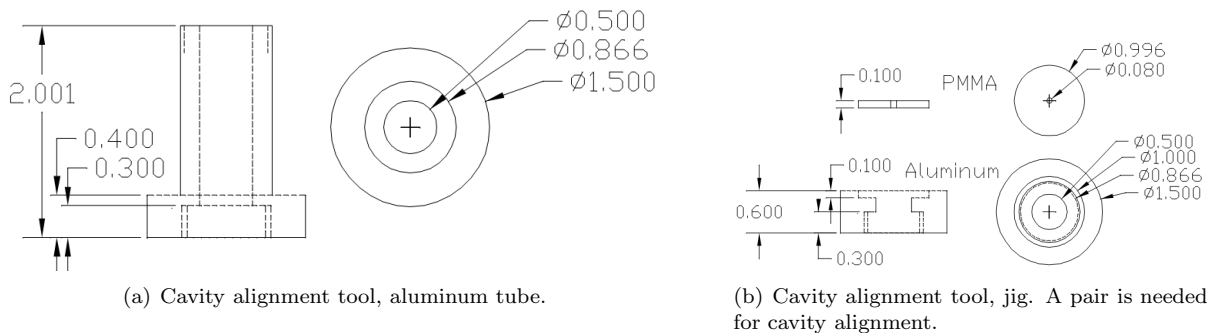
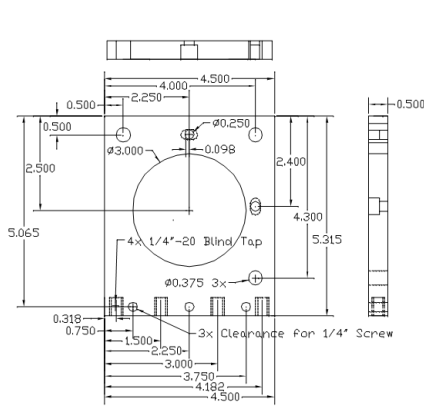


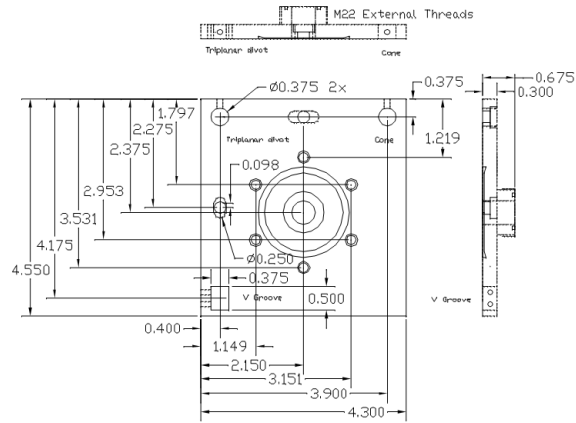
Figure C.3: Schematics for cavity alignment tools.

C.4 Brass Cavity Mounts II

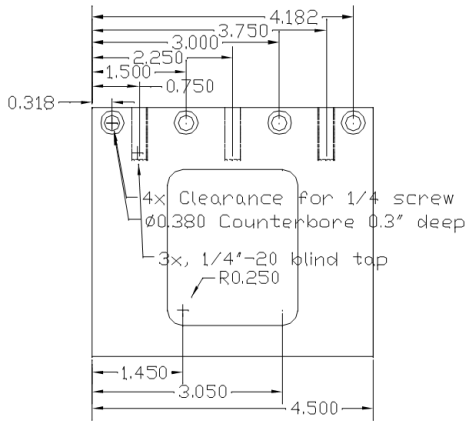
In several circumstances it is helpful to have the cavity mirrors directly connected to the vacuum chamber. It was determined, however, that such mirror mounts cannot be placed on vibration dampening Sorbothane, as the pressure of the atmosphere on the mounts tends to bend the mounts towards the vacuum. While it is possible to obtain a cavity ring-down signal with such mounts without Sorbothane, it is currently unknown if it is possible to lock a cavity which is not mounted on the Sorbothane. However, the construction of these mounts is still described in this section under the assumption that they will be used in the system at some future time. Schematics for the construction of these mounts are shown in Figure C.4.



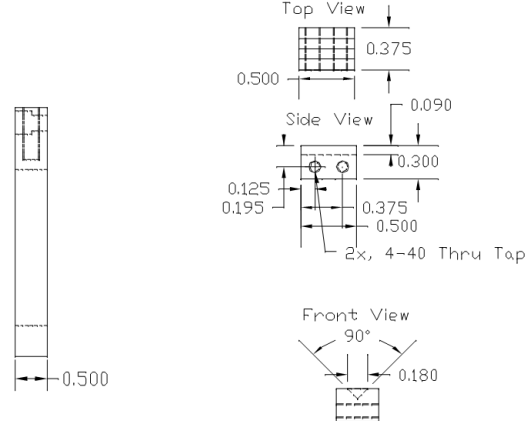
(a) Cavity mount back plate.



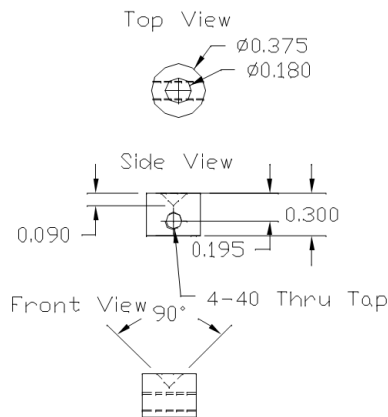
(b) Cavity mount front plate. A 2-3/4" knife edge is cut into one face, and M22 metric threads are cut into the other face. A O16 oring groove is cut into the pace of the M22 threads.



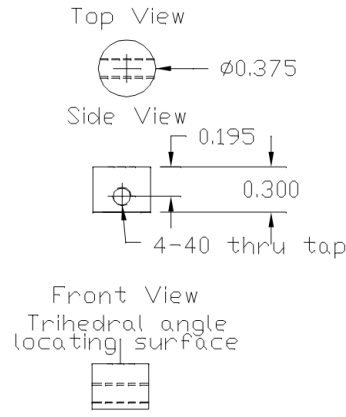
(c) Cavity mount base plate.



(d) Stainless steel V-channel inserts.



(e) Stainless steel cone inserts.



(f) Stainless steel trihedral divot inserts.

Figure C.4: Schematics for vacuum compatible brass cavity mounts. The front, back, and base plates are machined from brass, while three stainless steel inserts are used for precision alignment.

C.5 LabVIEW Data File Output

A LabVIEW program was constructed which runs the spectroscopic data collection, and saves the data collected by the DAQ card and frequency comb computer. Two data points of the an example file are shown in Table C.4. Twenty-three columns are data are given, and the number of rows correspond to the number of data points intended for a specific scan. The columns of data and a description are found in Table C.3.

Column Name	Description
PiezoVoltage	Voltage of reference cell piezoelectric transducer, changes laser wavelength.
Wavemeter	Wavelength of laser as read by wavemeter.
Lock-InX	X-channel – digital lock-in amplifier – dispersion heterodyne signal.
Lock-InY	Y-channel – digital lock-in amplifier – dispersion heterodyne signal.
CEVMS_X	X-channel – digital lock-in amplifier – absorption heterodyne signal.
CEVMS_Y	Y-channel – digital lock-in amplifier – absorption heterodyne signal.
VMSX	Blank.
FastDetector	DC level of fast photodiode.
RepRateCounter	Downmixed repetition rate as explained in Section 3.1.1.
CalculatedRepRate	Repetition rate calculated using Equation 3.6.
OffsetFrequency	Offset frequency SHG doubled comb. Sign assigned in LabVIEW program.
Matisse	Cw beat frequency for Ti:Sapphire laser
Beat	Cw with sign assigned in the LabVIEW program.
Mode	The mode number (assumed mode number)
Number	input into the LabVIEW program.
Difference (MHz)	The difference in frequency of the laser determined by the wavemeter and frequency comb.
Wavelength FromComb	The wavelength of the Ti:Sapphire laser as determined by the frequency comb.
TimeStamp	The time of the data reading in Unix time.
IncorrectMode	The mode number calculated by the
NumberCalculated	LabVIEW program using Equation 3.7.
TimeStamp	The time of the data reading in Unix time.
Scan Mode	The direction which the comb needed to be scanned to keep the Matisse beat in the bandwidth of detection.
Picoammeter	The current being read on the Faraday cup, usually after the drift region with apertures in place.
Pressure	Blank.
VMSY	Blank.
wavemeter	The frequency of the Ti:Sapphire laser
wavenumber	as measured by the wavemeter in cm^{-1} .
keithleyvoltage	An approximate measure of the beam voltage from Keithley sourcemeter.

Table C.3: Column names and description.

PiezoVoltage	Wavemeter	Lock-InX	Lock-InY
0.122010	921.360827	-0.179566	0.077069
0.122020	921.360794	-0.199697	0.083860
CEVMS_X	CEVMS_Y	VMSX	FastDetector
0.226554	0.168487	1.181869	3.099246
0.240478	0.243178	0.417089	3.124544
RepRateCounter	CalculatedRepRate	OffsetFrequency	MatisseBeat
20017600.000000	100001760.000000	-40000099.030000	-22845685.391000
20017600.000000	100001760.000000	-40000001.912000	-22758501.895000
ModeNumber	Difference(MHz)	WavelengthFromComb	TimeStamp
3253744.000000	-14.435433	921.360868	1313007287.000000
3253744.000000	-26.263629	921.360868	1313007288.000000
IncorrectModeNumberCalculated	ScanMode	Picoammeter	Pressure
3253744.144352	0.000000	0.764427	1.000000
3253744.262632	0.000000	0.764295	1.000000
VMSY	wavemeterwavenumber	keithleyvoltage	
1.049578	10853.511137	4144.161000	
1.050929	10853.511535	4144.217000	

Table C.4: Example of data file.

C.6 Lookup Table of Bessel Functions

The values for the Bessel functions, including the modulation index (β), J_0^2 , J_1^2 , J_2^2 , the ratio squared, and the values multiplied are given in Table C.5.

Table C.5: Values of Bessel functions.

β	J_0	J_1	J_0^2 %	J_1^2 %	J_2^2 %	Ratio Squared	Multiplied
0.30	0.978	0.148	95.6	2.2	0.012	43.4	0.145
0.31	0.976	0.153	95.3	2.3	0.014	40.6	0.149
0.32	0.975	0.158	95.0	2.5	0.016	38.1	0.154
0.33	0.973	0.163	94.7	2.6	0.018	35.7	0.158
0.34	0.971	0.168	94.3	2.8	0.020	33.6	0.163
0.35	0.970	0.172	94.0	3.0	0.023	31.7	0.167
0.36	0.968	0.177	93.7	3.1	0.026	29.9	0.171
0.37	0.966	0.182	93.3	3.3	0.029	28.2	0.176
0.38	0.964	0.187	93.0	3.5	0.032	26.7	0.180
0.39	0.962	0.191	92.6	3.7	0.035	25.3	0.184
0.40	0.960	0.196	92.2	3.8	0.039	24.0	0.188
0.41	0.958	0.201	91.9	4.0	0.043	22.8	0.192
0.42	0.956	0.205	91.5	4.2	0.047	21.7	0.196
0.43	0.954	0.210	91.1	4.4	0.052	20.6	0.200

Continued on next page. . .

Table C.5 continued.

β	J_0	J_1	J_0^2 %	J_1^2 %	J_2^2 %	Ratio Squared	Multiplied
0.44	0.952	0.215	90.7	4.6	0.057	19.7	0.204
0.45	0.950	0.219	90.3	4.8	0.062	18.8	0.208
0.46	0.948	0.224	89.8	5.0	0.068	17.9	0.212
0.47	0.946	0.229	89.4	5.2	0.073	17.1	0.216
0.48	0.943	0.233	89.0	5.4	0.080	16.4	0.220
0.49	0.941	0.238	88.5	5.7	0.087	15.7	0.224
0.50	0.938	0.242	88.1	5.9	0.094	15.0	0.227
0.51	0.936	0.247	87.6	6.1	0.10	14.4	0.231
0.52	0.934	0.251	87.1	6.3	0.11	13.8	0.235
0.53	0.931	0.256	86.7	6.5	0.12	13.2	0.238
0.54	0.928	0.260	86.2	6.8	0.13	12.7	0.242
0.55	0.926	0.265	85.7	7.0	0.14	12.2	0.245
0.56	0.923	0.269	85.2	7.2	0.15	11.8	0.248
0.57	0.920	0.274	84.7	7.5	0.16	11.3	0.252
0.58	0.918	0.278	84.2	7.7	0.17	10.9	0.255
0.59	0.915	0.282	83.7	8.0	0.18	10.5	0.258
0.60	0.912	0.287	83.2	8.2	0.19	10.1	0.261
0.61	0.909	0.291	82.6	8.5	0.20	9.76	0.265
0.62	0.906	0.295	82.1	8.7	0.22	9.41	0.268
0.63	0.903	0.300	81.6	9.0	0.23	9.09	0.271
0.64	0.900	0.304	81.0	9.2	0.24	8.77	0.274
0.65	0.897	0.308	80.5	9.5	0.26	8.48	0.276
0.66	0.894	0.312	79.9	9.8	0.28	8.19	0.279
0.67	0.891	0.317	79.4	10.0	0.29	7.92	0.282
0.68	0.888	0.321	78.8	10.3	0.31	7.66	0.285
0.69	0.884	0.325	78.2	10.6	0.33	7.41	0.287
0.70	0.881	0.329	77.7	10.8	0.35	7.17	0.290
0.71	0.878	0.333	77.1	11.1	0.36	6.95	0.292
0.72	0.875	0.337	76.5	11.4	0.38	6.73	0.295
0.73	0.871	0.341	75.9	11.6	0.41	6.52	0.297
0.74	0.868	0.345	75.3	11.9	0.43	6.32	0.300
0.75	0.864	0.349	74.7	12.2	0.45	6.12	0.302
0.76	0.861	0.353	74.1	12.5	0.47	5.94	0.304
0.77	0.857	0.357	73.5	12.8	0.50	5.76	0.306
0.78	0.854	0.361	72.9	13.0	0.52	5.59	0.308
0.79	0.850	0.365	72.2	13.3	0.55	5.42	0.310
0.80	0.846	0.369	71.6	13.6	0.57	5.26	0.312
0.81	0.843	0.373	71.0	13.9	0.60	5.11	0.314
0.82	0.839	0.376	70.4	14.2	0.63	4.96	0.316
0.83	0.835	0.380	69.7	14.5	0.66	4.82	0.318
0.84	0.831	0.384	69.1	14.7	0.69	4.69	0.319
0.85	0.827	0.388	68.5	15.0	0.72	4.55	0.321
0.86	0.823	0.391	67.8	15.3	0.75	4.43	0.322
0.87	0.820	0.395	67.2	15.6	0.79	4.30	0.324
0.88	0.816	0.399	66.5	15.9	0.82	4.18	0.325
0.89	0.812	0.402	65.9	16.2	0.86	4.07	0.327
0.90	0.808	0.406	65.2	16.5	0.89	3.96	0.328
0.92	0.799	0.413	63.9	17.1	0.97	3.75	0.330
0.94	0.791	0.420	62.6	17.6	1.05	3.55	0.332
0.96	0.783	0.427	61.2	18.2	1.14	3.36	0.334
0.98	0.774	0.433	59.9	18.8	1.23	3.19	0.335
1.00	0.765	0.440	58.6	19.4	1.32	3.02	0.337
1.02	0.756	0.446	57.2	19.9	1.42	2.87	0.338
1.04	0.747	0.453	55.9	20.5	1.52	2.72	0.338

Continued on next page...

Table C.5 continued.

β	J_0	J_1	J_0^2 %	J_1^2 %	J_2^2 %	Ratio Squared	Multiplied
1.06	0.738	0.459	54.5	21.1	1.63	2.59	0.339
1.08	0.729	0.465	53.1	21.6	1.75	2.46	0.339
1.10	0.720	0.471	51.8	22.2	1.86	2.34	0.339
1.12	0.710	0.477	50.4	22.7	1.99	2.22	0.339
1.14	0.701	0.482	49.1	23.3	2.12	2.11	0.338
1.16	0.691	0.488	47.7	23.8	2.25	2.01	0.337
1.18	0.681	0.493	46.4	24.3	2.39	1.91	0.336
1.20	0.671	0.498	45.0	24.8	2.54	1.81	0.334
1.22	0.661	0.503	43.7	25.3	2.69	1.73	0.333
1.24	0.651	0.508	42.4	25.8	2.85	1.64	0.331
1.26	0.641	0.513	41.1	26.3	3.01	1.56	0.329
1.28	0.630	0.518	39.8	26.8	3.18	1.48	0.326

C.7 Saturation Modeling Program

C.7.1 Experimental NIR Saturation

Some useful complex number identities are given in Equations C.2 and C.3.

$$\text{Erfi}[z] = -i \text{Erf}[iz] = \frac{2}{\sqrt{\pi}} \int_0^z \text{Exp}[s^2] ds \quad (\text{C.2})$$

$$\text{Erfc}[z] = 1 - \text{Erf}[z] = \frac{2}{\sqrt{\pi}} \int_z^\infty \text{Exp}[-(s^2)] ds \quad (\text{C.3})$$

The Mathematica file used to simulate the saturation effects on the ion beam line shape is shown below.

```
(*Change the fm to the value you want. Ma or Exp *)
(*Choose the y you want (by changing a=) *)
muu = 10000;
HWHM = 0.0125750701317101; (*Dopplerl angular half*)
(*fm=0.020120112; (* Ma2008 *) *)
fm = 0.02368304874805400; (* Experimental *)
dx[x_] := x - muu;
xneg1[x_] := 1 (dx[x] - fm)*Sqrt[Log[2.]]/HWHM;
xpos1[x_] := 1 (dx[x] + fm)*Sqrt[Log[2.]]/HWHM;
xzero[x_] := 1 (dx[x])*Sqrt[Log[2.]]/HWHM;
yneg1[Gminus_, y_] := y*Sqrt[1 + Gminus];
ypos1[Gplus_, y_] := y*Sqrt[1 + Gplus];
yzero[Gzero_, y_] := y*Sqrt[1 + Gzero];
zneg1[x_, Gminus_, y_] := xneg1[x] + I*yneg1[Gminus, y];
zpos1[x_, Gplus_, y_] := xpos1[x] + I*ypos1[Gplus, y];
zzero[x_, Gzero_, y_] := xzero[x] + I*yzero[Gzero, y];
dubyajneg1[x_, Gminus_, y_] := (1 + I*Erfi[zneg1[x, Gminus, y]])* E^- (zneg1[x, Gminus, y]^2);
dubyajpos1[x_, Gplus_, y_] := (1 + I*Erfi[zpos1[x, Gplus, y]])* E^- (zpos1[x, Gplus, y]^2);
dubyajzero[x_, Gzero_, y_] := (1 + I*Erfi[zzero[x, Gzero, y]])* E^- (zzero[x, Gzero, y]^2);
Dispneg1[x_, Gminus_, y_] := Im[dubyajneg1[x, Gminus, y]];
Disppos1[x_, Gplus_, y_] := Im[dubyajpos1[x, Gplus, y]];
```

```

Dispzero[x_, Gzero_, y_] := -1*Im[dubyaajzero[x, Gzero, y]];
TotalDisp[x_, Gminus_, Gzero_, Gplus_, y_] := Dispneg1[x, Gminus, y] + Dispzero[x, Gzero, y] + Disppos1[x, Gplus,
y];
Absneg1[x_, Gminus_, y_] := Re[dubyaajneg1[x, Gminus, y]];
Abspos1[x_, Gplus_, y_] := Re[dubyaajpos1[x, Gplus, y]];
TotalAbs[x_, Gminus_, Gplus_, y_] := (1/Sqrt[1 + Gplus]) (-Absneg1[x, Gminus, y] + Abspos1[x, Gplus, y]);
DirectoryName["C:\\Documents and Settings\\Andrew\\Desktop\\"];
a = 0.1
xwave = Range[9999.9, 10000.1, .0001];
ywave1 = TotalDisp[xwave, 0, 0, 0, a];
ywave2 = TotalDisp[xwave, .03, .97, .03, a];
ywave3 = TotalDisp[xwave, .09, 2.91, .09, a];
ywave4 = TotalDisp[xwave, .3, 9.7, .3, a];
ywave5 = TotalDisp[xwave, .9, 29.1, .9, a];
ywave6 = TotalDisp[xwave, 3, 97, 3, a];
ywave7 = TotalDisp[xwave, 30, 970, 30, a];
ywave8 = TotalDisp[xwave, 300, 9700, 300, a];
Export["xwave.xls", xwave];
Export["ywave1.xls", ywave1];
Export["ywave2.xls", ywave2];
Export["ywave3.xls", ywave3];
Export["ywave4.xls", ywave4];
Export["ywave5.xls", ywave5];
Export["ywave6.xls", ywave6];
Export["ywave7.xls", ywave7];
Export["ywave8.xls", ywave8];
ywave11 = TotalAbs[xwave, 0, 0, a];
ywave12 = TotalAbs[xwave, .03, .03, a];
ywave13 = TotalAbs[xwave, .09, .09, a];
ywave14 = TotalAbs[xwave, .3, .3, a];
ywave15 = TotalAbs[xwave, .9, .9, a];
ywave16 = TotalAbs[xwave, 3, 3, a];
ywave17 = TotalAbs[xwave, 30, 30, a];
ywave18 = TotalAbs[xwave, 300, 300, a];
Export["ywave11.xls", ywave11];
Export["ywave12.xls", ywave12];
Export["ywave13.xls", ywave13];
Export["ywave14.xls", ywave14];
Export["ywave15.xls", ywave15];
Export["ywave16.xls", ywave16];
Export["ywave17.xls", ywave17];
Export["ywave18.xls", ywave18];
(*Ion Beam Simulations*)
a = 0.028
xwave = Range[9999.9, 10000.1, .0001];
ywave1=TotalDisp[xwave,0,0,0,a];
ywave2=TotalDisp[xwave,.15,.7,.15,a];
ywave3=TotalDisp[xwave,.45,2.1,.45,a];
ywave4=TotalDisp[xwave,1.5,7,1.5,a];
ywave5=TotalDisp[xwave,4.5,21,4.5,a];
ywave6=TotalDisp[xwave,15,70,15,a];
ywave7=TotalDisp[xwave,150,700,150,a];
ywave8 = TotalDisp[xwave, 1500, 7000, 1500, a];
ywave9=TotalDisp[xwave,6311,30299,6311,a];
Export["xwave.xls",xwave];
Export["ywave1.xls",ywave1];
Export["ywave2.xls",ywave2];
Export["ywave3.xls",ywave3];

```

```

Export["ywave4.xls",ywave4];
Export["ywave5.xls",ywave5];
Export["ywave6.xls",ywave6];
Export["ywave7.xls",ywave7];
Export["ywave8.xls", ywave8];
Export["ywave9.xls",ywave9];
ywave11=TotalAbs[xwave,0,0,a];
ywave12=TotalAbs[xwave,.15,.15,a];
ywave13=TotalAbs[xwave,.45,.45,a];
ywave14=TotalAbs[xwave,1.5,1.5,a];
ywave15=TotalAbs[xwave,4.5,4.5,a];
ywave16=TotalAbs[xwave,15,15,a];
ywave17=TotalAbs[xwave,150,150,a];
ywave18=TotalAbs[xwave,1500,1500,a];
ywave19=TotalAbs[xwave,6311,6311,a];
Export["ywave11.xls",ywave11];
Export["ywave12.xls",ywave12];
Export["ywave13.xls",ywave13];
Export["ywave14.xls",ywave14];
Export["ywave15.xls",ywave15];
Export["ywave16.xls",ywave16];
Export["ywave17.xls",ywave17];
Export["ywave18.xls",ywave18];
Export["ywave19.xls",ywave19];
Plot[TotalDisp[x, 0, 0, 0, 0.028], TotalDisp[x, .15, .7, .15, 0.028], TotalDisp[x, .45, 2.1, 4.5, 0.028], TotalDisp[x, 1.5,
7, 1.5, 0.028], TotalDisp[x, 4.5, 21, 4.5, 0.028], TotalDisp[x, 15, 70, 15, 0.028], TotalDisp[x, 150, 700, 150, 0.028],
TotalDisp[x, 1500, 7000, 1500, 0.028], TotalDisp[x, 6311, 30229, 6311, 0.028], x, 9999.90, 10000.1, PlotRange ->(*-
1.1*)All] (* Ion Beam Values*)
Plot[TotalDisp[x, 0, 0, 0, b], TotalDisp[x, .03, .97, .03, b], TotalDisp[x, .09, 2.91, .09, b], TotalDisp[x, .3, 9.7, .3, b],
TotalDisp[x, .9, 29.1, .9, b], TotalDisp[x, 3, 97, 3, b], TotalDisp[x, 30, 970, 30, b], TotalDisp[x, 300, 9700, 300, b], x,
9999.925, 10000.075, PlotRange -> All] (* Ma Different Values*)

```

C.7.2 Theoretical MIR Saturation

The parameters of the Mathematica simulation code was changed as indicated for the mid-IR calculations.

```

HWHM = 0.00419; (*Dopplerl angular half*)
(*Ion Beam Simulations*)
a = 0.011
xwave = Range[9999.9, 10000.1, .0001];
ywave1 = TotalDisp[xwave, 0, 0, 0, a];
ywave2 = TotalDisp[xwave, .15, .7, .15, a];
ywave3 = TotalDisp[xwave, .45, 2.1, .45, a];
ywave4 = TotalDisp[xwave, 1.5, 7, 1.5, a];
ywave5 = TotalDisp[xwave, 4.5, 21, 4.5, a];
ywave6 = TotalDisp[xwave, 9, 45, 9, a];
Export["xwave.xls", xwave];
Export["ywave1.xls", ywave1];
Export["ywave2.xls", ywave2];
Export["ywave3.xls", ywave3];
Export["ywave4.xls", ywave4];
Export["ywave5.xls", ywave5];
Export["ywave6.xls", ywave6];
ywave11 = TotalAbs[xwave, 0, 0, a];
ywave12 = TotalAbs[xwave, .15, .15, a];

```

```
ywave13 = TotalAbs[xwave, .45, .45, a];  
ywave14 = TotalAbs[xwave, 1.5, 1.5, a];  
ywave15 = TotalAbs[xwave, 4.5, 4.5, a];  
ywave16 = TotalAbs[xwave, 9, 9, a];  
Export["ywave11.xls", ywave11];  
Export["ywave12.xls", ywave12];  
Export["ywave13.xls", ywave13];  
Export["ywave14.xls", ywave14];  
Export["ywave15.xls", ywave15];  
Export["ywave16.xls", ywave16];
```


Appendix D

Appendix for Ion Beam System

D.1 Welch Pump Exhaust Adapter

Future mid infrared ion beam experiments will involve pumping hydrogen as part of the discharge. Therefore, the mechanical pump which vents the turbos needed to be vented to the ventilation system of RAL. The drawings for the adapter necessary to connect the welch pump to the building exhaust is shown in Figure D.1. 3/4" ID Tygon tubing connects this adapter to a quick-flange connection, that is welded into the pump room's exhaust pipe.

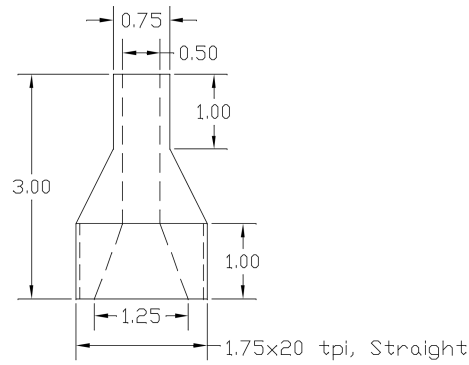
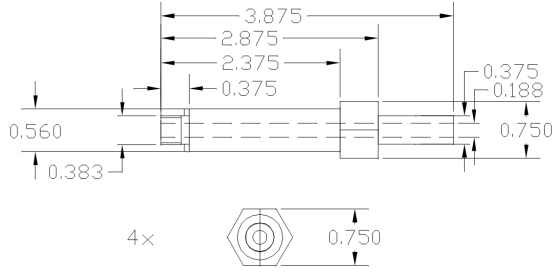


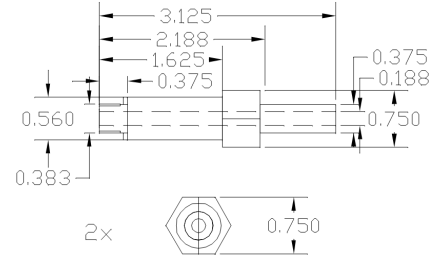
Figure D.1: Schematic of adapter for welch pump exhaust.

D.2 Varian Turbo Pump Water Cooling Adapters

Each Varian turbo pump has a British pipe thread inlet and outlet port tapped with 1/8" x 28 threads per inch parallel threads. Adapters to connect 3/8" Swagelok to this inlet were constructed from brass. A #110 O-ring is used on the threaded side, so a 1/8" recess for the threads is acceptable. The non-threaded side is connected with a 3/8" Swagelok connection. The drawings for the water cooling adapters are shown in Figure D.2.



(a) Schematic of water cooling adapters for Varian Navigator 550.



(b) Schematic of water cooling adapters for Varian Navigator 250.

Figure D.2: Schematics for water cooling adapters for Navigator 550 and 250 turbo pumps machined from brass.

D.3 80-20 Building Materials

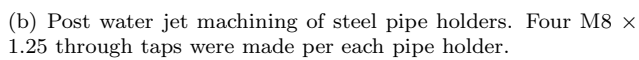
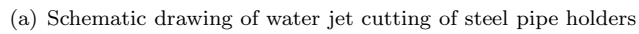
A heavy duty instrument base was constructed out of 2"x2" aluminum 80-20 extrusions. A list of 80-20 parts purchased for construction of ion beam base, as well as general lab construction, is shown in Table D.1. A schematic for the top view of the ion beam base is given in Figure 5.7.

Part #	Quantity	Length (")	Unit	Description
1010	20	72	IN	1"x1" T-Slot Extrusion
2020	8	72	IN	2"x2" T-Slot Extrusion
2020	26	22.5	IN	2"x2" T-Slot Extrusion
2020	34	12.75	IN	2"x2" T-Slot Extrusion
2020	4	90	IN	2"x2" T-Slot Extrusion
2020	4	26.645	IN	2"x2" T-Slot Extrusion
2020	6	7.917	IN	2"x2" T-Slot Extrusion
2142	8		Ea	10S 2"x2" Base Plate 3/8"-16 Tap in Corner
2299	8		Ea	2" Swivel Caster with 3/8"-16 Stem with Brake
2408	14		Ea	15 S base plate for 2715
2715	14		Ea	600 Lb leveling caster
3112	80		Ea	5/16" x 3/4" SHCS
3321	60		Ea	1/4"-20 x 1/2" FBHSCS & Econ T-Nut
3376	200		Ea	10 S Drop-in T-Nut 1/4"-20
3393	1420		Ea	1/4"-20 x 1/2" BHSCS Econ T-Nut
3458	56		Ea	5/16" x 7/8" SHCS Econ T-Nut
3916	100		Ea	1/4"-20 Drop in T-Nut with Ball and Spring
4113	40		Ea	10S 4 Hole Inside Corner Bracket
4114	130		Ea	10S 8 Hole Inside Corner Bracket
4119	60		Ea	10S 2 Hole Inside Corner Bracket
4166	30		Ea	10 S 6 Hole Joining Plate
4167	20		Ea	10 S 4 Hole Joining Plate

Table D.1: 80-20 parts purchased for construction of instrument base.

D.4 Steel Pipe Holders

Steel pipe holders were built to hold the 8" CF tubes that comprise the ion beam instrument, connect them to the instrument base, and center the pipes. The most cost effective way to have these parts made was to first water jet cut the general outline, use a band saw to cut them into two pieces, and then finish machining with an endmill. Figure D.3 contains the machining schematics for the steel pipe holders.



D.5 Source

Several parts were machined for the source, including the source ferrules, a holder for the source, and water and electrical connections for the back electrode of the source. Engineering schematics for the custom designed ferrules are shown in Figure D.4.

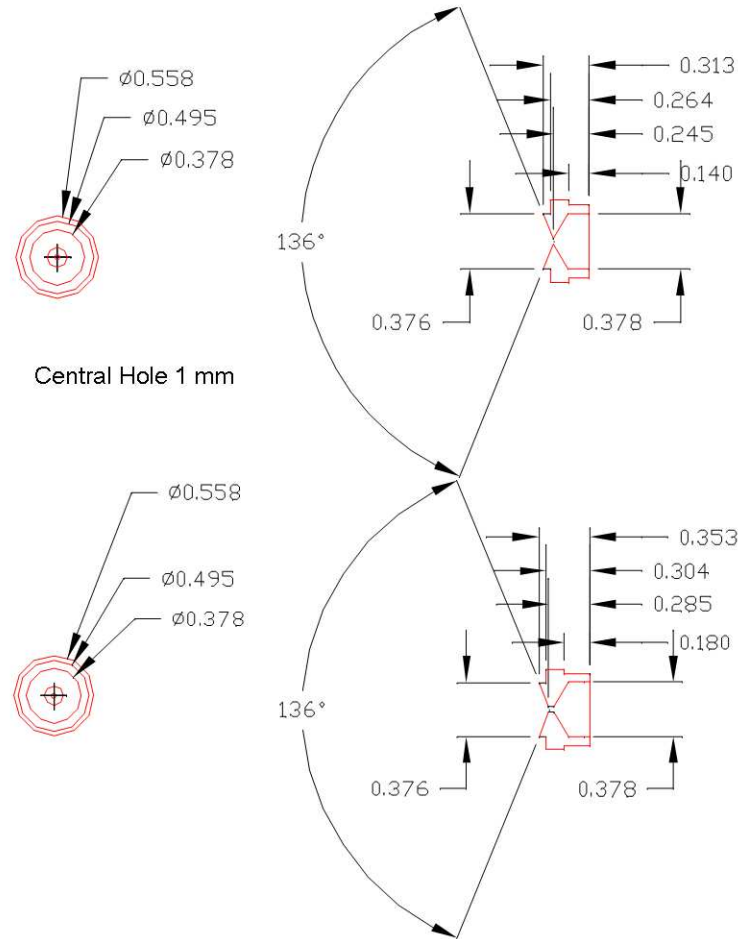


Figure D.4: Engineering schematic of the front ferrule, machined from stainless steel.

The back source electrode was sandwiched between an aluminum and PEEK pieces which threaded together. The PEEK piece was attached to the back flange of the source chamber, and can be translated in the X and Y directions. The engineering schematics for the aluminum and PEEK parts are shown in Figure D.5. An adapter for bringing a bias voltage to the back electrode of the cold cathode source is constructed out of PEEK, and threads into the 1/4"-28 threads in the aluminum source holder, and the engineering schematics for this part are found in Figure D.6.

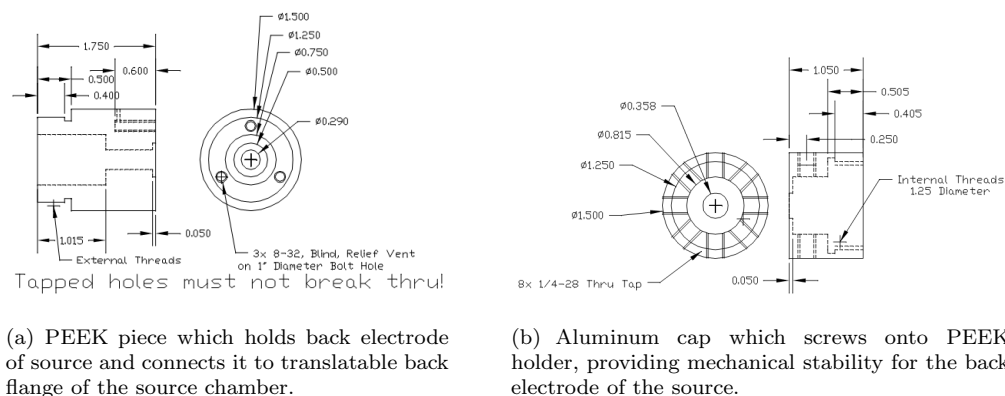


Figure D.5: Schematic for PEEK and aluminum back electrode adapters and holders.

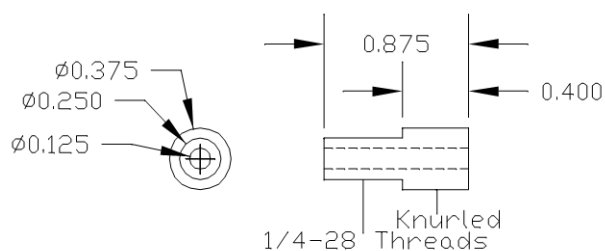


Figure D.6: Homemade PEEK adapter screw used for connecting discharge voltage to back electrode.

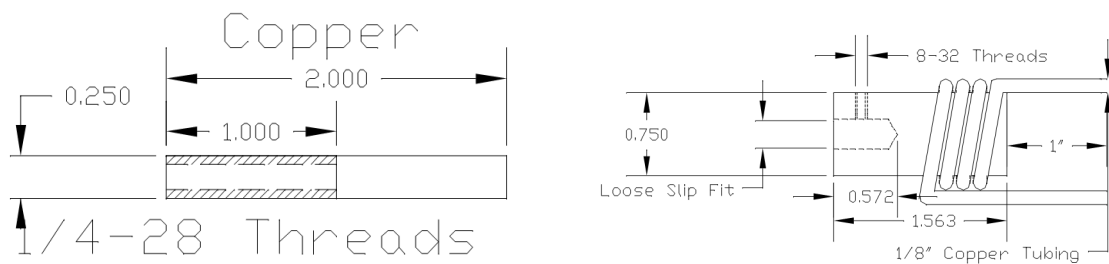
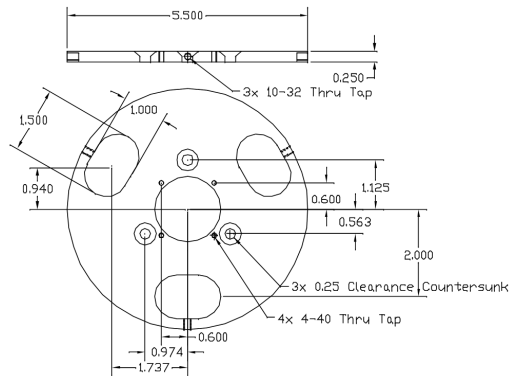


Figure D.7: Schematics for water cooling setup necessary for anodic extraction.

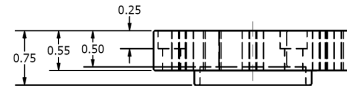
D.6 Einzel Lens 1

The positive ions that emerge from the ion source are extracted by a stainless steel plate and focused by the first Einzel lens. Drawings for the parts that comprise the Einzel lens are shown in Figure D.8. The aperture of the extractor plate diameter can be chosen by attaching a stainless steel plate with the desired aperture diameter to the extractor plate. The extractor plate typically had 0.25" diameter aperture attached (Kimball Physics, B Series, 5x5, 0.25" Round Diameter). The stainless steel Einzel lens was constructed by the University of Illinois machine shop and electropolished. It was assembled with high-temperature alumina ceramic balls (McMaster-Carr 9599K16 1/2" diameter) and tubes (McMaster-Carr 8746K18-0.375" OD, 0.25" ID x 1" long) used to electrically isolate the biased, central plate from the outer plates, which were connected to ground. Three 10-32 set screws are used to position the extractor plate into position, 2 of which have a springloaded plunger (McMaster-Carr 8688A141), and the other set screw with a flat end. Bias voltage for the Einzel lens via a 5 kV SHV feedthrough on a 2-3/4" flange located off of the source chamber.

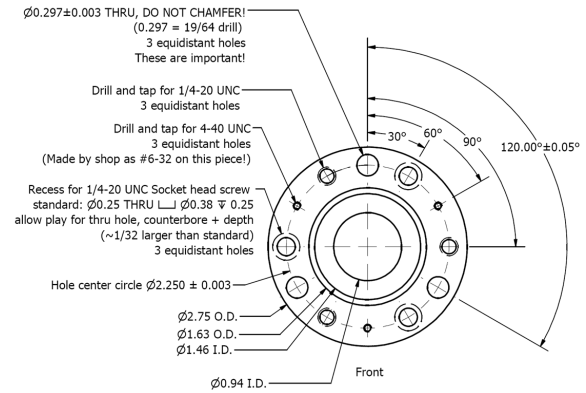
A photo of the assembled Einzel lens is shown in Figure D.9. Ceramic balls separate the middle electrode from the front and back ground electrodes. Ceramic tubes insulate the screws which attach the front and back ground electrodes from the middle electrode. High voltage is applied to the middle electrode.



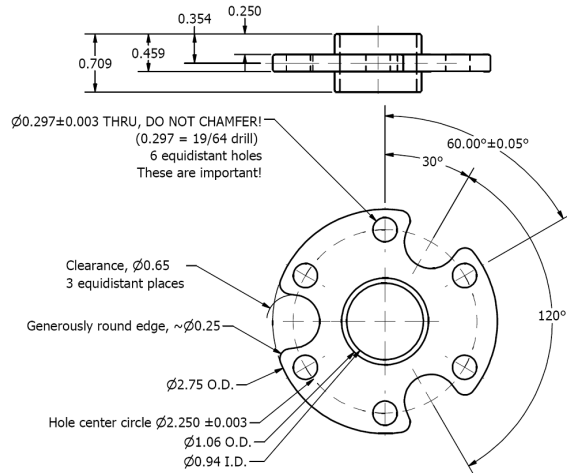
(a) Schematic of extractor plate.



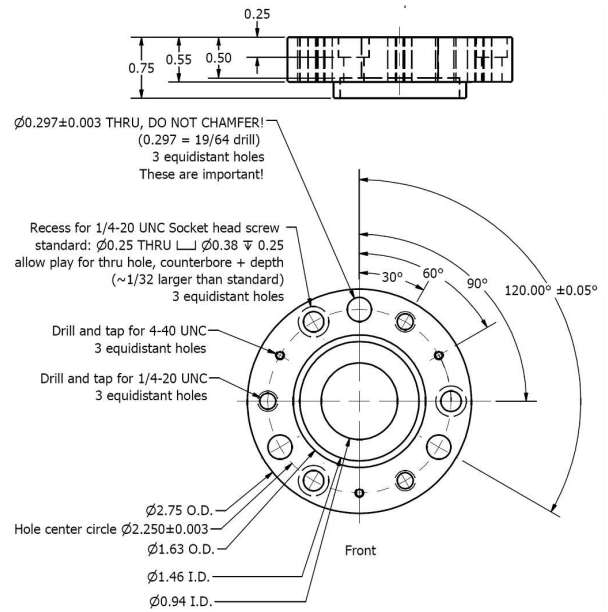
The $\phi 19/64$ THRU holes are important for aligning the different parts one to another (all three workpieces have these kinds of holes).



(b) Schematic of front plate.



(c) Schematic of middle plate.



(d) Schematic of back plate.

Figure D.8: Schematics for the first Einzel lens, machined out of stainless steel.

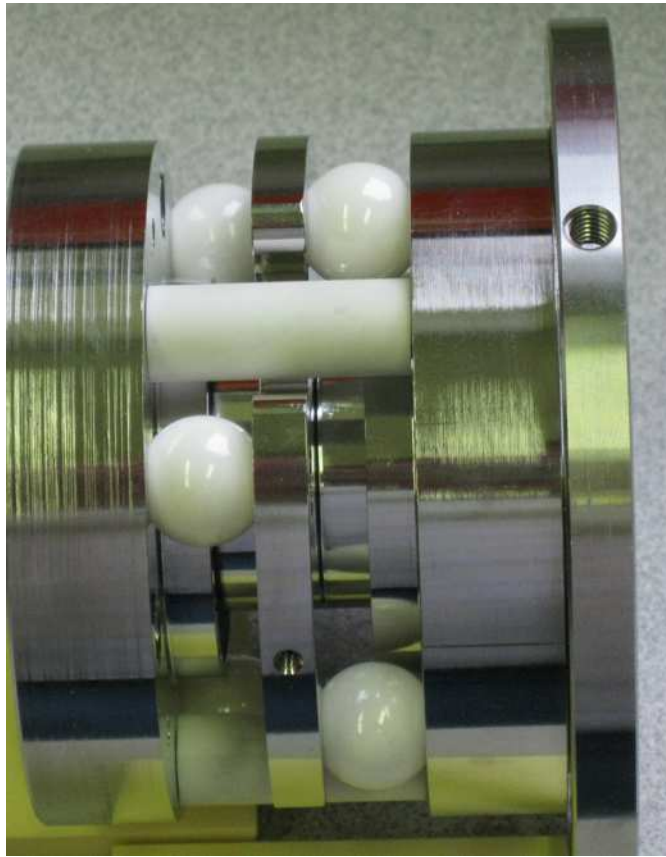


Figure D.9: Photo of assembled Einzel lens.

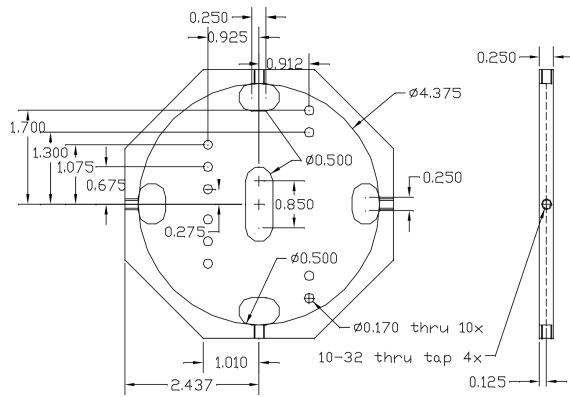
D.7 Steerers

The steerer assembly is constructed from $8 \times 1/4$ " thick plates, 1.5" wide by 1" long. The first set of 4 is separated from the second set of four with $1/8$ " ceramic spacers. There are no schematic drawings for the steerers.

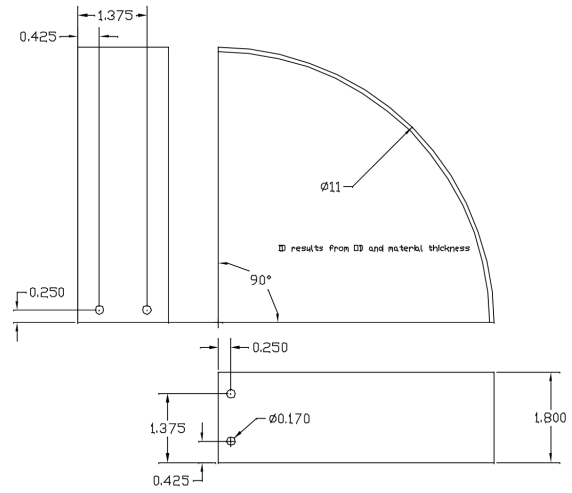
D.8 Cylindrical Deflectors

Technical drawings of the cylindrical deflectors are shown in Figure D.10. The benders were constructed from stainless steel sheets (McMaster Carr 89815K43 0.036" thick). Metal 6-32 screws were used to connect the bender plates to the blocks through ceramic spacers (McMaster-Carr 96109A160). PEEK screws (McMaster Carr 96367A477 6-32 threads, $3/4$ " long) were used to connect the front plates of the bender to the blocks also through the ceramic spacers. Four set screws (2 springloaded, 2 flat) (McMaster Carr 8688A141 and 94355A341) were used to center the plates of the bender to the 8" Conflat cross.

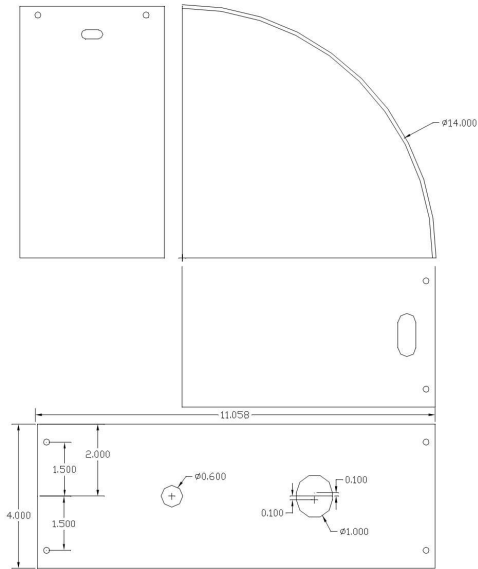
A photo of the assembled cylindrical bender is shown in Figure D.11.



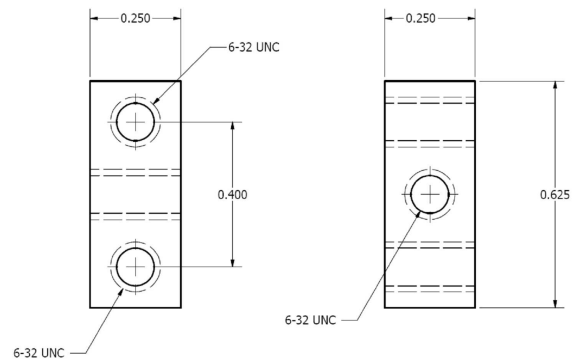
(a) Schematic of entrance and exit apertures of benders.



(b) Schematic of the inner bender plate.



(c) Schematic of the outer bender plate.



(d) Schematic of connection blocks.

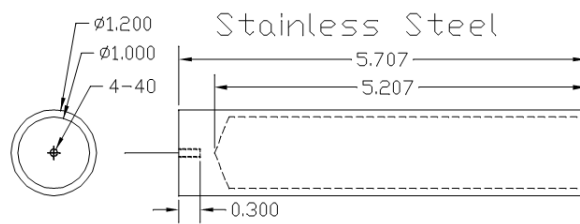
Figure D.10: Schematics for electrostatic benders, machined from stainless steel.



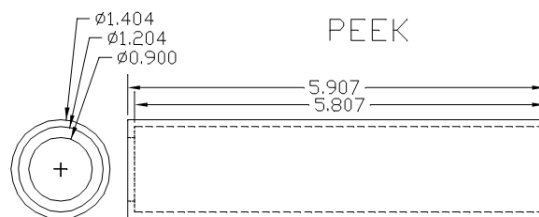
Figure D.11: Photo of assembled cylindrical bender.

D.9 Faraday Cup 1

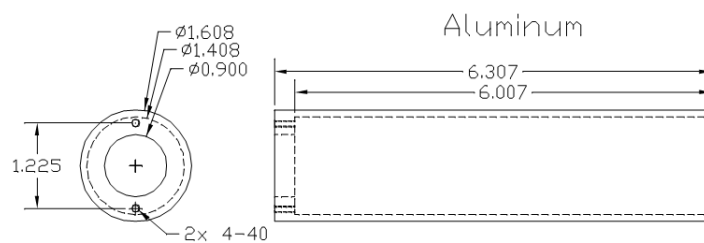
Technical drawings for the first Faraday cup are shown in Figure D.12. The collector of the Faraday cup was connected directly to a SHV-5 feedthrough.



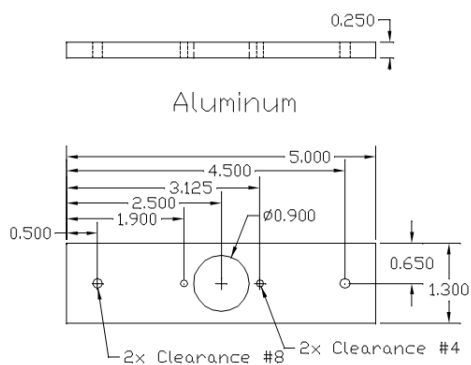
(a) Schematic of the ion collector.



(b) Schematic of the insulator.

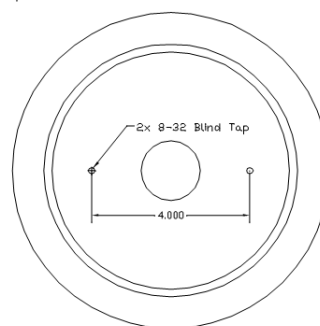


(c) Schematic of the ground covering.



(d) Schematic of adapter plate.

Add 2x 8-32 taps to a 8:2-3/4" conflat reducer
With the taps on the side of the 8" knife edge.



(e) Schematic of modifications made to 8" to 2-3/4" CF reducer to attach the Faraday cup.

Figure D.12: Schematics for the first Faraday cup.

D.10 Drift Region

A drift tube was modified from a stainless steel tube 1.25" in diameter, 10.72" long (McMaster-Carr 8989K308) by adding two slots, as illustrated in Figure 5.16. An additional 0.15" diameter hole in the tube is used to connect the drift tube to a BNC feedthrough. Iris plates (as illustrated in Figure D.13) were constructed. Two stainless steel 6-32 screws were used to connect the iris plates to the linear motion manipulators. Polycarbonate washers are used to electrically isolate that screw from the manipulator. A third hole was included in the iris plate to connect each iris plate to a BNC feedthroughs.

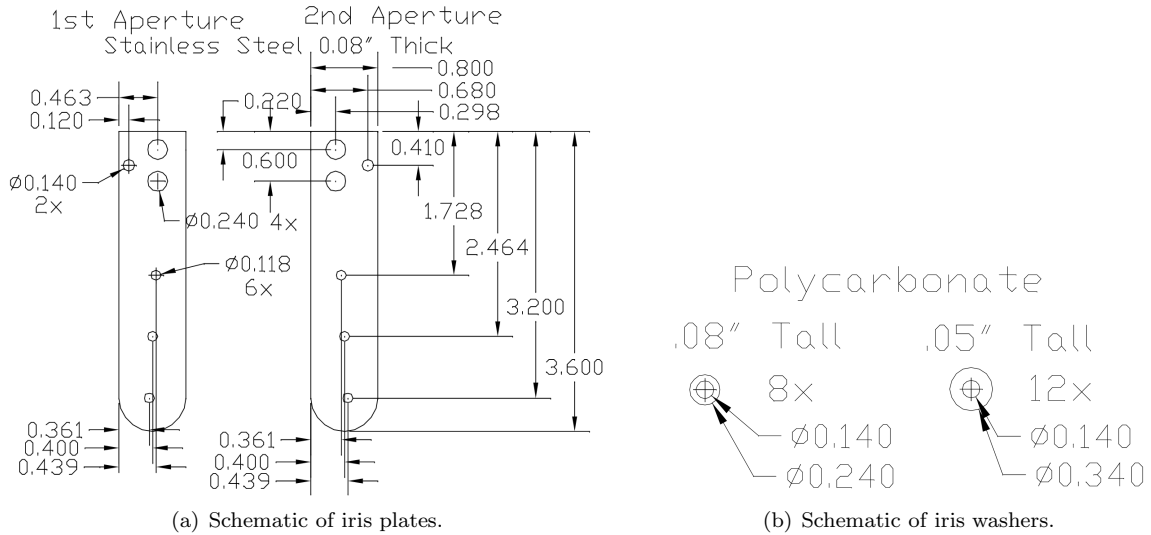


Figure D.13: Schematics for irises for achieving laser beam / ion beam overlap.

Each iris plate has three holes, each 3 mm in diameter, and horizontally offset from each other by 1 mm. Engineering schematics for the construction of the aperture plates, and plastic washers are shown in Figure D.13.

D.11 Einzel Lens 2

The second Einzel lens was constructed similar to the first lens diagrammed in Figure D.8. Modifications to the second lens are diagrammed in Figure D.14.

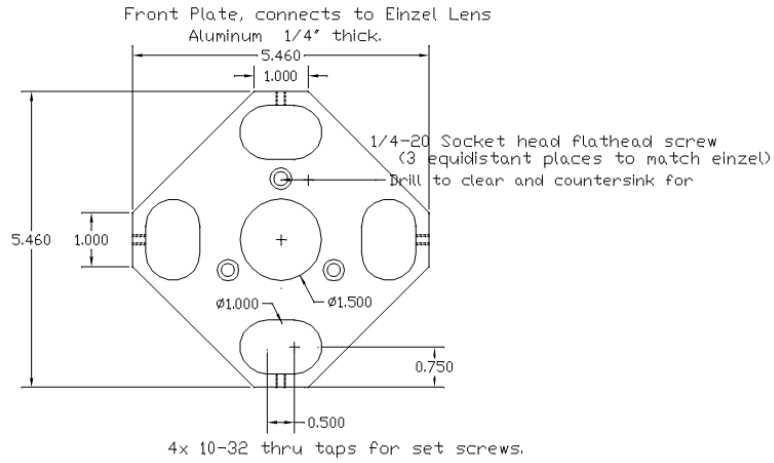
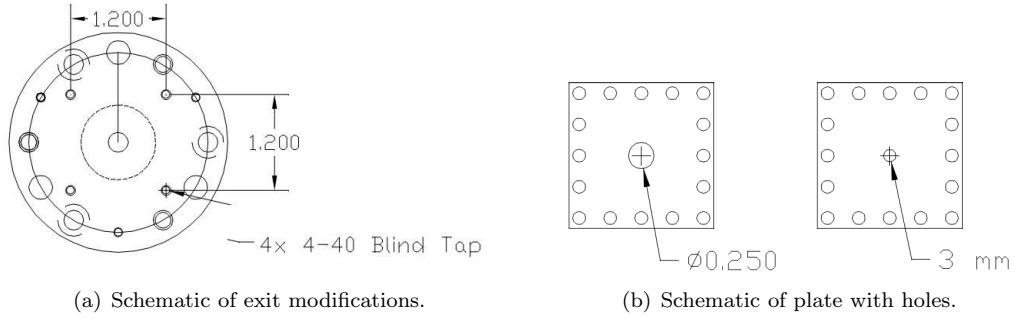
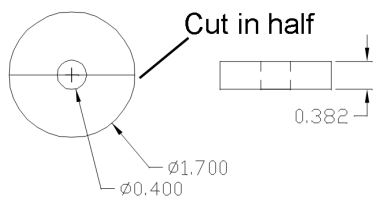


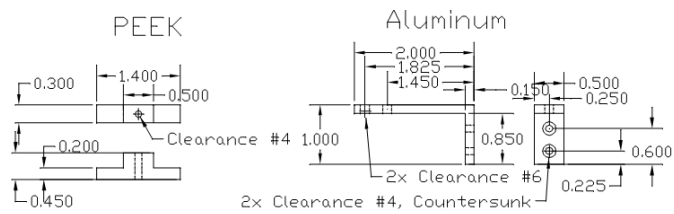
Figure D.14: Schematic drawing for modifications of Einzel lens shown in Figure D.8 for Einzel lens 2.

D.12 Faraday Cup 2

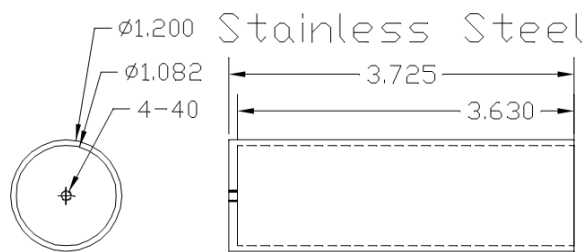
The second Faraday cup was constructed similar to the first Faraday cup, and schematics for the parts are shown in Figure D.15. The electrode of the Faraday cup is connected to a SHV-5 feedthrough, which is later connected to a picoammeter.



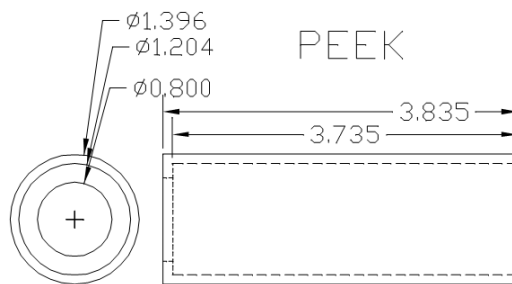
(a) Schematic of aluminum height jig.



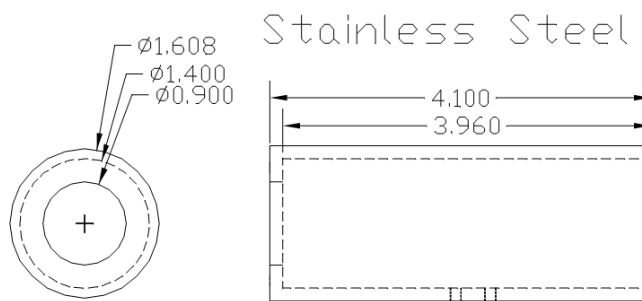
(b) Schematic of Faraday connector bracket and insulator.



(c) Schematic of Faraday cup 2 electrode.



(d) Schematic of Faraday cup 2 insulator.

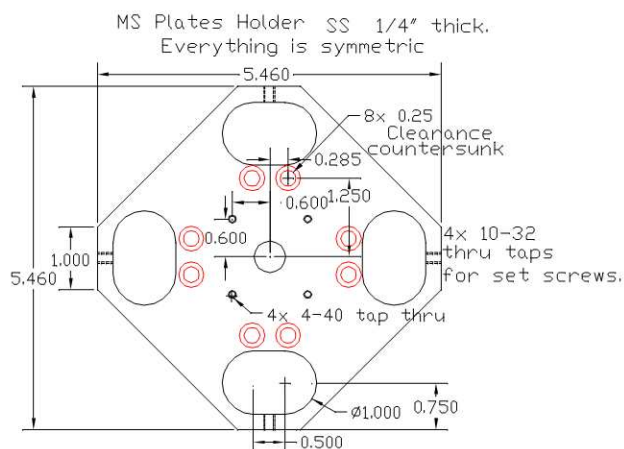


(e) Schematic of Faraday cup 2 ground connection.

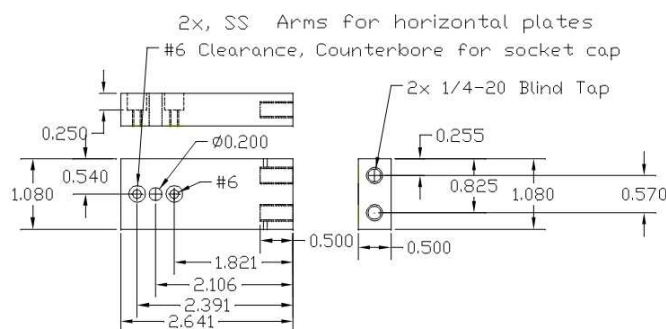
Figure D.15: Schematic drawings for Faraday cup 2.

D.13 Beam Modulated Time of Flight Pulser Plates

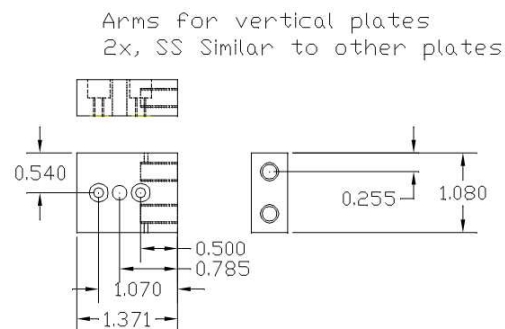
Schematics for the pulsing plates of the beam modulated time of flight mass spectrometer are shown in Figure D.16.



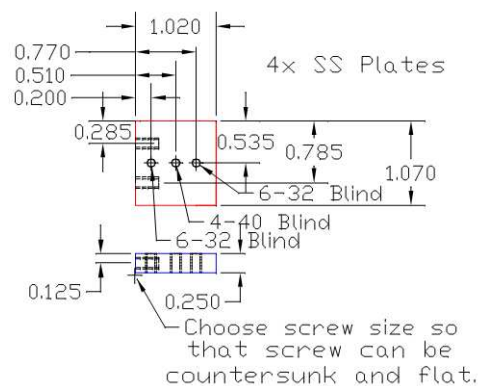
(a) Schematic of MS pulser connector.



(b) Schematic of pulser long arms.

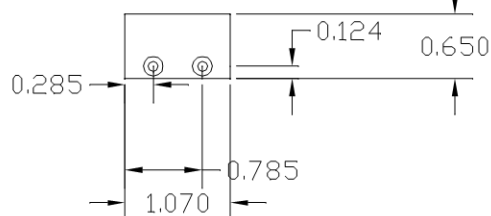


(c) Schematic of pulser short arms.



(d) Schematic of pulser electrodes.

4x SS Plates 0.05" thick
Clearance holes countersunk
Choose screw size so that screw can be countersunk and flat.



(e) Schematic of pulser protectors.

Figure D.16: Schematic drawings for MS ion optics pulser.

D.14 MS Iris

As part of the beam modulated time of flight mass spectrometer, an iris was constructed and positioned approximately 3" before the electron multiplier. The iris was positioned inside of the 4.5" 4-way cross, connected directly to the flange input flange. The design for this iris is shown in Figure D.17. A stainless steel piece of 1/16" sheet metal is machined so that it can form an iris. The tabs on the side are tapped so that 4-40 screws can be used to hold the piece inside of the cross, properly centering the iris.

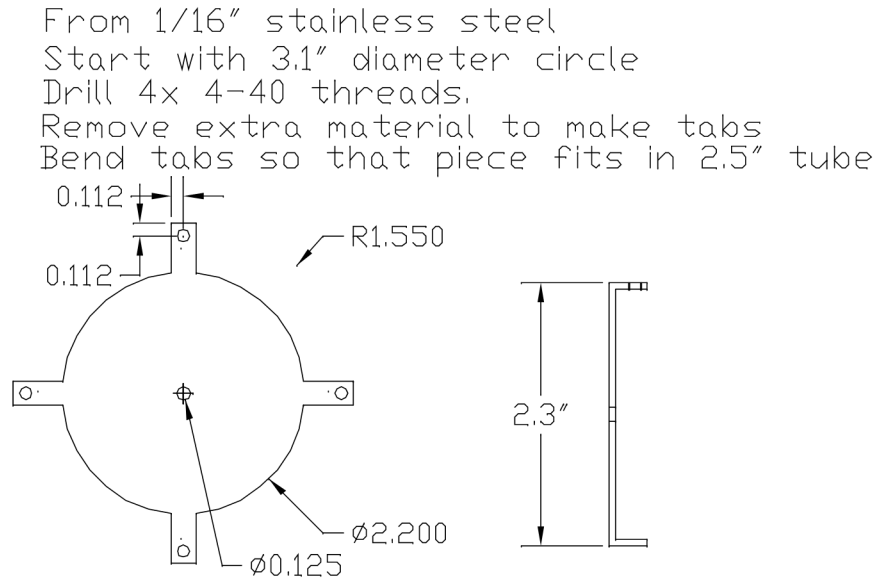
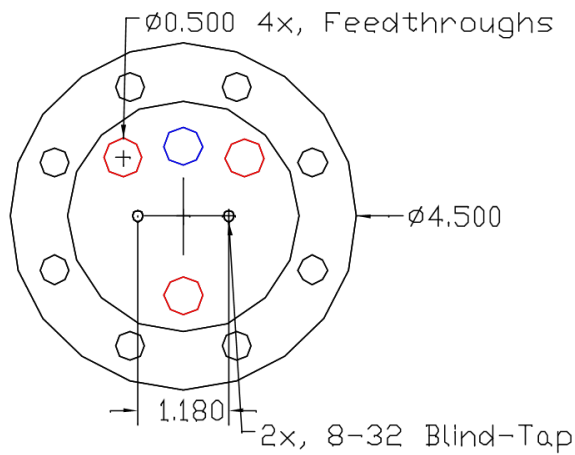


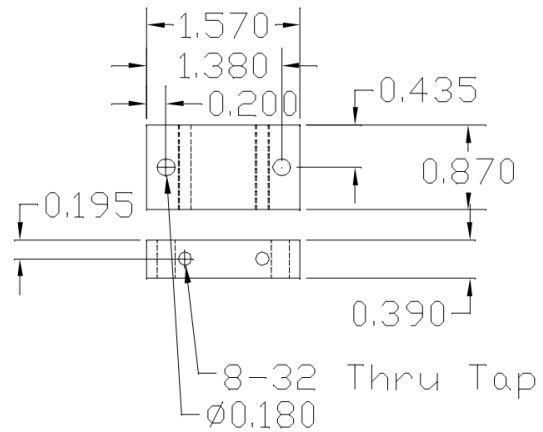
Figure D.17: Schematic drawing of end iris.

D.15 Electron Multiplier Mount

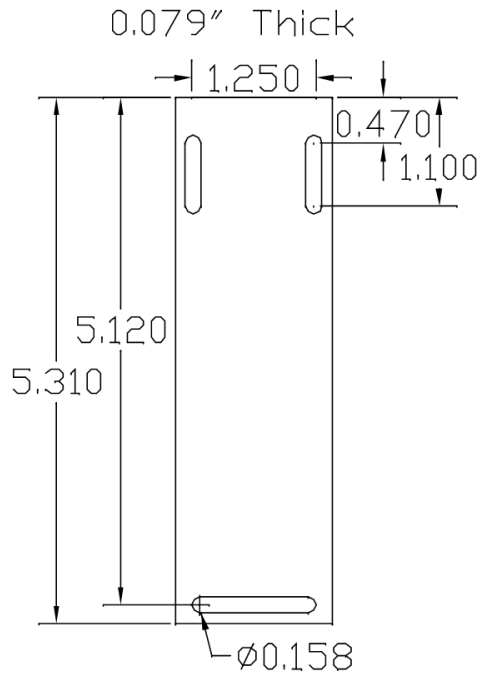
Schematic drawings of the modified 4.5" CF flange, block, and plate used to hold the electron multiplier are shown in Figure D.18. Three SHV-5 and one BNC feedthroughs were welded into the CF flange to allow for electrical connections to the detector.



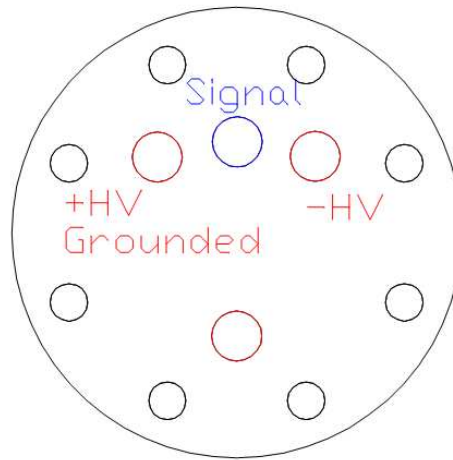
(a) Schematic of modifications made to 4.5" CF blank flange when viewed from the CF side. Four 1/2" holes were milled through and three SHV-5 feedthroughs were welded into place (red). One BNC feedthrough was welded into place in the top middle (blue).



(b) Schematic of aluminum block that connects the detector plate to the flange.



(c) Schematic of aluminum plate which connects the detector to the aluminum block.



(d) Electrical connections for detector flange as viewed from the outside the vacuum.

Figure D.18: Schematic drawings for plates, blocks, and flanges for connecting the electron multiplier to a 4.5" CF flange.

D.16 Brewster Windows

Two aluminum brewster window holders were designed for CaF_2 brewster windows. Engineering schematics for the holders are shown in Figure D.19.

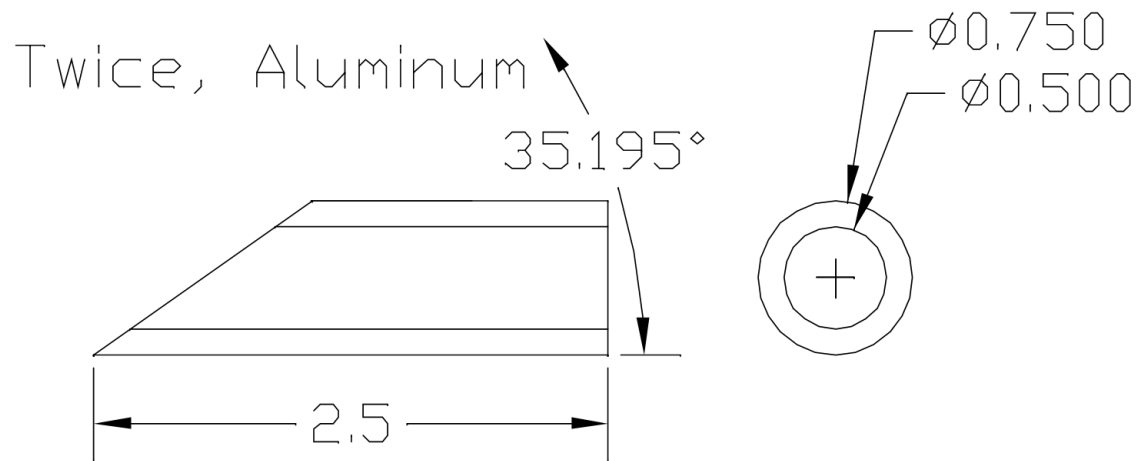


Figure D.19: Schematic drawing of Brewster window holders.

Appendix E

Appendix for N_2^+ in Ion Beam

E.1 Igor Data File Reader

The Igor procedure file to signal processing is shown below.

```
#pragma rtGlobals=1 // Use modern global access method.

// Modified September 3, 2011

// Various functions that also are necessary.
//function Singleload(numwaves,LI1Norm,LI2Norm, LI3Norm) // 22 uv/10, , ,
// makedoppler(suffix,voltage,plusvoltage,minusvoltage)
// killcomb(suffix) removes comb files, if unnecessary.
// redocomb(suffix). recalibrates the comb spectrum and redoes the AOMShiftComb
// modedet(suffix,low,high) makes a graph of a histogram of the mode numbers of the
//absolute comb mode number determination. input low and high as mode-.35 and mode+.35.
// addmode(suffix) adds the mode to the AMN graph.
// makedoppler(suffix,beamvoltage,plusmodvoltage,minusmodvoltage).
// Makes Fplus1_suffix, minus, 1,2
// adddoppler(suffix). Add's doppler lines to graph.
// fixgraph(). Makes bottom high trip 100000
// deletepnts(suffix,start,length). Deletes many points from the waves.
// tableone(suffix). Makes a table with the waves, with and without comb info.
// removeone(suffix). Deletes most if not all, waves with the suffix input.
// singlesplit(frequency,voltage,plusvoltage,minusvoltage).
// Gives a single split of a single frequency.
// changeheterodyne puts sidebands on shifted N2-lus lines. Less important.
// makemask(suffix,fewer). Makes a wave that has a 1 every "fewer"
// points and the rest are zeros.
// subgraphcomb(suffix,fewer). duplicates xasuffixf to xasuffixs and
// combshiftwnr to combshiftwnrs_suffix. Then applies mask and makes a sub graph.
// Only graphs one point every "fewer"
// subgraph(suffix,fewer). duplicates xasuffixf to xasuffixs and shiftwnr to
// shiftwnrs_suffix. Then applies mask and makes a sub graph.
// Only graphs one point every "fewer"
// suffix="14";appendtograph $("XaSmooth_"+ suffix) vs $("shiftwnr_"+ suffix);
// ModifyGraph rgb($("XaSmooth_"+ suffix))=(0,0,26112)
// smoothrotated(suffix)

// makeheterodyne(suffix, beam voltage, plusvoltage, minusvoltage, frequencymhz).
// Makes doppler and adds heterodyne, less important.
// addheterodyne2(suffix). Less Important.
// makegraphs(suffix1,suffix2). Makes graphs to compare to suffixs? Less important
// findsignalandnoise, right now nothing...
// rf_rot(x1,y1,x2,y2,degrees). Rotates across RF, maybe correct.
```

```

// rotator2(xa,ya,xb,yb,theta1,theta2) Rotates 2 x and y waves by different amounts.
// lorentz, DawsonF, GaussF, LorentzD, LorentzA, makedawson, makegaussian.
// Fitting functions
//function fullbinner(number,textwave1) // Andrew's binning program

function Singleload(numwaves,LI1Norm,LI2Norm, LI3Norm) // 23 uv/10, , ,
// Input normalization value, Normalization value = scale/10.
// So a 50 uV scale is 0.00005/10 = .000005.
variable numwaves, LI1Norm, LI2Norm, LI3Norm
// Open data file for reading
variable refNum
open/r refNum
fstatus refNum
print S_path
// Return file reading position back to beginning because
// we'll be returning to it later for meta data
fsetpos refNum,0
// Get Suffix to append to all wave names when loading data from .txt file
string suffix
prompt suffix, "Suffix:"
doprompt "Please type in a suffix",suffix

killthewaves(numwaves)
LoadWave /o/k=1/G/D /A=wave (S_path+S_filename) // (S_path+S_filename)//
// Load wave0 ... wave21
removezeros(numwaves)
allnumerical(numwaves)
namewaves(suffix)

make /d/o/n=70 $("StatS_" + suffix)
wave stats=$("StatS_" + suffix)
wavestats /Q $("P_" + suffix)

stats[0]=V_npnts
calibratespectrum(suffix)
// Wavelength_Suffix is unshifted
calibratespectrumComb(suffix)
// CombWavelength_Suffix is unshifted.
calibratedetector(suffix)
calibratePA(suffix)
normalizelockins(suffix, LI1Norm,LI2Norm, LI3Norm) // uV value
// Multiply Lock-In Values by normalization value. X1Norm_Suffix.
fractionalizelockins(suffix)
// X1Frac_Suffix.
DuplicateForRotation(suffix)

AOMShift(suffix)
// ShiftedWavelength_Suffix, ShiftWnr_Suffix
AOMShiftComb(suffix)
// CombShiftedWavelength_Suffix, ShiftWnr_Suffix
//killcomb(suffix)
rotator($("xa"+suffix) ,$("ya"+suffix),00)
rotator($("xb"+suffix) ,$("yb"+suffix),00)
makersnts(suffix)
smoothwaves(suffix)
smoothrotated(suffix)
DuplicateForNormalization(suffix)
normalizetovoltagecurrent(suffix)

```



```

getstats(suffix,LI1Norm,LI2Norm, LI3Norm)
smoothnormalized(suffix)

display $("xa"+ suffix) vs $("shiftwnr_"+ suffix)
// Display LockIn 1 vs shiftwnr
appendtograph $("ya"+ suffix) vs $("shiftwnr_"+ suffix)
appendtograph $("Xasmooth_"+ suffix) vs $("shiftwnr_"+ suffix)
appendtograph $("Yasmooth_"+ suffix) vs $("shiftwnr_"+ suffix)
ModifyGraph rgb($("Xa"+ suffix))=(48896,49152,65280)
ModifyGraph rgb($("Xasmooth_"+ suffix))=(0,0,39168)
ModifyGraph rgb($("Ya"+ suffix))=(65280,32768,32768)
ModifyGraph highTrip(bottom)=1e+07

display $("xa"+ suffix) vs $("combshiftwnr_"+ suffix)
// Display LockIn 1 vs combshiftwnr
appendtograph $("ya"+ suffix) vs $("combshiftwnr_"+ suffix)
appendtograph $("Xasmooth_"+ suffix) vs $("combshiftwnr_"+ suffix)
appendtograph $("Yasmooth_"+ suffix) vs $("combshiftwnr_"+ suffix)
ModifyGraph rgb($("Xa"+ suffix))=(48896,49152,65280)
ModifyGraph rgb($("Xasmooth_"+ suffix))=(0,0,39168)
ModifyGraph rgb($("Ya"+ suffix))=(65280,32768,32768)
ModifyGraph highTrip(bottom)=1e+07

display $("combwl_"+ suffix)
// Display Combwavelength // Unshifted
ShowInfo

display $("imn_"+ suffix); appendtograph $("amn_"+ suffix)
// Display Assumed and Calculated Mode numbers
ModifyGraph highTrip(left)=1e+07

//// display $("x2frac_"+ suffix) vs $("shiftwnr_"+ suffix)
// appendtograph $("y2frac_"+ suffix) vs $("shiftwnr_"+ suffix)
// ModifyGraph highTrip(bottom)=1e+07
//
// display $("x1frac_"+ suffix) vs $("shiftwnr_"+ suffix)
// appendtograph $("y1frac_"+ suffix) vs $("shiftwnr_"+ suffix)
// ModifyGraph highTrip(bottom)=1e+07

// display $("x2norm_"+ suffix) vs $("shiftwnr_"+ suffix)
// Display Lockin 2 vs shiftwnr
// appendtograph $("y2norm_"+ suffix) vs $("shiftwnr_"+ suffix)
// appendtograph $("X2NormSmooth_"+ suffix) vs $("shiftwnr_"+ suffix)
// appendtograph $("Y2NormSmooth_"+ suffix) vs $("shiftwnr_"+ suffix)
// ModifyGraph highTrip(bottom)=1e+07
// ModifyGraph rgb($("X2NormSmooth_"+ suffix))=(0,0,52224)
// ModifyGraph rgb($("X2Norm_"+ suffix))=(16384,28160,52224)

// display $("x1norm_"+ suffix) vs $("shiftwnr_"+ suffix)
// Display Lockin 1 vs shiftwnr
// appendtograph $("y1norm_"+ suffix) vs $("shiftwnr_"+ suffix)
// appendtograph $("X1NormSmooth_"+ suffix) vs $("shiftwnr_"+ suffix)
// appendtograph $("Y1NormSmooth_"+ suffix) vs $("shiftwnr_"+ suffix)
// ModifyGraph rgb($("X1NormSmooth_"+ suffix))=(0,0,52224)
// ModifyGraph rgb($("X1Norm_"+ suffix))=(16384,28160,52224)
// ModifyGraph highTrip(bottom)=1e+07

// display $("R1Smooth_"+ suffix) vs $("shiftwnr_"+ suffix)

```

```

// Display R Values. Not Very Important
// appendtograph $("R2Smooth_" + suffix) vs $("shiftwnr_" + suffix)
// ModifyGraph rgb($("R2Smooth_" + suffix))=(0,0,52224)
// ModifyGraph highTrip(bottom)=1e+07

// display $("xb" + suffix) vs $("shiftwnr_" + suffix)
// Display Lockin 2 vs shiftwnr
// appendtograph $("yb" + suffix) vs $("shiftwnr_" + suffix)
// appendtograph $("Xbsmooth_" + suffix) vs $("shiftwnr_" + suffix)
// appendtograph $("Ybsmooth_" + suffix) vs $("shiftwnr_" + suffix)
// ModifyGraph rgb($("Xb" + suffix))=(48896,49152,65280)
// ModifyGraph rgb($("Xbsmooth_" + suffix))=(0,0,39168)
// ModifyGraph rgb($("Yb" + suffix))=(65280,32768,32768)
// ModifyGraph highTrip(bottom)=1e+07
//
// display $("xanc" + suffix) vs $("shiftwnr_" + suffix)
// appendtograph $("yanc" + suffix) vs $("shiftwnr_" + suffix)
// appendtograph $("Xancsmooth_" + suffix) vs $("shiftwnr_" + suffix)
// appendtograph $("Yancsmooth_" + suffix) vs $("shiftwnr_" + suffix)
// ModifyGraph rgb($("Xanc" + suffix))=(48896,49152,65280)
// ModifyGraph rgb($("Xancsmooth_" + suffix))=(0,0,39168)
// ModifyGraph rgb($("Yanc" + suffix))=(65280,32768,32768)
// ModifyGraph highTrip(bottom)=1e+07
end

function Killthewaves(numwaves)
// using the number of waves goes through all waves wave0...wave22
// and kills them so they can be loaded.
variable numwaves
variable jj
string suffix
for(jj=0; jj<numwaves; jj+=1) // goes through number of waves
suffix=num2str(jj)
killwaves /z $("wave"+suffix)
endfor
end

function removezeros(numwaves) // goes through all waves wave0 ... wave22
// and removes the zeros from the bottom of the file
variable numwaves
variable fullfile=0, test=0, lastpoint, small, big
wavestats /Q wave0
fullfile=V_NPNTS
wave wave0
variable incremter=fullfile
do //Determine the last data point in the set, store as
if(wave0[incremter]==0)
incremter-=1
else
test=1
endif
while(test!=1) // end do while loop
lastpoint=incremter
string suffix
for(big=0; big<numwaves; big+=1) // goes through number of waves
suffix=num2str(big)
WAVE WA=$("wave"+suffix)
make /d/o/n =(incremter+1) $("wave"+suffix+"B")

```

```

WAVE WB=$("wave"+suffix+"B")
for(small=0; small <=incrementer; small+=1)
WB[small]=WA[small]
endfor
killwaves /Z WA
make /d/o/n=(incrementer+1) $("wave"+suffix)
wave WC=$("wave"+suffix)
WC=WB
killwaves /Z WB
endfor
end

function allnumerical(numwaves) // Puts waves in order of increasing
// piezo voltage (increasing wavelength, decreasing frequency)
variable numwaves
numwaves-=1 // This is correct
string wsuffix=""
variable length, ii, jj
wave wave0
wavestats /Q wave0
length=V_npnts-1
if(wave0[length]-wave0[0]>0) // This side doesn't work.
// for(jj=0; jj <=numwaves; jj+=1)
// wsuffix=num2str(jj)
// //print wsuffix
// wave WC=$("wave"+wsuffix)
// make /d/o/n =(length+1) $("wave"+wsuffix+"B")
// wave WD=$("wave"+wsuffix+"B")
// for(ii=0; ii <=length+1; ii+=1)
// WD[ii]=WC[ii] // first assignment
// endfor
// killwaves /z WC
// make /d/o/n =(length+1) $("wave"+wsuffix)
// wave WE=$("wave"+wsuffix)
// WE=WD // set back to good name
// killwaves /z WD
// endfor
endif
if(wave0[length]-wave0[0]<0) //print -1
// Then invert the waves, this is the wrong order // This side works
for(jj=0; jj <=numwaves; jj+=1)
wsuffix=num2str(jj)
//print suffix
wave WC=$("wave"+wsuffix)
make /d/o/n =(length+1) $("wave"+wsuffix+"B")
wave WD=$("wave"+wsuffix+"B")
for(ii=0; ii <=length+1; ii+=1)
WD[ii]=WC[length-ii] // first assignment
endfor
killwaves /z WC
make /d/o/n =(length+1) $("wave"+wsuffix)
wave WE=$("wave"+wsuffix)
WE=WD // set back to good name
killwaves /z WD
endfor
endif
end

```

```

function namewaves(suffix)
// Changes wave names from wave0...wave22 to "meaningful names."
string suffix
string P, W, X1, Y1, X2, Y2, X3, DC, RRC, CRR, OF, MB, AMN
string DMHZ, CombWL, TS, IMN, SM, PA, Pressure, Y3, WMWN, kv
P = "P_" + suffix // Piezo Voltage
W = "W_" + suffix // Wavemeter Wavelength
X1 = "X1_" + suffix // Digital Lock-In Channel X
Y1 = "Y1_" + suffix // Digital Lock-In Channel Y
X2 = "X2_" + suffix // Analog Lock-In Channel X
Y2 = "Y2_" + suffix // Analog Lock-In Channel Y
X3 = "X3_" + suffix // Third Lock-In (Optional) X
DC = "DC_" + suffix // DC component of Fast Detector
RRC = "RRC_" + suffix // Rep Rate Counter or Downmixed Repetition Rate
CRR = "CRR_" + suffix // Calculated Repetition Rate
OF = "OF_" + suffix // Signed Offset Frequency
MB = "MB_" + suffix // Signed cw Matisse beat Frequency
AMN = "AMN_" + suffix // Assumed mode number
DMHZ = "DMHZ_" + suffix
// Difference between comb calculated and wavemeter frequency in MHz
CombWL = "CombWL_" + suffix // Wavelength of Ti:Sapphire as determined by frequency comb
TS = "TS_" + suffix // Time stamp of frequency comb measurement
IMN = "IMN_" + suffix // "Incorrect" or calculated mode number
SM = "SM_" + suffix // Scanning mode
PA = "PA_" + suffix // Picoammeter
Pressure = "Pressure_" + suffix // Pressure Transducer
Y3 = "Y3_" + suffix // Third Lock-In (Optional) Y
WMWN = "WMWN_" + suffix // Wavemeter frequency in wavenumbers
kv = "KV_" + suffix // Keithley voltage reading

//rename waves
rename wave0 $P
rename wave1 $W
rename wave2 $X1
rename wave3 $Y1
rename wave4 $X2
rename wave5 $Y2
rename wave6 $X3
rename wave7 $DC
rename wave8 $RRC
rename wave9 $CRR
rename wave10 $OF
rename wave11 $MB
rename wave12 $AMN
rename wave13 $DMHZ
rename wave14 $CombWL
rename wave15 $TS
rename wave16 $IMN
rename wave17 $SM
rename wave18 $PA
rename wave19 $Pressure
rename wave20 $Y3
rename wave21 $WMWN
rename wave22 $kv
end

function calibratespectrum(suffix)
// Calibrate piezo voltage to wavemeter - AOM shift unaccounted for

```

```

string suffix          //killwindow graph0
wave piezo=$( "P_" +suffix)
wave wavemeter=$( "W_" +suffix)
//display wavemeter vs piezo
//showinfo            //UserCursorAdjust("Graph0")
Make /d/o/n=5 W_coef=0
Make /d/o/n=5 W_sigma=0
CurveFit/Q/NTHR=0 poly 5, wavemeter /X=piezo /D // WE[pcsr(B),pcsr(A)] /X=PVC /D
//Hideinfo
wave stats=$( "StatS_" +suffix)
stats[2]=W_coef[0]      // intercept
// Store wavemeter intercept in stats[2]
stats[3]=W_coef[1]      // x
// Store wavemeter linear term in stats[3]
Stats[4]=W_coef[2]      // x^2
// Store wavemeter quadratic term in stats[4]
Stats[5]=W_coef[3]      // x^3
// Store wavemeter cubic term in stats[5]
Stats[6]=W_coef[4]      // x^4
// Store wavemeter quartic term in stats[6]
Stats[7]=W_sigma[0]
Stats[8]=W_sigma[1] //
Stats[9]=W_sigma[2] //
Stats[10]=W_sigma[3] //
Stats[11]=W_sigma[4] //
// "Calibrate" spectrum with wavemeter. RAW VALUE.
variable incremter=stats[0]
make /o/D/n=(incremter) $( "Wavelength_" +suffix)
make /o/D/n=(incremter) tempwave
wave Wavelength=$( "Wavelength_" +suffix)
tempwave=Piezo^4*Stats[6]+Piezo^3*Stats[5]+Piezo^2*Stats[4]+Piezo*Stats[3]+Stats[2]
Wavelength=tempwave // AOM shift unaccounted for
end

function calibratespectrumcomb(suffix)
string suffix          //killwindow graph0
wave piezo=$( "P_" +suffix)
wave wavemeter=$( "combWL_" +suffix)
//display wavemeter vs piezo
//showinfo
//UserCursorAdjust("Graph0")
Make /d/o/n=5 W_coef=0
Make /d/o/n=5 W_sigma=0
CurveFit/Q/NTHR=0 poly 5, wavemeter /X=piezo /D // WE[pcsr(B),pcsr(A)] /X=PVC /D
//Hideinfo
wave stats=$( "StatS_" +suffix)
stats[2]=W_coef[0]      // intercept
stats[3]=W_coef[1]      // x
Stats[4]=W_coef[2]      // x^2
Stats[5]=W_coef[3]      // x^3
Stats[6]=W_coef[4]      // x^4
Stats[7]=W_sigma[0]
Stats[8]=W_sigma[1] //
Stats[9]=W_sigma[2] //
Stats[10]=W_sigma[3] //
Stats[11]=W_sigma[4] //
// "Calibrate" spectrum with wavemeter. RAW VALUE.
wavestats /Q $( "P_" +suffix)

```

```

stats[0]=V_npnts
variable incremter=stats[0]
make /o/D/n=(incremter) $("CombWavelength_"+suffix)
make /o/D/n=(incremter) tempwave
wave Wavelength=$("CombWavelength_"+suffix)
tempwave=Piezo^4*Stats[6]+Piezo^3*Stats[5]+Piezo^2*Stats[4]+Piezo*Stats[3]+Stats[2]
Wavelength=tempwave
end

function calibratedetector(suffix)
string suffix          //killwindow graph0
wave piezo=$("P_"+suffix)
wave detector=$("DC_"+suffix)
//display detector vs piezo
//showinfo
//UserCursorAdjust("Graph0")
Make /d/o/n=5 W_coef=0
Make /d/o/n=5 W_sigma=0
CurveFit/Q/NTHR=0 poly 5, detector /X=piezo /D // WE[pcsr(B),pcsr(A)] /X=PVC /D
//Hideinfo
wave stats=$("StatS_"+suffix)
stats[13]=W_coef[0]      // intercept
// Store detector intercept in stats[13]
stats[14]=W_coef[1]      // x
// Store detectorlinear term in stats[14]
Stats[15]=W_coef[2]      // x^2
// Store detector quadratic term in stats[15]
Stats[16]=W_coef[3]      // x^3
// Store detector cubic term in stats[16]
Stats[17]=W_coef[4]      // x^4
// Store detector quartic term in stats[17]
Stats[18]=W_sigma[0]
Stats[19]=W_sigma[1] //
Stats[20]=W_sigma[2] //
Stats[21]=W_sigma[3] //
Stats[22]=W_sigma[4] //
//"Calibrate" spectrum with wavemeter. RAW VALUE.
variable incremter=stats[0]
make /o/D/n=(incremter) $("DetBaseLine_"+suffix)
make /o/D/n=(incremter) tempwave
wave detbaseline=$("DetBaseLine_"+suffix)
tempwave=Piezo^4*Stats[17]+Piezo^3*Stats[16]+Piezo^2*Stats[15]+Piezo*Stats[14]+Stats[13]
detbaseline=tempwave
end

function calibratePA(suffix)
string suffix
//killwindow graph0
wave piezo=$("P_"+suffix)
wave ammeter=$("PA_"+suffix)
//display detector vs piezo
//showinfo
//UserCursorAdjust("Graph0")
Make /d/o/n=5 W_coef=0
Make /d/o/n=5 W_sigma=0
CurveFit/Q/NTHR=0 poly 5, ammeter /X=piezo /D // WE[pcsr(B),pcsr(A)] /X=PVC /D
//Hideinfo
wave stats=$("StatS_"+suffix)

```

```

stats[51]=W_coef[0]      // intercept
// Store picoammeter intercept in stats[51]
stats[52]=W_coef[1]      // x
// Store picoammeter linear term in stats[52]
Stats[53]=W_coef[2]      // x^2
// Store picoammeter quadratic term in stats[53]
Stats[54]=W_coef[3]      // x^3
// Store picoammeter cubic term in stats[54]
Stats[55]=W_coef[4]      // x^4
// Store picoammeter quartic term in stats[55]
Stats[56]=W_sigma[0]
Stats[57]=W_sigma[1] //
Stats[58]=W_sigma[2] //
Stats[59]=W_sigma[3] //
Stats[60]=W_sigma[4] //
// "Calibrate" spectrum with wavemeter. RAW VALUE.
variable incremter=stats[0]
make /o/D/n=(incremter) $("PABaseLine_"+suffix)
make /o/D/n=(incremter) tempwave
wave pabaseline=$("PABaseLine_"+suffix)
tempwave=Piezo^4*Stats[55]+Piezo^3*Stats[54]+Piezo^2*Stats[53]+Piezo*Stats[52]+Stats[51]
pabaseline=tempwave
end

```

```

function normalizelockins(suffix, LI1Norm, LI2Norm, LI3Norm)
string suffix
variable LI1Norm, LI2Norm, LI3Norm
wave stats=$("StatS_"+suffix)
variable incremter=stats[0]
wave X1C=$("X1_"+suffix)
wave Y1C=$("Y1_"+suffix)
wave X2C=$("X2_"+suffix)
wave Y2C=$("Y2_"+suffix)
wave X3C=$("X3_"+suffix)
wave Y3C=$("Y3_"+suffix)
make /o/D/n=(incremter) $("X1Norm_"+suffix)
make /o/D/n=(incremter) $("Y1Norm_"+suffix)
make /o/D/n=(incremter) $("X2Norm_"+suffix)
make /o/D/n=(incremter) $("Y2Norm_"+suffix)
make /o/D/n=(incremter) $("X3Norm_"+suffix)
make /o/D/n=(incremter) $("Y3Norm_"+suffix)
wave X1N=$("X1Norm_"+suffix)
wave Y1N=$("Y1Norm_"+suffix)
wave X2N=$("X2Norm_"+suffix)
wave Y2N=$("Y2Norm_"+suffix)
wave X3N=$("X3Norm_"+suffix)
wave Y3N=$("Y3Norm_"+suffix)
X1N=X1C*LI1Norm
Y1N=Y1C*LI1Norm
X2N=X2C*LI2Norm
Y2N=Y2C*LI2Norm
X3N=X3C*LI3Norm
Y3N=Y3C*LI3Norm
end

```

```

function fractionalizelockins(suffix)
// Finds fractional signal. MUST choose right factor!!!
string suffix

```

```

wave stats=$(StatS_"+suffix)
wave DetectorBaseline=$(DetBaseline_"+suffix)
variable incremter=stats[0]
wave detector=$(DC_"+suffix)
wave X1N=$(X1Norm_"+suffix)
wave Y1N=$(Y1Norm_"+suffix)
wave X2N=$(X2Norm_"+suffix)
wave Y2N=$(Y2Norm_"+suffix)
wave X3N=$(X3Norm_"+suffix)
wave Y3N=$(Y3Norm_"+suffix)
make /o/D/n=(incremter) $(X1Frac_"+suffix)
make /o/D/n=(incremter) $(Y1Frac_"+suffix)
make /o/D/n=(incremter) $(X2Frac_"+suffix)
make /o/D/n=(incremter) $(Y2Frac_"+suffix)
make /o/D/n=(incremter) $(X3Frac_"+suffix)
make /o/D/n=(incremter) $(Y3Frac_"+suffix)
wave X1F=$(X1Frac_"+suffix)
wave Y1F=$(Y1Frac_"+suffix)
wave X2F=$(X2Frac_"+suffix)
wave Y2F=$(Y2Frac_"+suffix)
wave X3F=$(X3Frac_"+suffix)
wave Y3F=$(Y3Frac_"+suffix)

variable base, maxs, xhalf, rate, ACGAIN, LIRF2Frac
variable Gain , oldGainMinus10, DCLEVEL, oldgain
wavestats /q $(DetBaseline_"+suffix)
DCLEVEL=V_avg

make /o/D/n=(incremter) $(ACBaseline_"+suffix)
wave ACBaseline=$(ACBaseline_"+suffix)
make /o/D/n=(incremter) $(ACBaselineOld_"+suffix)
wave ACBaselineOld=$(ACBaselineOld_"+suffix)
make /o/D/n=(incremter) $(ACBaselineDirect_"+suffix)
wave ACBaselineDirect=$(ACBaselineDirect_"+suffix)

// Calibrate AC Gain (V/A) based on DC LEVEL.
// Not NEEDED, AC level is so small...
// base=20803.058
// maxs=-12668.927
// xhalf=3.1777755
// rate=0.49094
// ACGAIN=base+maxs/(1+exp((xhalf-DCLEVEL)/rate))

// // calibrate AC voltgae to DC voltage
// variable base, maxs, xhalf, rate
// base=-1.8888
// maxs=6.83828
// xhalf=0.52693
// rate=.6408
// ACBaselineDirect=base+maxs/(1+exp((xhalf-DetectorBaseline)/rate))*Gain

// Gain = 7.798*ACGAIN/8077
OldGain = 7.798*20668/8077
OldGainMinus10 = 2.466*20668/8077
// GainMinus10=2.466*ACGAIN/8077

ACBaseline=DetectorBaseline*OldGain

```



```
// must decide if it's a 10 dB attenuation or not. Must somehow automate this.
```

```
LIRF2Frac=1.496235656*2.31739465/25.70395783*3.322259136
LIRF2Frac=1.496235656*2.31739465/25.70395783*3.322259136
// 1/PSloss 1/MixerLoss / amplifier gain / bessell ..
// 10 dB attenuator not taken into account
// Should not have bessell VALUE!!!
//LIRF2Frac=1.496235656*2.31739465/25.70395783*3.322259136*3.16227766
// 1/PSloss 1/MixerLoss / amplifier gain / bessell / 10 dB..
// With 10 dB attenuator taken into account //
X1F=X1N/ACBaseline
Y1F=Y1N/ACBaseline
X2F=X2N/ACBaseline
Y2F=Y2N/ACBaseline
X3F=X3N/ACBaseline
Y3F=Y3N/ACBaseline
end
```

```
function DuplicateForRotation(suffix)
string suffix
wave stats=("${StatS_}" + suffix)
variable incremter=stats[0]
duplicate /O $("${X1Norm_}" + suffix), $("${xa}" + suffix)
duplicate /O $("${Y1Norm_}" + suffix), $("${ya}" + suffix)
duplicate /O $("${X2Norm_}" + suffix), $("${xb}" + suffix)
duplicate /O $("${Y2Norm_}" + suffix), $("${yb}" + suffix)
// wave XRA=("${xa}" + suffix)
// wave YRA=("${ya}" + suffix)
// wave XRB=("${xb}" + suffix)
// wave YRB=("${yb}" + suffix)
end
```

```
function DuplicateForNormalization(suffix)
string suffix
wave stats=("${StatS_}" + suffix)
variable incremter=stats[0]
duplicate /O $("${xa}" + suffix), $("${xan}" + suffix)
duplicate /O $("${ya}" + suffix), $("${yan}" + suffix)
duplicate /O $("${xb}" + suffix), $("${xbn}" + suffix)
duplicate /O $("${yb}" + suffix), $("${ybn}" + suffix)
duplicate /O $("${xa}" + suffix), $("${xanc}" + suffix)
duplicate /O $("${ya}" + suffix), $("${yanc}" + suffix)
duplicate /O $("${xb}" + suffix), $("${xbnc}" + suffix)
duplicate /O $("${yb}" + suffix), $("${ybnc}" + suffix)
end
```

```
function AOMShift(suffix)
// Applies AOM shift.
//Red Shift Subtracts out 170 MHz.
//Blue Shift adds in 170 MHz.
string suffix
wave stats=("${StatS_}" + suffix)
variable incremter=stats[0]
wave Wavelength=("${Wavelength_}" + suffix)
```

```

make /o/D/n=(incrementer) $("UnshiftedFrequency_"+suffix)
wave FA=$("UnshiftedFrequency_"+suffix)
FA=299792458/(Wavelength/1e9)
make /o/D/n=(incrementer) $("ShiftedFrequency_"+suffix)
wave SF=$("ShiftedFrequency_"+suffix)
SF=FA-170000000 // 85 MHz * 2
// AOM red shifts means subtract out 85 MHz.
make /o/D/n=(incrementer) $("ShiftedWavelength_"+suffix)
wave SW=$("ShiftedWavelength_"+suffix)
SW=299792458/SF*1e9
make /o/D/n=(incrementer) $("ShiftWnr_"+suffix)
wave WNM=$("ShiftWnr_"+suffix)
WNM=1/(SW/1e7)
end

function AOMShiftComb(suffix)
string suffix
wave stats=$("StatS_"+suffix)
variable incrementer=stats[0]
wave Wavelength=$("CombWavelength_"+suffix)
make /o/D/n=(incrementer) $("CombUnshiftedFrequency_"+suffix)
wave FA=$("CombUnshiftedFrequency_"+suffix)
FA=299792458/(Wavelength/1e9)
make /o/D/n=(incrementer) $("CombShiftedFrequency_"+suffix)
wave SF=$("CombShiftedFrequency_"+suffix)
SF=FA-170000000 // 85 MHz * 2
// AOM red shifts means subtract out 85 MHz.
make /o/D/n=(incrementer) $("CombShiftedWavelength_"+suffix)
wave SW=$("CombShiftedWavelength_"+suffix)
SW=299792458/SF*1e9
make /o/D/n=(incrementer) $("CombShiftWnr_"+suffix)
wave WNM=$("CombShiftWnr_"+suffix)
WNM=1/(SW/1e7)
end

function killcomb(suffix)
string suffix
// string RRC, CRR, OF, MB, AMN, DMHZ, CombWL, TS, IMN, SM
wave RRC = $("RRC_"+ suffix)
wave CRR = $("CRR_"+ suffix)
wave OF = $("OF_"+ suffix)
wave MB = $("MB_"+ suffix)
wave AMN = $("AMN_"+ suffix)
wave DMHZ = $("DMHZ_"+ suffix)
wave CombWL = $("CombWL_"+ suffix)
wave TS = $("TS_"+ suffix)
wave IMN = $("IMN_"+ suffix)
wave SM = $("SM_"+ suffix)
killwaves /z RRC, CRR, OF, MB, AMN, DMHZ, CombWL, TS, IMN, SM
end

function rotator(xwaveA,ywaveA,theta1)
// rotates x wave and y wave by angle theta
wave xwaveA, ywaveA
variable theta1
duplicate xwaveA xwaveA2
duplicate ywaveA ywaveA2
variable thetaradians1

```

```

thetaradians1=theta1/180*pi
xwaveA=xwaveA2*cos(thetaradians1)-ywaveA2*sin(thetaradians1)
ywaveA=xwaveA2*sin(thetaradians1)+ywaveA2*cos(thetaradians1)
end

```

```

function makersnts(suffix) // Makes R wave, Theta wave
string suffix
wave X1 =$( "X1_" + suffix)
wave Y1 = $("Y1_" + suffix)
wave X2 = $("X2_" + suffix)
wave Y2 = $("Y2_" + suffix)
Duplicate/O $("X1_" + suffix), $("R1_" + suffix)
Duplicate/O $("X2_" + suffix), $("T1_" + suffix)
Duplicate/O $("Y1_" + suffix), $("R2_" + suffix)
Duplicate/O $("Y2_" + suffix), $("T2_" + suffix)
Duplicate/O $("Y1_" + suffix), $("RTotal_" + suffix)
Duplicate/O $("Y2_" + suffix), $("TTotal_" + suffix)
wave R1 = $("R1_" + suffix)
wave T1 = $("T1_" + suffix)
wave R2 = $("R2_" + suffix)
wave T2 = $("T2_" + suffix)
wave RTotal = $("RTotal_" + suffix)
Wave TTotal = $("TTotal_" + suffix)
R1=sqrt(X1^2+Y1^2)
T1=atan(Y1/X1)
T1=T1/pi*180
R2=sqrt(X2^2+Y2^2)
T2=atan(Y2/X2)
T2=T2/pi*180
RTotal=sqrt(R1^2+R2^2)
TTotal=atan(R2/R1)
end

```

```

function smoothwaves(suffix)
string suffix
wave X1N =$( "X1Norm_" + suffix)
wave Y1N = $("Y1Norm_" + suffix)
wave X2N = $("X2Norm_" + suffix)
wave Y2N = $("Y2Norm_" + suffix)
wave R1 = $("R1_" + suffix)
wave T1 = $("T1_" + suffix)
wave R2 = $("R2_" + suffix)
wave T2 = $("T2_" + suffix)
Duplicate/O $("X1Norm_" + suffix), $("X1NormSmooth_" + suffix)
Smooth/EVEN/B 20, $("X1NormSmooth_" + suffix)
Duplicate/O $("X2Norm_" + suffix), $("X2NormSmooth_" + suffix)
Smooth/EVEN/B 20, $("X2NormSmooth_" + suffix)
Duplicate/O $("Y1Norm_" + suffix), $("Y1NormSmooth_" + suffix)
Smooth/EVEN/B 20, $("Y1NormSmooth_" + suffix)
Duplicate/O $("Y2Norm_" + suffix), $("Y2NormSmooth_" + suffix)
Smooth/EVEN/B 20, $("Y2NormSmooth_" + suffix)
Duplicate/O $("R1_" + suffix), $("R1Smooth_" + suffix)
Smooth/EVEN/B 20, $("R1Smooth_" + suffix)
Duplicate/O $("T1_" + suffix), $("T1Smooth_" + suffix)
Smooth/EVEN/B 20, $("T1Smooth_" + suffix)
Duplicate/O $("R2_" + suffix), $("R2Smooth_" + suffix)
Smooth/EVEN/B 20, $("R2Smooth_" + suffix)
Duplicate/O $("T2_" + suffix), $("T2Smooth_" + suffix)

```

```

Smooth/EVEN/B 20, $("T2Smooth_" + suffix)
Duplicate/O $("RTotal_" + suffix), $("RTSmooth_" + suffix)
Smooth/EVEN/B 20, $("RTSmooth_" + suffix)
Duplicate/O $("TTotal_" + suffix), $("TTSmooth_" + suffix)
Smooth/EVEN/B 20, $("TTSmooth_" + suffix)
end

function smoothrotated(suffix)
string suffix
wave Xa = $("Xa" + suffix)
wave Ya = $("Ya" + suffix)
wave Xb = $("Xb" + suffix)
wave Yb = $("Yb" + suffix)
Duplicate/O $("Xa" + suffix), $("XaSmooth_" + suffix)
Smooth/EVEN/B 20, $("XaSmooth_" + suffix)
Duplicate/O $("Ya" + suffix), $("YaSmooth_" + suffix)
Smooth/EVEN/B 20, $("YaSmooth_" + suffix)
Duplicate/O $("Xb" + suffix), $("XbSmooth_" + suffix)
Smooth/EVEN/B 20, $("XbSmooth_" + suffix)
Duplicate/O $("Yb" + suffix), $("YbSmooth_" + suffix)
Smooth/EVEN/B 20, $("YbSmooth_" + suffix)
end

function smoothnormalized(suffix)
string suffix
Duplicate/O $("Xan" + suffix), $("XanSmooth_" + suffix)
Smooth/EVEN/B 20, $("XanSmooth_" + suffix)
Duplicate/O $("Yan" + suffix), $("YanSmooth_" + suffix)
Smooth/EVEN/B 20, $("YanSmooth_" + suffix)
Duplicate/O $("Xbn" + suffix), $("XbnSmooth_" + suffix)
Smooth/EVEN/B 20, $("XbnSmooth_" + suffix)
Duplicate/O $("Ybn" + suffix), $("YbnSmooth_" + suffix)
Smooth/EVEN/B 20, $("YbnSmooth_" + suffix)
Duplicate/O $("Xanc" + suffix), $("XancSmooth_" + suffix)
Smooth/EVEN/B 20, $("XancSmooth_" + suffix)
Duplicate/O $("Yanc" + suffix), $("YancSmooth_" + suffix)
Smooth/EVEN/B 20, $("YancSmooth_" + suffix)
Duplicate/O $("Xbnc" + suffix), $("XbncSmooth_" + suffix)
Smooth/EVEN/B 20, $("XbncSmooth_" + suffix)
Duplicate/O $("Ybnc" + suffix), $("YbncSmooth_" + suffix)
Smooth/EVEN/B 20, $("YbncSmooth_" + suffix)
end

function smoothfrac(suffix)
string suffix
Duplicate/O $("X1Frac_" + suffix), $("X1FracSmooth_" + suffix)
Smooth/EVEN/B 20, $("X1FracSmooth_" + suffix)
Duplicate/O $("Y1Frac_" + suffix), $("Y1FracSmooth_" + suffix)
Smooth/EVEN/B 20, $("Y1FracSmooth_" + suffix)
Duplicate/O $("X2Frac_" + suffix), $("X2FracSmooth_" + suffix)
Smooth/EVEN/B 20, $("X2FracSmooth_" + suffix)
Duplicate/O $("Y2Frac_" + suffix), $("Y2FracSmooth_" + suffix)
Smooth/EVEN/B 20, $("Y2FracSmooth_" + suffix)
end

function getstats(suffix, LI1Norm, LI2Norm, LI3Norm)
string suffix
variable LI1Norm, LI2Norm, LI3Norm

```

```

wave stats=$("StatS_" + suffix)
variable incremter=stats[0]
stats[24]=LI1Norm
// Stats[24]=L1Norm
stats[25]=LI2Norm
// Stats[25]=L2Norm
stats[26]=LI3Norm
// Stats[26]=L3Norm
wvestats /Q  $("DetBaseLine_" + suffix)
stats[28]=V_avg
// Stats[28]=Average of DetBaseline
stats[29]=V_sdev
// Stats[29]=Standard Deviation of DetBaseline
wvestats /Q  $("PABaseLine_" + suffix)
stats[31]=V_avg
// Stats[31]=Average of PaBaseline
stats[32]=V_sdev
// Stats[32]=Standard Deviation of PaBaseline
wvestats /Q  $("X1Norm_" + suffix)
stats[34]=V_sdev
// Stats[34]=Standard Deviation of X1Normalized
wvestats /Q  $("Y1Norm_" + suffix)
stats[35]=V_sdev
// Stats[35]=Standard Deviation of Y1Normalized
wvestats /Q  $("X2Norm_" + suffix)
stats[36]=V_sdev
// Stats[36]=Standard Deviation of X2Normalized
wvestats /Q  $("Y2Norm_" + suffix)
stats[37]=V_sdev
// Stats[37]=Standard Deviation of Y2Normalized
wvestats /Q  $("X1Frac_" + suffix)
stats[39]=V_sdev
// Stats[39]=Standard Deviation of X1Frac
wvestats /Q  $("Y1Frac_" + suffix)
stats[40]=V_sdev
// Stats[40]=Standard Deviation of Y1Frac
wvestats /Q  $("X2Frac_" + suffix)
stats[41]=V_sdev
// Stats[41]=Standard Deviation of X2Frac
wvestats /Q  $("Y2Frac_" + suffix)
stats[42]=V_sdev
// Stats[42]=Standard Deviation of Y2Frac
wvestats /Q  $("X3_" + suffix)
stats[44]=V_avg
// Stats[44]=Standard Deviation of X3Frac
wvestats /Q  $("Y3_" + suffix)
stats[45]=V_sdev
// Stats[45]=Standard Deviation of Y3Frac
wvestats /Q  $("X1NormSmooth_" + suffix)
stats[47]=V_max-V_min
// Stats[47]=Height of X1 Channel Signal
wvestats /Q  $("X2NormSmooth_" + suffix)
stats[48]=V_max-V_min
// Stats[48]=Height of X2 Channel Signal
wvestats /Q  $("Y1NormSmooth_" + suffix)
stats[49]=V_max-V_min
// Stats[49]=Height of Y1 Channel Signal
wvestats /Q  $("Y2NormSmooth_" + suffix)

```

```

stats[50]=V_max-V_min
// Stats[50]=Height of Y2 Channel Signal
end

```

```

function normalizetovoltagecurrent(suffix)
string suffix
wave stats=($"StatS_"+suffix)
variable incrementer=stats[0]
wave X1D=($"xan"+suffix)
wave Y1D=($"yan"+suffix)
wave X2D=($"xbn"+suffix)
wave Y2D=($"ybn"+suffix)
wave X1DC=($"xanc"+suffix)
wave Y1DC=($"yanc"+suffix)
wave X2DC=($"xbnc"+suffix)
wave Y2DC=($"ybnc"+suffix)
wave DBL=($"DetBaseLine_"+suffix)
wave PAB=($"PABaseline_"+suffix)
X1D/=DBL
X1D/=PAB
Y1D/=DBL
Y1D/=PAB
X2D/=DBL
X2D/=PAB
Y2D/=DBL
Y2D/=PAB
X1DC/=PAB
X2DC/=PAB
Y1DC/=PAB
Y2DC/=PAB
end

```

```

function redocomb(suffix)
string suffix
calibratespectrumComb(suffix)
AOMShiftComb(suffix)
end

```

```

function modedet(suffix,low,high)
string suffix
variable low,high
wave stats=($"StatS_"+suffix)
variable incrementer=stats[0]
make /o/D/n=2 $($"xwave_"+suffix)
make /o/D/n=2 $($"ywavea_"+suffix)
make /o/D/n=2 $($"ywaveb_"+suffix)
wave xwave=($"xwave_"+suffix)
wave ywavea=($"ywavea_"+suffix)
wave ywaveb=($"ywaveb_"+suffix)
xwave[0]=0
xwave[1]=incrementer
ywavea=low
ywaveb=high
make /o/D/n=2 $($"xwaveb_"+suffix)
make /o/D/n=2 $($"xwavec_"+suffix)
make /o/D/n=2 $($"xwaved_"+suffix)
make /o/D/n=2 $($"ywave_"+suffix)
wave xwaveb=($"xwaveb_"+suffix)

```

```

wave xwavec="$xwavec_"+suffix)
wave xwaved="$xwaved_"+suffix)
wave ywave="$ywave_"+suffix)
xwaveb=low
xwavec=high
ywave[0]=0
ywave[1]=incrementer
Make/N=1000/0 $("IMN_"+suffix+"_Hist")
Histogram/B=1 $("IMN_"+suffix),$("IMN_"+suffix+"_Hist")
display $("IMN_"+suffix+"_Hist")
ModifyGraph highTrip(bottom)=1e+08
ModifyGraph mode($("IMN_"+suffix+"_Hist"))=1
appendtograph $("ywave_"+suffix) vs $("xwaveb_"+suffix)
appendtograph $("ywave_"+suffix) vs $("xwavec_"+suffix)
appendtograph $("ywave_"+suffix) vs $("xwaved_"+suffix)
CurveFit/M=2/W=0 gauss, $("IMN_"+suffix+"_Hist")/D
ModifyGraph rgb($("ywave_"+suffix))=(0,0,65280)
ModifyGraph rgb($("ywave_"+suffix)#1)=(0,0,65280)
ModifyGraph rgb($("ywave_"+suffix)#2)=(0,0,0)
ModifyGraph rgb($("fit_IMN_"+suffix+"_Hist"))=(0,0,65280)
wave W_coef
ywave[1]=W_coef[1]*1.5
xwaved=W_coef[2]
end

function addmode(suffix)
string suffix
appendtograph $("ywaveb_"+suffix) vs $("xwave_"+suffix)
//ModifyGraph rgb($("ywavea_"+suffix))=(0,0,65280)
appendtograph $("ywavea_"+suffix) vs $("xwave_"+suffix)
//ModifyGraph rgb($("ywavea_"+suffix))=(0,0,65280)
end

function makedoppler(suffix,voltage,plusvoltage,minusvoltage)
// ("2", 4000, 10, -10)
string suffix
variable voltage, plusvoltage,minusvoltage
wave fn2plus,in2plus
variable nln2plus, factorA, factorB
wavestats /Q LN2plus //determine number of rows in input N2+ wave
nLN2plus=V_npnts
make /d/o/n=(nLN2plus) $("Fplus1_"+suffix)=0
make /d/o/n=(nLN2plus) $("Fminus1_"+suffix)=0
make /d/o/n=(nLN2plus) $("Fminus2_"+suffix)=0
make /d/o/n=(nLN2plus) $("Fplus2_"+suffix)=0
wave FP1W=$("Fplus1_"+suffix)
wave FM1W=$("Fminus1_"+suffix)
wave FP2W=$("Fplus2_"+suffix)
wave FM2W=$("Fminus2_"+suffix)
//Fplus1=0, Fminus1=0,Fplus2=0, Fminus2=0
// make the waves for the doppler split lines,
variable VoltageA=voltage-plusvoltage //3865 - 10
variable VoltageB=voltage-minusvoltage //3865 - -10
factorA=sqrt(2*1.60217646e-19*VoltageA/4.6517405810e-26/299792458/299792458)
// factor = v/c=sqrt(2*q*V/m/c/c)
factorB=sqrt(2*1.60217646e-19*VoltageB/4.6517405810e-26/299792458/299792458)
// factor = v/c=sqrt(2*q*V/m/c/c)
FP1W=fn2plus*sqrt((1+factorA)/(1-factorA)) // Fully Equal

```

```

FP2W=fN2plus*sqrt((1+factorB)/(1-factorB)) // Fully Equal
FM1W=fN2plus*sqrt((1-factorA)/(1+factorA)) // Fully Equal
FM2W=fN2plus*sqrt((1-factorB)/(1+factorB)) // Fully Equal
//FP1W=fN2plus*(1+factorA) //Approximation
//FP2W=fN2plus*(1+factorB) //Approximation
//FM1W=fN2plus*(1-factorA) //Approximation
//FM2W=fN2plus*(1-factorB) //Approximation
end
function changegraphs()
ModifyGraph highTrip(bottom)=1e+06
end

function adddoppler(suffix)
string suffix
getaxis bottom
SetAxis /A=0 /Z bottom V_min,V_max
appendtograph /r in2plus vs $("Fminus2_"+suffix)
ModifyGraph rgb(In2plus)=(13056,0,0)
appendtograph /r in2plus vs $("Fminus1_"+suffix)
ModifyGraph rgb(In2plus#1)=(13056,0,0)
appendtograph /r in2plus vs $("Fplus1_"+suffix)
ModifyGraph rgb(In2plus#2)=(0,0,52224)
appendtograph /r in2plus vs $("Fplus2_"+suffix)
ModifyGraph rgb(In2plus#3)=(0,0,52224)
ModifyGraph mode(In2plus)=1,mode(In2plus#1)=1,mode(In2plus#2)=1,mode(In2plus#3)=1
//,mode(In2plus#4)=1,mode(In2plus#5)=1,mode(In2plus#6)=1, mode(In2plus#7)=1
end

function fixgraph()
ModifyGraph highTrip(bottom)=100000
//addheterodyne2(suffix)
end

function deletepnts(suffix,start,length)
string suffix
variable start,length
DeletePoints start,length, $("P_"+ suffix)
DeletePoints start,length, $("W_"+ suffix)
DeletePoints start,length, $("X1_"+ suffix)
DeletePoints start,length, $("Y1_"+ suffix)
DeletePoints start,length, $("X2_"+ suffix)
DeletePoints start,length, $("Y2_"+ suffix)
DeletePoints start,length, $("X3_"+ suffix)
DeletePoints start,length, $("DC_"+ suffix)
DeletePoints start,length, $("PA_"+ suffix)
DeletePoints start,length, $("Pressure_"+ suffix)
DeletePoints start,length, $("Y3_"+ suffix)
DeletePoints start,length, $("xa"+ suffix)
DeletePoints start,length, $("xb"+ suffix)
DeletePoints start,length, $("ya"+ suffix)
DeletePoints start,length, $("yb"+ suffix)
DeletePoints start,length, $("ShiftWnr_"+ suffix)
DeletePoints start,length, $("shiftedfrequency_"+ suffix)
DeletePoints start,length, $("shiftedwavelength_"+ suffix)
DeletePoints start,length, $("unshiftedfrequency_"+ suffix)
DeletePoints start,length, $("wavelength_"+ suffix)
DeletePoints start,length, $("xan"+ suffix)
DeletePoints start,length, $("yan"+ suffix)

```



```

DeletePoints start,length, $("xnb"+ suffix)
DeletePoints start,length, $("ybn"+ suffix)
DeletePoints start,length, $("DetBaseLine_"+ suffix)
DeletePoints start,length, $("PABaseLine_"+ suffix)
DeletePoints start,length, $("RTotal_"+ suffix)
DeletePoints start,length, $("RTSmooth_"+ suffix)
DeletePoints start,length, $("R1Smooth_"+ suffix)
DeletePoints start,length, $("R1_"+ suffix)
DeletePoints start,length, $("R2Smooth_"+ suffix),$("R2_"+ suffix)
DeletePoints start,length, $("TTTotal_"+ suffix)
DeletePoints start,length, $("TTSmooth_"+ suffix)
DeletePoints start,length, $("T1Smooth_"+ suffix)
DeletePoints start,length, $("T1_"+ suffix)
DeletePoints start,length, $("T2Smooth_"+ suffix)
DeletePoints start,length, $("T2_"+ suffix)
DeletePoints start,length, $("X1Frac_"+ suffix)
DeletePoints start,length, $("Y2Frac_"+ suffix)
DeletePoints start,length, $("X2Frac_"+ suffix),$("X1Norm_"+ suffix)
DeletePoints start,length, $("Y3Frac_"+ suffix)
DeletePoints start,length, $("X3Frac_"+ suffix)
DeletePoints start,length, $("Y1Frac_"+ suffix)
DeletePoints start,length, $("Y1Norm_"+ suffix)
DeletePoints start,length, $("Y2Norm_"+ suffix)
DeletePoints start,length, $("X2Norm_"+ suffix)
DeletePoints start,length, $("X3Norm_"+ suffix)
DeletePoints start,length, $("Y3Norm_"+ suffix)
DeletePoints start,length, $("X1NormSmooth_"+ suffix)
DeletePoints start,length, $("Y1NormSmooth_"+ suffix)
DeletePoints start,length, $("Y2NormSmooth_"+ suffix)
DeletePoints start,length, $("X2NormSmooth_"+ suffix)
DeletePoints start,length, $("xasmooth_"+ suffix)
DeletePoints start,length, $("xbsmooth_"+ suffix)
DeletePoints start,length, $("yasmooth_"+ suffix)
DeletePoints start,length, $("ybsmooth_"+ suffix)
DeletePoints start,length, $("xanc"+suffix)
DeletePoints start,length, $("yanc"+suffix)
DeletePoints start,length, $("xbnc"+suffix)
DeletePoints start,length, $("ybnc"+suffix)
DeletePoints start,length, $("XanSmooth_"+ suffix)
DeletePoints start,length, $("YanSmooth_"+ suffix)
DeletePoints start,length, $("XbnSmooth_"+ suffix)
DeletePoints start,length, $("YbnSmooth_"+ suffix)
DeletePoints start,length, $("XancSmooth_"+ suffix)
DeletePoints start,length, $("YancSmooth_"+ suffix)
DeletePoints start,length, $("XbncSmooth_"+ suffix)
DeletePoints start,length, $("YbncSmooth_"+ suffix)
DeletePoints start,length, $("wmwn_"+ suffix)
DeletePoints start,length, $("kv_"+ suffix)
DeletePoints start,length, $("MB_"+ suffix)
DeletePoints start,length, $("AMN_"+ suffix)
DeletePoints start,length, $("DMHZ_"+ suffix)
DeletePoints start,length, $("CombWL_"+ suffix)
DeletePoints start,length, $("TS_"+ suffix)
DeletePoints start,length, $("IMN_"+ suffix)
DeletePoints start,length, $("SM_"+ suffix)
DeletePoints start,length, $("RRC_"+ suffix)
DeletePoints start,length, $("CRR_"+ suffix)
DeletePoints start,length, $("OF_"+ suffix)

```

```

DeletePoints start,length, $("combshiftedfrequency_"+ suffix)
DeletePoints start,length, $("combunshiftedfrequency_"+ suffix)
DeletePoints start, length, $("combshiftedwavelength_"+ suffix)
DeletePoints start,length, $("combwavelength_"+ suffix)
DeletePoints start,length, $("combshiftwnr_"+ suffix)
end

function tableone(suffix)
string suffix
edit $("P_"+ suffix), $("W_"+ suffix), $("X1_"+ suffix), $("Y1_"+ suffix)
appendtotable $("X2_"+ suffix), $("Y2_"+ suffix), $("X3_"+ suffix), $("DC_"+ suffix)
//appendtotable $("MB_"+ suffix), $("AMN_"+ suffix), $("DMHZ_"+ suffix)
//appendtotable $("CombWL_"+ suffix), $("TS_"+ suffix), $("IMN_"+ suffix)
//appendtotable $("SM_"+ suffix), $("RRC_"+ suffix), $("CRR_"+ suffix), $("OF_"+ suffix)
appendtotable $("PA_"+ suffix), $("Pressure_"+ suffix), $("Y3_"+ suffix)
appendtotable $("ShiftWnR_"+ suffix), $("xa"+ suffix), $("xb"+ suffix)
appendtotable $("ya"+ suffix), $("yb"+ suffix), $("XASmooth_"+ suffix)
appendtotable $("YASmooth_"+ suffix), $("XBSmooth_"+ suffix), $("YBSmooth_"+ suffix)
appendtotable $("xan"+suffix),$("yan"+suffix),$("xbn"+suffix),$("ybn"+suffix)
appendtotable $("DetBaseLine_"+suffix),$("PABaseline_"+suffix)
appendtotable $("RTotal_"+ suffix), $("RTSmooth_"+ suffix), $("R1Smooth_"+ suffix)
appendtotable $("R1_"+ suffix), $("R2Smooth_"+ suffix), $("R2_"+ suffix)
appendtotable $("shiftedfrequency_"+ suffix) , $("shiftedwavelength_"+ suffix)
appendtotable $("unshiftedfrequency_"+ suffix), $("wavelength_"+ suffix)
appendtotable $("TTotal_"+ suffix), $("TTSmooth_"+ suffix)
appendtotable $("T1Smooth_"+ suffix), $("T1_"+ suffix)
appendtotable $("T2Smooth_"+ suffix), $("T2_"+ suffix)
appendtotable $("X3Norm_"+ suffix), $("X3Frac_"+ suffix), $("Y3Norm_"+ suffix)
appendtotable $("Y3Frac_"+ suffix) , $("X2Norm_"+ suffix) , $("X2NormSmooth_"+ suffix)
appendtotable $("X2Frac_"+ suffix), $("X1Norm_"+ suffix)
appendtotable $("X1NormSmooth_"+ suffix), $("X1Frac_"+ suffix)
appendtotable $("YaSmooth_"+ suffix), $("YbSmooth_"+ suffix)
appendtotable $("Y2Norm_"+ suffix), $("Y2NormSmooth_"+ suffix), $("Y2Frac_"+ suffix)
appendtotable $("Y1Norm_"+ suffix), $("Y1NormSmooth_"+ suffix), $("Y1Frac_"+ suffix),
appendtotable $("fit_DC_"+ suffix), $("fit_PA_"+ suffix), $("fit_W_"+ suffix)
appendtotable $("Stats_"+ suffix)
appendtotable $("XanSmooth_"+ suffix), $("YanSmooth_"+ suffix)
appendtotable $("XbnSmooth_"+ suffix), $("YbnSmooth_"+ suffix)
appendtotable $("xanc"+suffix) , $("yanc"+suffix) , $("xbnc"+suffix)
appendtotable $("ybnc"+suffix) , $("XancSmooth_"+ suffix), $("YancSmooth_"+ suffix)
appendtotable $("XbncSmooth_"+ suffix), $("YbncSmooth_"+ suffix)
appendtotable $("wmwn_"+suffix) , $("kv_"+suffix), $("CombShiftedFrequency_"+ suffix)
appendtotable $("CombUnshiftedFrequency_"+ suffix)
appendtotable $("combshiftedwavelength_"+ suffix), $("combwavelength_"+ suffix)
appendtotable $("combshiftwnr_"+ suffix)
end

function removeone(suffix)
string suffix
// string P, W, X1, Y1, X2, Y2, X3, DC, RRC, CRR, OF,
// string MB, AMN, DMHZ, CombWL, TS, IMN, SM, PA, Pressure, Y3
wave P = $("P_"+ suffix)
wave W = $("W_"+ suffix)
wave X1 = $("X1_"+ suffix)
wave Y1 = $("Y1_"+ suffix)
wave X2 = $("X2_"+ suffix)
wave Y2 = $("Y2_"+ suffix)
wave X3 = $("X3_"+ suffix)

```

```

wave DC = $("DC_" + suffix)
wave RRC = $("RRC_" + suffix)
wave CRR = $("CRR_" + suffix)
wave OF = $("OF_" + suffix)
wave MB = $("MB_" + suffix)
wave AMN = $("AMN_" + suffix)
wave DMHZ = $("DMHZ_" + suffix)
wave CombWL = $("CombWL_" + suffix)
wave TS = $("TS_" + suffix)
wave IMN = $("IMN_" + suffix)
wave SM = $("SM_" + suffix)
wave PA = $("PA_" + suffix)
wave Pressure = $("Pressure_" + suffix)
wave Y3 = $("Y3_" + suffix)
wave shiftwnr = $("ShiftWnR_" + suffix)
wave xa = $("xa" + suffix)
wave xb = $("xb" + suffix)
wave ya = $("ya" + suffix)
wave yb = $("yb" + suffix)
wave xas = $("XASmooth_" + suffix)
wave yas = $("YASmooth_" + suffix)
wave xbs = $("XBSmooth_" + suffix)
wave ybs = $("YBSmooth_" + suffix)
wave X1D=$("xan"+suffix)
wave Y1D=$("yan"+suffix)
wave X2D=$("xbn"+suffix)
wave Y2D=$("ybn"+suffix)
wave DBL=$("DetBaseLine_" + suffix)
wave PAB=$("PABaseline_" + suffix)
wave fdc=$("fit_DC_" + suffix)
wave fpa=$("fit_PA_" + suffix)
wave fwa=$("fit_W_" + suffix)
wave RT=$("RTotal_" + suffix)
wave RTS=$("RTSmooth_" + suffix)
wave R1S=$("R1Smooth_" + suffix)
wave R1=$("R1_" + suffix)
wave R2S=$("R2Smooth_" + suffix)
wave R2=$("R2_" + suffix)
wave stats=$("Stats_" + suffix)
wave sf=$("shiftedfrequency_" + suffix)
wave sl=$("shiftedwavelength_" + suffix)
wave usf=$("unshiftedfrequency_" + suffix)
wave wl=$("wavelength_" + suffix)
wave TT=$("TTotal_" + suffix)
wave TTS=$("TTSmooth_" + suffix)
wave T1S=$("T1Smooth_" + suffix)
wave T1=$("T1_" + suffix)
wave T2S=$("T2Smooth_" + suffix)
wave T2=$("T2_" + suffix)
wave X3N=$("X3Norm_" + suffix)
wave X3F=$("X3Frac_" + suffix)
wave Y3N=$("Y3Norm_" + suffix)
wave Y3F=$("Y3Frac_" + suffix)
wave X2N=$("X2Norm_" + suffix)
wave X2S=$("X2NormSmooth_" + suffix)
wave X2F=$("X2Frac_" + suffix)
wave X1N=$("X1Norm_" + suffix)
wave X1S=$("X1NormSmooth_" + suffix)

```

```

wave X1F=$("X1Frac_" + suffix)
wave YAS=$("YaSmooth_" + suffix)
wave YBS=$("YbSmooth_" + suffix)
wave Y2N=$("Y2Norm_" + suffix)
wave Y2S=$("Y2NormSmooth_" + suffix)
wave Y2F=$("Y2Frac_" + suffix)
wave Y1N=$("Y1Norm_" + suffix)
wave Y1S=$("Y1NormSmooth_" + suffix)
wave Y1F=$("Y1Frac_" + suffix)
wave xans = $("XanSmooth_" + suffix)
wave yans = $("YanSmooth_" + suffix)
wave xbns = $("XbnSmooth_" + suffix)
wave ybns = $("YbnSmooth_" + suffix)
wave X1DC=$("xanc"+suffix)
wave Y1DC=$("yanc"+suffix)
wave X2DC=$("xbnc"+suffix)
wave Y2DC=$("ybnc"+suffix)
wave xancs = $("XancSmooth_" + suffix)
wave yancs = $("YancSmooth_" + suffix)
wave xbncs = $("XbncSmooth_" + suffix)
wave ybncs = $("YbncSmooth_" + suffix)
wave wmwns = $("wmwn_" + suffix)
wave kvs = $("kv_" + suffix)
wave csf = $("combshiftedfrequency_" + suffix)
wave cuf = $("combunshiftedfrequency_" + suffix)
wave csw = $("combshiftedwavelength_" + suffix)
wave cwl = $("combwavelength_" + suffix)
wave cswn = $("combshiftwnr_" + suffix)
killwaves /z P, W, X1, Y1, X2, Y2, X3, DC, RRC, CRR, OF, MB
killwaves /z AMN, DMHZ, CombWL, TS, IMN, SM, PA, Pressure, Y3
killwaves /z shiftwnr, xa, xb, ya, yb, xas, yas, xbs, ybx, x1d
killwaves /z y1d, x2d, y2d, dbl, pab
killwaves /z fdc, fpa, fwa, RT, RTS, R1S, R1, R2S, R2, stats
killwaves /z sf, sl, usf, wl, TT, TTS, T1S, T1, T2S, T2, X3N, X3F
killwaves /z Y3N, Y3F, X2N, X2S, X2F, X1N, X1S, X1F, YAS, YBS, Y2N
killwaves /z Y2S, Y2F, Y1N, Y1S, Y1f, XANS, YANS, XBNS, YBNS, X1DC
killwaves /z Y1Dc, X2DC,Y2DC, xancs, yancs, xbncs, ybncs
killwaves /z wmwns, kvs, csf, cuf, csw, cwl, cswn
end

```

```

function rotatorr(x, y, degrees)
wave x, y
variable degrees
duplicate x x1
duplicate y y1
variable rads = degrees*pi/180
x = x1 * cos(rads) - y1 * sin(rads)
y = x1 * sin(rads) + y1 * cos(rads)
end

```

```

function rf_rot(x1, y1, x2, y2, degrees)
wave x1, y1, x2, y2
variable degrees
rotatorr(x1, x2, degrees)
rotatorr(y1, y2, degrees)
end

```

```

function rotator2(xwaveA,ywaveA,xwaveB,ywaveB,theta1,theta2)

```

```

wave xwaveA, ywaveA, xwaveB, ywaveB
variable theta1,theta2
duplicate xwaveA xwaveA2
duplicate ywaveA ywaveA2
duplicate xwaveB xwaveB2
duplicate ywaveB ywaveB2
variable thetaradians1,thetaradians2
thetaradians1=theta1/180*pi
thetaradians2=theta2/180*pi
// print thetaradians
xwaveA=xwaveA2*cos(thetaradians1)-ywaveA2*sin(thetaradians1)
ywaveA=xwaveA2*sin(thetaradians1)+ywaveA2*cos(thetaradians1)
xwaveB=xwaveB2*cos(thetaradians2)-ywaveB2*sin(thetaradians2)
ywaveB=xwaveB2*sin(thetaradians2)+ywaveB2*cos(thetaradians2)
end

// lorentz, DawsonF, GaussF, LorentzD, LorentzA, makedawson, makegaussian. Fitting functions
function lorentz(f, g, f0)
variable f, g, f0
return  $-(100/\pi) * ((f0^2 - f^2)^2) / ((f0^2 - f^2) + (g^2)*(f^2))$ 
end

function DawsonF(nu, fwhm, nu0)
variable nu, nu0, fwhm
variable gam =  $2*\text{Sqrt}(\text{Ln}(2))*(\text{nu}-\text{nu0})/\text{fwhm}$ 
return  $(-2/\text{Sqrt}(\pi))*\text{dawson}(\text{gam})$ 
end

function GaussF(nu, fwhm, nu0)
variable nu, nu0, fwhm
return  $\exp(-(4*\text{Ln}(2)) * ((\text{nu}-\text{nu0})^2) / (\text{fwhm}^2))$ 
end

function LorentzD(nu, fwhm, nu0)
variable nu, nu0, fwhm
return  $\text{nu0}*\text{fwhm}*(\text{nu0}^2 - \text{nu}^2) / ((\text{nu0}^2-\text{nu}^2)^2 + (\text{nu}^2)*(\text{fwhm}^2))$ 
end

function LorentzA(nu, fwhm, nu0)
variable nu, nu0, fwhm
return  $\text{nu0}*\text{fwhm}*\text{nu}*\text{fwhm} / ((\text{nu0}^2-\text{nu}^2)^2 + (\text{nu}^2)*(\text{fwhm}^2))$ 
end

function makedawson(xwave,ywave,fwhm,mu)
wave xwave, ywave
variable fwhm, mu
killwaves /z gam
duplicate xwave gam
gam =  $2*\text{Sqrt}(\text{Ln}(2))*(\text{xwave}-\text{mu})/\text{fwhm}$ 
//display gam vs xwave
ywave=  $(-2/\text{Sqrt}(\pi))*\text{dawson}(\text{gam})$ 
//display ywave vs xwave
end

function makegaussian(xwave,ywave,fwhm,mu)

```

```

wave xwave, ywave
variable mu, fwhm
ywave=exp( -(4*Ln(2)) * ((xwave-mu)^2) / (fwhm^2) )
end

function singlesplit(frequency,voltage,plusvoltage,minusvoltage)
// pos, pos, negative
variable frequency, voltage, plusvoltage,minusvoltage
variable factorA, factorB, F1, F2, F3, F4
variable VoltageA=voltage-plusvoltage //3865 - 10
variable VoltageB=voltage-minusvoltage //3865 - -10
factorA=sqrt(2*1.60217646e-19*VoltageA/4.6517405810e-26/299792458/299792458)
// factor = v/c=sqrt(2*q*V/m/c/c)
factorB=sqrt(2*1.60217646e-19*VoltageB/4.6517405810e-26/299792458/299792458)
// factor = v/c=sqrt(2*q*V/m/c/c)
F1=frequency*sqrt((1+factorA)/(1-factorA)) // Fully Equal
F2=frequency*sqrt((1+factorB)/(1-factorB)) // Fully Equal
F3=frequency*sqrt((1-factorA)/(1+factorA)) // Fully Equal
F4=frequency*sqrt((1-factorB)/(1+factorB)) // Fully Equal
print F1
print F2
print F3
print F4
wave wave50
wave50[1]=F1
wave50[2]=F2
wave50[3]=F3
wave50[4]=F4
wave50[0]=frequency
end

function makemask(suffix,fewer)
string suffix
variable fewer
variable ii
wavestats /q $("xa"+suffix+"f")
make /o/d/n=(V_npnts) testwave
testwave=1
for(ii=0; ii<=V_npnts; ii+=1) // goes through entire
    if(mod(ii, fewer)==0)
        testwave[ii]=1
    else
        testwave[ii]=0
    endif
endfor
make /o/d/n=(V_npnts) $("Mask_"+suffix)
wave mask=$("Mask_"+suffix)
mask=testwave
//edit testwave, $("Mask_"+suffix)
end

function subgraphcomb(suffix,fewer)
string suffix
variable fewer
variable ii, jj
wavestats /q $("P_"+suffix)
Duplicate/0 $("x1frac_"+suffix), $("x1frac_"+suffix+"S")
//Duplicate/0 $("xa"+suffix+"f"), $("xa"+suffix+"S")

```

```

wave datawaveone = $("x1frac_"+suffix)
wave datawavetwo=$("x1frac_"+suffix+"S")
Duplicate/O $("CombShiftWnr_"+suffix), $("combshiftwnrS_"+suffix)
wave xwaveone=$("combshiftwnr_"+suffix)
wave xwavetwo=$("combshiftwnrS_"+suffix)
for(ii=0; ii<=V_npnts; ii+=1) // goes through entire
    if(mod(ii, fewer)==0)
        datawavetwo[ii]=datawaveone[ii]
        xwavetwo[ii]=xwaveone[ii]
    else
        datawavetwo[ii]=0
        xwavetwo[ii]=0
    endif
endfor
variable newlength
newlength=floor(V_npnts/fewer)
print newlength
make /o/d/n=(newlength) $("x1frac_"+suffix+"SS")
//make /o/d/n=(newlength) $("xa"+suffix+"SS")
make /o/d/n=(newlength) $("combshiftwnrSS_"+suffix)
//wave newywave=$("xa"+suffix+"SS")
wave newywave=$("x1frac_"+suffix+"SS")
wave newxwave=$("combshiftwnrSS_"+suffix)
jj=0
for(ii=0; ii<=V_npnts; ii+=1) // goes through new entire wave
    if(xwavetwo[ii]==0) // It's never taking this case
    else
        newywave[jj]=datawavetwo[ii]
        newxwave[jj]=xwavetwo[ii]
        jj=1+jj
    endif
endfor
display $("x1frac_"+suffix+"SS") vs $("combshiftwnrSS_"+suffix)
ModifyGraph highTrip(bottom)=1e+06
ModifyGraph mode=2,lsize=3,rgb=(0,0,0)
appendtograph $("fit_x1frac_"+suffix)
end

function subgraph(suffix,fewer)
string suffix
variable fewer
variable ii, jj
wavestats /q $("P_"+suffix)
print V_npnts
Duplicate/O $("x1frac_"+suffix), $("x1frac_"+suffix+"S")
print "duplicated data"
wave datawaveone = $("x1frac_"+suffix)
wave datawavetwo=$("x1frac_"+suffix+"S")
Duplicate/O $("ShiftWnr_"+suffix), $("ShiftWnrS_"+suffix)
print "duplicated xwave"
wave xwaveone=$("shiftwnr_"+suffix)
wave xwavetwo=$("shiftwnrS_"+suffix)
for(ii=0; ii<=V_npnts; ii+=1) // goes through entire
    if(mod(ii, fewer)==0)
        datawavetwo[ii]=datawaveone[ii]
        xwavetwo[ii]=xwaveone[ii]
    else

```

```

        datawavetwo[ii]=0
        xwavetwo[ii]=0
    endif
endfor
print "made mask"
variable newlength
newlength=floor(V_npnts/fewer)
print newlength
make /o/d/n=(newlength) $("x1frac_"+suffix+"SS")
make /o/d/n=(newlength) $("shiftwnrSS_"+suffix)
wave newywave=$("x1frac_"+suffix+"SS")
wave newxwave=$("shiftwnrSS_"+suffix)
jj=0
for(ii=0; ii<=V_npnts; ii+=1) // goes through new entire wave
    if(xwavetwo[ii]==0) // It's never taking this case
    else
        newywave[jj]=datawavetwo[ii]
        newxwave[jj]=xwavetwo[ii]
        jj=1+jj
    endif
endfor
display $("x1frac_"+suffix+"SS") vs $("shiftwnrSS_"+suffix)
ModifyGraph highTrip(bottom)=1e+06
ModifyGraph mode=2,lsize=3,rgb=(0,0,0)
appendto graph $("fit_x1frac_"+suffix)
end

function looper()
variable ii, beg=1, num=19
for(ii=0; ii<num; ii+=1) // goes through number of waves
makegrphs(num2str(beg+ii))
endfor
end

function recalcomb(suffix)
string suffix
display $("kv_"+suffix) vs $("CombShiftWnr_"+suffix)
ModifyGraph highTrip(bottom)=100000
end

function makegrphs(suffix)
string suffix
display $("kv_"+suffix) vs $("CombShiftWnr_"+suffix)
ModifyGraph highTrip(bottom)=100000
end

function looper2()
wave loopervariable
variable ii, beg=0, num=18
for(ii=0; ii<num; ii+=1) // goes through number of waves
difference(num2str(loopervariable[ii]))
endfor
end

function difference(suffix)//,beg,endg)
string suffix
variable beg, endg
//wavestats /q $("Xa_"+ suffix)

```



```

//print V_max-V_min
wavestats /q $( "PABaseline_" + suffix)
print V_avg
//wavestats /q /R=[beg,endg] $( "PA_" + suffix)
//print V_sdev
wavestats /q $( "DetBaseline_" + suffix)
print V_avg
end

function findsignalandnoise(suffix)
string suffix
wave WN =$( "ShiftWnr_" + suffix)
wave X1N =$( "X1Norm_" + suffix)
wave Y1N = $( "Y1Norm_" + suffix)
wave X2N = $( "X2Norm_" + suffix)
wave Y2N = $( "Y2Norm_" + suffix)
wave X1S =$( "X1Norm_" + suffix)
wave Y1S = $( "Y1Norm_" + suffix)
wave X2S = $( "X2Norm_" + suffix)
wave Y2S = $( "Y2Norm_" + suffix)
wave R1S = $( "R1Smooth_" + suffix)
wave T1S = $( "T1Smooth_" + suffix)
wave R2S = $( "R2Smooth_" + suffix)
wave T2S = $( "T2Smooth_" + suffix)
wave R1 = $( "R1_" + suffix)
wave T1 = $( "T1_" + suffix)
wave R2 = $( "R2_" + suffix)
wave T2 = $( "T2" + suffix)
wave RT = $( "RTotal_" + suffix)
wave TT = $( "TTotal_" + suffix)
wave RTS = $( "RTSmooth_" + suffix)
wave TTS = $( "TTSmooth_" + suffix)
//display RTS vs WN
//ModifyGraph highTrip(bottom)=1e+06
//wavestats /q
//display r1s vs WN
//ModifyGraph highTrip(bottom)=1e+06
//display r2s vs WN
//ModifyGraph highTrip(bottom)=1e+06
//display RT vs WN
//ModifyGraph highTrip(bottom)=1e+06
//display RTS vs WN
//ModifyGraph highTrip(bottom)=1e+06
end

function makegraphs(suffix1,suffix2)
string suffix1, suffix2
display $( "X1Norm_" + suffix1) vs $( "shiftwnr_" + suffix1)
appendtograph $( "X1Norm_" + suffix2) vs $( "shiftwnr_" + suffix2)
ModifyGraph highTrip(bottom)=100000
appendtograph $( "X1NormSmooth_" + suffix1) vs $( "shiftwnr_" + suffix1)
appendtograph $( "X1NormSmooth_" + suffix2) vs $( "shiftwnr_" + suffix2)
ModifyGraph rgb$( "X1NormSmooth_" + suffix1)=(0,0,65280)
ModifyGraph rgb$( "X1Norm_" + suffix2 )=(0,0,0)
ModifyGraph rgb$( "X1NormSmooth_" + suffix2 )=(0,65280,0)
end

function addheterodyne2(suffix)

```

```

string suffix
wave in2plus
getaxis bottom
SetAxis /A=0 /Z bottom V_min,V_max
wave FP1W=$( "Fplus1_" +suffix)
wave FM1W=$( "Fminus1_" +suffix)
wave FP2W=$( "Fplus2_" +suffix)
wave FM2W=$( "Fminus2_" +suffix)
wave FP1A = $( "Fplus1A_" +suffix)
wave FP1B = $( "Fplus1B_" +suffix)
wave FP2A = $( "Fplus2A_" +suffix)
wave FP2B = $( "Fplus2B_" +suffix)
wave FM1A = $( "Fminus1A_" +suffix)
wave FM1B = $( "Fminus1B_" +suffix)
wave FM2A = $( "Fminus2A_" +suffix)
wave FM2B = $( "Fminus2B_" +suffix)
appendtograph /r in2plus vs FM2W
ModifyGraph rgb(In2plus)=(13056,0,0)
appendtograph /r in2plus vs $( "Fplus2_" +suffix)
ModifyGraph rgb(In2plus)=(13056,0,0)
appendtograph /r in2plus vs FM1W
ModifyGraph rgb(In2plus#1)=(13056,0,0)
appendtograph /r in2plus vs FP1W
ModifyGraph rgb(In2plus#2)=(0,0,52224)
appendtograph /r in2plus vs FP2W
ModifyGraph rgb(In2plus#3)=(0,0,52224)
appendtograph /r in2plus vs FM2A
ModifyGraph rgb(In2plus#4)=(13056,0,0)
appendtograph /r in2plus vs FM2B
ModifyGraph rgb(In2plus#5)=(13056,0,0)
appendtograph /r in2plus vs FM1A
ModifyGraph rgb(In2plus#6)=(13056,0,0)
appendtograph /r in2plus vs FM1B
ModifyGraph rgb(In2plus#7)=(13056,0,0)
appendtograph /r in2plus vs FP2A
ModifyGraph rgb(In2plus#8)=(0,0,52224)
appendtograph /r in2plus vs FP2B
ModifyGraph rgb(In2plus#9)=(0,0,52224)
appendtograph /r in2plus vs FP1A
ModifyGraph rgb(In2plus#10)=(0,0,52224)
appendtograph /r in2plus vs FP1B
ModifyGraph rgb(In2plus#11)=(0,0,52224)
ModifyGraph mode(In2plus)=1,mode(In2plus#1)=1,mode(In2plus#2)=1
ModifyGraph mode(In2plus#3)=1,mode(In2plus#4)=1,mode(In2plus#5)=1
ModifyGraph mode(In2plus#6)=1, mode(In2plus#7)=1, mode(In2plus#8)=1
ModifyGraph mode(In2plus#9)=1, mode(In2plus#10)=1, mode(In2plus#11)=1
end

function makeheterodyne(suffix,voltage,plusvoltage,minusvoltage,frequencyMHz)
// pos, pos, negative, frequency
string suffix
variable voltage, plusvoltage,minusvoltage, frequencyMHz
variable frequency // cm-1
makedoppler(suffix,voltage,plusvoltage,minusvoltage)
changeheterodyne(suffix,frequencyMHz)
end

function changeheterodyne(suffix,frequencyMHz)

```

```

string suffix
variable frequencyMHz
variable nln2plus, frequency // cm-1
wavestats /Q LN2plus //determine number of rows in input N2+ wave
nLN2plus=V_npnts
wave fminus2, fminus1, fplus1,fplus2
frequency=frequencyMHz/1000/29.9792458
make /o/n=(nLN2plus) $("Fplus1A_"+suffix)=0
make /o/n=(nLN2plus) $("Fplus1B_"+suffix)=0
make /o/n=(nLN2plus) $("Fplus2A_"+suffix)=0
make /o/n=(nLN2plus) $("Fplus2B_"+suffix)=0
make /o/n=(nLN2plus) $("Fminus1A_"+suffix)=0
make /o/n=(nLN2plus) $("Fminus1B_"+suffix)=0
make /o/n=(nLN2plus) $("Fminus2A_"+suffix)=0
make /o/n=(nLN2plus) $("Fminus2B_"+suffix)=0
// make /d/o/n=50 $("StatS_"+ suffix)
// wave stats=$("StatS_"+ suffix)
wave FP1A = $("Fplus1A_"+suffix)
wave FP1B = $("Fplus1B_"+suffix)
wave FP2A = $("Fplus2A_"+suffix)
wave FP2B = $("Fplus2B_"+suffix)
wave FM1A = $("Fminus1A_"+suffix)
wave FM1B = $("Fminus1B_"+suffix)
wave FM2A = $("Fminus2A_"+suffix)
wave FM2B = $("Fminus2B_"+suffix)
//Fplus1A=0, Fminus1A=0,Fplus2A=0, Fminus2A=0, Fplus1B=0,
//Fminus1B=0,Fplus2B=0, Fminus2B=0
Fp1A=Fplus1+frequency
Fp1B=Fplus1-frequency
Fp2A=Fplus2+frequency
Fp2B=Fplus2-frequency
Fm1A=Fminus1+frequency
Fm1B=Fminus1-frequency
Fm2A=Fminus2+frequency
Fm2B=Fminus2-frequency
end

function fullbinner(number,textwave1) // Andrew's binning program
wave/T textwave1
variable number

string suffix
variable start,stop,step
variable binlength, ii,bin, low, jj
start=10853.4
stop=10853.5
step=((20)/1e3)/29.9792458
binlength=ceil((stop-start)/step)

make /o/d/n=(binlength) binaxis=0
make /o/d/n=(binlength) bincount=0
make /o/d/n=(binlength) binAX=0
make /o/d/n=(binlength) binAY=0
make /o/d/n=(binlength) binBX=0
make /o/d/n=(binlength) binBY=0

for(ii=0; ii <=binlength; ii+=1) // fills bin x axis
binaxis[ii]=ii*step+start

```

```

endfor

for(jj=0; jj <(number); jj+=1) // goes through loader program each time
suffix=textWave1[jj]
wave AX= $("x1frac_"+suffix) // previously had C / D
wave AY=$("y1frac_"+suffix)
wave BX=$("x2frac_"+suffix)
wave BY=$("y2frac_"+suffix)
wave wn = $("ShiftWnr_"+suffix)
wavestats /Q $("ShiftWnr_"+suffix)
low=V_npnts-1
for(ii=0; ii <=low; ii+=1) // bins each load
bin=0
bin=trunc((wn[ii]-start)/step)
bincount[bin]+=1
binAX[bin]+=AX[ii]
binAY[bin]+=AY[ii]
binBX[bin]+=BX[ii]
binBY[bin]+=BY[ii]
endfor
endfor
for(ii=0; ii <=binlength; ii+=1) // bins each load
binax[ii]=binax[ii]/bincount[ii]
binbx[ii]=binbx[ii]/bincount[ii]
binby[ii]=binby[ii]/bincount[ii]
binay[ii]=binay[ii]/bincount[ii]
endfor

display binAX vs binaxis
ModifyGraph mode=0
getaxis bottom
SetAxis /A=0 /Z bottom V_min,V_max
ModifyGraph highTrip(bottom)=1e+08
Label bottom "Frequency (cm\\S-1\\M)"
Label left "NICE OHMS Fractional Absorption"
//addheterodyne()
//SetAxis right 0,5

display binAY vs binaxis
ModifyGraph mode=0
getaxis bottom
SetAxis /A=0 /Z bottom V_min,V_max
ModifyGraph highTrip(bottom)=1e+08
Label bottom "Frequency (cm\\S-1\\M)"
Label left "NICE OHMS Fractional Absorption"
//addheterodyne()
//SetAxis right 0,5

display binBX vs binaxis
ModifyGraph mode=0
getaxis bottom
SetAxis /A=0 /Z bottom V_min,V_max
ModifyGraph highTrip(bottom)=1e+08
Label bottom "Frequency (cm\\S-1\\M)"
Label left "NICE OHMS Fractional Absorption"
//addheterodyne()
//SetAxis right 0,5

```

```

display binBY vs binaxis
ModifyGraph mode=0
getaxis bottom
SetAxis /A=0 /Z bottom V_min,V_max
ModifyGraph highTrip(bottom)=1e+08
Label bottom "Frequency (cm\\S-1\\M)"
Label left "NICE OHMS Fractional Absorption"
//addheterodyne()
//SetAxis right 0,5
end

```

Abbreviations

Table E.1: Abbreviations used in this dissertation.

Abbreviation	Definition
AC	Alternating current
AOM	Acoustooptic modulator
β	Heterodyne modulation depth
BiFi	Birefringent filter
BPM	Beam profile monitor
CF	Conflat
CRDS	Cavity ringdown spectroscopy
cw	Continuous wave
DC	Direct current
DFG	Difference frequency generation laser
DDS	Direct digital synthesizer
DLASFIB	Direct laser absorption spectroscopy of a fast ion beam
DMRR	Downmixed repetition rate
DRO	Dielectric resonant oscillator
DSP	Digital signal processor
EDFA	Erbium doped fiber laser
EOM	Electrooptic modulator
F	Finesse
FIB	Fast Ion Beam
FM	Frequency modulation
FM1	Folding mirror 1
FOB	Fraction of band
FWHM	Full width half max
FSR	Free spectral range
f_{REP}	Frequency comb repetition frequency
f_{CEO}	Frequency comb carrier envelope offset frequency
fs	femtosecond
G^+	Saturation parameter
HWHM	Half width half max
HWP	Half wave plate
JILA	Joint Institute for laboratory Astrophysics
LED	Light emitting diode
LP	Low pass
MOS	Matisse optical set
NIR	Near infrared
NICE-OHMS	Noise-immune cavity-enhanced optical-heterodyne molecular spectroscopy
ν^+	Blue shifted Doppler component
ν^-	Red shifted Doppler component
OC	Output coupler
PBS	Polarizing beam splitter
PCF	Photonic crystal fiber
PEEK	Polyether ether ketone
PM	Pump Mirror
PMMA	Polymethyl methacrylate
PPLN	Periodically poled lithium niobate crystal
PZETL	Piezoetalon (thick etalon)
QWP	Quarter wave plate
QPM	Quasi phase matching

Continued on next page...

Table E.1 continued.

Abbreviation	Definition
RAM	Residual amplitude modulation
RF	Radiofrequency
SCRIBES	Sensitive cooled resolved ion beam spectroscopy
SHG	Sum harmonic generation laser
SHV-5	Safe high voltage connector (5 kV)
SHV-20	Safe high voltage connector (20 kV)
TE	Thin etalon
Ti:Sapphire	Titanium sapphire laser
θ_B	Brewster's angle
TGG	Terbium gallium garnet
TOF	Time of flight mass spectrometry
VMS	Velocity modulation spectroscopy
XPS	Frequency comb carrier envelope offset interferometer.
YAG	Yttrium aluminum garnet laser

References

- [1] C. S. Gudeman, M. H. Begemann, J. Pfaff, and R. J. Saykally. Velocity modulated IR laser spectroscopy of molecular ions: The ν_1 band of HNN^+ . *Journal of Chemical Physics*, **78**(9) 5837–5845 (1983).
- [2] J. C. Owruksy, C. S. Gudeman, C. C. Martner, L. M. Tack, N. H. Rosenbaum, and R. J. Saykally. Determination of the equilibrium structure of protonated nitrogen by high resolution infrared laser spectroscopy. *Journal of Chemical Physics*, **84**(2) 605 (1986).
- [3] R. J. Saykally, T. A. Dixon, T. G. Anderson, P. G. Szanto, and R. C. Woods. Laboratory microwave-spectrum and rest frequencies of HN_2^+ ion. *Astrophysical Journal*, **205**(2) L101–L103 (1976).
- [4] K. V. L. N. Sastry, P. Helminger, E. Herbst, and F. C. De Lucia. Millimeter and sub-millimeter spectra of HN_2^+ and DN_2^+ . *Chemical Physics Letters*, **84**(2) 286–287 (1981).
- [5] P. Verhoeve, E. Zwart, M. Versluis, M. Drabbels, J. J. Termeulen, W. L. Meerts, A. Dymanus, and D. B. McLay. A far infrared-laser sideband spectrometer in the frequency region 550–2700 GHz. *Review of Scientific Instruments*, **61**(6) 1612–1625 (1990).
- [6] S. G. Cox, A. D. J. Critchley, I. R. McNab, and F. E. Smith. High-resolution spectroscopy of ion beams. *Measurement Science & Technology*, **10**(9) R101–R128 (1999).
- [7] E. T. White, J. Tang, and T. Oka. CH_5^+ : The infrared spectrum observed. *Science*, **284**(5411) 135–137 (1999).
- [8] Sirah, editor. *Matisse User’s Guide*. Sirah Laser- und Plasmatechnik GmbH (V1.10).
- [9] I. T. Sorokina and K. L. Vodopyanov, editors. *Solid-State Mid-Infrared Laser Sources*, chapter Mid-IR Difference Frequency Generation, (page 116). Springer-Verla (2003).
- [10] MenloSystems. *FC1500 Optical Frequency Synthesizer*. MenloSystems GmbH, 1.1 edition (2011).
- [11] W. Ma, A. Foltynowicz, and O. Axner. Theoretical description of doppler-broadened noise-immune cavity-enhanced optical heterodyne molecular spectroscopy under optically saturated conditions. *Journal of the Optical Society of America B-Optical Physics*, **25**(7) 1144–1155 (2008).
- [12] J. V. Coe, J. C. Owruksy, E. R. Keim, N. V. Agman, D. C. Hovde, and R. J. Saykally. Sub-Doppler direct infrared laser absorption spectroscopy in fast ion beams: The fluorine hyperfine structure of HF^+ . *The Journal of Chemical Physics*, **90**(8) 3893–3902 (1989).
- [13] B. M. Siller, A. A. Mills, and B. J. McCall. Cavity-enhanced velocity modulation spectroscopy. *Optics Letters*, **35**(8) 1266–1268 (2010).
- [14] A. G. Gaydon. *Flames, Their Structure, Radiation, and Temperature. Fourth Edition*. Chapman & Hall; (1979).
- [15] J. A. Barnard and J. N. . Bradley. *Flame and combustion*, chapter Special Aspects of Gaseous Combustion, (page 176). Chapman and Hall (1985).
- [16] J. W. Coburn and H. F. Winters. Plasma-etching - A discussion of mechanisms. *CRC Critical Reviews In Solid State and Materials Sciences*, **10**(2) 119–141 (1981).
- [17] E. E. Ferguson and F. Arnold. Ion chemistry of the stratosphere. *Accounts of Chemical Research*, **14**(11) 327–334 (1981).
- [18] E. Herbst and W. Klemperer. Formation and depletion of molecules in dense interstellar clouds. *The Astrophysical Journal*, **185**(2) 505–533 (1973).
- [19] T. Oka and M. F. Jagod. Infrared spectrum of H as an astronomical probe. *Journal of the Chemical Society, Faraday Transactions*, **89**(13) 2147–2154 (1993).
- [20] C. S. Gudeman, M. H. Begemann, J. Pfaff, and R. J. Saykally. Velocity-modulated infrared-laser spectroscopy of molecular-ions - The ν_1 band of HCO^+ . *Physical Review Letters*, **50**(10) 727–731 (1983).

- [21] G. Herzberg. Spectra and structures of molecular ions. *Quarterly Reviews*, **25**(2) 201 (1971).
- [22] T. A. Dixon and R. C. Woods. Microwave-absorption spectrum of CO^+ ion. *Physical Review Letters*, **34**(2) 61–63 (1975).
- [23] R. C. Woods, T. A. Dixon, R. J. Saykally, and P. G. Szanto. Laboratory microwave-spectrum of HCO^+ . *Physical Review Letters*, **35**(19) 1269–1272 (1975).
- [24] T. Oka. Observation of the infrared-spectrum of H_3^+ . *Physical Review Letters*, **45**(7) 531–534 (1980).
- [25] P. Bernath, M. Wong, and T. Amano. Infrared-laser spectroscopy of HeH^+ and NeH^+ . *Journal of the Optical Society of America*, **72**(12) 1778–1778 (1982).
- [26] M. Wong, P. Bernath, and T. Amano. Observation of the infrared-absorption spectra of $^{20}\text{NeH}^+$ and $^{22}\text{NeH}^+$ with a difference frequency laser. *Journal of Chemical Physics*, **77**(2) 693–696 (1982).
- [27] J. W. Brault and S. P. Davis. Fundamental vibration-rotation bands and molecular-constants for the ArH^+ ground-state ($^1\Sigma^+$). *Physica Scripta*, **25**(2) 268–271 (1982).
- [28] S. K. Stephenson and R. J. Saykally. Velocity modulation spectroscopy of ions. *Chemical Reviews*, **105**(9) 3220–3234 (2005).
- [29] D. E. Tolliver, G. A. Kyrala, and W. H. Wing. Observation of the infrared spectrum of the helium-hydride molecular ion $^4\text{HeH}^+$. *Physical Review Letters*, **43**(23) 1719–1722 (1979).
- [30] J. T. Shy, J. W. Farley, W. E. Lamb, and W. H. Wing. Observation of the infrared-spectrum of the triatomic deuterium molecular ion D_3^+ . *Physical Review Letters*, **45**(7) 535–537 (1980).
- [31] J. T. Shy, J. W. Farley, R. Deserio, and W. H. Wing. Observation of the infrared-spectra of the triatomic hydrogen molecular-ions H_2D^+ and HD_2^+ . *Abstracts of Papers of the American Chemical Society*, **182** 171 (1981).
- [32] C. S. Gudeman and R. J. Saykally. Velocity modulation infrared laser spectroscopy of molecular ions. *Annual Review of Physical Chemistry*, **35**(1) 387–418 (1984).
- [33] J. C. Owruksy, N. H. Rosenbaum, L. M. Tack, and R. J. Saykally. The vibration-rotation spectrum of the hydroxide anion OH^- . *Journal of Chemical Physics*, **83**(10) 5338–5339 (1985).
- [34] J. Owruksy, N. Rosenbaum, L. Tack, M. Grubele, M. Polak, and R. J. Saykally. Velocity-modulation infrared-laser spectroscopy of molecular anions. *Philosophical Transactions of the Royal Society of London Series A-Mathematical Physical and Engineering Sciences*, **324**(1578) 97–108 (1988).
- [35] J. W. Farley. Theory of the resonance line-shape in velocity-modulation spectroscopy. *Journal of Chemical Physics*, **95**(8) 5590–5602 (1991).
- [36] W. Y. Fan and P. A. Hamilton. Velocity and magnetic modulation methods applied to emission spectroscopy. *Chemical Physics Letters*, **230**(6) 555 – 560 (1994).
- [37] C. Savage and L. M. Ziurys. A millimeter/submillimeter velocity modulation spectrometer for studies of molecular ions. *Review of Scientific Instruments*, **76**(4) 043106 (2005).
- [38] D. T. Halfen and L. M. Ziurys. Laboratory detection of FeCO^+ ($X^4\Sigma^-$) by millimeter/submillimeter velocity modulation spectroscopy. *Astrophysical Journal*, **657**(1, Pt. 2) L61–L64 (2007).
- [39] D. T. Halfen and L. M. Ziurys. Millimeter/submillimeter velocity modulation spectroscopy of FeO^+ ($X^6\Sigma^+$): Characterizing metal oxide cations. *Chemical Physics Letters*, **496**(1-3) 8–13 (2010).
- [40] C. Duan, R. Zheng, S. Li, R. Wang, and G. Huang. Infrared laser spectroscopy of the ν_2 fundamental band of D_2O^+ . *Journal of Molecular Spectroscopy*, **251**(1-2) 22–26 (2008).
- [41] S. Li, R. Zheng, G. Huang, and C. Duan. Mid-infrared diode laser spectroscopy of SO^+ . *Journal of Molecular Spectroscopy*, **252**(1) 22–24 (2008).
- [42] R. Zheng, R.-B. Wang, S. Li, G.-M. Huang, and C.-X. Duan. Extended measurement of the ν_2 ($1^- \leftarrow 0^+$) band of H_3O^+ by mid-infrared diode laser spectroscopy. *Chinese Physics Letters*, **24**(9) 2569–2571 (2007).
- [43] M. H. Suh, X. C. Hong, and T. A. Miller. He metastable concentration measurements in a glow discharge. *Chemical Physics*, **228**(1-3) 145–156 (1998).
- [44] J. L. Gottfried, B. J. McCall, and T. Oka. Near-infrared spectroscopy of H_3^+ above the barrier to linearity. *Journal of Chemical Physics*, **118**(24) 10890–10899 (2003).
- [45] C. P. Morong, J. L. Gottfried, and T. Oka. H_3^+ as the benchmark for rigorous ab initio theory. *Journal of Molecular Spectroscopy*, **255**(1) 13–23 (2009).

- [46] A. A. Mills, B. M. Siller, and B. J. McCall. Precision cavity enhanced velocity modulation spectroscopy. *Chemical Physics Letters*, **501**(1-3) 1 – 5 (2010).
- [47] M. F. A. Harrison. The determination of atomic collision cross sections using crossed electron and ion beams (and some sources of error in such experiments). *British Journal of Applied Physics*, **17**(3) 371–382 (1966).
- [48] J. L. Hall, E. J. Robinson, and Branscom.LM. Laser double-quantum photodetachment of I^- . *Physical Review Letters*, **14**(25) 1013 (1965).
- [49] W. C. Lineberger and B. W. Woodward. High resolution photodetachment of S^- near threshold. *Physical Review Letters*, **25**(7) 424 (1970).
- [50] S. M. Trujillo, R. H. Neynaber, and E. W. Rothe. Merging beams a different approach to collision cross section measurements. *Review of Scientific Instruments*, **37**(12) 1655–1661 (1966).
- [51] S. L. Kaufman. High-resolution laser spectroscopy in fast beams. *Optics Communications*, **17**(3) 309–312 (1976)<http://www.faihtpromotingrumor.com/2011/09/canon-and-culture-the-scriptures-made-me-do-it/>).
- [52] H. D. Zeman. Deflection of an ion beam in the two-dimensional electrostatic quadrupole field. *Review of Scientific Instruments*, **48** 1079–1086 (1977).
- [53] W. H. Wing, G. A. Ruff, W. E. Lamb, and J. J. Spezeski. Observation of infrared-spectrum of hydrogen molecular ion HD^+ . *Physical Review Letters*, **36**(25) 1488–1491 (1976).
- [54] R. D. Brown, P. D. Godfrey, J. G. Crofts, Z. Ninkov, and S. Vaccani. Molecular ion fluorescence excitation spectrum from an ion-beam. *Chemical Physics Letters*, **62**(2) 195–197 (1979).
- [55] S. D. Rosner, T. D. Gaily, and R. A. Holt. Laser-fluorescence ion-beam magnetic-resonance - Xe^+ hyperfine-structure. *Physical Review Letters*, **40**(13) 851–854 (1978).
- [56] S. D. Rosner, T. D. Gaily, and R. A. Holt. First measurement of hyperfine structure in N_2^+ . *Physical Review A*, **26**(1) 697 (1982).
- [57] S. D. Rosner, T. D. Gaily, and R. A. Holt. Fine and hyperfine structure in $^{14}N_2^+$. *Journal of Molecular Spectroscopy*, **109**(1) 73–84 (1985).
- [58] J. D. I. Jr. and S. R. Crouch. *Spectrochemical Analysis*, chapter Introduction to Molecular Spectroscopy, (page 339). Prentice Hall (1988).
- [59] A. Tabche-fouhaille, J. Durup, J. T. Moseley, J.-B. Ozenne, C. Pernot, and M. Tadjeddine. Laser photofragment spectroscopy of O_2^+ : $a^4\Pi_u \rightarrow ^4\Pi_g$. *Chemical Physics*, **17**(1) 81–89 (1976).
- [60] A. Carrington, P. G. Roberts, and P. J. Sarre. Laser-induced predissociation spectrum of O_2^+ in an ion-beam. *Molecular Physics*, **34**(1) 291–295 (1977).
- [61] M. Tadjeddine, R. Abouaf, P. C. Cosby, B. A. Huber, and J. T. Moseley. Predissociation photofragment spectroscopy of O_2^+ quartet states. *Journal of Chemical Physics*, **69**(2) 710–719 (1978).
- [62] H. Helm and P. C. Cosby. Laser photofragment spectroscopy of N_2^+ : Evidence for predissociation of $B^2\Sigma_g^+$. *Journal of Chemical Physics*, **77**(11) 5396–5406 (1982).
- [63] P. C. Cosby, R. Moller, and H. Helm. Photofragment spectroscopy of N_2^{2+} . *Physical Review A*, **28**(2) 766–772 (1983).
- [64] H. Helm, P. C. Cosby, and D. L. Huestis. Observation of the $1^2\Pi_u \leftarrow X^2\Sigma_g^+$ system in Cs^{2+} . *Journal of Chemical Physics*, **78**(11) 6451–6454 (1983).
- [65] D. M. Neumark, K. R. Lykke, T. Andersen, and W. C. Lineberger. Infrared-spectrum and autodetachment dynamics of NH^- . *Journal of Chemical Physics*, **83**(9) 4364–4373 (1985).
- [66] K. R. Lykke, K. K. Murray, D. M. Neumark, and W. C. Lineberger. High-resolution studies of autodetachment in negative ions. *Philosophical Transactions of the Royal Society of London. Series A, Mathematical and Physical Sciences*, **324**(1578) 179–196 (1988).
- [67] W. Lineberger and T. Patterson. Two photon photodetachment spectroscopy: The C_2^- $^2\Sigma$ states. *Chemical Physics Letters*, **13**(1) 40–44 (1972).
- [68] J. R. Smith, J. B. Kim, and W. C. Lineberger. High-resolution threshold photodetachment spectroscopy of OH^- . *Physical Review A*, **55**(3) 2036–2043 (1997).
- [69] D. M. Neumark, K. R. Lykke, T. Andersen, and W. C. Lineberger. Laser photodetachment measurement of the electron-affinity of atomic oxygen. *Physical Review A*, **32**(3) 1890–1892 (1985).
- [70] D. M. Neumark, L. K. R., T. Andersen, and W. C. Lineberger. Autodetachment spectroscopy of negative-ions. *Abstracts of Papers of the American Chemical Society*, **189**(APR-) 137 (1985).

- [71] A. A. Mills, B. M. Siller, M. W. Porambo, M. Perera, H. Kreckel, and B. J. McCall. Ultra-sensitive high precision spectroscopy of a fast molecular ion beam. *Journal of Chemical Physics*, **In Press** (2011).
- [72] K. C. Thompson, D. L. Crittenden, and M. J. T. Jordan. CH_5^+ : Chemistry’s chameleon unmasked. *Journal of the American Chemical Society*, **127**(13) 4954–4958 (2005).
- [73] G. A. Olah, G. Klopman, and S. R. H. Chemistry in super acids. III protonation of alkanes and intermediacy of alkanonium ions pentacoordinated carbon cations of CH_5^+ type. Hydrogen exchange protolytic cleavage hydrogen abstraction and polycondensation of methane ethane 2,2-dimethylpropane (neopentane) and 2,2,3,3-tetramethylbutane in $\text{FSO}_3\text{H-SbF}_5$ (“magic acid”) solution. *Journal of the American Chemical Society*, **91**(12) 3261–68 (1969).
- [74] S. Davis, M. Farnik, D. Uy, and D. J. Nesbitt. Concentration modulation spectroscopy with a pulsed slit supersonic discharge expansion source. *Chemical Physics Letters*, **344**(1-2) 23–30 (2001).
- [75] D. T. Anderson, S. Davis, T. S. Zwier, and D. J. Nesbitt. An intense slit discharge source of jet-cooled molecular ions and radicals ($T_{\text{rot}} < 30$ K). *Chemical Physics Letters*, **258**(1-2) 207–212 (1996).
- [76] C. Savage, F. Dong, and N. D. J. Toward a quantum-mechanical understanding of the high-resolution infrared spectrum of CH_5^+ . In *International Symposium on Molecular Spectroscopy 61st Meeting*, Talk TA5. The Ohio State University, Columbus, OH (2006).
- [77] X. C. Huang, A. B. McCoy, J. M. Bowman, L. M. Johnson, C. Savage, F. Dong, and D. J. Nesbitt. Quantum deconstruction of the infrared spectrum of CH_5^+ . *Science*, **311**(5757) 60–63 (2006).
- [78] J. C. Owruksy, E. R. Keim, J. V. Coe, and R. J. Saykally. Absolute IR intensities of the ν_1 bands of HN_2^+ and HCO^+ determined by direct laser-absorption spectroscopy in fast ion-beams. *Journal of Physical Chemistry*, **93**(16) 5960–5963 (1989).
- [79] E. R. Keim, M. L. Polak, J. C. Owruksy, J. V. Coe, and R. J. Saykally. Absolute infrared vibrational band intensities of molecular-ions determined by direct laser-absorption spectroscopy in fast ion-beams. *Journal of Chemical Physics*, **93**(5) 3111–3119 (1990).
- [80] K. N. Crabtree, C. A. Kauffman, and B. J. McCall. Note: A modular and robust continuous supersonic expansion discharge source. *Review of Scientific Instruments*, **81**(8) 086103 (2010).
- [81] J. Ye, L.-S. Ma, and J. L. Hall. Ultrasensitive detections in atomic and molecular physics: Demonstration in molecular overtone spectroscopy. *Journal of the Optical Society of America B-Optical Physics*, **15**(15) 6–15 (1998).
- [82] D. W. Ferguson, K. N. Rao, P. A. Martin, and G. Guelachvili. High-resolution infrared Fourier-transform emission-spectra of the $^{14}\text{N}_2^+$ Meinel system - $\text{A}^2\Pi_u - \text{X}^2\Sigma_g^+$. *Journal of Molecular Spectroscopy*, **153**(1-2) 599–609 (1992).
- [83] K. W. Busch and M. A. Busch, editors. *Cavity-Ringdown Spectroscopy. An Ultratrace-Absorption Measurement Technique*. American Chemical Society (1999).
- [84] R. F. Stebbings, A. C. H. Smith, and B. R. Truner. Charge transfer in oxygen, nitrogen, and nitric oxide. *Journal of Chemical Physics*, **38**(9) 2277 (1963).
- [85] R. W. P. Drever, J. L. Hall, F. V. Kowalski, J. Hough, G. M. Ford, A. J. Munley, and H. Ward. Laser phase and frequency stabilization using an optical-resonator. *Applied Physics B-photonics and Laser Chemistry*, **31**(2) 97–105 (1983).
- [86] B. M. Siller, A. A. Mills, M. W. Porambo, and B. J. McCall. Noise immune cavity enhanced optical heterodyne velocity modulation spectroscopy. *Optics Express*, **In Press** (2011).
- [87] W. Koechner. *Solid-State Laser Engineering*. Springer-Verlag, Berlin, Heidelberg, New York, 5th edition (1999).
- [88] A. W. Tucker, M. Birnbaum, C. L. Fincher, and J. W. Erler. Stimulated-emission cross-section at 1064 and 1342 nm in Nd-YVO₄. *Journal of Applied Physics*, **48**(12) 4907–4911 (1977).
- [89] R. A. Fields, M. Birnbaum, and C. L. Fincher. Highly efficient Nd-YVO₄ diode-laser end-pumped laser. *Applied Physics Letters*, **51**(23) 1885–1886 (1987).
- [90] G. L. Lippi, J. R. Tredicce, N. B. Abraham, and F. T. Arecchi. Deterministic mode alternation, giant pulses and chaos in a bidirectional CO₂ ring laser. *Optics Communications*, **53**(2) 129–132 (1985).
- [91] J. R. Tredicce, G. L. Lippi, F. T. Arecchi, and N. B. Abraham. Stable oscillations in a bistable, bidirectional CO₂ ring laser. *Philosophical Transactions of the Royal Society of London Series A-Mathematical Physical and Engineering Sciences*, **313**(1525) 411–415 (1984).

- [92] F. T. Arecchi, G. Lippi, J. R. Tredicce, and N. B. Abraham. Spontaneous oscillations, generalized multistability, and intermittency route to chaos in a bidirectional CO₂ ring laser. *Journal of the Optical Society of America B-Optical Physics*, **1**(3) 497–497 (1984).
- [93] K. Nyholm, M. Merimaa, T. Ahola, and A. Lassila. Frequency stabilization of a diode-pumped Nd:Yag laser at 532 nm to iodine by using third-harmonic technique. *IEEE Transactions On Instrumentation and Measurement*, **52**(2) 284–287 (2003).
- [94] B. A. Tom, V. Zhaunerchyk, M. B. Wiczer, A. A. Mills, K. N. Crabtree, M. Kaminska, W. D. Geppert, M. Hamberg, M. af Ugglas, E. Vigren, W. J. van der Zande, M. Larsson, R. D. Thomas, and B. J. McCall. Dissociative recombination of highly enriched para-H₃⁺. *Journal of Chemical Physics*, **130**(3) 031101 (2009).
- [95] B. A. Tom, A. A. Mills, M. B. Wiczer, K. N. Crabtree, and B. J. McCall. Communications: Development and characterization of a source of rotationally cold, enriched para-H₃⁺. *Journal of Chemical Physics*, **132**(8) 081103 (2010).
- [96] B. A. Tom. *Nuclear Spin Dependence in Reactions of H₃⁺ in the Laboratory and the Interstellar Medium*. Ph.D. thesis, University of Illinois at Urbana-Champaign (2009).
- [97] A. S. Pine. Doppler-limited molecular spectroscopy by difference-frequency mixing. *Journal of the Optical Society of America*, **64**(12) 1683–1690 (1974).
- [98] G. D’Amico, G. Pesce, G. Rusciano, and A. Sasso. A DFG spectrometer at 3 μ m for high resolution molecular spectroscopy and trace gas detection. *Optics and Lasers in Engineering*, **37**(5) 481–493 (2002).
- [99] M. W. Fischer, Cornelia & Sigrist. *Solid-State Mid-Infrared Laser Sources*, volume 89 of *Topics in Applied Physics*, chapter Mid-IR Difference Frequency Generation, (pages 97–140). Springer-Verlag, Berlin, Heidelberg, New York (2003).
- [100] J. A. Armstrong, N. Bloembergen, J. Ducuing, and P. S. Pershan. Interactions between light waves in a nonlinear dielectric. *Physical Review*, **127**(6) 1918 (1962).
- [101] I. A. Ghambaryan, R. Guo, R. K. Hovsepyan, A. R. Poghosyan, E. S. Vardanyan, and V. G. Lazaryan. Periodically poled structures in lithium niobate crystals: Growth and photoelectric properties. *Journal of Optoelectronics and Advanced Materials*, **5**(1) 61–68 (2003).
- [102] D. H. Jundt. Temperature-dependent Sellmeier equation for the index of refraction, n_e , in congruent lithium niobate. *Optics Letters*, **22**(20) 1553–1555 (1997).
- [103] L. H. Deng, X. M. Gao, Z. S. Cao, W. D. Chen, Y. Q. Yuan, W. J. Zhang, and Z. B. Gong. Improvement to Sellmeier equation for periodically poled LiNbO₃ crystal using mid-infrared difference-frequency generation. *Optics Communications*, **268**(1) 110–114 (2006).
- [104] M. Takahashi, S. Ohara, T. Tezuka, H. Ashizawa, M. Endo, S. Yamaguchi, K. Nanri, and T. Fujioka. Trace gas monitor based on difference frequency generation at 4 μ m using mass-production laser diodes as pump and signal light sources. *Applied Physics B-lasers and Optics*, **78**(2) 229–233 (2004).
- [105] Z. Cao, X. Gao, L. Deng, W. Chen, Y. Yuan, W. Zhang, and Z. Gong. A difference frequency generation spectrometer and its detection of atmospheric N₂O. *Spectrochimica Acta Part A: Molecular and Biomolecular Spectroscopy*, **68**(1) 74–77 (2007).
- [106] Nobelprize.org. The nobel prize in physics 2005. WEB. Accessed 16 Sept 2010.
- [107] T. Udem, J. Reichert, R. Holzwarth, M. Niering, M. Weitz, and T. W. Hansch. Measuring the frequency of light with mode-locked lasers. *Frequency Measurement and Control Advanced Techniques and Future Trends*, **79** 275–294 (2000).
- [108] Y. H. Wang, R. Dumke, T. Liu, A. Stejskal, Y. N. Zhao, J. Zhang, Z. H. Lu, L. J. Wang, T. Becker, and H. Walther. Absolute frequency measurement and high resolution spectroscopy of ¹¹⁵In⁺ 5s² ¹S₀ – 5s5p ³P₀ narrowline transition. *Optics Communications*, **273**(2) 526–531 (2007).
- [109] R. Gebs, T. Dekorsy, S. A. Diddams, and A. Bartels. 1-GHz repetition rate femtosecond OPO with stabilized offset between signal and idler frequency combs. *Optics Express*, **16**(8) 5397–5405 (2008).
- [110] A. Bartels, D. Heinecke, and S. A. Diddams. Passively mode-locked 10 Ghz femtosecond Ti:Sapphire laser. *Optics Letters*, **33**(16) 1905–1907 (2008).
- [111] A. Bartels, D. Heinecke, and S. A. Diddams. 10-GHz self-referenced optical frequency comb. *Science*, **326**(5953) 681–681 (2009).
- [112] C. J. Wang and P. Sahay. Breath analysis using laser spectroscopic techniques: Breath biomarkers, spectral fingerprints, and detection limits. *Sensors*, **9**(10) 8230–8262 (2009).

- [113] C. Gohle, B. Stein, A. Schliesser, T. Udem, and T. W. Hansch. Frequency comb Vernier spectroscopy for broadband, high-resolution, high-sensitivity absorption and dispersion spectra. *Physical Review Letters*, **99**(26) 263902 (2007).
- [114] G. Walker. Extrasolar planets: With a coarse-tooth comb. *Nature*, **452**(7187) 538–539 (2008).
- [115] D. A. Braje, M. S. Kirchner, S. Osterman, T. Fortier, and S. A. Diddams. Astronomical spectrograph calibration with broad-spectrum frequency combs. *European Physical Journal D*, **48**(1) 57–66 (2008).
- [116] C. H. Li, A. G. Glenday, A. J. Benedick, G. Q. Chang, L. J. Chen, C. Cramer, P. Fendel, G. Furesz, F. X. Kartner, S. Korzennik, D. F. Phillips, D. Sasselov, A. Szentgyorgyi, and R. L. Walsworth. In-situ determination of astro-comb calibrator lines to better than 10 cm s^{-1} . *Optics Express*, **18**(12) 13239–13249 (2010).
- [117] M. T. Murphy, T. Udem, R. Holzwarth, A. Sizmann, L. Pasquini, C. Araujo-Hauck, H. Dekker, S. D’Odorico, M. Fischer, T. W. Hansch, and A. Manescau. High-precision wavelength calibration of astronomical spectrographs with laser frequency combs. *Monthly Notices of the Royal Astronomical Society*, **380**(2) 839–847 (2007).
- [118] T. Shioda, K. Fujii, K. Kashiwagi, and T. Kurokawa. High-resolution spectroscopy combined with the use of optical frequency comb and heterodyne detection. *Journal of the Optical Society of America B-Optical Physics*, **27**(7) 1487–1491 (2010).
- [119] F. Adler, P. Maslowski, A. Foltynowicz, K. C. Cossel, T. C. Briles, I. Hartl, and J. Ye. Mid-infrared Fourier transform spectroscopy with a broadband frequency comb. *Optics Express*, **18**(21) 21861–21872 (2010).
- [120] I. Coddington, W. C. Swann, and N. R. Newbury. Coherent dual-comb spectroscopy at high signal-to-noise ratio. *Physical Review A*, **82**(4) 043817 (2010).
- [121] N. R. Newbury, I. Coddington, and W. Swann. Sensitivity of coherent dual-comb spectroscopy. *Optics Express*, **18**(8) 7929–7945 (2010).
- [122] T. Yasui, M. Nose, A. Ihara, K. Kawamoto, S. Yokoyama, H. Inaba, K. Minoshima, and T. Araki. Fiber-based, hybrid terahertz spectrometer using dual fiber combs. *Optics Letters*, **35**(10) 1689–1691 (2010).
- [123] V. Ilchenko and A. Matsko. Optical resonators with whispering-gallery modes - part II: Applications. *IEEE Journal of Selected Topics in Quantum Electronics*, **12**(1) 15–32 (2006).
- [124] L. Helt, Z. Yang, M. Liscidini, and J. Sipe. Spontaneous four-wave mixing in microring resonators. *Optics Letters*, **35**(18) 3006–3008 (2010).
- [125] D. Mazzotti, S. Borri, P. Cancio, G. Giusfredi, and P. De Natale. Low-power lamb-dip spectroscopy of very weak CO_2 transitions near $4.25 \mu\text{m}$. *Optics Letters*, **27**(14) 1256–1258 (2002).
- [126] Z. D. Sun, Q. Liu, R. M. Lees, L. H. Xu, M. Y. Tret'yakov, and V. V. Dorovskikh. Saturation-dip measurements in the $2\nu_2$ overtone band of OCS with a CO_2 -laser/microwave-sideband spectrometer. *Applied Physics B-Lasers and Optics*, **78**(6) 791–795 (2004).
- [127] I. Sherstov, S. Liu, C. Lisdat, H. Schnatz, S. Jung, H. Knockel, and E. Tiemann. Frequency measurements in the $\text{B } ^3\Pi(0_u^+) - \text{X } ^1\Sigma_g^+$ system of K_2 . *European Physical Journal D*, **41**(3) 485–492 (2007).
- [128] P. Malara, P. Maddaloni, G. Gagliardi, and P. De Natale. Absolute frequency measurement of molecular transitions by a direct link to a comb generated around $3 \mu\text{m}$. *Optics Express*, **16**(11) 8242–8249 (2008).
- [129] S. Borri, S. Bartalini, I. Galli, P. Cancio, G. Giusfredi, D. Mazzotti, A. Castrillo, L. Gianfrani, and P. De Natale. Lamb-dip-locked quantum cascade laser for comb-referenced IR absolute frequency measurements. *Optics Express*, **16**(15) 11637–11646 (2008).
- [130] K. Takahata, T. Kobayashi, H. Sasada, Y. Nakajima, H. Inaba, and F.-L. Hong. Absolute frequency measurement of sub-Doppler molecular lines using a $3.4\text{-}\mu\text{m}$ difference-frequency-generation spectrometer and a fiber-based frequency comb. *Physical Review A*, **80**(3) 032518 (2009).
- [131] T. Udem, R. Holzwarth, and T. W. Hansch. Optical frequency metrology. *Nature*, **416**(6877) 233–237 (2002).
- [132] P. Maddaloni, P. Cancio, and P. De Natale. Optical comb generators for laser frequency measurement. *Measurement Science & Technology*, **20**(5) 052001 (2009).
- [133] M. Kourogi, K. Imai, B. Widiyatmoko, and M. Ohtsu. Generation of expanded optical frequency combs. *Frequency Measurement and Control Advanced Techniques and Future Trends*, **79** 315–335 (2000).
- [134] R. Holzwarth, M. Zimmermann, T. Udem, and T. W. Hansch. Optical clockworks and the measurement of laser frequencies with a mode-locked frequency comb. *IEEE Journal of Quantum Electronics*, **37**(12) 1493–1501 (2001).

- [135] F. L. Hong, K. Minoshima, A. Onae, H. Inaba, H. Takada, A. Hirai, and H. Matsumoto. Broad-spectrum frequency comb generation and carrier-envelope offset frequency measurement by second-harmonic generation of a mode-locked fiber laser. *Optics Letters*, **28**(17) 1516–1518 (2003).
- [136] B. Parvitte, V. Zeninari, C. Thiebaux, A. Delahaigue, and D. Courtois. Infrared laser heterodyne systems. *Spectrochimica Acta Part A-molecular and Biomolecular Spectroscopy*, **60**(5) 1193–1213 (2004).
- [137] E. A. Donley, T. P. Heavner, F. Levi, M. O. Tataw, and S. R. Jefferts. Double-pass acousto-optic modulator system. *Review of Scientific Instruments*, **76**(6) 063112 (2005).
- [138] E. D. Black. An introduction to Pound-Drever-Hall laser frequency stabilization. *American Journal of Physics*, **69**(1) 79–87 (2001).
- [139] H. Kogelnik and T. Li. Laser beams and resonators. *Applied Optics*, **5**(5) 1550–67 (1966).
- [140] S. W. North, X. S. Zheng, R. Fei, and G. E. Hall. Line shape analysis of Doppler broadened frequency-modulated line spectra. *Journal of Chemical Physics*, **104**(6) 2129–2135 (1996).
- [141] G. C. Bjorklund, M. D. Levenson, W. Lenth, and C. Ortiz. Frequency-modulation (FM) spectroscopy - Theory of lineshapes and signal-to-noise analysis. *Applied Physics B-Photophysics and Laser Chemistry*, **32**(3) 145–152 (1983).
- [142] F. M. Schmidt, A. Foltynowicz, W. G. Ma, and O. Axner. Fiber-laser-based noise-immune cavity-enhanced optical heterodyne molecular spectrometry for doppler-broadened detection of C₂H₂ in the parts per trillion range. *Journal of the Optical Society of America B-Optical Physics*, **24**(6) 1392–1405 (2007).
- [143] R. J. Butcher. Sub-Doppler laser spectroscopy. *Optical and Quantum Electronics*, **25**(2) 79–95 (1993).
- [144] A. Foltynowicz, W. G. Ma, F. M. Schmidt, and O. Axner. Doppler-broadened noise-immune cavity-enhanced optical heterodyne molecular spectrometry signals from optically saturated transitions under low pressure conditions. *Journal of the Optical Society of America B-Optical Physics*, **25**(7) 1156–1165 (2008).
- [145] W. Demtroder. *Laser spectroscopy : Basic concepts and instrumentation*, chapter Widths and profiles of spectral lines, (page 83). Springer-Verlag, Berlin ; New York :, 4 edition (2008).
- [146] W. Demtroder. *Laser spectroscopy : Basic concepts and instrumentation*, chapter Widths and profiles of spectral lines, (page 70). Springer-Verlag, Berlin ; New York :, 4 edition (2008).
- [147] A. v. Engel. *Ionized Gases*, chapter ionization and extraction in an electric field, (page 195). American institute of Physics (1965).
- [148] K. N. Crabtree, C. A. Kauffman, B. A. Tom, E. Beka, B. A. McGuire, and B. J. McCall. Nuclear spin dependence of the reaction of H₃⁺ with H₂. II. experimental measurements. *Journal of Chemical Physics*, **134** 194311 (2011).
- [149] J. M. B. Bakker. Beam-modulated time-of-flight mass-spectrometer 1. Theoretical considerations. *Journal of Physics E-Scientific Instruments*, **6**(8) 785–789 (1973).
- [150] J. M. B. Bakker. Beam-modulated time-of-flight mass-spectrometer 2. Experimental work. *Journal of Physics E-Scientific Instruments*, **7**(5) 364–368 (1974).
- [151] J. H. Moore, C. C. Davis, and M. A. Coplan. *Building Scientific Aparatus*, chapter Charged particle optics, (pages 371–372). Perseus Books (2002).
- [152] J. R. Pierce. Rectilinear electron flow in beams. *Journal of Applied Physics*, **11**(8) 548–554 (1940).
- [153] D. A. Dahl. SIMION for the personal computer in reflection. *International Journal of Mass Spectrometry*, **200**(1-3) 3–25 (2000).
- [154] SIMION 3D 8.0. <http://www.simion.com> (2008).
- [155] D. W. O. Heddle. *Electrostatic Lens Systems*, chapter The optics of simple lens systems, (pages 61–65). Institute of Physics Publishing, 2nd edition (2000).
- [156] H. Kreckel, H. Bruhns, K. A. Miller, E. Wahlin, A. Davis, S. Hockh, and D. W. Savin. A simple double-focusing electrostatic ion beam deflector. *Review of Scientific Instruments*, **81**(6) 063304 (2010).
- [157] J. H. Moore, C. C. Davis, and M. A. Coplan. *Building Scientific Aparatus*, chapter Charged particle optics, (pages 389–390). Perseus Books (2002).
- [158] M. G. Inghram and H. R. J. A handbook on mass spectroscopy. In *Nuclear Science Series* (1954).
- [159] J. Anderson and D. Swann. A bunching and chopping system for the generation of short duration ion bursts. *Nuclear Instruments and Methods*, **30**(1) 1–22 (1964).

- [160] T. Fowler and W. Good. A theory on obtaining short bursts of ions from a beam of ions. *Nuclear Instruments and Methods*, **7**(3) 245–252 (1960).
- [161] A. M. Shaw. *Astrochemistry: from astronomy to astrobiology*, chapter The interstellar medium, (page 130). Wiley (2006).
- [162] G. H. Dunn and B. Vanzyl. Electron impact dissociation of H_2^+ . *Physical Review*, **154**(1) 40– (1967).
- [163] D. Bates and I. Estermann, editors. *Advances in atomic and molecular physics*, volume 10, (page 332). Academic Press (1980).
- [164] P. C. Souers. *Hydrogen Properties for Fusion Energy*, chapter Reactions in Irradiated Hydrogen, (page 244). University of California Press (1986).
- [165] W. Demtroder. *Laser spectroscopy : Basic concepts and instrumentation*, chapter Laser spectroscopy in molecular beams, (pages 553–555). Springer-Verlag, Berlin ; New York :, 4 edition (2008).
- [166] A. B. Meinel. A new band system of N_2^+ in the infrared auroral spectrum. *Astrophysical Journal*, **112** 562–563 (1950).
- [167] A. B. Meinel. The analysis of auroral emission bands from the A $^2\Pi$ state of N_2^+ . *Astrophysical Journal*, **114** 431–432 (1951).
- [168] W. Benesch, D. Rivers, and J. Moore. High-resolution spectrum of the N_2^+ meinel system to 11 250 Å. *Journal of the Optical Society of America*, **70**(7) 792–799 (1980).
- [169] M. B. Radunsky and R. J. Saykally. Electronic absorption-spectroscopy of molecular-ions in plasmas by dye-laser velocity modulation - The A \leftarrow X system of N_2^+ . *Journal of Chemical Physics*, **87**(2) 898–901 (1987).
- [170] D. T. Cramb, A. G. Adam, D. M. Steunenberg, A. J. Merer, and M. C. L. Gerry. Electronic absorption-spectroscopy of N_2^+ using velocity modulation - rotational structure in the (6, 1) and (13, 6) vibrational bands of the A-X system. *Journal of Molecular Spectroscopy*, **141**(2) 281–289 (1990).
- [171] B. Lindgren, P. Royen, and M. Zackrisson. The rotational structure of the (8, 3) band of the $\text{A}_2\Pi_u$ -X $^2\Sigma_g^+$ system of N_2^+ studied by velocity modulation laser spectroscopy. *Journal of Molecular Spectroscopy*, **146**(2) 343 – 350 (1991).
- [172] M. Turek, A. Pysznik, A. Drozdziel, J. Sielanko, A. Latuszynski, D. Maczka, Y. Vaganov, and Y. Yushkevich. Numerical model for extraction of ions from plasma. *Instruments and Experimental Techniques*, **52**(1) 90–98 (2009-01-01).
- [173] I. Langmuir. Positive ion currents from the positive column of mercury arcs. *Science*, **58**(1502) 290–291 (1923).
- [174] A. Carrington and J. Buttenshaw. Vibration-rotation spectroscopy of the HD^+ ion near the dissociation limit .1. Experimental methods and measurements of the $\nu=18$ -16 band. *Molecular Physics*, **44**(2) 267–285 (1981).
- [175] S. J. Hill, editor. *Inductively Coupled Plasma Spectrometry and its Applications*, (page 39). Sheffield Analytical Chemistry Series. Wiley-Blackwell (2007).
- [176] C. M. Western. Pgopher, a program for simulating rotational structure. <http://pgopher.chm.bris.ac.uk> (2009).
- [177] A. Foltynowicz, W. G. Ma, and O. Axner. Characterization of fiber-laser-based sub-Doppler NICE-OHMS for quantitative trace gas detection. *Optics Express*, **16**(19) 14689–14702 (2008).
- [178] S. Green, M. J. A., and P. Thaddeus. Tentative identification of U93.174 as molecular ion HN_2^+ . *Astrophysical Journal*, **193**(2) L89–L91 (1974).
- [179] T. G. Anderson, T. A. Dixon, N. D. Piltch, R. J. Saykally, P. G. Szanto, and R. C. Woods. Laboratory rest frequencies for DN_2^+ . *Astrophysical Journal*, **216**(2) L85–L86 (1977).
- [180] J. C. Pearson and B. J. Drouin. Laboratory measurement of the J= 1-0 transition of CH^+ . *The Astrophysical Journal*, **647** L83–L86 (2006).
- [181] R. Kobayashi, H. Koch, P. Jorgensen, and T. J. Lee. Comparison of coupled-cluster and Brueckner coupled-cluster calculations of molecular properties. *Chemical Physics Letters*, **211** 94 (1993).
- [182] B. Follmeg, P. Rosmus, and H. J. Werner. Vibration-rotation transition-probabilities in CH^+ and CD^+ . *Chemical Physics Letters*, **136**(6) 562–565 (1987).
- [183] A. Carrington and D. A. Ramsay. Some new emission bands of the A $^1\Pi$ -X $^1\Sigma^+$ system of CH^{++} . *Physica Scripta*, **25** 272–274 (1982).
- [184] S. Kwok. *Physics and Chemistry of the Interstellar Medium*, chapter Interstellar Molecules, (page 247). University Science Books (2006).

- [185] F. van den Heuvel and A. Dymanus. Observation of far-infrared transitions of HCO^+ , CO^+ and HN_2^+ . *Chemical Physics Letters*, **92**(3) 219 (1982).
- [186] S. Chin and W. B. Person. Quantitative prediction of infrared spectra of isolated molecular ions and radicals. 1. Carbonyl (CO^+), carbon dioxide cation (CO_2^+), and carbon disulfide cation (CS_2^+). *Journal of Physical Chemistry*, **88** 553–559 (1984).
- [187] P. B. Davies and W. J. Rothwell. Infrared laser spectrum of the fundamental band of CO^+ ($X^2\Sigma^+$). *Journal of Chemical Physics*, **83** 5450–5453 (1985).
- [188] N. N. Haese and R. Woods. Configuration interaction electric dipole moments for HCN, HNC, HNN^+ , HCO^+ , HBO, HBF^+ , and HCNH^+ . *Chemical Physics Letters*, **61**(2) 396–398 (1979).
- [189] T. G. Anderson, G. C. S., T. A. Dixon, and R. C. Woods. Pressure broadening of the HCO^+ J=0-1 transition by hydrogen. *Journal of Chemical Physics*, **72** 1332–1338 (1980).
- [190] R. J. Saykally and R. C. Woods. High resolution spectroscopy of molecular ions. *Annual Reviews*, **32** 403–431 (1981).
- [191] M. Bogey, C. Demuyne, and J. L. Destombes. Centrifugal distortion effects in HCO^+ from its millimetre spectrum. *Molecular Physics*, **43**(5) 1043–1050 (1981).
- [192] T. Amano. The ν_1 fundamental-band of HCO^+ by difference frequency laser spectroscopy. *Journal of Chemical Physics*, **79**(7) 3595–3595 (1983).
- [193] C. S. Gudeman and R. C. Woods. Microwave spectroscopy of the formyl ion (HCO^+), the isoformyl ion (HOC^+), the thioformyl ion (HCS^+), and hydrogen-cyanide. *Abstracts of Papers of the American Chemical Society*, **187**(APR) 39 (1984).
- [194] K. Kawaguchi, C. Yamada, S. Saito, and E. Hirota. Magnetic field modulated infrared laser spectroscopy of molecular ions: The ν_2 band of HCO^+ . *Journal of Chemical Physics*, **82** 1750–1756 (1985).
- [195] G. A. Blake, K. B. Laughlin, R. C. Cohen, K. L. Busarow, and R. J. Saykally. Laboratory measurement of the pure rotational spectrum of vibrationally excited HCO^+ ($\nu_2 = 1$) by far-infrared laser side-band spectroscopy. *Astrophysical Journal*, **316**(1) L45–L48 (1987).
- [196] E. Hirota and Y. Endo. Microwave spectroscopy of HCO^+ and DCO^+ in excited vibrational states. *Journal of Molecular Spectroscopy*, **127** 527–534 (1988).
- [197] T. Amano and T. Nakanaga. Laboratory measurements of the abundance ratio $[\text{HCO}^+]/[\text{HOC}^+]$ and their astrophysical implications. *Astrophysical Journal*, **328**(1) 373–379 (1988).
- [198] J. D. Rogers and J. J. Hillman. Ab initio calculation of infrared intensities for the linear isoelectronic series HCN, HNC, CO, HCO^+ , and HOC^+ . *Journal of Chemical Physics*, **77**(7) 3615 (1982).
- [199] K. V. L. N. Sastry, E. Herbst, and F. C. De Lucia. Millimeter and submillimeter spectra of HCO^+ and DCO^+ . *Journal of Chemical Physics*, **75** 4169 (1981).
- [200] T. Nakanaga and T. Amano. Infrared detection of HOC^+ by difference frequency laser spectroscopy. *Journal of Molecular Spectroscopy*, **121** 502–504 (1987).
- [201] T. Amano and A. Maeda. Double-modulation submillimeter-wave spectroscopy of HOC^+ in the ν_2 excited vibrational. *Journal of Molecular Spectroscopy*, **203** 140–144 (2000).
- [202] L. Margles, F. Lewen, G. Winnewisser, P. Botschwina, and H. S. P. Muller. The rotational spectrum up to 1 THz and the molecular structure of thiomethylum, HCS^+ . *Physical Chemistry and Chemical Physics*, **5** 2770–2773 (2003).
- [203] A. A. Mills, A. Perera, R. J. Bartlett, M. Keceli, and B. J. McCall. Theoretical support for high resolution spectroscopy of C_3H_3^+ . *Journal of Physical Chemistry A*, **In Preparation** (2012).
- [204] P. Michaud, J. Delfau, and A. Barassin. The positive ion chemistry in the post-combustion zone of sooting premixed acetylene low pressure flat flames. *Symposium (International) on Combustion*, **18**(1) 443–451 (1981).
- [205] K. C. Smyth, S. G. Lias, and P. Ausloos. The ion-molecule chemistry of C_3H_3^+ and the implications for soot formation. *Combustion Science and Technology*, **28**(3) 147–154 (1982).
- [206] A. Korth, M. L. Marconi, D. A. Mendis, F. R. Krueger, A. K. Richter, R. P. Lin, D. L. Mitchell, K. A. Anderson, C. W. Carlson, H. Reme, J. A. Sauvaud, and C. Duston. Probable detection of organic-dust-borne aromatic C_3H_3^+ ions in the coma of comet halley. *Nature*, **337**(6202) 53–55 (1989).
- [207] K. D. Retherford, G. R. Gladstone, and E. F. Young. Tentative detection of cyclopropenyl ion emissions in the jovian aurorae with IRTF/CSHELL observation. In *Bulletin of the American Astronomical Society*, volume 38, (page 558). Southwest Research Institute, American Astronomical Society (2006).

- [208] W. M. Irvine. Organic molecules in the gas phase of dense interstellar clouds. *Advances in Space Research*, **15**(3) 35–43 (1995).
- [209] P. Thaddeus, J. M. Vrtilek, and C. A. Gottlieb. Laboratory and astronomical identification of cyclopropenyldene, C_3H_2 . *Astrophysical Journal*, **299**(1) L63–L66 (1985).
- [210] P. Cox, R. Gusten, and C. Henkel. Observations of C_3H_2 in the diffuse interstellar-medium. *Astronomy and Astrophysics*, **206**(1) 108–116 (1988).
- [211] N. C. Craig, J. Pranata, S. J. Reinganum, J. R. Sprague, and P. S. Stevens. Vibrational spectra of cyclopropenyl cations ($C_3H_3^+$, $C_3D_3^+$, $C_3H_2D^+$, and $C_3D_2H^+$) and force constants for this ion system. *Journal of the American Chemical Society*, **108**(15) 4378–4386 (1986).
- [212] M. Wyss, E. Riaplov, and J. P. Maier. Electronic and infrared spectra of $H_2C_3H^+$ and cyclic $C_3H_3^+$ in neon matrices. *Journal of Chemical Physics*, **114**(23) 10355–10361 (2001).
- [213] O. Dopfer, D. Roth, and J. P. Maier. Interaction of $C_3H_3^+$ isomers with molecular nitrogen: Ir spectra of $C_3H_3^+-(N_2)_n$ clusters ($n=1-6$). *International Journal of Mass Spectrometry*, **218**(3) 281–297 (2002).
- [214] O. Dopfer, D. Roth, and J. P. Maier. Infrared spectra of $C_3H_3^+-N_2$ dimers: Identification of proton-bound *c*- $C_3H_3^+-N_2$ and $H_2CCCH^+-N_2$ isomers. *Journal of the American Chemical Society*, **124**(3) 494–502 (2002).